



The University of
Nottingham

UNITED KINGDOM · CHINA · MALAYSIA

Abdulkadir, Mukhtar. (2011) Experimental and computational fluid dynamics (CFD) studies of gas-liquid flow in bends. PhD thesis, University of Nottingham.

Access from the University of Nottingham repository:

http://eprints.nottingham.ac.uk/12218/1/MUKHTAR_ABDULKADIR%27S_COMPLETE_PhD_THESIS_%28_2011_%29.pdf

Copyright and reuse:

The Nottingham ePrints service makes this work by researchers of the University of Nottingham available open access under the following conditions.

- Copyright and all moral rights to the version of the paper presented here belong to the individual author(s) and/or other copyright owners.
- To the extent reasonable and practicable the material made available in Nottingham ePrints has been checked for eligibility before being made available.
- Copies of full items can be used for personal research or study, educational, or not-for-profit purposes without prior permission or charge provided that the authors, title and full bibliographic details are credited, a hyperlink and/or URL is given for the original metadata page and the content is not changed in any way.
- Quotations or similar reproductions must be sufficiently acknowledged.

Please see our full end user licence at:

http://eprints.nottingham.ac.uk/end_user_agreement.pdf

A note on versions:

The version presented here may differ from the published version or from the version of record. If you wish to cite this item you are advised to consult the publisher's version. Please see the repository url above for details on accessing the published version and note that access may require a subscription.

For more information, please contact eprints@nottingham.ac.uk



The University of
Nottingham

UNITED KINGDOM • CHINA • MALAYSIA

Department of Chemical and Environmental
Engineering

**Experimental and Computational Fluid Dynamics (CFD) Studies
of Gas-Liquid Flow in Bends**

By

Mukhtar Abdulkadir, BEng, MSc

Thesis submitted to the University of Nottingham for the
degree of Doctor of Philosophy

August 2011

ABSTRACT

Within the oil industry there is a need to measure and predict the form of the multiphase liquid and gas flows that are present within oil production and processing pipelines. Knowledge of the flow regimes present allows the engineer to optimise the configuration of the pipeline and downstream processes to achieve the most, economic and reliable design. The applications of these technologies are collectively known as flow assurance. Within oil production systems, one component which has received little attention is the characterisation of the multiphase flow around bends under various process conditions. To predict the flow regimes in greater details requires the development of instrumentation that can measure and characterise the flow within the pipes.

To circumvent this challenge, two experimental investigations were carried out in two rigs available in the Chemical and Environmental Engineering Laboratories at the University of Nottingham. These are: (1) a 67 mm internal diameter pipe joined to a 90° bend, in which air/silicone oil flows were investigated using advanced instrumentation: Electrical Capacitance Tomography (ECT), Wire Mesh Sensor Tomography (WMS), and high-speed video. The first two provide time and cross-sectionally resolved data on void fraction. The ECT probes were mounted 10 diameters upstream of the bend whilst the WMS was positioned either immediately upstream or immediately downstream of the bend. The downstream pipe was maintained horizontal whilst the upstream pipe was mounted either vertically or horizontally. The bend ($R/D = 2.3$) was made of transparent acrylic resin. The superficial velocities of the air ranged from 0.05 to

4.73 ms⁻¹ and for the silicone oil from 0.05 to 0.38 ms⁻¹. (2) a 127 mm internal diameter riser joined to a vertical 180° bend, in which measurements of film fraction and liquid film thickness distribution for an air-water system were obtained using the electrical conductance technique. The former was measured using the ring conductance probes placed 17 and 21 diameters, respectively upstream and downstream of the bend, 45°, 90° and 135° within the bend. The latter were obtained using pin and parallel wire probes. The pin probes were used for thin films measurement whilst the parallel wire probes for thick films. The bend, made of transparent acrylic resin, has a curvature ratio (R/D = 3). The superficial velocities of the air ranged from 3.5 to 16.1 ms⁻¹ and for the water from 0.02 to 0.2 ms⁻¹.

The experimental results for the 90° bend study reveal that bubble/spherical cap bubble, slug, unstable slug and churn flows were observed before the bend for the vertical pipe and plug, slug, stratified wavy and annular flows when the pipe was horizontal. Bubble, stratified wavy, slug, semi-annular and annular flows are seen after the bend for the vertical 90° bend, the flow patterns remained the same as before the horizontal 90° bend. These results were confirmed by the high-speed videos taken around the bend. For the vertical 180° return bend, the average film fraction was identified to be higher in straight pipes than in bends. For low liquid and higher gas flow rates, due to the action of gravity drainage, film breakdown occurs at the 45° bend. A previously proposed criterion, to determine stratification after the 90° bend, based on a modified Froude number have been shown to be valid for a liquid different from that tested in the original paper. Similarly, for the 180° return bend, the condition for which the liquid goes either

to the inside or outside of the bend are identified based on published material. Variations between average liquid film thickness and bend angles are reported for the vertical 180° bend. Contrary to the conclusions reached by Hills (1973) and Anderson and Hills (1974), the liquid film thickness becomes annular flow in the 180° bend at low liquid flow rates and stratified flow at higher liquid superficial velocities.

In addition, a CFD code has been used to successfully model the hydrodynamics of the slug flow pattern in a riser and vertical 90° bend, using the Volume of Fluid model based on the Eulerian approach, implemented in the commercial CFD package Star-CCM+. The modelling results are validated with the experiments and also provide more detailed information on the flow such as the velocity field.

LIST OF PUBLICATIONS

Abdulkadir, M., D. Zhao, Azzi, A., Lowndes, I. S. & Azzopardi, B. J. Two phase air-water flow through a large diameter vertical 180° return bend. *Chemical Engineering Science* (Under review).

Abdulkadir, M., Hernandez-Perez, V., Lo, S., Lowndes, I. S. & Azzopardi, B. J. Experimental and computational fluid dynamic study of slug flow in a vertical riser. *Chemical Engineering Science* (Under review).

Hernandez-Perez, V., Abdulkadir, M., Abdulkareem, L., Abdulahi, A. & Azzopardi, B. J., 2011. The effect of the liquid physical properties on inclined gas-liquid flow. *Journal of Fluids Engineering* (Under review)

Abdulkadir, M., Zhao, D., Sharaf, S., Abdulkareem, L., Lowndes, I.S., Azzopardi, B.J., 2011. Interrogating the effect of 90° bends on air-silicone oil flows using advanced instrumentation. *Chemical Engineering Science* 66, 2453-2467

Hernandez-Perez, V., Abdulkadir, M., & Azzopardi, B. J., 2011. Grid generation issues in the CFD modelling of two-phase flow in a pipe. *The Journal of Computational Multiphase Flow* 3, 13-26

Abdulkadir, M., Hernandez-Perez, V., Lowndes, I. S. & Azzopardi, B. J., 2011. Experimental and computational fluid dynamic study of the characteristics of slug flow in a vertical riser. 8th International Conference on CFD on Oil & Gas, Metallurgical and Process Industries, SINTEF/ NTNU, Trondheim, Norway. 21-23 June

Abdulkadir, M., Azzopardi, B. J., and Lowndes, I. S., 2011. The characterisation of the behaviour of gas-liquid flow using validated Computational Fluid Dynamics (CFD) models. A poster presented at the Engineering Symposium, University of Nottingham. 8 June

Abdulahi, A., Abdulkareem, L., Sharaf, S., Abdulkadir, M., Hernandez-Perez, V. & Azzopardi, B. J., 2011. Investigating the effect of pipe inclination on two-phase gas-liquid flows using advanced instrumentation. 8th ASME/ JSME Thermal Engineering Joint Conference, Honolulu, Hawaii, USA. 13-17 March

Abdulkadir, M., Hernandez-Perez, V., Sharaf, S., Lowndes, I. S. & Azzopardi, B. J., 2010. Phase distributions of an air-silicone oil mixture in a vertical riser. In: 7th International Conference on Heat Transfer, Fluid Mechanics and Thermodynamics, Antalya, Turkey. 19-21 July, pp. 2311-2316

Hernandez-Perez, Abdulkadir, M., Azzopardi, B. J. & da Silva, M., 2010. Slugging frequency correlation for inclined gas-liquid flow. In: 7th International Conference on Heat Transfer, Fluid Mechanics and Thermodynamics, Antalya, Turkey. 19-21 July, pp. 2227-2231

Abdulkadir, M., Hernandez-Perez, V., Sharaf, S., Lowndes, I. S. & Azzopardi, B. J., 2010. Experimental investigation of phase distributions of an air-silicone oil flow in a vertical pipe. World Academy of Science, Engineering and Technology (WASET) 61, 52-59

Hernandez-Perez, Abdulkadir, M., & Azzopardi, B. J., 2010. Slugging frequency correlation for inclined gas-liquid flow. World Academy of Science, Engineering and Technology (WASET) 61, 44-51

Abdulkadir, M., Hernandez-Perez, V., Abdulkareem, L., Lowndes, I. S. & Azzopardi, B. J., 2010. Characteristics of slug flow in a vertical riser. In: 34th SPE Annual International Conference and Exhibition, Tinapa-Calabar, Nigeria. July 31- August 7, SPE 140681, Volume 2, 875-881

Abdulkadir, M., Zhao, D., Sharaf, S., Abdulkareem, L., Lowndes, I.S., Azzopardi, B.J., 2010. Interrogating the effect of bends on gas-liquid flow using advanced instrumentation. ICMF 2010, 7th International Conference on Multiphase Flow, Tampa, Florida, USA. May 30-June 7

Azzopardi, B. J., and Abdulkadir, M., 2010. Modelling and measurements of annular flow in serpentine geometries as in fired reboilers. A paper presented at Cranfield University. 30 November

Azzopardi, B. J., Abdulkareem, L, Sharaf, S., Abdulkadir, M., & Ijioma, A., 2010. Using tomography to interrogate gas-liquid flow. In: 28th UIT Heat Transfer Congress, Brescia, Italy. 21-23 June, pp. 3-13

Abdulkadir, M., Hernandez-Perez, V., Lowndes, I. S., Azzopardi, B. J. & Abdulkareem, L. Experimental study of the hydrodynamic behaviour of slug flow in a vertical riser. (In preparation for journal publication)

Abdulkadir, M., Hernandez-Perez, V., Lo, S., Lowndes, I. S. & Azzopardi, B. J. Experimental and computational fluid dynamic study of slug flow in a vertical 90° bend. (In preparation for journal publication)

Abdulkadir, M., Hernandez-Perez, V., Sharaf, S., Lowndes, I. S. & Azzopardi, B. J., 2011. Phase distributions of a gas-liquid flow in a vertical riser. (In preparation for journal publication).

DEDICATION

I dedicate this project to the memories of my late mother. One whose love I can never forget.

ACKNOWLEDGEMENT

I would like to express sincere appreciation to the Nigerian government through the Petroleum Technology Development Fund (PTDF) for providing the funding of my doctoral studies. I would also like to express my appreciation to the Federal University of Technology, Minna, for granting me a study fellowship for the duration of my studies.

This work has been undertaken within the Joint Project on Transient Multiphase Flows and Flow Assurance. I wish to acknowledge the contributions made to this project by the UK Engineering and Physical Sciences Research Council (EPSRC) and the following:-Advantica; BP Exploration; CD-adapco; Chevron; ConocoPhillips; ENI; ExxonMobil; FEESA; IFP; Institutt for Energiteknikk; Norsk Hydro; PDVSA (INTERVEP); Petrobras; PETRONAS; Scandpower PT; Shell; SINTEF; Statoil and TOTAL. I wish to express my sincere gratitude for this support.

I want to express my deep appreciation to Professor Barry Azzopardi, my main supervisor, for his guidance, support, understanding and constant patience throughout this investigation. My academic development owes much to Professor Azzopardi's Multiphase flow research Laboratory which provided a challenging and friendly environment.

In addition, I would like to thank my second supervisor, Dr. Ian Lowndes, for having given me the opportunity to carry out research on Computational Fluid Dynamics (CFD). I would like to thank him for his guidance, support and encouragement.

I am particularly grateful to Dr. Simon Lo of CD-Adapco who graciously provided the CFD software, Star-CD and Star-CCM+ and also offered substantial time and support. His suggestions for code improvement are much appreciated. My sincere appreciation also goes to Malcolm Byars of Process Tomography for his technical assistance with regards to the ECT.

Special thanks to the laboratory technicians at the L3 laboratories of the Department of Chemical and Environmental Engineering at the University of Nottingham, particularly Phil, Mel, Mick, Reg, Paul, Vicky and Marion for their efforts, support and useful suggestions.

I would also like to thank Professor Azzi who visited Nottingham in the winter of 2009 from the Université des Sciences et de la Technologie Houari Boumediene (USTHB), Algiers, Algeria. His enthusiasm and knowledge on the subject led to many interesting discussions and opened up new avenues of thought. I would like to acknowledge Professor Idris Bugaje for his candid advice whenever I was in need of it.

I am pleased to acknowledge Dr. Donglin Zhao, who helped in conducting the calibration of the pin and wire probes. Without his assistance and ideas, this thesis would have been a much formidable undertaking. The aid of Safa Sharaf and Dr. Loqman Abdulkareem for analysis of respectively, WMS and ECT data is not forgotten.

I wish to express my immense gratitude to Dr. Valente Hernandez-Perez for his help and friendship throughout the years. He is the Leonard Messi of multiphase flow, and quite frankly, this would have taken much longer without his precious

advice. Thanks a lot, Valente.

I thank my fellow students Peter, Dr. Bayo, Dr. Mohammed, Dr. Loqman, Safa, Nazrul, Abdullahi, Ameh, Timothy, Ezekiel, Vicky and Stephen for the many conversations concerning this research, in hand with some utterly purposeless topics which made some afternoons less mundane. Thank you to everyone in the Postgraduate Room B06 for the great times we shared.

A big thank you to all the friends back in Nigeria for their support and encouragement, and to everyone that I have known over the years.

I do not know how many times I thought about this very moment when the thesis will be written up, all wrapped up, ready for submission. To be sincere, I have a hard time believing I did it (I guess the Viva is there to remind me it is not over yet!)... Something tells me I am not the only one to believe it though. How many times have my family and close friends been answered “next month, I think...” to the fierce but legitimate question “when are you finishing? And for the constant patience, the ubiquitous and endless support they showed me throughout the past few years, I am truly and continually grateful.

Without a doubt, I would never have started this research, much less been able to finish, without the love and care of my family. My father, Abdulkadir A., never wavered in his support of my studies. His patience allowed me to find my own path. My brothers and sister Abdullahi, Ibrahim, Usman, Mohammed and Aisha were a great help, supporting me with their words. I would also like to acknowledge my father-in-law for his kind support and understanding. Lastly, and most important, I want to thank my beautiful and remarkable wife, Hauwa. She

inspired me over these many years and supported me in more ways than I put into words. Hauwa gave me the unending love that in the end helped bring this research project to a successful completion. Special love thanks to my son, Faisal for his cheerful face and Maijidda for their constant source of motivation and delight.

Lastly, this acknowledgement would not be complete without thanking God for His abundant grace in my life.

TABLE OF CONTENTS

ABSTRACT	ii	
PUBLISHED PAPERS	v	
DEDICATION	vii	
ACKNOWLEDGEMENTS	viii	
TABLE OF CONTENTS	xii	
LIST OF FIGURES	xv	
LIST OF TABLES	xxiv	
CHAPTER 1	INTRODUCTION	1
1.1	GENERAL INTRODUCTION	1
1.2	BACKGROUND TO THE RESEARCH	1
1.2.1	Slug flow in a vertical riser	1
1.2.2	Gas-liquid two-phase flow in 90° bends	4
1.2.3	Gas-liquid two-phase flow in 180° bends	6
1.3	PROBLEM STATEMENT	7
1.4	AIMS AND OBJECTIVES	7
1.5	METHODOLOGY	8
1.5.1	Experimental method	9
1.5.2	Computational method	10
1.6	STRUCTURE OF THE THESIS	10
CHAPTER 2	LITERATURE REVIEW	13
2.1	FLOW REGIMES IN TWO-PHASE GAS-LIQUID FLOW IN PIPES	13
2.1.1	Flow regime identification	14
2.2	FLOW PATTERN MAPS	23
2.3	FLOW PATTERN IDENTIFICATION	27
2.3.1	Electrical tomography	30
2.3.1.1	Conductance tomography	31
2.3.1.2	Capacitance tomography	33
2.4	SLUG FLOW IN STRAIGHT PIPES	34
2.5	FLOW IN BENDS	42
2.5.1	Single-phase flow	42
2.5.2	Two-phase flow in 90° bends	43
2.5.3	Two-phase flow in 180° bends	48

CHAPTER 3	EXPERIMENTAL DESIGN	59
3.1	OVERVIEW OF THE FLOW FACILITY	60
3.2	SYSTEM (TEST FLUID)	61
3.3	DESCRIPTION OF FLOW FACILITY	62
3.4	INSTALLATION OF A 90° BEND	65
3.5	FLOW FACILITY COMPONENTS	68
3.5.1	Gas-liquid mixing section	69
3.5.2	Gas-liquid separation cyclone	69
3.5.3	Flow measurement section	70
3.5.4	Differential pressure cell (DP cell)	70
3.5.5	Data acquisition	72
3.5.6	High speed video system	73
3.5.7	Void fraction measurement	75
3.5.7.1	Wire mesh sensor (WMS)	75
3.5.7.1.1	Principle of operation of the WMS	77
3.5.7.1.2	Processing of void fraction profiles	80
3.5.7.2	Electrical capacitance tomography (ECT)	83
3.5.7.2.1	Image reconstruction model	85
3.5.7.2.2	Calibration procedure	91
3.6	METHODOLOGY DURING AN EXPERIMENTAL RUN	92
3.7	HAZARD ANALYSIS OF EXPERIMENTAL FACILITY	93
3.8	UNCERTAINTY ANALYSIS OF EXPERIMENTAL MEASUREMENTS	93
3.8.1	Random uncertainty	94
3.8.2	Systematic uncertainty	95
3.8.3	Uncertainty propagation	95
3.9	SUMMARY	99
CHAPTER 4	GAS-LIQUID FLOW IN A VERTICAL 67 mm PIPE	100
4.1	SLUG FLOW IN THE VERTICAL RISER	101
4.2	DETERMINATION OF THE CHARACTERISATION PARAMETERS	103
4.2.1	Rise velocity of a Taylor bubble (structure velocity)	103
4.2.2	Liquid film thickness	104
4.2.3	Slug frequency	105
4.2.4	Lengths of the slug unit, the Taylor bubble and the liquid slug	106
4.3	RESULTS AND DISCUSSION	108
4.3.1	Structure velocity of the Taylor bubble	112
4.3.2	Void fraction in liquid slug, Taylor bubble and liquid film thickness	114

4.3.3	Total pressure and frictional pressure drops	117
4.3.4	Slug frequency	120
4.3.5	Lengths of the liquid slug, the Taylor bubble and the slug unit	123
4.3.6	Comparison of the length of liquid slug with the Khatib and Richardson (1984) method	127
4.4	SUMMARY	127
CHAPTER 5	GAS-LIQUID FLOW IN BENDS OF DIFFERENT ORIENTATIONS	
		130
5.1	TESTING OF INSTRUMENTS	131
5.2	COMPARISON OF PDFs of VOID FRACTION FOR THE ECT AND WMS FOR THE RISER BEFORE THE VERTICAL 90° BEND	132
5.2.1	Reconstructed images of the two-phase flow before the vertical 90° bend as depicted by the WMS	135
5.3	COMPARISON of PDFs of VOID FRACTION BEFORE AND AFTER THE BEND USING THE WMS	136
5.4	FLOW PATTERNS IDENTIFICATION USING HIGH SPEED VIDEO IMAGES	143
5.4.1	Flow regimes in vertical riser (vertical 90° bend)	144
5.4.2	Flow regimes in bend (vertical 90° bend)	147
5.4.3	Flow patterns in the upstream flowline (horizontal 90° bend)	150
5.4.4	Flow patterns in the bend (horizontal 90° bend)	151
5.5	CROSS-SECTIONALLY AVERAGED VOID FRACTION	152
5.6	COMPETITION BETWEEN CENTRIFUGAL AND GRAVITATIONAL FORCES	158
5.7	SUMMARY	160
CHAPTER 6	EXPERIMENTAL DESIGN	163
6.1	OVERVIEW OF THE EXPERIMENTAL FACILITY	164
6.1.1	The experimental procedure	168
6.2	THE WORKING FLUIDS	171
6.3	EXPERIMENTAL APPARATUS AND CALIBRATION PROCEDURES	172
6.3.1	Film fraction measurement	172
6.3.2	Liquid film thickness measurement	175
6.4	CROSS CHECKING OF CONDUCTANCE RING DATA WITH THOSE FROM THE LIQUID FILM THICKNESS PROBES	186
6.5	DATA ACQUISITION	189
6.6	SAFETY FEATURES	190
6.7	SUMMARY	191

CHAPTER 7	GAS-LIQUID FLOW IN A 127 mm PIPE AND BEND	192
7.1	FILM FRACTION	194
7.1.1	Flow development	195
7.1.2	Time series and PDF of dimensionless liquid film thickness before, around and after the 180° bend	196
7.1.3	Variation of average film fraction with gas superficial velocity	201
7.1.4	The effect of gas superficial velocity on the average film fraction	206
7.1.5	Competition between gravitational and centrifugal forces	210
7.1.6	Comparison of the present work with that of Usui et al. (1983) flow pattern map	213
7.1.7	Comparison of the present study with that of Hills (1973)	215
7.2	SUMMARY OF THE FILM FRACTION DISTRIBUTION AROUND THE 180° BEND	216
7.3	LIQUID FILM THICKNESS	219
7.3.1	Time averaged cross-sectional liquid film thickness in the 180° bends	221
7.3.2	Movement of the liquid film in the bend	225
7.3.3	Circumferential liquid film thickness variation in the bend	227
7.3.4	Spatial variation of the average liquid film thickness in the bend	230
7.4	COMPARISON BETWEEN EXPERIMENTS AND COMPUTATIONAL FLUID DYNAMICS (CFD) BASED ON SPATIAL LIQUID FILM THICKNESS VARIATION IN THE BEND	236
7.5	SUMMARY OF THE LIQUID FILM THICKNESS DISTRIBUTION IN THE 180° BEND	239
CHAPTER 8	CFD-MODELLING AND SOLUTION METHODOLOGY	242
8.1	OVERVIEW OF COMPUTATIONAL FLUID DYNAMICS (CFD)	244
8.1.1	Computational fluid dynamics	244
8.1.2	Equations governing fluid flow	245
8.2	CFD SIMULATION PROCESS	246
8.2.1	CFD pre-processing: domain discretization and meshing	246
8.2.2	CFD solution and post-processing	248
8.3	DESCRIPTION OF THE PROBLEM	250
8.3.1	Computational domain	250
8.3.2	Boundary conditions	253
8.3.3	Initial conditions	255
8.3.4	CFD model	255

8.3.5	Governing equations	256
8.3.6	Turbulence model	259
8.3.7	Discretization and method of solution	261
8.3.8	Solver controls	261
8.3.9	Grid generation	262
8.3.10	Stability constrain	264
8.3.11	Mesh independence study	265
CHAPTER 9	MODELLING SLUG TWO-PHASE FLOW WITH CFD	270
9.1	FLOW DEVELOPMENT	270
9.2	THE EFFECT OF THE METHOD OF INTRODUCING LIQUID INTO THE FLOW DOMAIN	274
9.2.1	Qualitative comparison between CFD and experiments	274
9.2.2	Quantitative comparison between CFD and experiments	281
9.2.3	Summary for the comparison between the results of CFD and experiments: riser	290
9.3	RESULTS AND DISCUSSION FOR CHARACTERISTICS OF SLUG FLOW IN A VERTICAL 90° BEND USING EXPERIMENTS AND CFD	291
9.3.1	Comparison between the CFD and experiments before the vertical 90° bend (first case)	292
9.3.2	Comparison between the CFD and experiments after the vertical 90° bend (second case)	295
9.3.3	Flow development downstream of the bend	298
9.3.4	Summary for the comparison between the results of CFD and experiments	301
CHAPTER 10	CONCLUSIONS AND FURTHER WORK	303
	REFERENCES	317
	NOMENCLATURE	332
	APPENDIX A	335
	APPENDIX B	350
	APPENDIX C	356
	APPENDIX D	358

List of Figures

Figure 1.1	Offshore oil and gas installation	3
Figure 1.2	Structure of the thesis	12
Figure 2.1	Transition from slug to churn	17
Figure 2.2 a	Flow patterns in a vertical pipe	18
Figure 2.2 b	Flow regimes in gas-liquid vertical flow	19
Figure 2.3	Horizontal slug flow	21
Figure 2.4 a	Flow patterns in a horizontal pipe	23
Figure 2.4 b	Flow patterns in a horizontal pipe	23
Figure 2.5	Flow pattern map by Taitel et al. (1980) for vertical flow	26
Figure 2.6	Flow pattern map in horizontal pipe	26
Figure 2.7	Flow pattern map in slightly inclined flow	27
Figure 2.8	Flow identification by Power Spectral Density of pressure Gradient	28
Figure 2.9	Flow pattern identification by Probability Density Function of void fraction	30
Figure 2.10	Void fraction traces and corresponding PDFs	30
Figure 2.11	Schematic representation of the measuring chain for wire mesh tomographic measurement technique	32
Figure 2.12	Simplified scheme of the two-plane electrode mesh device used by Prasser et al. (1998)	33
Figure 3.1	Picture of the inclinable rig	61
Figure 3.2	Diagram showing the inclinable rig converted to a vertical 90° bend	63
Figure 3.3	Schematic diagram of the vertical 90° bend	67
Figure 3.4	The major components of the rig	68
Figure 3.5	Picture of the differential cell (DP cell)	71

Figure 3.6	Arrangement for DP cell calibration	72
Figure 3.7	DP cell calibration	72
Figure 3.8	Block diagram assembled in Labview for the DP cell	73
Figure 3.9	High speed video arrangement	74
Figure 3.10	wire mesh sensor (WMS)	76
Figure 3.11	24×24 wire mesh sensor for pipe flow measurement	76
Figure 3.12	Weight coefficients for the cross-section averaging of local fractions measured by the WMS	82
Figure 3.13	Weight coefficients for the cross-section averaging of local void fractions over a number of ring-shaped domains	82
Figure 3.14	The electrical capacitance tomography (ECT) sensor	84
Figure 3.15	Parallel capacitance model	88
Figure 3.16	% error (uncertainty) against (a) gas superficial velocity and (b) liquid superficial velocity	96
Figure 3.17	% error (uncertainty) against mixture superficial velocity for different liquid superficial velocities	98
Figure 4.1	PDF of cross-sectional averaged void fraction for the case of Slug flow measured from the experiments using air- silicone oil	109
Figure 4.2	Comparison between the cross-sectional void fraction obtained from the ECT when the WMS sensor was placed before and after the vertical 90° bend	110
Figure 4.3	Variation of % error with gas superficial velocity	110
Figure 4.4	Experimentally measured structure velocity versus mixture superficial velocity	113
Figure 4.5	The determined mean void fractions in the liquid slug at different liquid and gas superficial velocities	114
Figure 4.6	The determined mean void fractions in the Taylor bubble at different liquid and gas superficial velocities	115
Figure 4.7	The determined dimensionless film thickness at different liquid and gas superficial velocities	116

Figure 4.8	A plot of the relationship between the void fraction in the liquid slug and the mean void fraction	116
Figure 4.9	The influence of the gas superficial velocity on the total and frictional pressure drop	119
Figure 4.10	Variation of slug frequency with mixture superficial velocity at different liquid superficial velocity	120
Figure 4.11	Log-log plot of the dimensionless Strouhal number vs (a) the liquid quality (b) the Lockhart-Martinelli parameter	123
Figure 4.12	The determined lengths of liquid slug at different liquid and gas superficial velocities	125
Figure 4.13	Influence of gas superficial velocity on the ratio of average lengths of the Taylor bubble to pipe diameter	125
Figure 4.14	Influence of gas superficial velocity on the ratio of average lengths of the slug unit to pipe diameter	126
Figure 4.15	Comparison between the experimental data and the Khatib and Richardson method (1984)	127
Figure 5.1	Comparison of 3-D plot of PDFs of void fraction for the before the vertical 90° bend obtained from the ECT and WMS	134
Figure 5.2	Reconstructed images of the two-phase flow patterns from spherical cap bubble to churn flow	135
Figure 5.3	PDF of void fraction before and after the bend	137
Figure 5.4	Flow pattern maps for the vertical and horizontal 90° bends	143
Figure 5.5	Video image of spherical cap bubble for a riser at liquid and gas superficial velocities of 0.14 and 0.05 ms ⁻¹ , respectively	144
Figure 5.6	Video image of slug flow for a riser at liquid and gas superficial velocities of 0.14 and 0.54 ms ⁻¹ , respectively	145
Figure 5.7	Video image of unstable slug flow for a riser at liquid and gas superficial velocities of 0.14 and 0.95 ms ⁻¹ , respectively	146

Figure 5.8	Video image of churn flow for a riser at liquid and gas superficial velocities of 0.14 and 2.36 ms ⁻¹ , respectively	146
Figure 5.9	Video image of spherical cap bubble flow passing through a vertical 90° bend at liquid and gas superficial velocities of 0.14 and 0.05 ms ⁻¹ , respectively	147
Figure 5.10	Video image of stable slug flow passing through a vertical 90° bend at liquid and gas superficial velocities of 0.14, and 0.54 ms ⁻¹ , respectively	148
Figure 5.11	Video image of churn flow passing through a vertical 90° bend at liquid and gas superficial velocities of 0.14 and 2.36 ms ⁻¹ , respectively	149
Figure 5.12	Sequence of frames at 1 ms intervals showing the location of the gas, top and bottom of the pipe	150
Figure 5.13	Influence of gas superficial velocity on mean void fraction before the vertical and horizontal 90° bends 0 (U _{SL} = 0.05, 0.14, 0.28 and 0.38 ms ⁻¹)	153
Figure 5.14	Influence of gas superficial velocity on mean void fraction after the vertical and horizontal 90° bends (U _{SL} = 0.05, 0.14, 0.28 and 0.38 ms ⁻¹)	155
Figure 5.15	Influence of liquid superficial velocity on mean void fraction before the vertical and horizontal 90° bends (U _{SG} = 0.05, 0.4, 2.36 and 4.73 ms ⁻¹)	156
Figure 5.16	Influence of liquid superficial velocity on mean void fraction after the vertical and horizontal 90° bends (U _{SG} = 0.05, 0.4, 2.36 and 4.73 ms ⁻¹)	158
Figure 5.17	Influence of gas superficial velocity on the modified Froude number with liquid superficial velocity as a parameter	159
Figure 6.1	Flow pattern map for the range of flow rates in the present Study	164
Figure 6.2	Schematic diagram of the experimental facility	166
Figure 6.3	The major components of the rig	167
Figure 6.4	The locations of the measurement of film fraction on the transparent test section of the riser	170
Figure 6.5	Calibration curves for the conductance ring probes for	

	annular flow with respect to different liquid conductivities	174
Figure 6.6	Sketch of the test section for liquid film thickness at the bottom of pipe	178
Figure 6.7	Sketch of the test section for liquid film thickness at the bottom of pipe (present study)	178
Figure 6.8	Calibration curves for the 5 parallel wire probes	179
Figure 6.9	Calibration lines for probe C for different liquid Conductivities	180
Figure 6.10	Picture of the flush mounted pin probes in modular sections	181
Figure 6.11	Cross-sectional view of the test section for liquid film thickness measurements at the top of the pipe	181
Figure 6.12	Cross-sectional view of the test section for liquid film thickness measurements at the top of the pipe (present study)	182
Figure 6.13	Calibration curves for the parallel pin probes	185
Figure 6.14	Typical comparison between the film fraction obtained from the ring and liquid film thickness probes. Liquid superficial velocity = 0.2 ms^{-1}	188
Figure 6.15	Variation of average liquid film thickness for the second 5 seconds third 5 seconds against first 5 seconds	189
Figure 6.16	Block diagram of the Labview program for data acquisition	190
Figure 7.1	A typical the (a) time series film fraction (b) PDF of film fraction and (c) the PSD of film fraction for liquid and gas superficial velocities of 0.2 and 14.22 ms^{-1} , respectively	196
Figure 7.2	A typical time series and PDF of dimensionless liquid film thickness around the 180° return bend for liquid and gas superficial velocity of 0.2 and 14.2 ms^{-1} , respectively	199
Figure 7.3	Variation of average film fraction with gas superficial velocity before, around and after the 180° return bend at liquid superficial velocity of (a) 0.02 ms^{-1} (b) 0.04 ms^{-1} (c) 0.08 ms^{-1} (d) 0.1 ms^{-1} superficial and (e) 0.2 ms^{-1}	203
Figure 7.4	Variation of average film fraction with axial distance before, around and after the 180° return bend at liquid superficial velocity of (a) 0.02 ms^{-1} (b) 0.04 ms^{-1}	

	(c) 0.08 ms ⁻¹ (d) 0.1 ms ⁻¹ and (e) 0.2 ms ⁻¹	209
Figure 7.5	Influence of gas superficial velocity on the modified Froude number for different liquid superficial velocities of (a) 0.02 ms ⁻¹ (b) 0.04 ms ⁻¹ (c) 0.08 ms ⁻¹ (d) 0.1 ms ⁻¹ and (e) 0.2 ms ⁻¹	212
Figure 7.6	Flow pattern map of Usui et al. (1983)	214
Figure 7.7	Comparison of mean film fractions (present study) with those of Hills (1973). Liquid superficial velocity = 0.04 ms ⁻¹	216
Figure 7.8	Variation of average liquid film thickness with the bend angle	223
Figure 7.9	A typical average liquid film thickness distribution in the bend over 15 one second at liquid and gas superficial velocities of 0.1 and 14.8 ms ⁻¹ , respectively	226
Figure 7.10	Polar plots of average liquid film thickness in the bend for Different liquid and gas superficial velocities	230
Figure 7.11	Spatial liquid film distribution at liquid superficial velocity of (a) 0.02 ms ⁻¹ and (b) 0.2 ms ⁻¹	232
Figure 7.12	The distribution of liquid film thickness in the bend at (a) liquid and superficial velocities of 0.1 and 11.24 ms ⁻¹ , respectively and (b) liquid and superficial velocities of 0.2 and 12.5 ms ⁻¹ , respectively	238
Figure 8.1	3-D geometry of the riser computational domain showing the location of the recording sections that correspond to the locations of the experimental measurement transducers	252
Figure 8.2	3-D geometry of the vertical 90° bend computational domain showing the location of the recording sections that correspond to the locations of the experimental measurement transducers	253
Figure 8.3	Computational mesh used for simulations (a) riser and (b) vertical 90° bend	263
Figure 8.4	Cross-sectional view of different sizes of computational grid used for mesh independent study (a) 26400 cells (b) 36000 cells (c) 54600 cells (d) 76800 cells (e) 84000 cells and (f) 102600 cells	268
Figure 9.1	Comparison between experimental data and CFD	

	simulation results at steady-state (different methods of introducing liquid into the flow domain)	276
Figure 9.2	Comparison of contours of phase distribution, same inlet velocity condition for between (a) CFD and WMS and for (b) CFD and ECT	278
Figure 9.3	Contours of phase distribution (cross-sectional void fraction of air) for the Taylor bubble obtained from (a) CFD and (b) WMS and for (c) CFD and (d) ECT	279
Figure 9.4	Velocity field around the (a) Taylor bubble (b) wake region of the Taylor bubble for liquid and gas superficial velocity of 0.05 and 0.34 ms^{-1} , respectively obtained from CFD	280
Figure 9.5	Time delay of a Taylor bubble passing through two different measuring locations along the pipe. The liquid and gas superficial velocities are 0.05 and 0.34 ms^{-1} , respectively (a) CFD and (b) Experiment	288
Figure 9.6	Static pressure contour plot for liquid and gas superficial of 0.05 and 0.34 ms^{-1} , respectively obtained from CFD	289
Figure 9.7	Contour plot of void fraction	295
Figure 9.8	(a) Cross-sectional contour plot of void fraction at 90° into the bend and (b) velocity vector plot of void fraction at 90° into the bend	298

Table captions:

Table 2.1	Data from experiments in bends	56
Table 3.1	Properties of the fluids	62
Table 4.1	Properties of the fluids and dimensionless numbers	102
Table 4.2	Table of the flowchart for experimental measurement used to obtain the parametrical characterisation of the slug flow regime	103
Table 6.1	Properties of the fluids	171
Table 7.1	The range of variables	193
Table 8.1	The results obtained from the CFD mesh independence Studies	268
Table 9.1	Interrogating flow development in a vertical 67 mm internal diameter and 6 m long riser	271
Table 9.2a	Comparison between the CFD and experiments for the large trailing Taylor bubble (Start-up)	282
Table 9.2b	Comparison between the CFD and experiments for the large trailing Taylor bubble (Start-up)	283
Table 9.3a	Comparison between the CFD and experiments for the leading Taylor bubble (Steady state)	285
Table 9.3b	Comparison between the CFD and experiments for the leading Taylor bubble (Steady state)	286
Table 9.4	Flow pattern comparison between experiment and CFD before the vertical 90° bend (Steady-state)	294
Table 9.5	Flow pattern comparison between experiment and CFD after the vertical 90° bend	297
Table 9.6	Interrogating flow development downstream of the bend	299

Chapter 1

Introduction

1.1 General Introduction:

Within the oil industry there is a need to measure and predict the form of the multiphase liquid and gas flows that are present within oil production and processing pipelines. Knowledge of the flow regimes present allows the engineer to optimise the configuration of the pipeline and downstream processes to achieve the most economic and reliable design. The applications of these technologies are collectively known as flow assurance. Within oil production systems, one component which has received little attention is the characterisation of the multiphase flow around bends under various process conditions. To predict the flow regimes in greater details requires the development of instrumentation that can measure and characterise the flow within the pipes. Therefore, this work is concerned with gas-liquid flows in a riser and confluent 90° and 180° bends, which are of particular interest to oil and gas industry applications.

1.2 Background to the research:

1.2.1 Slug flow in a vertical riser:

The power, nuclear and chemical industries have provided a platform for strong interest in the study of multiphase flow. Examples of such studies are steam-water flow for power generation and flow reactors for heat and mass transfer.

Hitherto, applications in the petroleum industry provide another strong motivation

for multiphase flow research. The transportation of multiphase flows involving, oil and gas in pipes may significantly reduce the cost of reservoir development. However, the main challenge confronting process engineers is the development of multiphase technology for the transportation of oil and gas from subsea production units as shown in Figure 1.1 at large water depths to processing facilities at nearby platforms or onshore facilities, Zoetewij (2007). The flows in the subsea pipelines usually contain multiple phases, like oil, water and/or gas, whose composition is not known a priori. The variation in the composition of fluids inside the long subsea network can lead to serious operational problems, ranging from non-continuous production or shut-down to damage equipment. Gas with large amounts of water and or oil-water mixtures may be produced simultaneously, resulting in multiphase flow conditions in the transporting pipe system between the source and the production platform. As the fields grow older, the produced multiphase mixture contains an increasing amount of water, giving rise to different mixture compositions, which affect the flow pattern and flow characteristics. For upward inclined and vertical pipe flow, slug flow can be considered as the dominant flow pattern, Hernandez-Perez (2008). This can enhance corrosion, as Kaul (1996) noted that the corrosion rate is accelerated when the flow pattern is slug flow. This flow pattern is usually characterised by an alternating flow of gas pockets and liquid slugs. Most of the gas-phase is concentrated in large bullet-shaped gas pockets, characterised as Taylor bubbles. The Taylor bubbles are separated by intermediate liquid slugs, which may contain small entrained gas bubbles. A major characteristic of slug flows are their inherent unsteadiness. As this kind of flow occurs over a wide range of

intermediate flow rates of gas and liquid, it is of major interest to a wide range of industrial processes that employ pipeline transport systems.



Figure 1.1: Offshore oil and gas installations

The presence of liquid slugs in the flow system gives an irregular output in terms of gas and liquid flow at the outlet of the system, or at the next processing stage. This can pose problems to the designer and operator of two-phase flow systems. The pressure drops experienced for slug flow may be substantially higher as compared to other flow regimes, and the maximum possible length of a liquid slug that might be encountered in the flow system needs to be known. In the 67 mm pipe flow experimental facility used for the current research study, slugs

were observed to be of about 10 pipe diameters in length, i.e. long enough for the rise velocity to be independent of the length (Griffith and Wallis (1961)). For large capacity systems in industry, these liquid slugs can even grow longer, and possess significant momentum. Often, slug catching devices are used to collect the slugs, and avoid any damage to the downstream equipment.

For the design of such slug catchers, it is important to know the length, speed and frequency of the slugs to anticipate. The important questions of when, and how, these slugs are formed have received much attention from research workers. However, reports on the study of the behaviour of these slugs in more industry relevant fluids are limited. For that reason, it is important to study the behaviour of slug flow in great detail for the optimal, efficient and safe design and operation of two-phase gas-liquid slug flow systems.

1.2.2 Gas-liquid two-phase flow in 90° bends:

Production and transportation engineers in the onshore and offshore oil and gas industries have always been facing technical and environmental challenges associated with multiphase flows. For example, in an offshore environment, it is economically preferable to transport both gas and liquid through a single flow line and separate them onshore. In this way, a significant cost can be saved by eliminating the separate pipelines and phase separators at the offshore platform of Floating Production and Storage Operation. Hitherto, applications in the petroleum industry provide another strong motivation for multiphase flow research. However, the instability problems caused by the multiphase flow can ultimately damage the pipeline system and this is unacceptable. The pipeline geometry contains not just straight pipes but also fittings such as, bends, valves,

junctions and other fittings which make the flow of gas and liquid mixtures more complex. These fittings may lead to secondary flow, strongly fluctuating void fractions, flow excursions, flow separation, pressure pulsations and other unsteady flow phenomena. These phenomena can cause problems such as burn-out, corrosion, and tube failure, resulting in expensive outages, repairs, and early replacement affecting plant reliability and safety. Among these fittings, bends are often encountered in oil/gas production system because of: terrain undulation; flow line/riser combinations and at delivery points to production facilities. The presence of a bend can drastically change the flow patterns immediately downstream.

It is in view of this that it is of major interest to a wide range of industrial processes that utilize pipeline transport systems. Also, the requirements for economic design, optimization of operating conditions, and evaluation of safety factors create the need for quantitative information about such flows. As the capital and operating costs become competitive and the importance of reliability increases, the need for accurate information becomes even more important. However, the redistribution of multiphase flows around bends has received little attention in the peer review literature. Most of the investigations have been restricted to single-phase flow (Eustice (1910); Dean (1927; 1928); Jayanti (1990); Dewhurst et al. (1990) and Spedding et al. (2004)). A few papers, Gardner and Neller (1969), Oshinowo and Charles (1974), Carver (1984), Carver and Salcudean (1986), Ellul and Issa (1987), Legius and van der Akker (1997), Azzi et al. (2002), Azzi et al. (2005), Spedding and Benard (2006), and Shannak et al. (2009), address the issue of gas-liquid systems but most of the reported

experiments are confined to pipes of diameters that are much smaller than those used in industry. In addition, the physical properties of the fluids employed are very different from those dealt with by industry.

1.2.3 Gas-liquid two-phase flow in 180° bends:

Vertical 180° return bends are widely used in waste heat reboilers, nuclear reactors and steam generators, evaporators, and heat exchangers. For instance, waste heat boilers with U-shaped tube are used in synthetic ammonia fertilizer plants with daily output of a 1000 tonnes to recover heat from high temperature gas and generate 180 tonne/hour steam at 10.6 MPa (Tingkuan et al. (1986)). This is significant for increasing the economic efficiency of the plants. However, in the operation of the boiler, an accident occurred in the bend due to overheating. In order to clarify the cause of the tube failure, experimental studies of gas-liquid two-phase flow pattern transitions in vertical 21.5 mm internal diameter U-shaped tubes were conducted by Tingkuan et al. (1986).

Tingkuan et al. (1986) predicted the flow patterns using visual observation and physical measurements using electrical conductance probes. They compared their transition data to those reported by Mandhane et al. (1974) and Weisman et al. (1981). They concluded that their data fitted both the Mandhane et al. (1974) and Weisman et al. (1981) transition criteria well and that the major effect of bend on the flow patterns is the considerable expansion of the stratified flow region. This conclusion confirmed the earlier work of Hills (1973), who performed experiments on a 25.4 mm internal diameter pipe attached to a vertical 180° return bend of radius of curvature 305 mm using air and water. However, it is

well established fact that the flow patterns in large diameter pipes are remarkably different to those of smaller pipes Omebere-Iyari et al. (2006).

Considerable effort has been dedicated to flow in straight or inclined small internal diameter pipes. However, real industrial plant units rarely consist entirely of straight pipes and with small internal diameter. In that environment, equipment contains numerous fittings such as bends, valves and contractions connected to pipes of large internal diameter.

1.3 Problem statement:

A series of experimental investigations to study the behaviour of gas-liquid mixtures around a riser, and confluent 90 and 180° bends will be conducted to obtain and analyse new data and to improve the fundamental understanding of the flow regimes promoted through them. Measurements of the void fraction and/or liquid holdup, film fraction, liquid film thickness and pressure drop for different flow and pipe configurations will be used to validate Computational Fluid Dynamics (CFD) models that may subsequently be used to study industrial scale problems.

1.4 Aims and objectives:

To design two-phase flow lines, fluid treatment and separation facilities requires a good knowledge of the characteristics of the flow, such as: the operating flow regime, the pressure drop and the void fraction. However, at present the prediction of these flow characteristics for oil and gas flows is based either on incomplete mathematical models or on experimental data obtained from small diameter pipes with air and water typically being the operating fluids. Hence,

there is a need to carry out reliable experimental work for two-phase flows in large diameter pipes and/or using a more viscous liquid other than water.

Therefore, the main **aims** and **objectives** of the present study are:

- 1) To carry out experimental investigation on an inclinable rig with an internal diameter of 67 mm, in a bend of 154.4 mm radius of curvature rig to study air-silicone oil flows in vertical and horizontal orientations. The objectives are (a) to improve the description of slug flow in a vertical pipe, (b) to investigate the effect of 90° bends on air-silicone oil flows.
- 2) To carry out experimental investigations in a large diameter pipe of 127 mm attached to a vertical 180° return bend having a 381 mm radius of curvature rig using air-water as the model fluids. The objectives are to measure, film fraction and local liquid film distributions in the churn-annular flow regimes around a 180° vertical return bend.
- 3) To develop a reliable CFD methodology to model the slug flow regimes experienced in the riser and the vertical 90° bend and to validate these CFD models with experimental data obtained from the experimental campaigns detailed above.

1.5 Methodology:

Two particular approaches are usually deployed in multiphase flow studies: experimental and numerical/computational. Prior to the 1990s, most of the research was based on an experimental approach. However, with the advent of Computational Fluid Dynamics (CFD) and the growth in the available computational power to support it, researchers have increasingly employed CFD in their work and have used previous published experimental work to validate the

CFD models developed. The wider use of validated CFD models is motivated in part by the higher cost involved in carrying out experimental work and the limitations of available experimental techniques to investigate complex flows.

Hence, this present research study used a more systematic research design which combined both an experimental and computational approach to achieve the aforementioned objectives. The execution of the scale experiments generated the measurement data required to validate the computational fluid dynamic models, which were then subsequently used to further investigate slug flow phenomena in risers and confluent bends.

1.5.1 Experimental method:

The experimental studies were carried out on two rigs: (1) a 67 mm internal diameter inclinable rig that can be inclined from -5° to 90° . Two bend positions were investigated: (a) vertical bend (upstream-vertical riser/downstream-horizontal flowline) and (b) horizontal bend (upstream-horizontal flow lines upstream/and downstream). The multiphase fluids used were air and silicone oil.

The behaviour of the air-silicone oil mixture was examined using advanced instrumentation: Electrical capacitance tomography (ECT) and Wire Mesh Sensor (WMS). High speed visualization techniques were used to examine the behaviour of the two-phase flow from the riser to the vertical 90° bend. An introduction to the experimental rig and method used to study the multiphase flows experienced within a confluent vertical riser and 90° bend flows are discussed in Chapter 3 whilst the results of these experimental studies are presented and discussed in Chapters 4 and 5. The second experimental rig used to study the multiphase

flows experienced within a confluent vertical riser and 180° bend flows is discussed in Chapter 6. The behaviour of the air-water mixture was examined using electrical conductance methods: conductance probes, for film fraction measurements, pin and wire probes for measuring thin and thick film thickness, respectively, around the bend. The experimental technique and results are discussed in Chapters 6 and 7, respectively.

1.5.2 Computational method:

The computational models were formulated using the commercial computational fluid dynamic software Star-CD and Star-CCM+. Computational models were constructed to study different multiphase flow patterns, including slug flow experienced in the 67 mm internal diameter experimental rig. The slug flow regime experienced in the riser and the vertical 90° bend were modelled using the Volume of Fluid (VOF) method. The construction of the computational model and a presentation, analysis and discussion of the results of this study are presented in Chapters 8 and 9, respectively.

1.6 Structure of the thesis:

The layout of this thesis is summarised as follows and presented in Figure 1.2.

Chapter 1 – Introduction – This Chapter provides an introduction to the thesis, defining the problems, aims and objectives of the study, methodology and the structure of the thesis.

Chapter 2 –Literature Review – This chapter is concerned with discussing the two-phase flow patterns found in vertical and horizontal pipes, flow pattern maps and their identification. This is followed by a critical review of the published peer review research literature concerned with the study of gas-liquid flow in bends and slug flow in straight pipes.

Chapter 3 – Experimental Arrangement for the 67 mm pipe internal diameter – The characteristics of slug flow in a vertical riser and the effect of 90° bends on air-silicone oil flows are the main subjects of this study. This chapter also describes the experimental facility and includes a brief description of important components such as the mixing section and instrumentation. Installations of 90° bend, methodology during the experimental run, hazard analysis of experimental facility, uncertainty analysis of experimental measurements are also discussed.

Chapter 4 – Gas-Liquid Flow in a Vertical 67 mm riser pipe – Presents and discusses the experimental results obtained from the experiments performed with a 67 mm internal diameter pipe (Chapter 3).

Chapter 5 – Gas-Liquid Flow in Bends of Different Orientations – Presents and discusses the experimental results obtained in the experiments performed on a 67 mm internal diameter pipe attached to a 90° bend (Chapter 3). The pipe may be fixed in a vertical or horizontal position.

Chapter 6 – Experimental Arrangement for the 127 mm pipe internal diameter Pipe and bend – The behaviour of two-phase air-water through a large diameter vertical 180° return bend is the subject of this study. The chapter describes the experimental facility, the properties of the fluids used and the instrumentation for the measurement of film fraction and circumferential variation of liquid film thickness.

Chapter 7 – Gas-Liquid Flow in a 127 mm pipe and 180° Bend –The chapter presents and discusses the experimental results obtained from the experiments performed with vertical 127 mm internal diameter riser pipe and a 180° bend.

Chapter 8 – CFD – Modelling and Solution Methodology – This chapter overviews the background and modelling methodology associated with the construction and use of computational fluid dynamic models.

Chapter 9 – The use of Computational Fluid Dynamics (CFD) models to simulate Two-Phase Slug Flow – This chapter presents and discusses the simulation results predicted by the CFD models of slug flow hydrodynamics. Comparison between

the experimental and the model data is performed to validate the results of the model studies.

Chapter 10 – Conclusions and Further Work – This chapter brings together all the key conclusions from this work. Recommendations for further work are also provided.

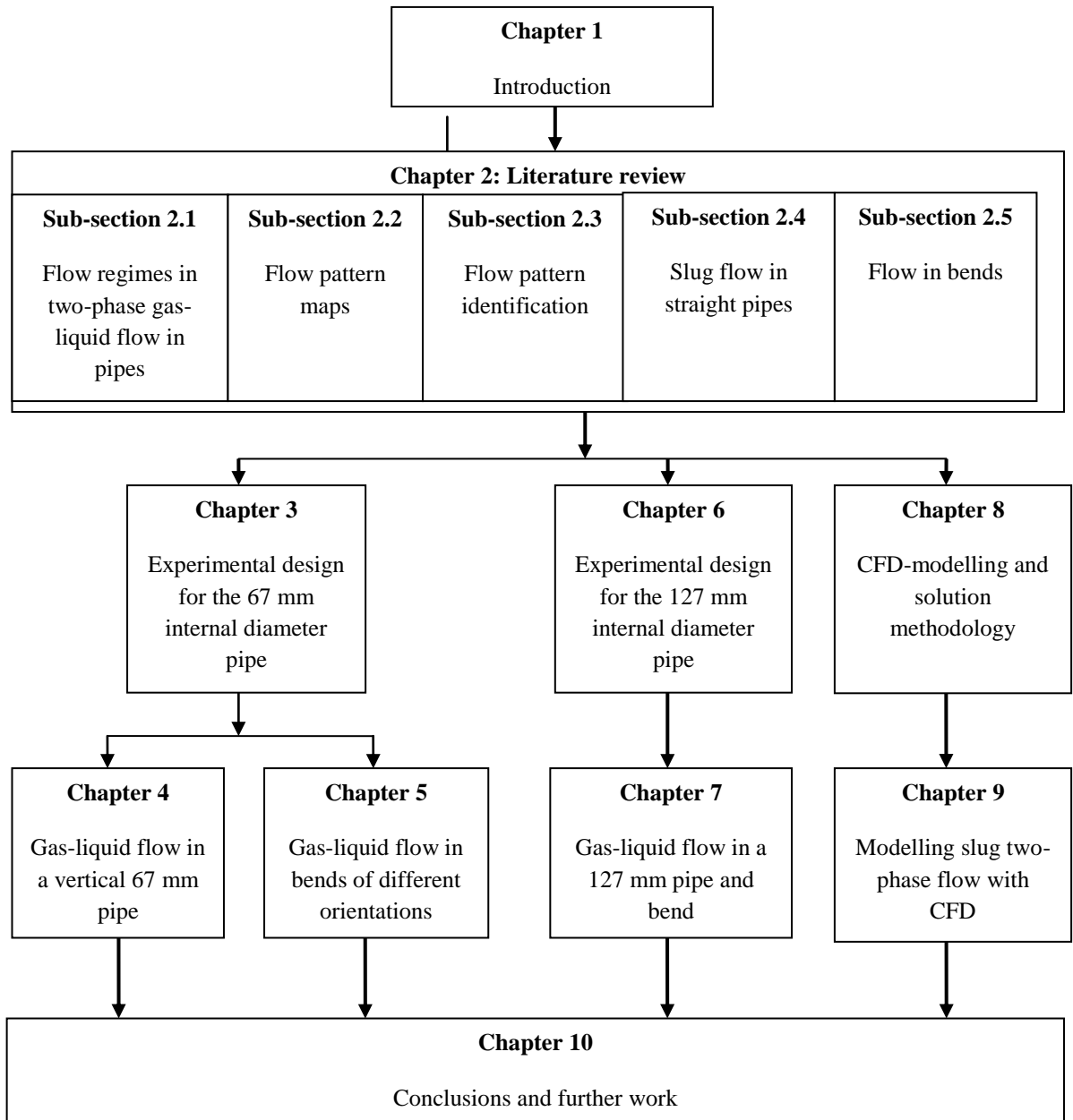


Figure 1.2: Structure of the thesis

Chapter 2

Literature Review

Two-phase gas liquid flows occur widely in the power generation, nuclear, chemical reactors, process and the oil industries. Analysis of the flow of two fluid phases, one of which is compressible while the other is not, is complicated by the fact that the interface between the phases is deformable. The fluids tend to flow in a number of different ways, which depend primarily upon their relative flow rates and densities. To understand and control two-phase flow behaviour and its heat and mass transfer characteristics, it is necessary to understand the hydrodynamics of the system.

This chapter will provide the reader with a broad understanding of the fundamentals of two-phase gas-liquid flow. In particular those relating to vertical and horizontal flows as these have direct relevance to this study. It will also discuss flow pattern maps and the methods of their identification. Finally, it will provide a critical literature review of slug flow in straight pipes and gas-liquid flow in bends.

2.1 Flow regimes in two-phase gas-liquid flow in pipes:

The identification of flow regime and the definition of the transitions between them have been the subject of numerous investigations. Govier and Aziz (1972), Delhaye et al. (1981), and Hewitt (1982) published detailed reviews of the earlier

work that focused on two-phase flow patterns and pattern transitions. Collier and Thome (1994) provided reviews of more recent experimental and semi theoretical studies.

This chapter provides brief overviews of the flow patterns (regimes) according to the type of pipe flow, and in particular vertical or horizontal flows.

2.1.1 Flow regime classification:

When two phase flow concurrently in a pipe, they can distribute themselves in a number of different configurations. The gas may be uniformly dispersed throughout the liquid in the form of small bubbles. There can be an annulus of liquid and core of vapour with or without drops of liquid in it. The interface can be smooth or wavy. To describe satisfactorily how the phases are distributed, it is necessary to categorise the form taken by different flow regimes, and to relate the different types of flow regime to mathematical relationships that categorise the flow regime, including the change in pressure drop as studied by Griffith and Wallis (1961). Knowledge of the flow pattern is necessary to define the underlying fluid mechanics in multiphase flow. An example of the need for this knowledge occurs in oil production from older subsea oil wells.

Usually a distinction is made between the flow regimes that may exist within horizontal, vertical, and inclined pipes. According to Legius (1997), for vertical pipes, the flows may be specified as either bubbly, slug, churn or annular flows, Figures 2.2a and 2.2b. In horizontal and inclined pipes, these flow patterns are extended to include smooth stratified, stratified wavy and plug flows, Figures 2.4a and 2.4b.

Vertical flow

- **Bubbly flow:** in bubbly flow, the gas phase is distributed as discrete bubbles in the continuous liquid phase. As the gas flow rate is increased, the number of bubbles increases and therefore collisions between the bubbles occur more often. This accounts for a rise in the observed bubble coalescence. Griffith and Wallis (1961) suggested that the bubble/slug transition occurred at a void fraction of about 0.25 - 0.30.
- **Slug flow:** is characterised by large bullet shaped bubbles which occupy virtually the entire cross-section of the tube. The nose of the bubble is rounded and the tail generally flat. These bubbles are surrounded by a thin film of falling liquid, and are separated from each other by regions of liquid, as shown in Figure 2.1. These intermediate regions of liquid flow may or may not contain small gas bubbles distributed in the slug following the large bubble. As the gas velocity is increased the slug/churn transition is approached. According to Jayanti and Hewitt (1992), four major theories have been proposed to explain the transition from slug flow to churn flow in vertical pipes. These are:
 - 1) The entrance effect: Taitel et al. (1980) as well as Taitel (1986) and Mao and Dukler (1993) regarded the churn flow as an entrance phenomenon that leads to stable slug flow some distance downstream from the pipe entrance if the length of the pipe is long enough. An expression to evaluate the entrance length, L_e , required to form stable slugs for a given flow condition was also derived as the result of the research work of Dukler and Taitel (1986):

$$L_e = 42.6 \left(\frac{U_{SG} + U_{SL}}{\sqrt{gD}} + 0.29 \right) \quad (2.1)$$

Where L_e , is the estimated entrance length, U_{SG} and U_{SL} are the gas and liquid superficial velocities, g is the acceleration due to gravity, and D is the pipe diameter. If the length of the pipe is less than calculated, L_e , then churn flow is observed in the entire pipe, and if not, slug flow will prevail.

- 2) The flooding mechanism: McQuillan and Whalley (1985) suggested that for slug flow the reason for the transition of the flow to churn flow was due to a flooding of the liquid film surrounding the Taylor bubble. They proposed that the flooding occurs when the liquid film in the counter-current flow of gas and liquid is broken down by the formation of large interfacial waves.
- 3) The wake effect: Mishima and Ishii (1984) proposed that the churn flow is created as the result of a collapse of liquid slugs due to the wake effect trailing the Taylor bubbles. In detail, they assumed that at the point of transition the liquid slugs are so short that the wake of the Taylor bubble is strong enough to destabilise the liquid slug and hence dissipate it. Mathematically, this transition occurs when the mean void fraction of the Taylor bubble region becomes equal to the averaged void fraction in the pipe.

$$\varepsilon_g = \frac{U_{SG}}{C_0 U_M + 0.35 \sqrt{\frac{Dg(\rho_L - \rho_G)}{\rho_L}}} \quad (2.2)$$

$$\varepsilon_{TB} = 1 - 0.813 \left[\frac{(C_0 - 1)(U_{SL} + U_{SG}) + 0.35 \left(\sqrt{\frac{Dg(\rho_L - \rho_G)}{\rho_L}} \right)}{U_M + 0.75 \sqrt{\frac{Dg(\rho_L - \rho_G)}{\rho_L}} \left[\frac{D^3 \rho_L (\rho_L - \rho_G)}{\eta_L^2} \right]^{1/18}} \right] \quad (2.3)$$

Where C_0 is the distribution coefficient, U_M is the mixture superficial velocity and is a sum of U_{SL} and U_{SG} , η_L is the liquid viscosity, ε_g is the mean cross-sectional void fraction, ε_{TB} is the mean void fraction in the Taylor bubble, ρ_L and ρ_G are the densities of the liquid and gas, respectively.

- 4) The bubble coalescence mechanism: Brauner and Barnea (1986) proposed that the slug to churn flow transition takes place due to aeration within the liquid slugs. It was postulated that when the average void fraction within the liquid slug reaches the maximum bubble cubic volumetric packing (0.52), a local coalescence of bubbles occur within the liquid slug. This results in the destruction of the liquid bridge and hence, churn flow occurs.

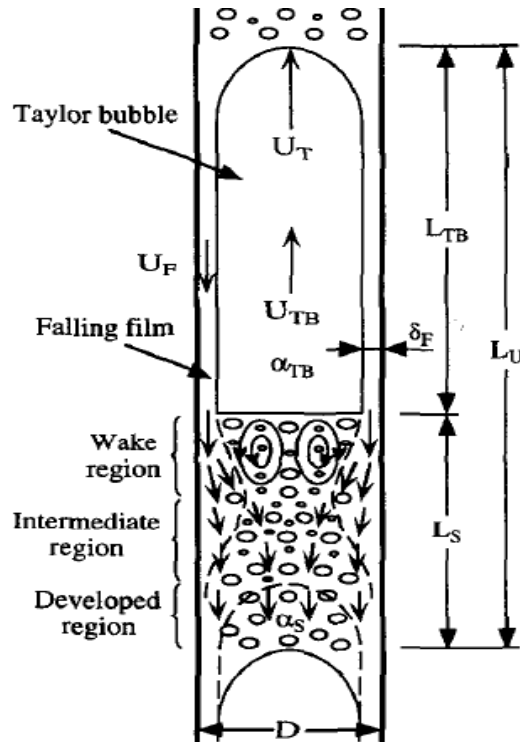


Figure 2.1: Transition from slug to churn flow. Adapted from Fernandes et al. (1983)

- Churn flow:** also referred to as froth flow and semi-annular flow is a highly disturbed flow of gas and liquid in which an increase in the gas velocity causes the liquid slug to become unstable, leading to break-up and fall. This liquid merges with the approaching slug, which then resumes its upward motion until it becomes unstable and after which it falls once again as shown in Figure 2.1. The oscillatory nature of the liquid flow, though not periodic and regular manner, is typical of churn flow, as illustrated in Figures 2.2a and 2.2b.
- Annular flow:** this type of flow is characterised by a central core of fast flowing gas and a slower moving liquid film that travels around the pipe wall. The shearing action of the gas at the gas-liquid interface generates small amplitude waves on the liquid surface, known as ripples. By

increasing the flow conditions beyond critical gas and liquid flow rates, large amplitude surges or disturbance waves appear. Liquid is torn from the surface of these waves giving rise to drop entrainment in the gas core. The deposition of these drops maintains the liquid film on the pipe walls.

As the liquid flow is increased, the drop concentration in the gas core rises. Eventually, these drops agglomerate to form large lumps (wisps) of liquid. The resulting flow pattern is known as wispy-annular flow.

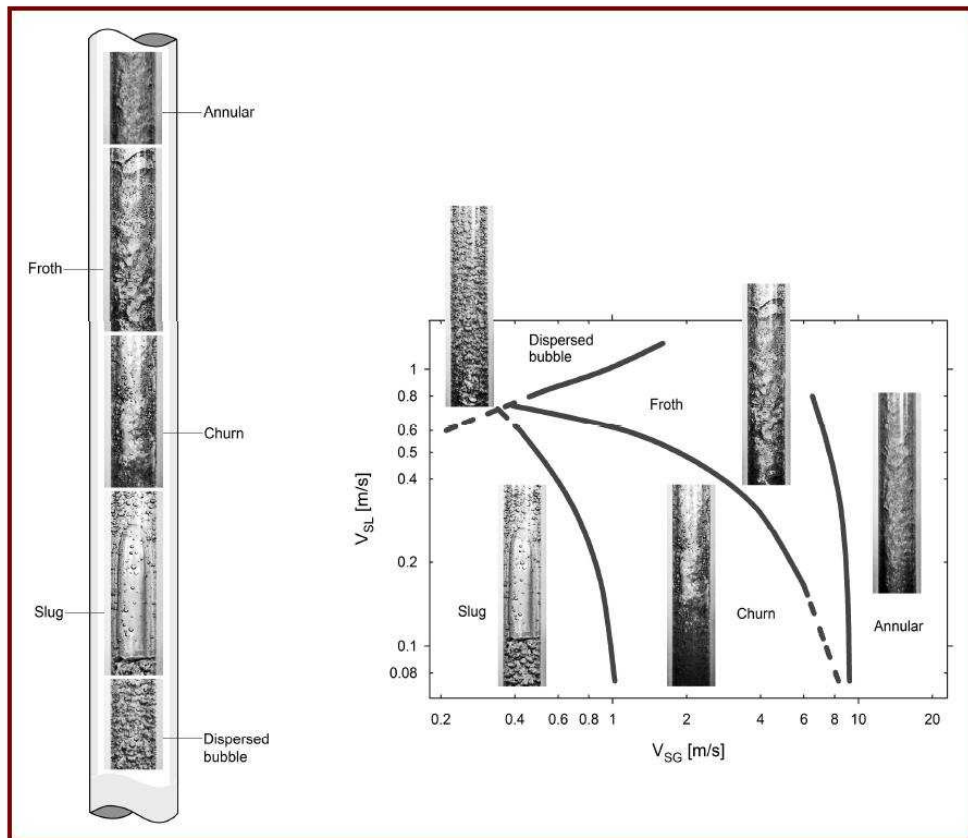


Figure 2.2a: Flow patterns in a vertical pipe. Adapted from Abbas (2010)

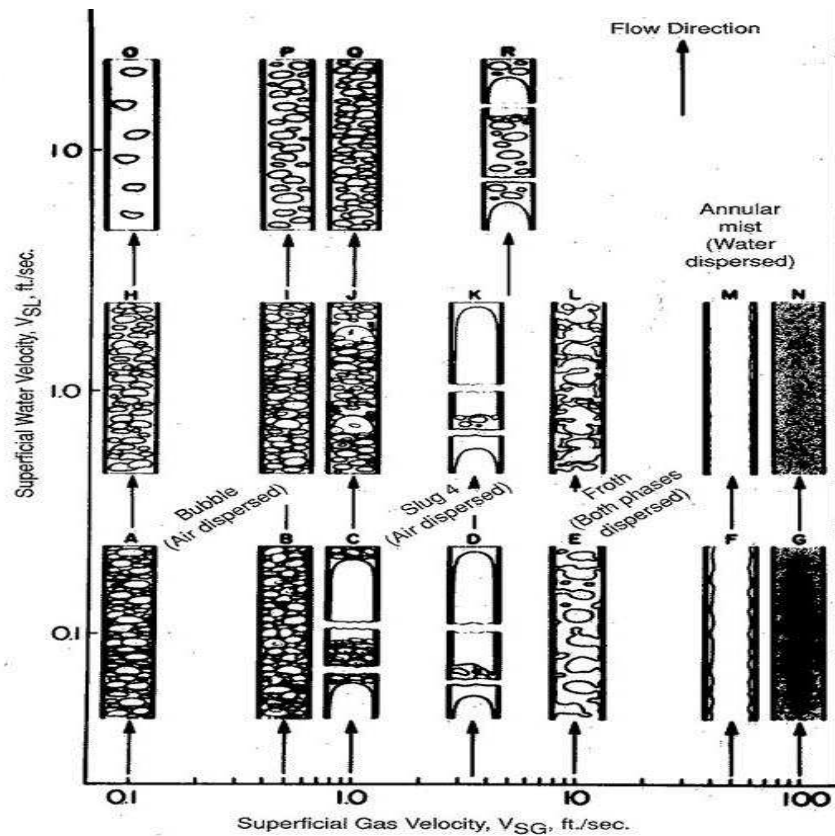


Figure 2.2 b: Flow regimes in gas-liquid vertical flow (Govier and Aziz (1972))

Horizontal flow

In horizontal pipe two phase flow conditions, gravity introduces an asymmetry to the flow regimes created: the density difference between the phases causes the liquid to travel preferentially along the bottom of the tube. Hewitt (1982) identified several potential flow patterns that may be created:

- **Bubbly flow:** as with vertical bubbly flow, the high degree of turbulence in the liquid phase causes the gas to be distributed as discrete bubbles within a liquid continuum. Buoyant forces however, cause the bubbles to flow along the upper part of the tube.

At lower liquid flows, where turbulent mixing is less pronounced; Taitel and Dukler (1976) suggested that the buoyant forces dominate. This causes the bubbles to rise and agglomerate to form gas plugs

- **Plug flow:** horizontal plug flow is similar to vertical slug flow, but gravity effects cause the gas plugs to move along the top of the tube.
- **Stratified flow:** In stratified flow the liquid travels along the bottom of the pipe whilst the gas passes over it. At low gas and liquid flows, the interface is smooth (smooth stratified flow). At higher gas velocities, the shearing action of the gas at the interface generates small 2-Dimensional waves (wavy stratified flow). At even higher velocities, large amplitude waves are seen on the liquid surface. Liquid is torn from the surface of these waves giving drop entrainment in the gas. The deposition of these drops may partially wet the top of the tube and eventually form rivulets. By increasing the liquid flow the slug flow regime is approached.
- **Slug flow:** Is characterised by the intermittent appearance of frothy slugs of liquid which bridge the entire pipe section and move at almost the gas velocity.

Pressure fluctuations typify this flow; here the gas pressure behind the slugs is greater in front of the slug as shown in Figure 2.3.



Figure 2.3: Horizontal slug flow

- **Pseudo-slug flow:** This flow pattern is characterised by the presence of liquid disturbances which have the appearance of slugs, but which do not give the identifying pressure pattern a slug does and do not travel at the gas velocity. These disturbances can touch the top of the tube momentarily, but do not block the entire pipe section. In this way pressure build-up behind the pseudo-slug is prevented.

The pseudo-slug flow occurs near the annular/slug, stratified/slug and stratified/annular flow transitions.

- **Annular flow:** At higher gas rates, the liquid slug is pierced by a gas core and the flow becomes essentially annular. At extreme gas flow rates horizontal annular flow can be approximately vertical annular flow, but at low gas flows the film is thicker at the bottom of the tube as shown in Figures 2.4a and 2.4b.

Taitel and Dukler (1976) suggest that the transition from stratified to either slug or annular flow depends uniquely on the liquid height, h_i of the stratified layer. They further suggested that when this height is above the pipe centre line, slug flow will develop, on the other hand if $\frac{h_i}{D} = 0.5$, annular flow begins.

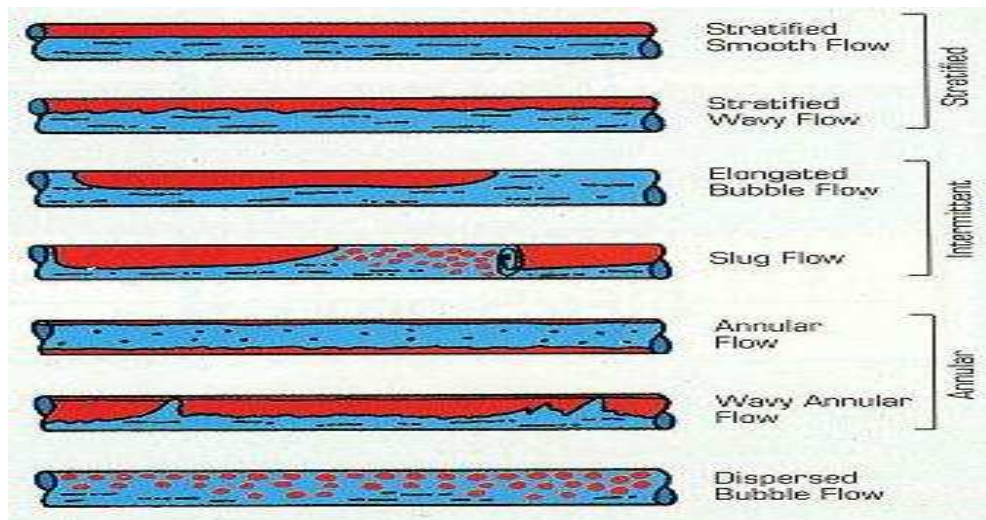


Figure 2.4 a: Flow patterns in a horizontal pipe (Loilier (2006))

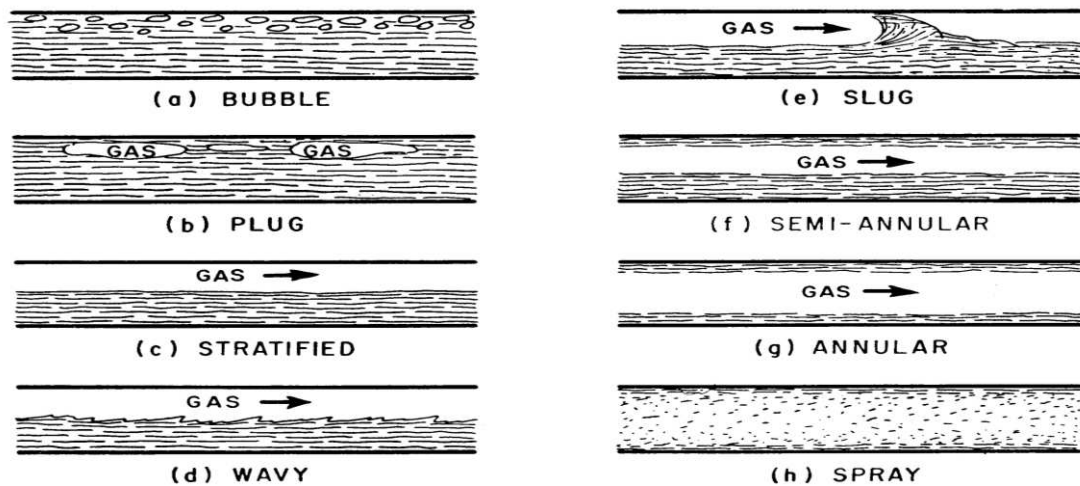


Figure 2.4 b: Flow patterns in a horizontal pipe (Loilier (2006))

The fundamental difficulty in constructing a flow map is being able to identify visually the flow patterns according to these definitions.

2.2 Flow pattern maps:

When one is confronted with a two-phase gas-liquid flow design problem, the typical approach is to begin the study with an analysis of the potential flow regimes that may be created within the pipe flow geometry under study. Without

a direct visualisation observation of the flow, the only way to determine the flow pattern is to use flow pattern maps.

A flow pattern map represents the existence of flow patterns in a two dimensional domain in terms of system variables. Flow pattern maps usually consist of flow regimes separated by transition lines and result from attempts to describe and classify the various flow patterns Omebere-Iyari (2006). The flow pattern that one observes in practice depends upon the flow rates, fluid properties, orientation of pipe, pipe size and operating conditions. The knowledge of which flow pattern actually exists under certain conditions is very important as each flow pattern results in different hydrodynamic characteristics. These characteristics further influences aspects such as pressure drop and mass, heat and momentum transfer capabilities.

Unfortunately, the characterisation of the different hydrodynamic properties is a highly complex task and most general two-phase flow correlations and models suffer from a lack of physically-sound flow regime models. Thus, the flow regimes form the basis of many of the proposed two-phase flow models. Parametric relationships are developed, valid for a limited range of flow patterns, to describe the dependence of the predicted/measured flow properties on the consequent flow conditions. It is wholly assumed that the flow regime present is either clearly recognisable or known a priori.

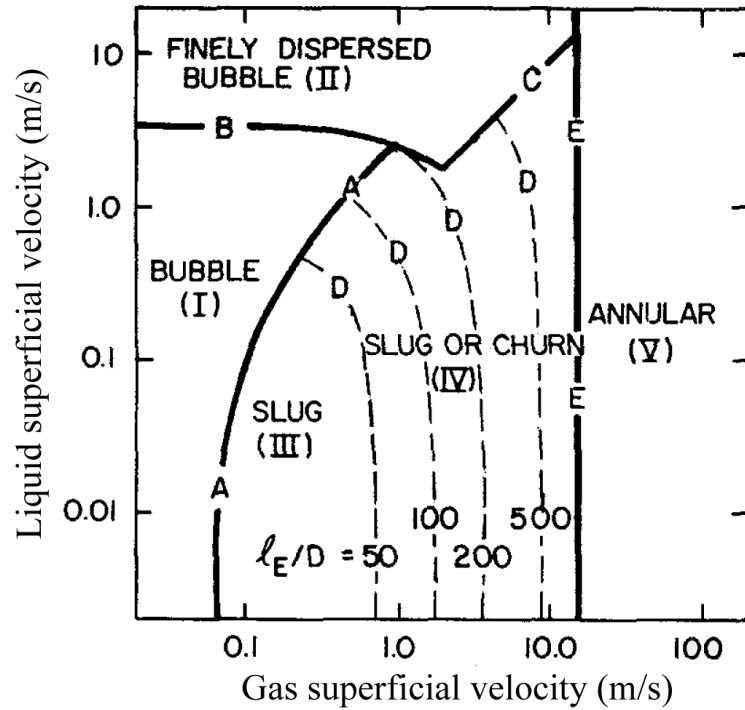
The set of conditions under which certain flow regimes occur, is represented with the aid of flow regime transition lines on the developed flow pattern maps. Since the number of parameters on which the flow regime depends is high, the classification is often simplified by using superficial velocities or dimensionless

groups, such as the Reynolds number and the Froude number, along the axes of the maps while assuming constant fluid properties and pipe geometry.

Several flow pattern maps for various operating conditions are available in the literature. Unfortunately, there is a poor agreement between most of them. Some of the best established for horizontal and vertical flow are shown in Figures 2.5 to 2.6.

This (semi-) empirical approach towards flow regime classification restricts the application of most flow regime maps to the experimental conditions under which they have been determined, which in most cases involve air/water flows at atmospheric pressure and ambient temperature in long straight pipes. The effect of fluid properties or pipe geometry on the flow regimes is either unknown or is shown as a series of such flow pattern maps. For instance, the influence of pipe diameter and inclination on flow regime has to be deduced from Figures 2.6 and 2.7. This is an essential point when applying flow pattern maps in complex pipe systems having relatively small length over diameter ratios. In these cases, the flow pattern may often differ from the pattern in long pipes with fully developed flows; as a result, the usual flow maps are of very limited use.

Furthermore, the distinctions between different flow regimes are not always very clear and transitions difficult to observe accurately. Therefore, the transition lines have to be interpreted as a best estimate or most likely option of where the actual transition takes place, and the flow maps applied with care.



(a)

Figure 2.5: (a) Flow pattern map by Taitel et al. (1980) for vertical flow (b) Flow regime map for vertical upflow Taitel et al. (1980) and Mishima and Ishii (1984) transitions. Adapted from Mishima and Ishii (1984).

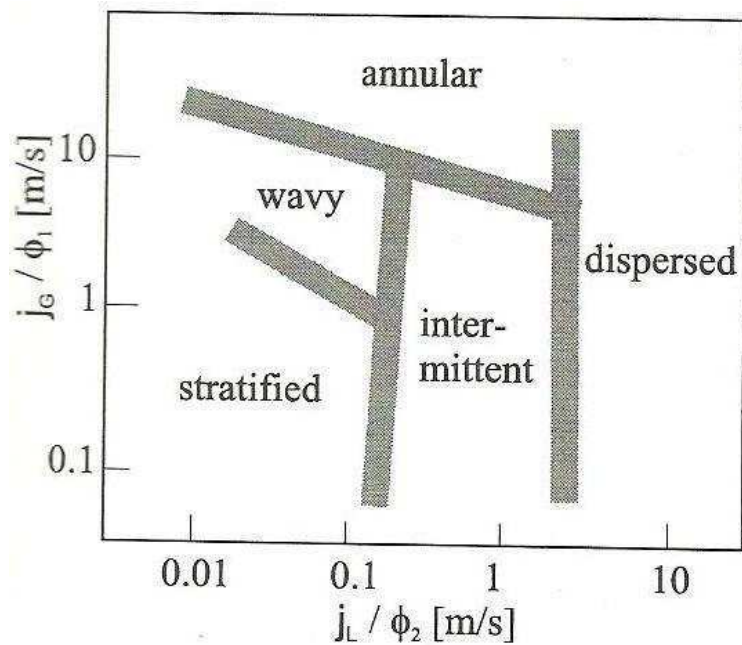


Figure 2.6: Flow pattern map in horizontal pipe (Weisman and King (1981))

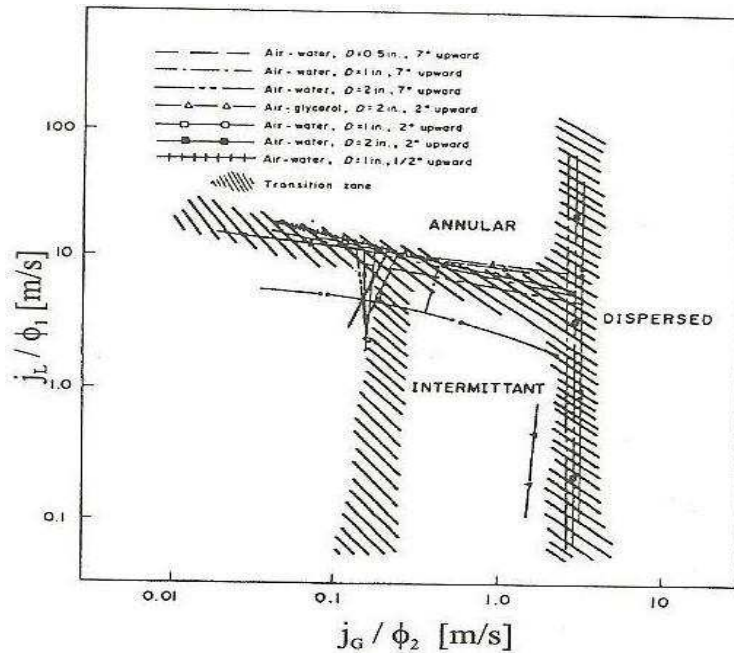


Figure 2.7: Flow pattern map in slightly inclined flow (Weisman and King (1981))

2.3 Flow pattern identification:

The simplest way to determine the gas-liquid flow pattern is to merely observe them flowing along transparent pipes. This allows for personal judgement and interpretation which prevents the flow patterns from being objectively and precisely ascertained. Where this is not feasible because of high gas and liquid flow rates, high speed photography is often employed. These methods are of no use within actual industrial pipeline that are generally not transparent Hernandez-Perez (2008). Other techniques are briefly described below.

The method of Hubbard and Dukler (1966) for flow regime determination involved the use of spectral analysis to examine the observed pressure fluctuations. The approach depends on the concept that the gas/liquid flow patterns were characterised by fluctuations in wall pressure. The power spectral density (PSD) of digitised time response obtained from a pressure transducer

located flush to the wall of the flow pipe was computed using the autocorrelation method. Three types of power spectral distributions were obtained and used to categorise the various flow regimes measured for horizontal air/water pipe flows. These are illustrated in Figure 2.8 and are as follows: (1) separated flows; containing a peak at zero frequency; this type of response is obtained from stratified and wavy flows, (2) dispersed flows; possessing a flat and relatively uniform spectrum and (3) intermittent flows; with a characteristic peak; this is obtained for plug and slug flows.

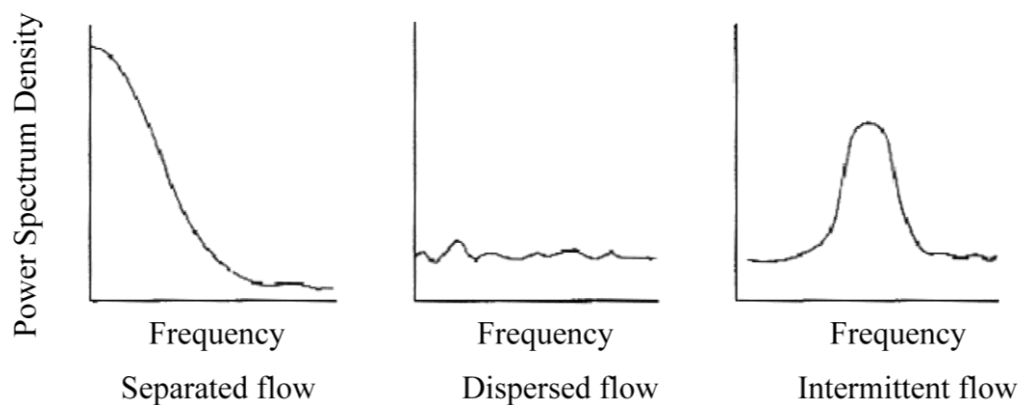


Figure 2.8: Flow identification by Power Spectrum Density of pressure gradient Hubbard and Dukler (1966). Adapted from Hewitt (1978)

The conclusions of this research work represented the first attempt to objectively classify flow patterns and was followed by the studies performed by Nishikawa et al. (1969) and Kutataledze (1972). Subsequent investigations, including that of Tutu (1982) and Matsui (1984), analysed the time variation of pressure gradient and pressure fluctuations respectively. Tutu (1982) used the probability density distribution to identify the flow patterns observed in vertical flow systems. However, Keska and Williams (1999) concluded that the pressure system they investigated did not offer an improved flow pattern recognition method when

compared to capacitive and resistive systems. Jones and Zuber (1975) pioneered the use of the photon attenuation technique, to measure the time-varying, cross-sectional averaged void fraction. This system utilised a dual x-ray beam device for a two-phase mixture of air and water, flowing vertically. It was found that the probability density function (PDF) of the void fraction fluctuations shown in Figure 2.9 could be used as an objective and quantitative flow pattern discriminator. Vince and Lahey (1982) obtained a series of chordal-averaged void fraction measurements using a dual beam x-ray system for low pressure air/water flow in a vertical tube. Their results were used to generate corresponding PDF and PSD functions of the recorded signals. It was concluded that the computed moments were sensitive to the velocity of the liquid phase. Costigan and Whalley (1997) further developed the PDF methodology of Jones and Zuber using segmented impedance electrodes and successfully classified flow patterns into six: discrete bubble, spherical cap bubble, stable slug, unstable slug, churn and annular flow as shown in Figure 2.10. From Figure 2.10, (i) a single peak at low void fraction represents bubble flow, (ii) a double peak feature with one at low void fraction whilst the other at a higher void fraction represents slug flow (iii) a single peak at low void fraction accompanied by a broadening tail represents spherical cap bubble whilst (iv) a single peak at a high void fraction with a broadening tail represents churn flow and (v) a single peak at high void fraction is defined as annular flow.

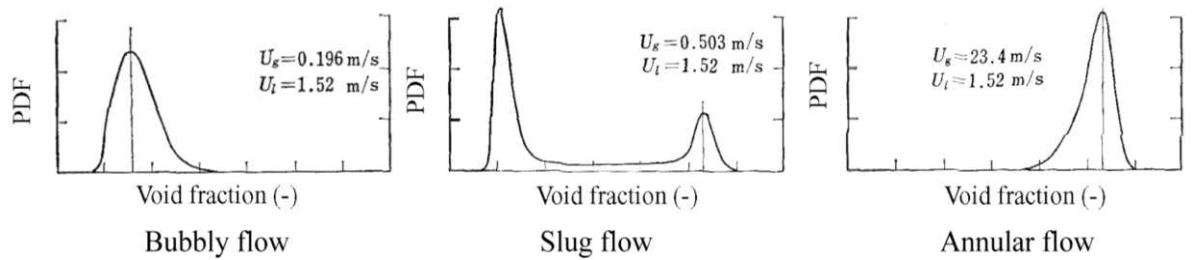


Figure 2.9: Flow pattern identification by Probability Distribution Function of void fraction Jones and Zuber (1975)

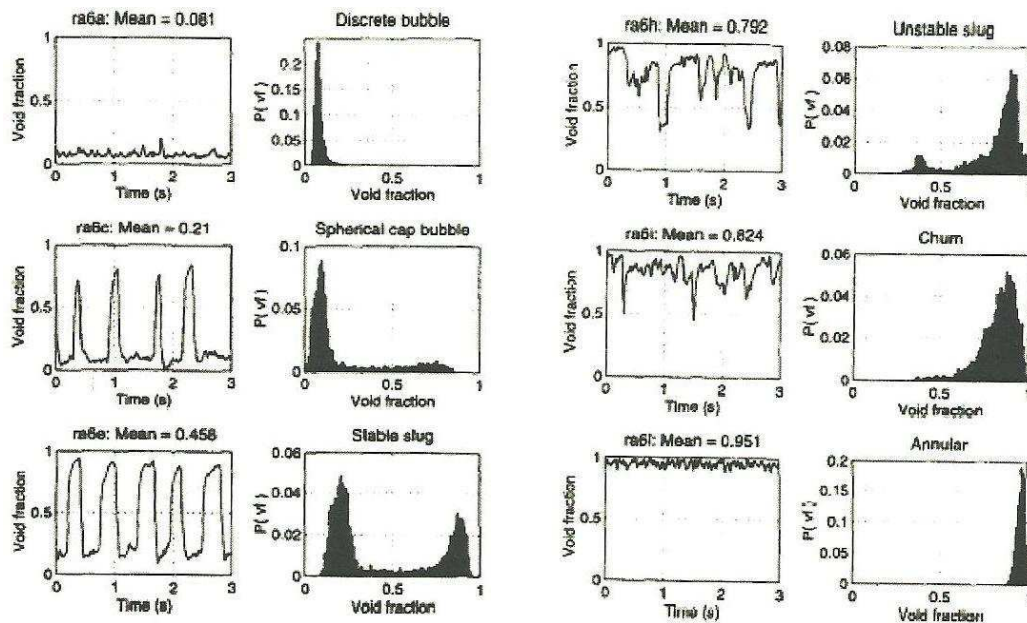


Figure 2.10: Void fraction traces and corresponding PDFs from Costigan and Whalley (1997)

2.3.1 Electrical tomography:

The field of electrical tomography may be subcategorised into two distinct areas based upon the method by which the electric field is produced, using either electrical conductance or capacitance. The choice of the potential application of each method is based primarily on the electrical properties of the fluids, and in particular their conductance.

2.3.1.1 Conductance tomography:

Conductance tomography consists of multiple conductance probes flush-mounted and evenly distributed around an interior section of the flow pipe. There are essentially two methods of measurements, either by the use of a constant current to measure the resulting potential at other electrodes, or by the application of a constant potential between two electrodes and to measure the resultant induced current. Since there is a need for the electrodes to be in direct electrical contact with the conducting fluid, tomographic imaging of certain flow patterns, for example slug and churn flows, cannot be achieved with this flush-mounted method.

To overcome this shortfall Reinecke et al. (1998) proposed an extension of the conductance approach which employs wire-mesh electrodes. Their arrangement, shown in Figure 2.11, consisted of three planes of 29 thin wires each with a diameter of 0.1 mm. The measurement planes are set 3 mm apart and the wires of two successive planes are offset by an angle of 60° .

By measuring the impedance between all pairs of adjacent wires in the same plane a projection of the conductivity distribution along the direction of the wires is obtained. For each plane, the impedance measurement is carried out with a high frequency (1000 Hz) alternating current, with the sampling of the individual electrode pairs performed by a multiplex unit. This process results in three independent projections, which are then transformed into a conductivity distribution and then further interpreted as the inherent void fraction distribution Hernandez-Perez (2008).

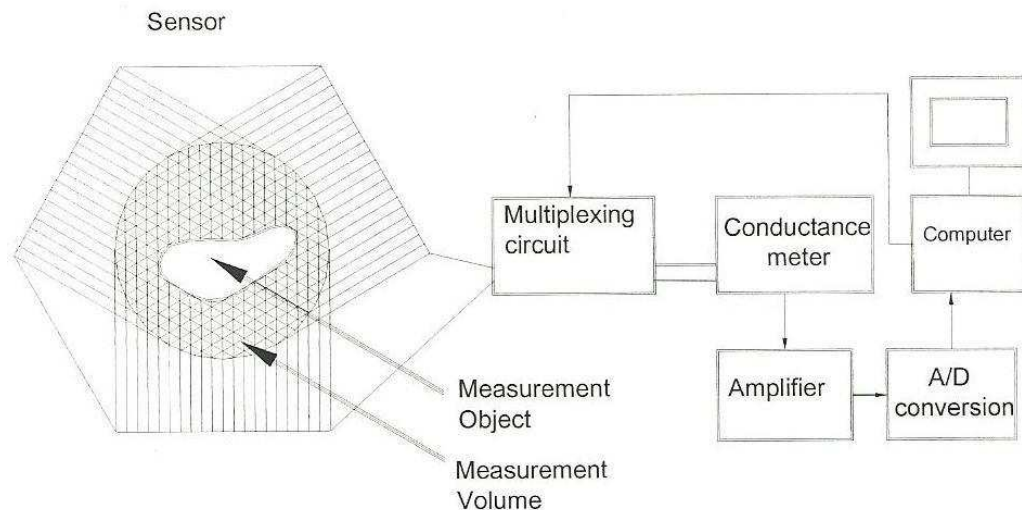


Figure 2.11: Schematic representation of the measuring chain for wire mesh tomographic measurement technique by Reinecke et al. (1998).

Prasser et al. (1998) concluded that the main disadvantage of the approach developed by Reinecke et al. (1998) was the image reconstruction step, both in terms of the relatively large computational time and the undetermined nature of the equations needed to be solved. In view of this, Prasser et al. (1998) presented a new wire mesh sensor for fast tomographic imaging without the need for time consuming and potentially inaccurate image reconstruction procedures. The sensor, shown schematically in Figure 2.12, uses two electrodes planes 1.5 mm apart, one for transmitting and the other for receiving signals. Each plane consisted of sixteen 0.12 mm diameter electrode wires, producing a grid of 16×16 measurements points evenly distributed across the pipe cross-section. The grid had a free area of approximately 96 %, with a negligible pressure drop. In one measurement cycle, the transmitter electrodes are activated by a multiplex circuit in successive order, Hernandez-Perez (2008).

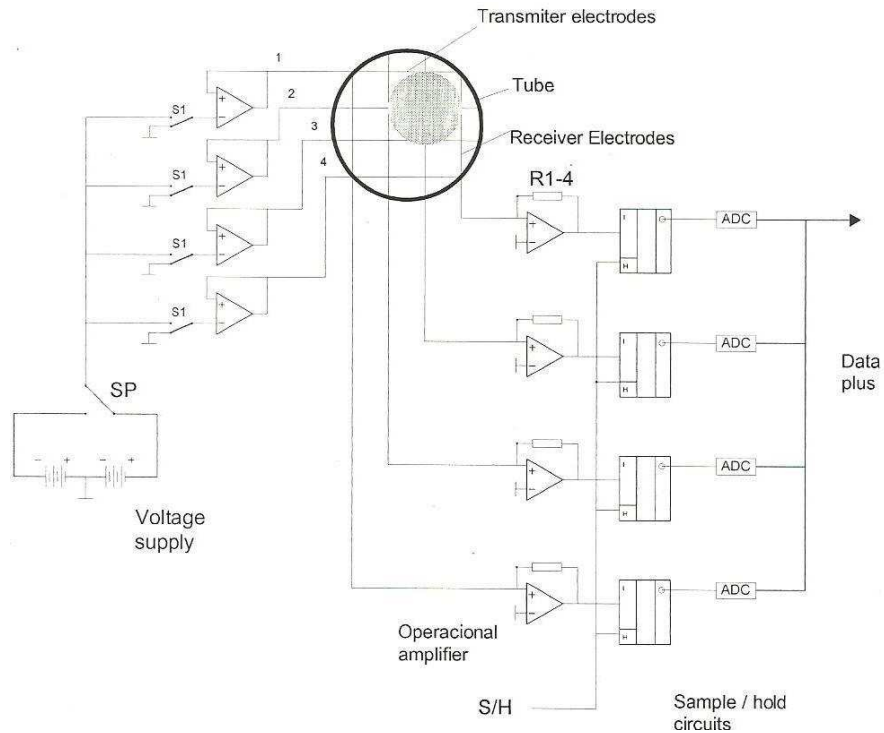


Figure 2.12: simplified scheme of the two-plane electrode-mesh devise used by Prasser et al. (1998)

2.3.1.2 Capacitance tomography:

Electrical capacitance tomography (ECT) technology is a process tomography technology that provides a new way to resolve void fraction measurement. The results of many research studies using this method have been reported in the literature. However, ECT technology is still at the stage of a developing laboratory research methodology. The ECT is a non-invasive technique since the sensing electrodes are not in contact with the fluid under observation but are located around the pipe exterior. The imaging parameter, the electrical permittivity, is the dielectric property of each of the phases in the two-phase system. An ECT image may be subsequently reconstructed based on the permittivity distribution obtained from the measurements made by the electrical capacitance taken between the possible pairs of electrodes, Hernandez-Perez

(2008). ECT has recently been used by Baker (2003) to study two phase horizontal pipe flow.

2.4 Slug flow in straight pipes:

The occurrence of slug flow in a vertical riser is a very common phenomenon under normal operating conditions within a two-phase flow facility, such as in an oil production riser. Over the past thirty years there has been a large number of research studies in this field published in the peer review literature. One of the earliest published contributions to slug flow characterization was carried out by Nicklin et al. (1962), who proposed an empirical relationship to describe the rise velocity of single Taylor air bubble in a static water column. Nicklin's empirical relationship, given by equation (2.4) below, describes the rise velocity of the Taylor bubble as a linear function of the mixture velocity. For the air-water system in a 26 mm bore tube considered, the values of the constants C_o and k were determined to be 1.2 and 0.35, respectively.

$$U_N = C_o U_M + k\sqrt{gD} \quad (2.4)$$

The results of the independent study performed by Moissis (1963) agreed that U_N predicted by equation (2.4). Akagawa and Sakaguchi (1966) confirmed the applicability of equation (2.4) to an air-water system in a 26 mm diameter pipe, and further concluded that the effect of the term $k\sqrt{gD}$ is negligible except at low gas and liquid velocities. They suggested that the presence of small bubbles in the liquid slug has a slight effect on the rise velocity of the Taylor bubbles and that their data indicated that C_o is in the range of 1.25 - 1.35.

Brown (1965) found experimentally that the analytical solutions for the bubble velocity derived by Dumitrescu (1943) and Davies and Taylor (1950) described the behaviour of gas bubbles in low viscosity liquids well, however they were not suitable for high viscosity liquids.

Vince and Lahey (1982) claimed that an excellent correlation between the absolute gas velocity, U_N and the mixture superficial velocity, U_M was given by the equation (2.5):

$$U_N = 1.29U_M + 0.15 \quad (2.5)$$

Following an analysis of experimental data for a 50 mm diameter tube, Fernandes et al. (1983) determined a slightly higher value of 1.29 for C_0 . They ascribed the increase in the constant C_0 to the pipe diameter effect or to the contribution made by heading and trailing Taylor bubbles. Barnea and Shemer (1989) verified equation (2.4), using their own measurements on a 50 mm diameter tube, and used it in their calculations. A more physically based interpretation of the proposed increase in the constant was later provided by Mao and Dukler (1985). They used an aqueous electrolytic solution and air in a 50.8 mm diameter tube. They took into consideration the fact that the liquid slug in front of a Taylor bubble is aerated, and coalescence takes place between the small bubbles and the Taylor bubbles. This results in an increase of the velocity of the Taylor bubble. They derived a mathematical relationship to determine the Taylor bubble velocity, equation (2.6).

$$U_N = C_0 U_{LLS} + 0.35\sqrt{gD} + \Delta U_N \quad (2.6)$$

where,

$$\Delta U_N = (U_N - U_{GLS}) \frac{\varepsilon_{gs}}{\varepsilon_{TB}} \quad (2.7)$$

$$U_{GLS} = U_o + U_{LLS} = 1.53 \left[\frac{\sigma g (\rho_L - \rho_G)}{\rho_L^2} \right]^{1/4} (1 - \varepsilon_{gs})^{1/2} + U_{LLS} \quad (2.8)$$

Defining β as the ratio of the void fraction in the liquid slug and Taylor bubble:

$$\beta = \frac{\varepsilon_{gs}}{\varepsilon_{TB}} \quad (2.9)$$

$$U_M = U_{SL} + U_{SG} = U_{GLS} \varepsilon_{gs} + U_{LLS} (1 - \varepsilon_{gs}) \quad (2.10)$$

By performing a substitution of equation (2.8) into (2.10) we obtain the expressions

$$U_M = \varepsilon_{gs} U_o + \varepsilon_{gs} U_{LLS} + U_{LLS} - \varepsilon_{gs} U_{LLS} = \varepsilon_{gs} U_o + U_{LLS} \quad (2.11)$$

$$U_{LLS} = U_M - \varepsilon_{gs} U_o$$

And following a substitution of equations (2.7) and (2.11) into (2.6) and rearranging yields,

$$U_N = \frac{1}{(1 - \beta)} [(C_o - \beta)(U_M - U_o \varepsilon_{gs}) + 0.35 \sqrt{gD} - \beta U_o] \quad (2.12)$$

As can be seen, this model equation (2.12) requires as input data values ε_{gs} , ε_{TB} and β . The value of β is dependent on the values of ε_{gs} and ε_{TB} and is determined experimentally or from the results of existing correlations. In this study, the values of ε_{gs} and ε_{TB} were determined experimentally as the maximum void fraction in the liquid slug and Taylor bubble, respectively.

Over the range of flow conditions studied, Mao and Dukler (1985) confirmed that the parameters ε_{gs} and ε_{TB} were nearly constant at $\varepsilon_{gs} \approx 0.27$ and $\varepsilon_{TB} \approx 0.85$, these values were substituted in equation (2.12) to obtain equation (2.13).

$$U_N = 1.29U_M + 0.35\sqrt{gD} \quad (2.13)$$

In their detailed study of liquid slugs, van Hout et al. (1992) evaluated U_N from equation (2.4); and Legius et al. (1995) also found excellent agreement with their air-water data in a 50 mm diameter tube.

White and Beardmore (1962) have carried out an extensive experimental investigation of the rise velocity of a Taylor bubble in a variety of liquids covering a wide range of properties. They found out that three dimensionless parameters are required to describe the buoyant rise of Taylor bubbles rising buoyantly in liquid-filled tubes in different systems. These are the:

Froude number:

$$Fr = \frac{U_o}{\sqrt{gD}} \quad (2.14)$$

Morton number:

$$Mo = \frac{g\eta^4}{\rho\sigma^3} \quad (2.15)$$

Eotvos number:

$$Eo = \frac{\rho g D^2}{\sigma} \quad (2.16)$$

where,

U_o represents the terminal ascent velocity of the slug, g is the gravitational acceleration constant, D is the internal diameter of the tube and η , ρ , and σ are the viscosity, density, and surface tension of the liquid, respectively. In the region given by $Mo < 10^{-6}$ and $Eo > 100$, the effects of the viscous and surface tension forces are negligible. Therefore, slugs are inertially controlled and rise at their maximum velocity in vertical tubes, given by $Fr = 0.35$. According to Wallis (1969), when $Eo > 100$, the surface tension plays little role in determining the slug ascent velocity.

In a later critical review of the literature concerned with the modelling of two-phase slug flow, Fabre and Line (1992) concluded that the rise velocity of a Taylor bubble depends on the liquid velocity through the liquid Reynolds number. They proposed the following relationship between the motion of Taylor bubbles and the viscosity:

$$N_f = \frac{\rho D^{3/2} g^{1/2}}{\eta} = \left[\frac{Eo^3}{Mo} \right]^{1/4} \quad (2.17)$$

They concluded that the viscosity acts essentially to develop the liquid velocity profile far ahead of the bubbles, but has no influence near the front where the inertia dominates. This condition is satisfied provided $N_f > 300$. They claimed that for surface tension forces to be relevant, $N_f < 2$. This occurs at Reynolds numbers for which the upstream liquid flow can be either laminar or turbulent. Collins et al. (1978) used the Poisson equation to obtain an approximate solution for both the laminar and the turbulent flow regimes. The solution they obtained using equation (2.4) are $C_0 = 2.27$ for laminar flow and $1.2 < C_0 < 1.4$ for turbulent

flows, dependant on the value of the Reynolds number. The value they obtained for laminar flow $C_0 = 2.27$ was found to be in good agreement with the results first obtained by Taylor (1961).

As the most general parameter that characterises two-phase flow in vertical slug flows, the void fraction has also been investigated. Akagawa and Sakaguchi (1966) studied the fluctuation of the void fraction in air-water two-phase flow in vertical pipes. They examined the relationship between the void fraction in a liquid slug and the mean void fraction. They concluded that the void fraction present in a liquid slug was a function of the mean void fraction, which can be represented by the relationship:

$$\varepsilon_{gs} = \varepsilon_g^{1.8} \quad (2.18)$$

where,

ε_{gs} is the void fraction in the liquid slug and ε_g , the mean cross-sectional void fraction.

Later, Sylvester (1987) proposed an empirical equation to represent the void fraction in a liquid slug as a function of the liquid and gas superficial velocities:

$$\varepsilon_{gs} = \frac{U_{SG}}{C_1 + C_2(U_{SG} + U_{SL})} \quad (2.19)$$

where $C_1 = 0.033$ and $C_2 = 1.25$

Following an analysis of the experimental observations made for air-water flows up a 10 mm diameter riser, de Cachard and Delhaye (1996) concluded that the

void fraction in the liquid slug is zero. In a previous study, Ros (1961) had shown that the condition for a non-aerated liquid slug is given by:

$$\frac{(\rho_L - \rho_G)gD^2}{\sigma} < 140 \quad (2.20)$$

More recently, Mori et al. (1999) extended the work of Akagawa and Sakaguchi (1966) to study the interfacial structure and void fraction of a liquid slug present in an upward flow of an air-water mixture. They proposed an alternative linear correlation to predict the void fraction in liquid slug as follows:

$$\varepsilon_{gs} = 0.523\varepsilon_g \quad (2.21)$$

The length of the liquid slug is one of the most important parameters in slug flow. It is important in determining the average pressure drop. The knowledge of the length of the liquid slugs exiting the pipe is very essential for the design of slug catchers. Akagawa and Sakaguchi (1966); Fernandes et al. (1983) and Van Hout et al. (2002) determined that the minimum stable slug length is between 10 and 20 pipe diameters. Khatib and Richardson (1984) proposed a mathematical method for determining the length of the liquid slug. They achieved this by taking a balance over the length of a pipe, containing N liquid slugs and N gas slugs and found out that, the length of the liquid slug, L_S can be determined in terms of the length of the slug unit, L_{SU} as:

$$L_S = L_{SU} \left[\frac{\varepsilon_g - \varepsilon_{TB}}{\varepsilon_{gs} - \varepsilon_{TB}} \right] \quad (2.22)$$

They made an important assumption that the void fraction in the liquid slug is negligible. However, the equation they presented took into consideration the

influence of the void fraction in the liquid slug. Akagawa and Sakaguchi (1966) had previously pointed out that in many cases, 10 to 20 % of the total gas volume fraction is contained in the liquid slug, and that this volume should not be neglected.

In addition, complete physically based models using the conservation of gas and liquid fluxes have been developed (Fernandes et al. (1983), Nydal (1991) and Brauner and Ullmann (2004)).

It is clear from the results of the air-water multiphase studies presented above that there are many parameters that influence the multiphase flow phenomena observed. Such parameters are translational velocity, slug frequency, void fraction in the liquid slug, void fraction in the Taylor bubble and pressure drop. It is expected when the model fluids are changed; the two-phase slug flow behaviour will be different. Therefore, to characterise the conditions that result in the onset of slug flows in more industry relevant fluids, an experimental study was conducted using air and silicone oil flow in a vertical riser. Chapter 4 therefore reports the results of an analysis of new experimental data to determine the range of the physical parameters that characterise the vertical slug flow phenomena observed. A comparative analysis of the experimental data obtained against previously published empirical relationships is also presented in Chapter 4. The experimental arrangement for these experimental studies is detailed in Chapter 3.

2.5 Flow in bends:

Fluid flowing through pipe networks often encounters fittings such as bends. The presence of a bend can modify drastically the conditions of the flow regimes experienced in the pipe sections upstream and downstream of the bend. Most of the investigations in this field have been restricted to single-phase flow, and only a few authors have published results for two phase gas-liquid flows. The results of these research studies are discussed below:

2.5.1 Single-phase flow:

Eustice (1910) one of the first authors to report flow in bends, showed by dye visualisation studies of water in a curved pipe that even for laminar flow separation, reversal of flow and greater turbulence was observed for a 90° bend when $\frac{R}{D} < 3$. His experiments demonstrated the existence of a transverse motion (secondary flow) superimposed on the primary flow, represented in the form of a pair of counter rotating longitudinal vortices.

Dean (1927; 1928) wrote the first theoretical approach on the subject, since then several works have been reported. A more recent experimental study by Dewhurst et al. (1990) includes flow measurements using a 3-Dimensional LDA system in a square sectioned (0.1×0.1 m) 90° vertical bend. Streamwise and secondary velocities were obtained by these authors for water flow upstream of the bend and at 80° on the bend. Most of the studies of bends have been carried out for single phase flow. Jayanti (1990) presented a review of these works, both under laminar and turbulent conditions. Two-phase flow in bends is discussed in the following sections.

2.5.2 Two-phase flow in 90° bends:

Two-phase flow patterns observed in bends are qualitatively the same as those seen in straight pipes. However, bends introduce a developing situation in the flow pattern, whereby the relative positions and local velocities of the two phases are redistributed.

Gardner and Neller (1969) carried out visual and experimental studies for bubble/slug flow using a transparent pipe of 76 mm diameter in a vertical 90° bends of 305 and 610 mm radii of curvature, using air-water at atmospheric pressure. The local air concentrations over chosen cross-sections were measured. The results of the analysis of their experimental data were used to interpret the competitive effects of the centrifugal and gravity forces on the resultant flow distributions observed around bends. They suggested that the ratio of centrifugal and gravitational forces can be represented by a modified Froude number. They found out that gas can either flow on the inside or outside of the bend depending on a critical Froude number defined as

$$Fr_{\theta} = \frac{U_M^2}{Rg \sin \theta} \quad (2.23)$$

where θ is the angle of the bend. Using this modified Froude number, they attempted to explain the flow regimes observed at different phase positions within the bend. They claimed that if Fr_{θ} is greater than unity, the air will be found on the inside of the bend, and if less than unity, the air will hug the outside of the bend. $Fr_{\theta}=1$ corresponds to both phases being in radial equilibrium. This

conclusion, however, may not be valid for working liquids with different viscosity, density and surface tension.

Carver (1984) carried out numerical 2D modelling studies to represent the flow around a vertical 90° bend. He compared his numerical simulation results with the results of the experimental studies conducted by Gardner and Neller (1969). The agreement was not particularly good. Carver and Salcudean (1986) recognized the limitations of using a 2-D numerical modelling approach to simulate what was in essence a truly 3-D flow phenomena. Thus, they proposed to extend the 2-D model to 3-D, and found that the results predicted by the 3-D computational model could generate results similar to those observed by Gardner and Neller (1969). Ellul and Issa (1987) developed an improved 3-D numerical simulation, in which a substantially different solution algorithm was adopted. A truncated gas momentum term was added to their momentum equations, and the models were applied for both air-water and gas-oil mixtures. The predicted simulation flow data gave improved agreement with the experimental data than those obtained by the 2-D model in Carver (1984). However, it is critically noted that no grid sensitivity analysis was reported in the work of Ellul and Issa (1987). The simulation result could not select the optimum mesh size. No experimental data was available at that time for them to validate their gas-oil simulation.

Legius and van der Akker (1997) carried out a numerical and experimental study in a bend of 630 mm radius of curvature using air-water at atmospheric pressure. The experimental facility consisted of a transparent acrylic horizontal flowline (9 m long) connected to a vertical riser (4 m in height) by the 630 mm radius bend. The diameter of all pipes was 100 mm. Visual observations: using a 200 Hz

digital camera and an auto-regressive modelling method were used to identify the observed flow regimes. Slug and churn flow in the riser and stratified, slug and a new regime called “geometry enhanced slugging” in the flowline were identified. The time dependent behaviour of two-phase flow was modelled by an in-house code named Solution Package for Hyperbolic Functions (SOPHY-2). Good agreement between the modelling and experiment results has been found under almost all conditions except at higher gas and lower liquid flow rates. However, the information presented for the characteristics of slug flow is limited. Important parameters like void fraction in liquid slug and Taylor bubble were not presented. The dependence of the Taylor bubbles and liquid slugs on the gas flow rates was not examined. The sample frequency of 50-100Hz used by these researchers seems too slow to get good spatial resolution of signals.

Azzi et al. (2002) in their later work pointed out that the total pressure loss in single-phase flow in a bend is conventionally assumed to be due to wall friction, vortex detachment, secondary flow generation and losses in the downstream pipe associated with the recovery of the initial fully developed symmetric upstream velocity profile. In a two-phase flow, they cited the additional effects of dissipation due to separation and remixing of the gas and liquid phases, and that the gravitational force influences the flow behaviour in both vertical and horizontal flows. In a comprehensive review of the empirical methods that have been proposed for two-phase flow in pipe bends, Azzi et al.(2000) concluded that the B-method of Chisholm (1980) gave the best predictions to the previously published data

In later published work, Azzi et al. (2006) further reinforces the results of the previous studies. According to Azzi et al. (2002) the two phase flow bend pressure loss, also known as Chisholm B method is related to that in single-phase liquid flow by means of the two-phase flow loss multiplier shown below

$$\phi_{lo}^2 = \frac{\Delta P_f}{\Delta P_{lo}} \quad (2.24)$$

$$\phi_{lo}^2 = 1 + \left[\frac{\rho_l}{\rho_g} - 1 \right] \left[B x_g (1 - x_g) + x_g^2 \right] \quad (2.25)$$

With

$$B = 1 + \frac{2.2}{K_{lo} \left(2 + \frac{R}{D} \right)} \quad (2.26)$$

and

$$K_{lo} = \frac{\lambda_{lo} l_e}{D} \quad (2.27)$$

For 90° bends K_{lo} , the loss coefficient for all of the flow travelling as liquid. For bend angles greater than 90°

$$B = 1 + (B_{90} - 1) \frac{K_{90}}{K} \quad (2.28)$$

Where

K_{90} , the loss coefficient for the 90° bend and K is the value for the actual bend.

Spedding and Benard (2006) reported experimental data for a two-phase air-water flow in a vertical to horizontal 90° bend. They compared the pressure drop in the vertical inlet tangent of the 90° bend to that of straight vertical pipe without bend. They also compared pressure drop for horizontal outlet tangent to horizontal pipe.

They found that the pressure drop in the vertical inlet tangent showed some significant differences to that found for straight vertical pipe while that of the horizontal outlet tangent gave good agreements with horizontal pipe. They presented a general correlation for the elbow bend pressure in terms of the total Reynolds numbers. They showed that the elbow bend pressure was best handled in terms of $\frac{l_e}{D}$ calculated using the actual pressure in the vertical tangent. The

$\frac{l_e}{D}$ was given as a function of total Reynolds number,

$$\frac{l_e}{D} = 0.001384 \text{Re}_T - 13.53 \quad (2.29)$$

Where

$\frac{l_e}{D}$ is the dimensionless equivalent length

Re_T is the total Reynolds number

Furthermore, the Lockhart-Martinelli bend parameters gave a useful method with which to present their data.

$$\phi_x = \left[\frac{\Delta P_{TP}}{\Delta P_{SX}} \right]_B^{1/2} \quad (2.30)$$

$$X = \left[\frac{\Delta P_{SL}}{\Delta P_{SG}} \right]_B^{1/2} \quad (2.31)$$

Where

ϕ , Lockhart-Martinelli pressure parameter

It may be concluded from an analysis of the results of most of the research studies reported in the literature to investigate the multiphase flow in 90° bends were

carried out in small diameter pipes with air-water as the model fluids. Emphasis was on the determination of the pressure drop and phase distribution inside the bends. The change of flow structure before and after the bends was mainly obtained by visualization and the underlining mechanisms governing the change of the observed flow patterns were not discussed. For that reason, it is important to study the effect of 90° bends on two-phase flow in more industry relevant fluids for the optimal, efficient and safe design and operation of the flow systems. The primary aim of the results of the research studies presented in Chapter 5 were to provide new data and a more fundamental understanding of the flow phenomenon that occur around 90° bends through the use of a comprehensive experimental investigation of both vertical and horizontal pipe flow systems. The chosen experimental fluids were air and silicone oil. Advanced instruments such as Electrical Capacitance Tomography (ECT), Wire Mesh Sensors (WMS) and high speed video camera described in Chapter 3 have been used to measure the void fractions observed both before and after the bend. The flow patterns were determined by analyzing the Probability Density Function (PDF) of the time series of void fractions. This analysis was validated by the flow visualisation in the bend with the aid of a high speed video camera. With this information a more fundamental understanding was developed to improve the effect of 90° bends on two-phase flows.

2.5.3 Two-phase flow in 180° bends:

The flow through vertical and horizontal 180° bends have previously been investigated experimentally: Oshinowo and Charles (1974), Anderson and Hills (1974), Geary (1975), Usui et al. (1980), Chisholm (1979), and Usui et al. (1983),

Hoang and Davis (1984), Tingkuan et al. (1986), Wang et al. (2003), Wang et al. (2004), Chen et al. (2007), Domanski and Hermes (2006), Wang et al. (2008) and Chen et al. (2008). Oshinowo and Charles (1974), Anderson and Hills (1974), Usui et al.(1983) and Wang et al.(2003;2008) studied the influence of return bends on flow patterns, whilst the remaining authors stated have attempted to predict the pressure drop encountered in the bend during two-phase flow.

Alves (1954) studied air-water and air-oil flow in a four pass one inch bore horizontal pipeline contactor. Between each pass there was a return bend in a vertical plane, the direction of flow being upwards. The curvature ratio of the bends $R/D = 14$. He observed that annular flow, which occurred in the horizontal passes for a superficial gas Reynolds number of greater 40000, was stable in the bend. Visual observation suggested that the liquid film was probably thicker on the inside of the bend than on the outside.

Owhadi and Bell (1967) investigated the behaviour of the entrained droplets and the annular film during boiling inside helically coiled tubes. Contrary to their expectations they found that although the mist flow regime was effectively suppressed, liquid remained well distributed on the entire tube surface to high qualities. The liquid film disappeared first at the 90° and 270° positions (taking the inside of the coil as 0°). They explained this in terms of a qualitative model. A secondary flow is postulated in the high velocity gas core similar to that which has been demonstrated to exist in single phase flow. This according to them imposes a shear stress on the liquid film causing flow from the outside to the inside of the coil. This is countered to some extent by the centrifugal forces acting on the liquid film, but the velocity of the film is very much less than that of the

gas so the magnitude of these forces is small. The film on the outer wall of the coil is continually replenished by deposition of entrained droplets, which travelling with velocities similar to that of the gas core are carried to the outer wall by reason of their high momentum. When the film finally breaks at high qualities the liquid will tend to accumulate at the 0° and 180° positions which are the stagnation points of the secondary flow.

Banerjee et al. (1967) investigated the behaviour of the liquid film in stratified flow in coils. As the liquid density is considerably greater than the gas density they had expected that the centrifugal forces would force the liquid up the outer wall of the coil. However, for certain ranges of gas and liquid flow rates, the liquid was observed to travel on the inner wall of the coiled tube. For a constant liquid flow rate, an increasing gas flow rate caused the liquid to move from the outer wall through a neutral position at the bottom of the tube to the inner wall. This could be explained in terms of the secondary flow pattern. However, they explained these phenomena in terms of the relative momentums of the gas and liquid phases. They further suggested that the resultant force on the liquid could be considered to act along a radius through the centre of gravity of the liquid film. Secondary circulation was neglected and the gas density assumed to be very much less than the liquid density. The angle of displacement of the liquid film, ϕ , was described by the expression

$$\tan \phi = \frac{(\rho_G V_G^2 - \rho_L V_L^2)}{Rg\rho_L} \quad (2.32)$$

where,

v_G and v_L are the actual velocity of the gas and liquid phases, respectively.

They showed that experimental results agreed with this equation to within $\pm 9\%$ except for the highest gas rates where there was considerable entrainment of liquid into the gas stream.

Oshinowo and Charles (1974) and Usui et al. (1980; 1983) discussed the interaction of the centrifugal force and gravity for the flow about a bend axis qualitatively. Usui et al. (1980; 1983) explained this interaction by proposing a modified form of the Froude number expressed in terms of v_L and v_G

$$Fr_\theta = \frac{v_L^2}{\frac{(\rho_L - \rho_G)}{\rho_L} R g \sin \theta} \left\{ 1 - \frac{\rho_G v_G^2}{\rho_L v_L^2} \right\} \quad (2.33)$$

From an evaluation of this expression, the relative positions of the liquid and gas phases across the radial direction of the bend may be estimated, namely: when $Fr_\theta > 1$, the liquid phase is in the outside of the bend, $Fr_\theta < 1$, is in the inner side. This approach is similar to that proposed by Oshinowo and Charles (1974). This led to a Froude number based on the assumption that the frictional and interfacial forces are negligible when compared to the pressure, centrifugal and gravitational forces. They carried out a force balance on the fluid elements in a direction normal to that of the flow at a point in the bend to yield:

$$\text{Pressure force} + \frac{\rho_L v_L^2}{R} - \rho_L g \sin \theta = f_{L\theta} \text{ for the liquid} \quad (2.34)$$

$$\text{Pressure force} + \frac{\rho_G v_G^2}{R} - \rho_G g \sin \theta = f_{G\theta} \text{ for the Gas} \quad (2.35)$$

Where $f_{L\theta}$ and $f_{G\theta}$ are the net forces and θ is the angle between the radius and the horizontal.

They also assumed that the net forces acting on each phase are equal ((2.34) = (2.35)), so that

$$\frac{\rho_L V_L^2}{R} - \rho_L g \sin \theta = \frac{\rho_G V_G^2}{R} - \rho_G g \sin \theta \quad (2.36)$$

Dividing through by $\rho_L g \sin \theta$, yields

$$\frac{V_L^2}{Rg \sin \theta} - \frac{\rho_G V_G^2}{\rho_L Rg \sin \theta} + \frac{\rho_G}{\rho_L} = 1 \quad (2.37)$$

This is essentially a sum of Froude numbers for the two phases. With these, they attempted an explanation for flow regime across different bend phase positions. They claimed that if the left hand side of equation 2.37 is greater than 1, then the liquid will move to the outside of the bend and that if less than 1, the liquid will move inside the bend. They made clear the effects of centrifugal and gravitational forces acting on each phase as a function of average void fraction.

Anderson and Hills (1974), reported experimental data that measured liquid film thickness, axial pressure profiles, gas velocity distribution, and droplet entrainment when air and water flowed concurrently in the annular flow regime in a bend mounted in a vertical plane at the top of a straight vertical tube. The diameter and radius of curvature of the bend they used were 25 and 305 mm, respectively. They reported that the behaviour of the liquid film is greatly affected by secondary flows caused by the centrifugal forces in the gas core.

Hoang and Davis (1984) utilised needle probes to measure the void fraction along an inverted U-bend attached to a 50.8 mm internal diameter pipe in the case of froth flow. The determination of the observed voidage distribution allowed the determination of the slip ratio, which was found to be greatly increased at the bend exit for low velocity conditions, after which it is diminished slightly in the downstream flow pipe. Later, Takemura et al. (1986) presented experimental results on the flow behaviour, pressure drop characteristics and dryout characteristics by the Joule heating of gas-water two-phase flows through U-shaped and inverted U-shaped bends, each having an internal diameter of 18 mm. They compared the results obtained from both bends and concluded that for the U-shaped bends, the gas phase flows along the inside of the bend, regardless of the flow rates of gas and water. Whilst in an inverted U-shaped bends, at lower gas and liquid flow rates, the tube wall at the outside of the bend in the vicinity of $\theta = 120 - 150^\circ$ is covered with gas phase. Also, that the inverted U-shaped bends have a wider safety region against dryout than the U-shaped bends.

Poulson (1991) measured and modelled mass transfer at horizontal 180° bends between horizontal tubes under annular two-phase flow conditions using the dissolution of copper in acid ferric chloride solutions. He concluded that mass transfer at bends relative to straight tubes increases with gas superficial velocities and is constant with low liquid superficial velocities. They successfully modelled the effect of bend geometry on mass transfer.

James et al. (2000) investigated the effect of a 90° horizontal bend on two-phase flow using computational and experimental studies. In their simulations using the Eulerian-Lagrangian method, they presented a suggestion as to whether droplets

of a given size deposit in the bend. This they achieved by carrying out calculations using droplets of various sizes: 10, 25, 50, 100, 250 and 500 μm diameter.

Sakamoto et al. (2004) carried out experimental work in a horizontal bend attached to a pipe of internal diameter 24 mm using air-water flow mixture. The conductance type void probe was employed to measure the liquid film thickness and an L-shaped stainless steel sampling tube to measure the local droplet flow rate. They investigated the distributions of annular liquid film thickness and the local drop flow rate in the gas core in a straight pipe and at the end of three U-bends at different angles to the horizontal. They found that the local flow rate of the liquid droplets in the gas core of horizontal pipe flow reaches a minimum near the lower wall of the pipe and a maximum near the upper wall.

For predicting and thus preventing dryout in serpentine channel of fired reboilers on a hydrocarbon plant, constituted of vertical tubes joined by 180° bends, Chong et al. (2005) proposed a new model which is the extension of the phenomenological model for annular flow in a single vertical channel of Azzopardi (1997). This model was found to confirm adequately the decrease of film flow rate to zero just before the last bend as earlier predicted by Balfour and Pearce (1978) for “C” bends. Balfour and Pearce conducted an experimental investigation on the distributions of water films and entrained droplets in air-water annular flows in 180° horizontal bend using sampling probes. They took a series of measurements with the probes positioned at 45° intervals around the tube exit and at varying radii. They concluded that in those annular flows where the air speed is high, many of the entrained droplets are thrown very rapidly to the wall

and that the entrained fraction tends to zero for high quality annular flows where the films are thin.

A critical review of the literature has revealed that the present state of understanding of two-phase gas-liquid flow in return bends is limited, either concerned with single phase flow or two-phase gas-liquid flow in small diameter pipes with air-water as the model fluids. The change of flow structure before and after the bends was mainly obtained by visualization and the underlining mechanism for the change of flow patterns was not discussed. In addition the film fraction is expected to be influenced by the centrifugal and gravity forces along the bend channel. Though, Usui et al. (1983) worked on plug and bubble flows, Anderson and Hills (1974) examined annular flow. Till date no work has been reported on churn flow, the least understood flow pattern. The location at which the liquid film thins out in the bend is very crucial. Its determination is very important as this will establish where insulation can be planned for against flame and when increasing the liquid flow rate above the minimum flow rate for dryout is necessary.

Therefore, both the film fraction and circumferential variation of liquid film thickness behaviour were examined quantitatively in more detail in a pipe with an internal diameter relevant to the oil and gas industry. To achieve these, measurements were made of the (1) film fraction distribution at: 17 pipe diameter upstream of the bend, 45, 90 and 135° into the bends, and 21 pipe diameter downstream of the bend and (2) the circumferential variation of liquid film thickness around the 45, 90 and 180° bend positions. The experimental arrangement used to meet the objectives and the results obtained are presented in

Chapters 6 and 7, respectively. The fluids examined are air and water. The conductance probe method based on the difference of conductivities between air and water was used to evaluate the flow pattern. The flow patterns were determined by analyzing the Probability Density Function (PDF) of the time series of film fraction. The observations reported in Chapter 7 on the behaviour of two-phase churn-annular flow on entering a vertical 180° return bend should lead to a deeper understanding of the mechanisms of two-phase flow.

Table 2.1: Data from experiments in bends

Reference	Fluids	Pipe diameter (mm)	Radius of curvature of the bend (mm)	Bend angle and direction	Measured parameters
Gardner and Neller (1969)	Air-water	76	305	90°, Vertical to horizontal (upward)	Void fraction
Anderson and Hills (1974)	Air- water	25	305	180°, Vertical return bend	Film thickness, Local drop distribution
Maddock et al. (1974)	Air-water	25.4	51,127,254	30,45,60,90° Vertical to horizontal (vertical)	Film thickness, film flow rate, local drop distribution
Oshinowo and Charles (1974)	Air-water	25.4	76.2, 152.4	Serpentine geometry	Void fraction
Balfour and Pearce (1978)	Air - water	25	48.5	180°, Horizontal to horizontal, (upward)	Film thickness
Usui et al. (1980)	Air-water	16 24	90, 132.5 135, 180	180° Horizontal to horizontal (upward)	Void fraction, pressure drop
Usui et al.(1981)	Air-water	16 24	90, 132.5 135, 180	180° Horizontal to horizontal (downward)	Void fraction, pressure drop

Usui et al.(1983)	Air-water	24	96	180°, vertical return bend	Local volume fraction
Hoang and Davis (1984)	Air- water	50.8	50.8, 76.2	180° Vertical return bend	Local gas velocity, Void fraction, Bubble size,
Takemura et al. (1986)	Air- water	18	116 435	180° Vertical to vertical. U and inverted U bends	Flow patterns, Pressure drop. Dryout
Poulson (1991)	Air-water	13 22.6	39,95 56.5	180°, Horizontal to horizontal (upward)	Erosion, Mass transfer
Usui (1992,1993)	Air-water	24	144	180° Horizontal to horizontal	Local film flow rate, Film thickness
Ribeiro et al. (2001)	Air- water	32	166	90°, Horizontal to horizontal	Drop size
Sakamoto et al.(2004)	Air- water	24	135	180° Horizontal to horizontal (upward), Vertical upward, 45° upward, Horizontal	Local film thickness, Drop flow rate.
Azzi et al. (2000,2002,2005)	Air- water	30	120, 180, 240 and 300	90° Vertical to horizontal (upward)	Pressure drop
Domanski et al. (2006)	R – 22 and R – 410 A	3.25, 11.63	6.35, 37.25	180°. Horizontal	Pressure drop
Spedding and Benard (2007)	Air- water	26	17	90° Vertical to horizontal (upward)	Pressure drop
Shannak et al. (2009)	Air- water	50	200, 300, 400, 500	90° Vertical to horizontal (upward)	Pressure drop

Abdulkadir et al. (2011)	Air-silicone oil	67	154.4	90° , Vertical to horizontal (upward) and horizontal to horizontal (upward)	Void fraction
--------------------------	------------------	----	-------	---	---------------

Experimental design

3.0 Experimental Arrangements:

The analyses performed on experimental laboratory data provide the main source of information about specific multiphase flow regimes. This chapter presents a summary of the results obtained from a series of two-phase air-silicone oil flow laboratory experiments that were performed on an inclinable pipe flow rig which is available within the L3 Laboratories of the Department of Chemical and Environmental Engineering at the University of Nottingham. This chapter presents a detailed description of the experimental rig used to study the flow behaviour present in vertical and horizontal orientated 90° bends. An overview of the experimental facility and the choice of test fluids are given in Sections 3.1 and 3.2, respectively. Further details of the capability of the flow facility and the modifications made to the inclinable rig are detailed in Sections 3.3 and 3.4, respectively. Detailed description of the inclinable rig is given in Section 3.5. Furthermore, Sections 3.6 and 3.7 provide the methodology used during the experiments and a summary of hazard analysis of the experimental facility, respectively. Finally, the uncertainties inherent in the analyses of the experimental measurement data are discussed in Section 3.8.

3.1 Overview of the experimental facility:

The first series of experiments were performed on an inclinable pipe flow rig, shown in Figure 3.1. This rig had previously been employed in multiphase annular flow studies executed by Azzopardi et al. (1997), Geraci et al. (2007a), Geraci et al. (2007b) and more recently for the study of bubbly, slug and churn flow by Hernandez-Perez (2008). The experimental facility consists of a main pipe flow test section made from transparent acrylic pipes of 0.067 m inside diameter and 6 m long to allow for the development of the injected flow over the length of the test section. The test section is constructed from a series of conjoined short sections of pipe with a flange joint at either end. Each of these smaller test sections may be easily installed or replaced, to lengthen or shorten the length of the test section. The rigid steel frame supporting the test pipe section is constructed to enable the test pipe section to be inclined at angles of from -5° to 90° to the horizontal. This enables the researcher to investigate the influence that different inclinations may have on the flow patterns generated. The experimental rig was charged with an air/silicone oil mixture. The experiments were all performed at an ambient laboratory temperature of approximately 20° C. The physical properties of the fluids used in the experiments are as shown on Table 3.1.



Figure 3.1: Picture of the inclinable rig.

3.2 System (test fluid):

The air-silicone oil system was selected for several reasons:

- Thermal stability and transfer qualities - at both hot and cold extremes
- Electrical insulation
- Fire resistance
- No toxicity, which makes it environmentally safe, and reasonable in cost
- No odour, taste or chemical transference
- Easily discernable in acrylic pipe
- Several proven techniques including the advanced instrumentation exist for liquid holdup and/or void fraction measurements for silicone oil.

The properties of the two fluids used in the experiments are shown in Table 3.1.

Table 3.1: Properties of the fluids at 1 bar and at the operating temperature of 20°C

Fluid	Density (kgm ⁻³)	Viscosity (kgm ⁻¹ s ⁻¹)	Surface tension (Nm ⁻¹)	Thermal conductivity (Wm ⁻¹ K ⁻¹)
Air	1.18	0.000018	0.02	0.1
Silicone oil	900	0.00525		

3.3 Description of Flow Facility:

The flow facility consists of a liquid storage tank, liquid centrifugal pump, compressed air line, liquid and air rotameters, and a cyclone (separator). A vertical 90° bend with a radius of curvature 154 mm was attached to the top of the pipe flow test section of the rig (Figures 3.2 and 3.3) to enable the effects that a 90° bend connected in series may have on air-silicone oil around the bend section. At the top of the pipe flow test section before the bend, ECT and WMS measurement transducers were installed at different axial positions (dimensionless axial distances from mixer are 66, 67 and 73 pipe diameters). Data provided by these transducers will allow for the measurement of the time varying liquid holdup and the void fraction, respectively. It should be noted that it was not possible to mount the WMS upstream of the ECT sensor, since a visual examination concluded that the intrusive wire mesh of the WMS changed the nature of the flow completely by breaking up large bubbles and temporarily homogenising the flow immediately downstream of the device. The large bubbles were observed to re-form within approximately one pipe diameter.

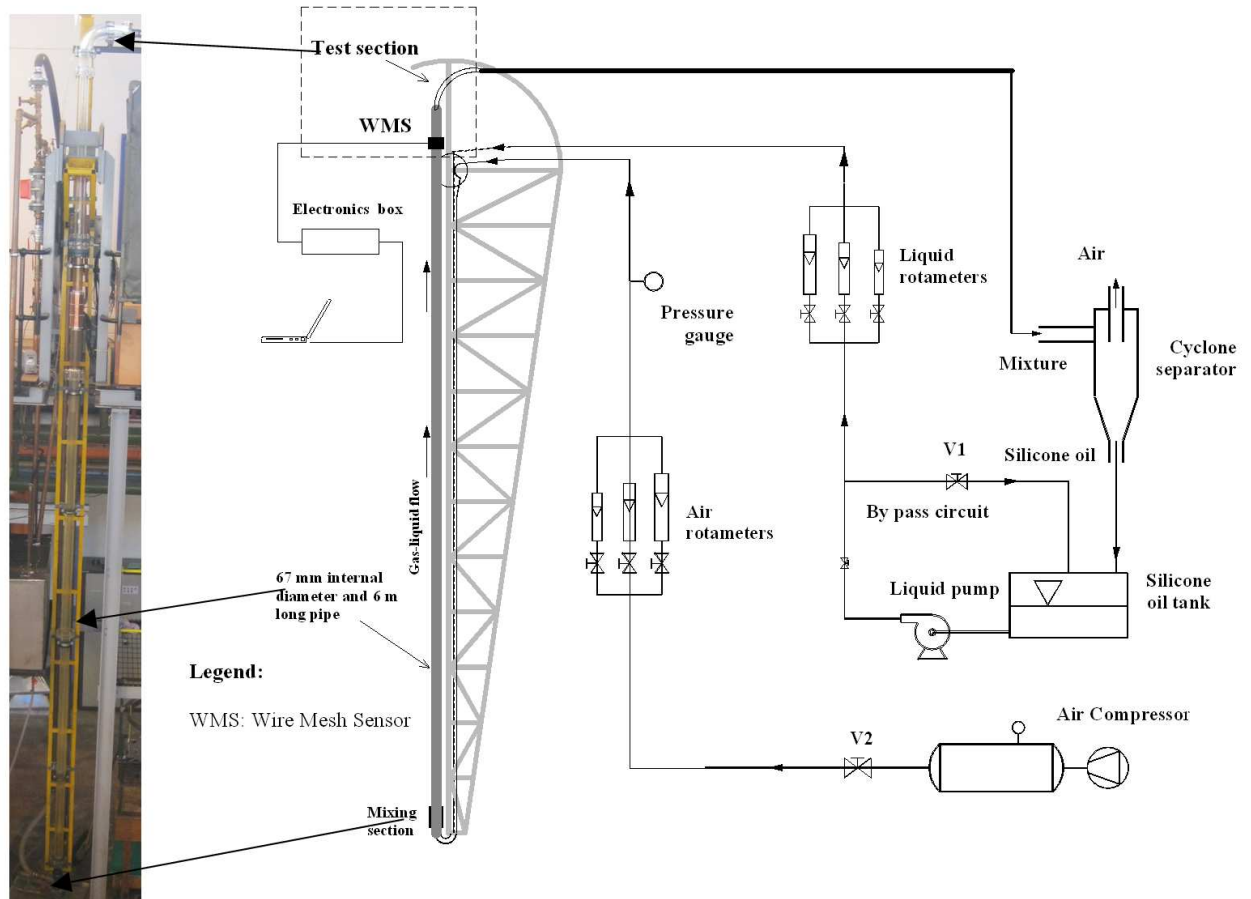


Figure 3.2: Diagram showing the inclinable rig converted to a vertical 90° bend. The left hand side of the figure shows the actual picture of the rig.

In addition, a pair of static pressure tapings (differential pressure cell) was mounted on either side of the ECT measurement planes to record the pressure drop along the vertical pipe flow test section. The output of the differential pressure cell (DP cell) was recorded through a computer using LABVIEW 7 software (National Instruments), and was taken at a sampling frequency of 1000 Hz over 60 seconds for each run. Immediately after the 90° bend test section, a WMS was placed at 0.21 m downstream of the bend (at a length of approx 3 pipe diameters). The silicone oil enters the mixing chamber (described in more detail in Section 3.5.1). This ensures that the gas and liquid were well mixed at the entry

region of the test pipe flow section. The inlet volumetric flow rates of the liquid and the air are determined by the use of rotameters mounted in line with the air and water pipe lines to the mixing chamber. The fluid inflow conditions for which experiments were carried out for both the vertical and horizontal 90° bends were over a liquid superficial velocity range of 0.05 – 0.38 ms⁻¹ and a gas superficial velocity of range 0.075 – 7.52 ms⁻¹. Across this range of gas-liquid injections the following flow patterns could be observed using the experimental rig: for the vertical 90° bend, spherical cap bubble, slug, unstable slug and churn flows. Plug, slug, stratified wavy and stratified flows were observed for the horizontal 90° bend.

Air was supplied to the mixing chamber from the laboratory compressed air rig main system at 3.2 barg through a control valve (V1). It was fed into the facility through a 22 mm internal diameter stainless steel pipe. Both the air flow rate and gauge pressure were measured prior to entering the mixing section using a set of two air flow rotameters mounted in parallel that covered a wide range of flow rates as well as a pressure gauge meter, respectively. An air distributor is installed whose function it is to make sure that all of the air coming into the pipe are well mixed and equally distributed across the cross section of the pipe.

The silicone oil is stored in a liquid storage tank shown in Figures 3.2 and 3.4b and was pumped into the mixing section using a centrifugal pump presented in Figure 3.4a. A bypass valve maintains the circulation of the liquid flow. In addition, two liquid rotameters mounted in parallel were installed to measure the flow rates of the silicone oil entering the test pipe flow section. The liquid flow rate is controlled by valves. The two separate phases are then mixed within the

gas-liquid mixing section. From the mixer, two phase mixture flows along the test pipe flow section before it reaches the measurement sections where the ECT, WMS and differential pressure (DP) Cells are located. The ECT and WMS sensors were located at distances of 4.4 m and 4.92 m, respectively from the mixer entry section at the base of the test pipe flow section. Though, the WMS was relocated at a distance of 0.21 m after the bend. The two ECT measurement planes are separated by a distance of 89 mm and placed around the circumference of the pipe. The capacitance measurements provide a pair of time series of liquid holdup. The use of two such circumferential rings of sensor electrodes, located at a specified distance apart (also, known as twin-plane sensors), enables the determination of the velocity of periodic structures such as Taylor bubbles and liquid slugs. As the air-silicone oil mixture exits the test pipe flow section it is fed through a cyclone separator. The air is released to atmosphere from the top of the separator and the liquid drains to the bottom under the influence of gravity and flows back to the main liquid storage tank (Figure 3.4e). During the course of the experimental campaign at high gas flow rates (churn flow), mists were observed coming out of the separator; this therefore necessitated the design and installation of a special filter at the top of the cyclone (Figure 3.4e) to prevent the release of the mist to the ambient.

3.4 Installation of a 90° bend:

A 90° bend was installed at the top end of the 6 m test flow pipe section as shown in Figures 3.2 and 3.3. It has a radius of curvature of 0.15 m and a diameter of 0.074 m. The inside diameter of the bend was slightly greater than that of the test pipe and the wire mesh sensor, requiring short transition pieces to be installed at

the inlet and outlet of the bend. Flanges were installed to mate with the test pipe and the outlet line. The joints were carefully machined without sharp corners to eliminate the effect of radius of curvature as a variable in the experiments. The new geometry shown in Figures 3.2 and 3.3 consists of an upstream and downstream pipe connected to a 90° bend. The rig was used to examine the behaviour of gas-liquid flows in the 90° bend using the following instrumentation: Electrical Capacitance Tomography (ECT) and Wire Mesh Sensor tomography (WMS). It was also used to study the characteristics of slug flow in a vertical riser using the data obtained from the ECT.

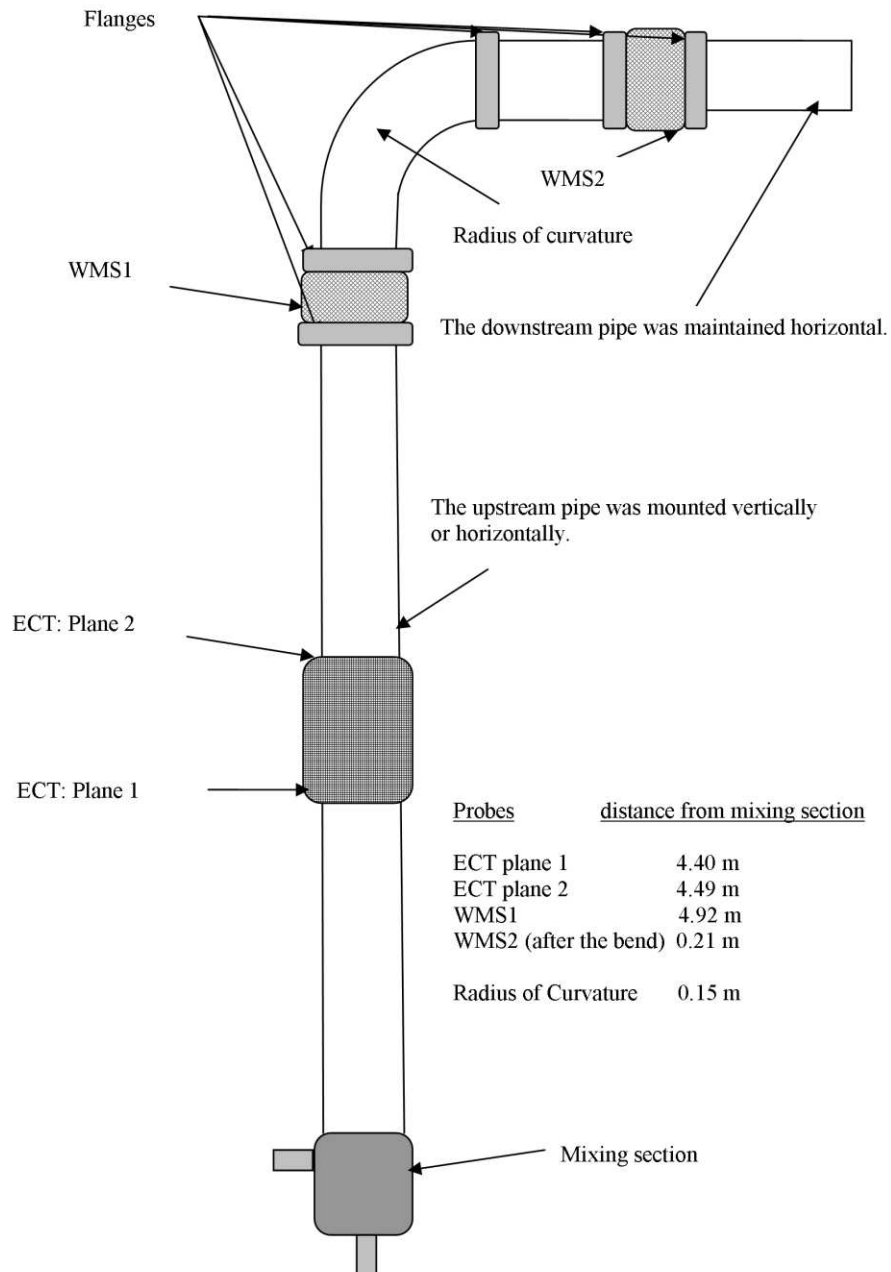


Figure 3.3: Schematic diagram of the vertical 90° bend

The upstream orientation of the 90° bend was changed from vertical to horizontal whilst maintaining the downstream pipe, horizontal. The purpose of doing this is to investigate the influence of changing the bend orientation on flow behaviour.

3.5 Flow facility components:

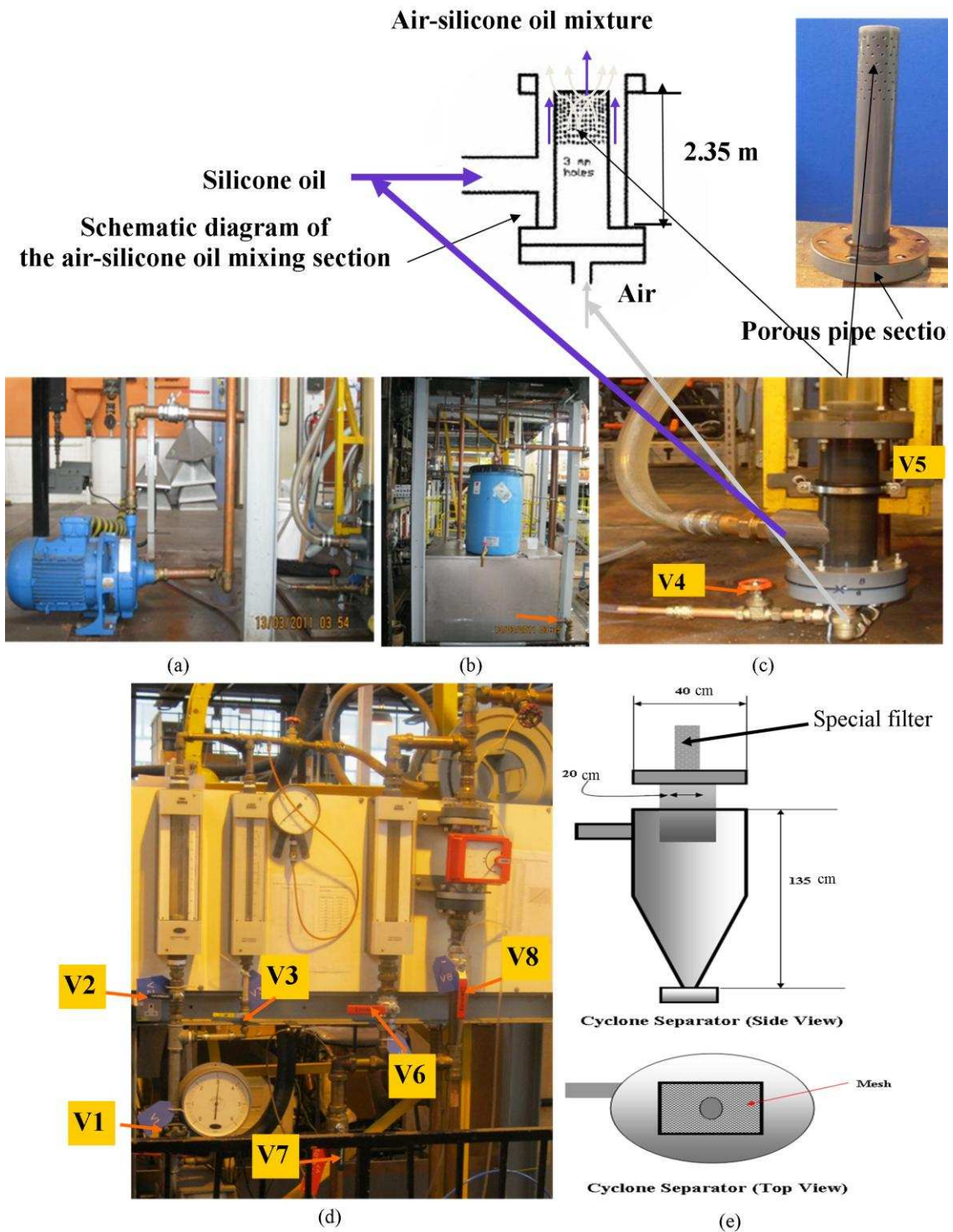


Figure 3.4: The major components of the rig (a) liquid pump (b) liquid tank (c) air-silicone oil mixing section (d) rotameters and (e) cyclone separator

3.5.1 Gas-liquid mixing section:

A number of different mixers for two-phase flow have been described by other investigators. The choice of mixer geometry is often dictated by the flow pattern that is of primary interest. For an investigation that covers the whole spectrum of flow patterns, of which the present study is an example, Govier et al. (1957) determined that the geometry of the mixing section affected the flow pattern only for a very short distance and that with an adequate calming section a simple “tee” was suitable.

It was intended that the mixing of the air and silicone oil phases took place in such a way as to reduce flow instability. Flow stability was achieved by using a purpose built mixing unit (annular section), providing maximum time for the two-phases to develop. The mixing section is made from PVC pipe as shown in Figure 3.4c. The silicone oil was introduced from one side of the mixer. Air is fed from the rear of the mixing section directly into the annulus through a distributor with 100 holes with a diameter of 3 mm each on the wall of the capped central pipe, thus creating a more even circumferential mixing section.

3.5.2 Gas-liquid separation cyclone:

In the cyclone, the gas and liquid are separated by a combination of gravity and centrifugal effects. The centrifugal force throws the aerated liquid onto the vessel walls whereby it drains under gravity as a film. The diameter of the separator is 23.5 cm and height 1.35 m. The two-phase mixture is fed into the top of the cyclone tangentially. The separated air stream exits the top of the cyclone and the silicone oil returns by gravity feed through the bottom of the cyclone to the silicone oil reservoir tank (Figure 3.4e).

3.5.3 Flow measurement section:

The sections of flow measurement for both air and silicone oil are similar. The flow meter element was a rotameter of the type (Variable Area Meter). The two air rotameters together cover the range 10-1000 Lmin⁻¹. A picture of the flow measurement section is presented in Figure 3.4d.

3.5.4 Differential pressure cell (DP Cell):

Pressure drop is the driving force for flow transport and is therefore a key parameter in terms of flow rates, stability of pipes, sizing of pumps and overall design of any two phase system. In order to measure the pressure drop, a differential pressure transducer (Rosemount 1151 smart model) with a range of 0 – 37.4 kPa and output voltage of 1 to 5 volts (Figure 3.5) was installed. In the selection of the DP cell, both the range and sensitivity were taken into account. The DP cell was used to measure the time varying, two-phase total pressure drop across the test section. The data acquisition frequency of the DP cell is 200 Hz. In the test pipe flow section, two pressure tapping are provided, located in the straight pipe before the bend. The exact axial locations of the tappings are 4.5 and 5.36 m (67 and 80 pipe diameters, respectively) from the bottom of the test pipe flow section. Thus, the total pressure drop was measured simultaneously together with the liquid holdup and void fraction. Prior to taking measurements of pressure drop, the DP cell was calibrated using the arrangement shown in Figure 3.6. This calibration from the sensor to the computer file gives the relationship between the output voltage of the DP cell and the differential pressure. The calibration curve is linear as given in the specifications of the DP cell. This is plotted in Figure 3.7.

The associated equations were programmed then into the data acquisition software.

It is worth mentioning that pressure tapings in two phase flow need to be purged continually with one of the phases whilst pressure measurements are being made. If purging is not carried out the pressure fluctuations tend to force a two phase mixture into the DP cell lines causing inaccuracies in the measured pressures arising from surface tension effects and uncertain static head. In view of this fact, a purging system was used to maintain a continuous liquid line from the pressure tapings to the DP cell.

The purge was operated before every run by opening and closing the valve from the liquid line. The separation distance between the tapings was 86 cm. To activate the purging system, high purging rate was set to get rid of any bubbles in the purging lines, it was then reduced to the optimum purging rate which is high enough to prevent air from entering the tapping line but the flow does not affect the measurement. Holt (1996) suggested that the purging rate should be less than 5 % of the total liquid flow rate.



Figure 3.5: Picture of a differential pressure cell (DP Cell)

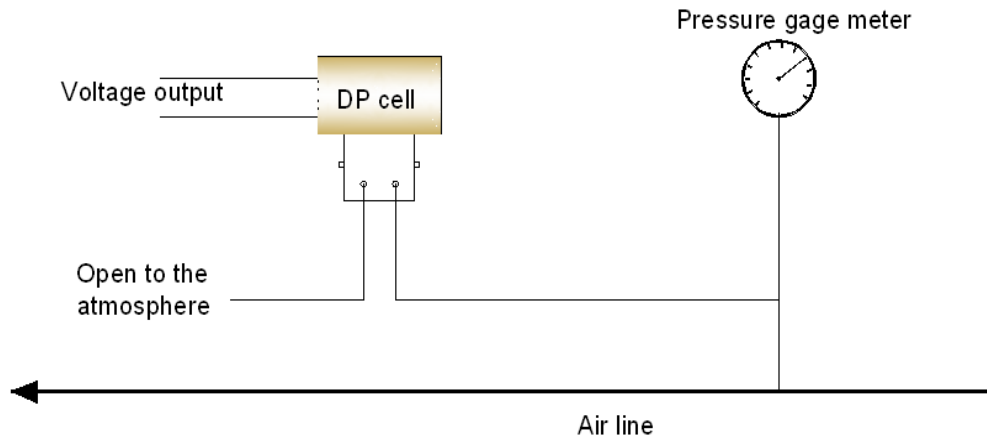


Figure 3.6: Arrangements for DP cell calibration

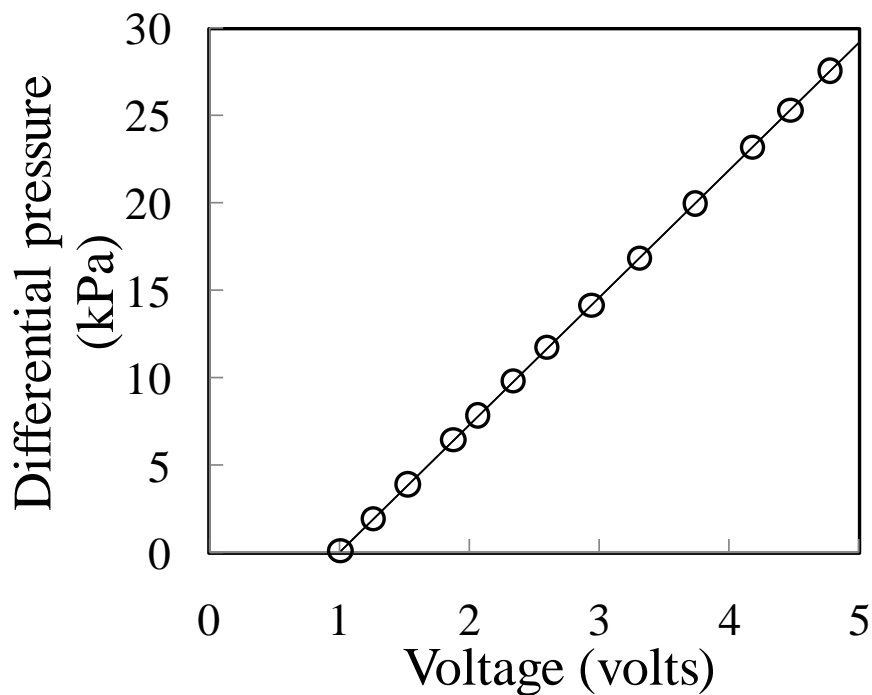


Figure 3.7: DP cell calibration

3.5.5 Data acquisition:

LABVIEW software (National Instruments) was used for data acquisition and conversion from the output voltage to physical values based on the calibration results obtained for each measurement device. The data acquisition rate may be controlled easily using built in functions present in the software. Because LABVIEW has the flexibility of a programming language combined with built-in tools designed specifically for test, measurement, and control, an application was

created and measurement data were recorded every 0.001 seconds over a 60 seconds experimental run period. An example of a data acquisition system involving LABVIEW is in Figure 3.8 for the DP cell used in the experiments.

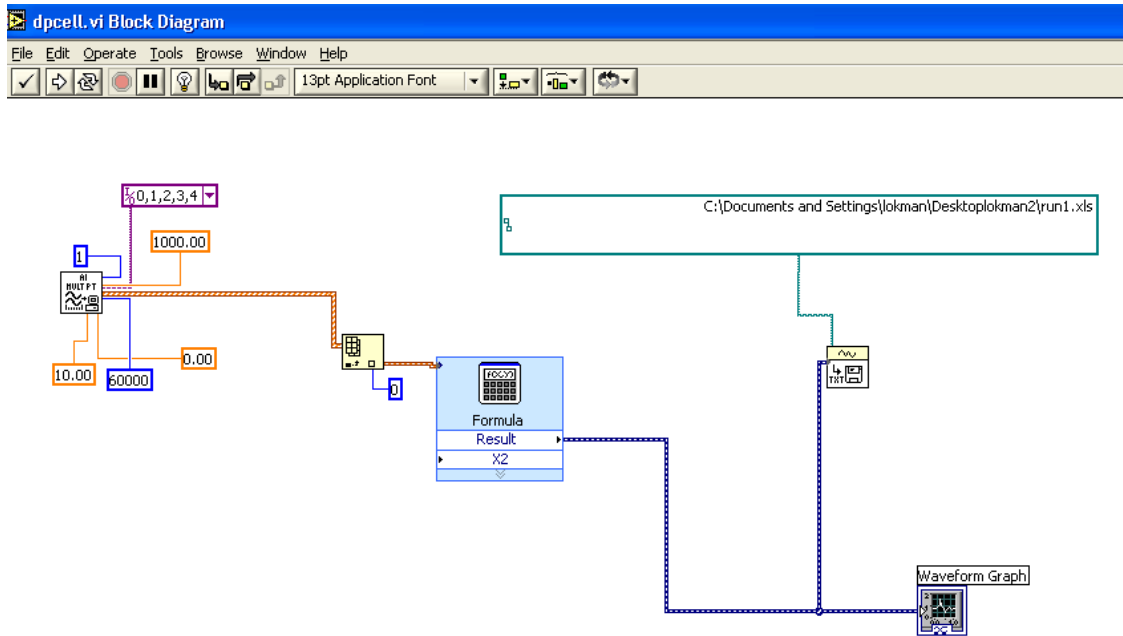
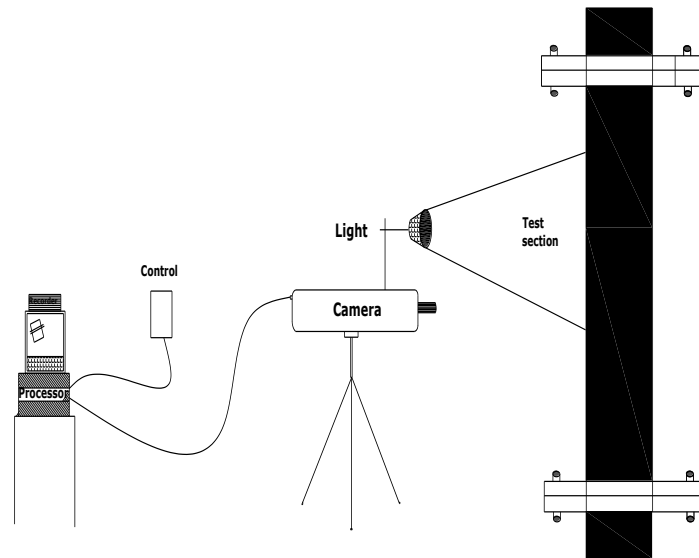


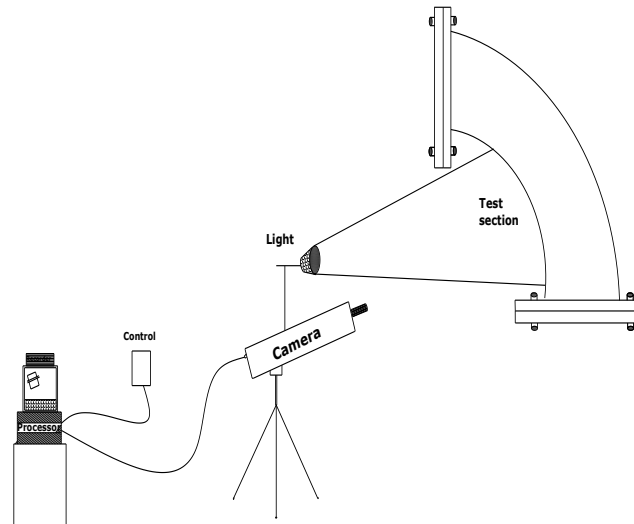
Figure 3.8: Block diagram assembled in LABVIEW for the DP cell

3.5.6 High speed video system:

A high speed video camera (Phantom, Fastcam-APX 120 K) with a resolution of 512×512 pixels operating at 60,000 frames per second was used to visualise and validate the flow regimes identified during the experiments. A schematic diagram of the experimental set up and the camera configuration is shown in Figure 3.9.



(a)



(b)

Figure 3.9: High speed video arrangement

The camera was run at 512×512 pixels using a recording rate that ranged from 150 – 1,000 frames/second depending on the flow condition. Images were initially carried out at a location of about 4.5 m (67 pipe diameters) from the mixing section. This technique allowed capturing the image sequence of the flow. The camera was then used to take images from the side of the bend.

3.5.7 Void fraction measurement:

In order to be able to determine the void fraction and/liquid holdup, it was necessary to use a liquid holdup measurement unit that fits the characteristics of this experimental work; the main factors that were taken into account are the fluid and flow pattern. The fluids are air-silicone oil and the flow patterns are spherical cap bubble, slug, unstable slug and churn flows. Particular emphasis was given to the slug flow regime. For the horizontal set up, the flow patterns are plug, slug, stratified wavy and stratified flows.

3.5.7.1 Wire Mesh Sensor:

Local time varying void fractions were obtained by using the WMS measurement transducer developed by Presser et al. (1998 and 2001). The sensor shown in Figure 3.11 consists of two parallel wire grids positioned orthogonally but offset by a small distance in the axial direction. One grid works as a transmitter while the other as a receiver. By activating each wire successively, the current at each crossing point is detected. The local instantaneous void fractions are calculated from the measured capacitance between crossing points, a series of 2 dimensional data sets can be obtained. By reconstructing these sets in time sequence a high speed visualization may be achieved.

In this study, a 24×24 wire configuration sensor was used that had been previously applied for conductivity measurements. The sensor comprises two planes of 24 stainless steel wires of 0.12 mm diameter, 2.8 mm wire separation within each plane, and 2 mm axial plane distance. The wires are evenly distributed over the circular pipe cross-section. Since the square sensor is installed in a circular pipe, only 440 of the total 576 wire crossing points are

within the radius of the pipe. The spatial resolution of the images generated by the sensor is 2.8 mm, which corresponds to the wire separation within a single plane. Data was acquired at a frequency of 1000 Hz for a 60 second experimental run period. An acrylic frame supports the sensor and allows fixation into the text flow pipe section. Figure 3.10 shows a photograph of the sensor.



Figure 3.10: Wire mesh sensor (WMS)

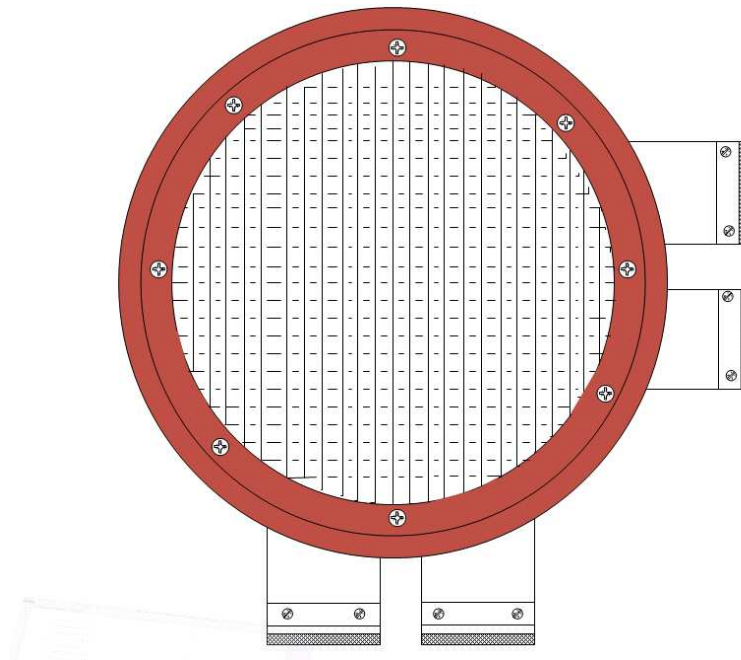


Figure 3.11: 24 × 24 wire mesh sensor for pipe flow measurement

3.5.7.1.1 Principles of operation of the WMS:

In the WMS, an associated electronic sensor measures the local permittivity in the gaps of all crossing points by successfully applying an excitation voltage (sine wave of 5 MHz) to each one of the sender electrodes at one wire plane whilst measuring in parallel the current flowing toward receiver electrodes at the other wire plane. The non activated transmitter wires are grounded. This step assures that the electrical field distribution is focused along the activated wire and allows for a sampling of only a defined region within the pipe, so that the measured currents are unambiguously related to the corresponding crossing point. For the permittivity measurements a sinusoidal alternating voltage is applied and a demodulation scheme is subsequently applied. After digitizing, the measured data are sent to a computer where they are processed and displayed. The method is able to generate up to 7,000 images per second. Details of the electronic circuits used may be found in da Silva et al. (2010).

The principle of operation of the wire mesh sensor is the direct and high speed imaging of the flow based on the capacitance measurements made at the wire crossing points. The wire mesh subdivides the flow channel cross-section into a number of independent sub regions, where each crossing point represents one region.

The output reading of a wire mesh sensor is in the form of a data matrix $V(i, j, k)$ representing the voltage measured at each (i, j) crossing point with $i \in (1, \dots, 0.24)$ and $j \in (1, \dots, 0.24)$ and at a given time step k . These voltage readings are proportional to the relative permittivity of two-phase mixture ϵ_m according to da Siva et al. (2010)

$$V = a \ln(\varepsilon_m) + b \quad (3.1)$$

Where a and b are constants that encompass the specific parameters of the electronics. Reference measurements are required to determine the constants a and b of equation 3.1, which in turn allows for the calculation of mixture permittivity at every crossing point. First, the sensor measures the empty pipe, i.e., gas ($\varepsilon_{r,G} = 1$), yielding the reference data matrix $V^G(i, j)$, which is normally an average of the raw data over a sufficient temporal range to suppress noise. The procedure is then repeated with the entire cross-section covered with the liquid phase having a permittivity value $\varepsilon_{r,L}$, full pipe, which gives another reference data matrix denoted by $V^L(i, j)$. Eventually, on the basis of equation (3.1) for the two described conditions, the measured mixture permittivity is calculated by

$$V(i, j, k) = a \ln \varepsilon_m(i, j, k) + b \quad (3.2)$$

subject to the boundary conditions:

$$\varepsilon_m(i, j, k) = \varepsilon_{r,G} = 1; V(i, j, k) = V^G(i, j)$$

$$\varepsilon_m(i, j, k) = \varepsilon_{r,L}; V(i, j, k) = V^L(i, j)$$

The values of the boundary conditions are then substituted into equation (3.2) and solving simultaneously as follows to obtain the values of the constants, a and b .

$$\text{For, } \varepsilon_m(i, j, k) = \varepsilon_{r,G} = 1; V(i, j, k) = V^G(i, j)$$

Equation (3.2) becomes

$$V^G(i, j) = a \ln 1 + b = b \quad (3.3)$$

$$\text{Also for, } \varepsilon_m(i, j, k) = \varepsilon_{r,L}; V(i, j, k) = V^L(i, j)$$

Substituting the boundary condition directly above into equation (3.2) becomes

$$V^L(i, j) = a \ln \varepsilon_{r,L} + b \quad (3.4)$$

Substituting equation (3.3) into equation (3.4) yields

$$V_L(i, j) = a \ln \varepsilon_{r,L} + V^G(i, j) \quad (3.5)$$

$$a = \frac{V^L(i, j) - V^G(i, j)}{\ln \varepsilon_{r,L}} \quad (3.6)$$

Substituting equations (3.6) and (3.3) into (3.2)

$$V(i, j, k) = \frac{V^L(i, j) - V^G(i, j)}{\ln \varepsilon_{r,L}} \ln \varepsilon_m(i, j, k) + V^G(i, j) \quad (3.7)$$

Rearranging equation (3.7) to obtain $\varepsilon_m(i, j, k)$

$$V(i, j, k) - V^G(i, j) = \frac{V^L(i, j) - V^G(i, j)}{\ln \varepsilon_{r,L}} \ln \varepsilon_m(i, j, k)$$

$$\ln \varepsilon_m(i, j, k) = \frac{V(i, j, k) - V^G(i, j)}{V^L(i, j) - V^G(i, j)} \ln \varepsilon_{r,L} \quad (3.8)$$

$$\varepsilon_m(i, j, k) = \exp \left[\left(\frac{V(i, j, k) - V^G(i, j)}{V^L(i, j) - V^G(i, j)} \right) \ln \varepsilon_{r,L} \right] \quad (3.9)$$

There are different models to describe the effective permittivity of a mixture based on different assumptions of how the phases are geometrically distributed Mckeen and Pugsley (2003). The most commonly used for gas-liquid flows is the parallel model, which states that the effective permittivity linearly depends on the

phase fraction. The void fraction is obtained from the measured permittivity ε_m according to

$$\alpha(i, j, k) = \frac{\varepsilon_{r,L} - \varepsilon_m(i, j, k)}{\varepsilon_{r,L} - \varepsilon_{r,G}} \quad (3.10)$$

Where $\varepsilon_{r,L}$ is the liquid permittivity and $\varepsilon_{r,G} (= 1)$ is the gas permittivity

To analyse the void fraction data $\alpha(i, j, k)$, which is a 3D matrix, different levels of complexity can be used. For instance, image sequences of the flow as well as cross-sectional images from the pipe can be generated. Three-dimensional contour images of the gas-liquid interface can be generated, showing for instance the shape of bubbles. Quantitative insights of the flow are obtained by averaging the measured void fraction in space and/or in time, yielding a time series of void fraction or mean void fraction over the entire measurement.

A unique feature of wire mesh sensors is that due to their high spatial and temporal resolution, bubble sizes and radial void fraction distribution can be estimated by proper data processing. The details of the process to derive radial and cross-sectional void fraction are presented in sections 3.5.7.1.2 and 3.5.7.1.3.

3.5.7.1.2 Processing of Void fraction profiles:

In order to obtain quantitative information on the flow, both time and cross-sectional averaging of the void fraction data were used, as explained in Prasser et al. (2002). The averaging was based on weight coefficients that define the contribution of each crossing point of wires (i, j) in the sensor matrix to the size of the domain, over which the averaging had to be done. The definition of the weight coefficients $(a_{i,j})$ necessary to obtain a cross-section averaged void

fraction is shown in Figure 3.12. The averaging was done by calculating for each sampling period individually:

$$\bar{\varepsilon} = \varepsilon(t_k) = \sum_i \sum_j a_{i,j} \cdot \varepsilon_{i,j,k} \quad (3.11)$$

Radial time averaged void fraction were calculated by averaging the local instantaneous void fractions over the measurement period and over a number of ring-shaped domains (m). This is done by the following equation:

$$\bar{\varepsilon} = \frac{1}{k_{\max}} \sum_k \sum_i \sum_j a_{i,j,m} \cdot \varepsilon_{i,j,k} \quad (3.12)$$

Where,

$a_{i,j,m}$ are the weight coefficients denoting the contribution of each measurement point with the indexes i, j to a ring with the number m and k_{\max} is the maximum time interval. This ring-shaped averaging domain covers a given radial distance from the centre of the sensor as shown in Figure 3.13.

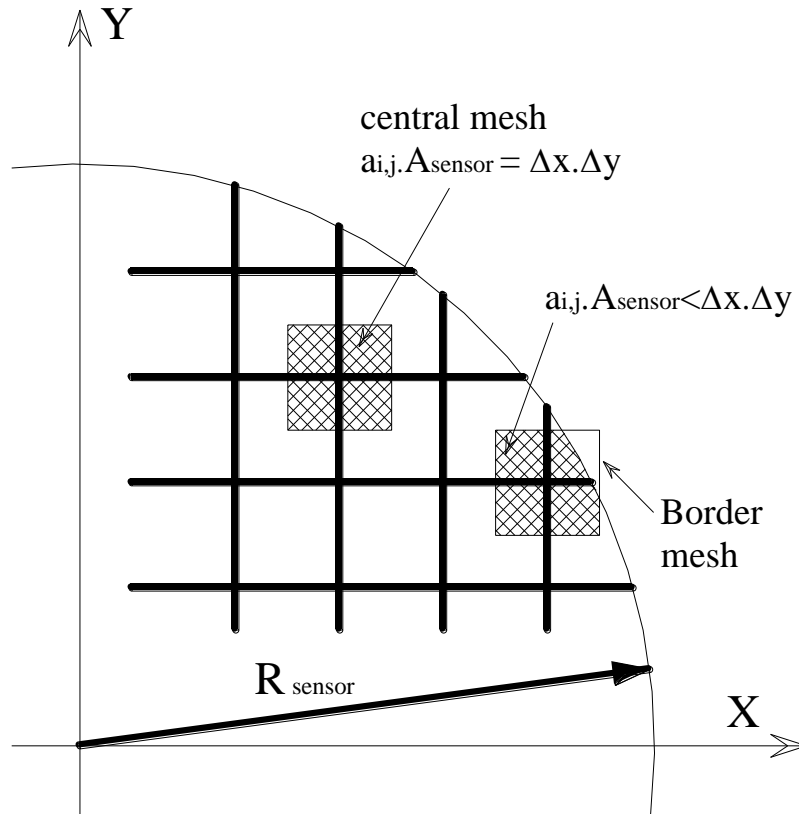


Figure 3.12: Weight coefficients for the cross-section averaging of local void fractions measured by the WMS (Prasser et al. (2002))

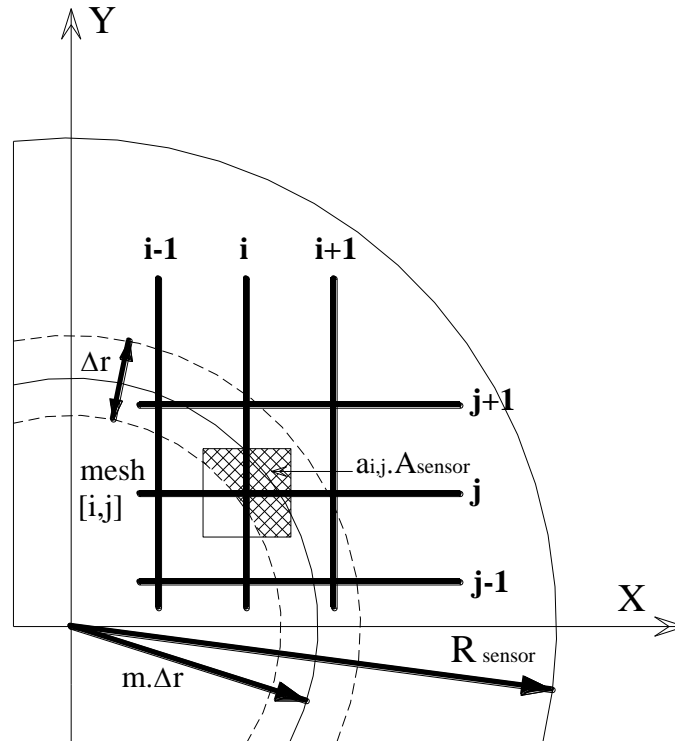


Figure 3.13: Weights coefficients for the cross-section averaging of local void fractions over a number of ring-shaped domains (Prasser et al. (2002))

3.5.7.2 Electrical Capacitance Tomography:

The basic idea of the ECT is to install a number of sensors around the internal circumference of the pipe to be imaged. The sensor output signals depend on the position of the component boundaries within their sensing zones. A computer is used to construct a tomographic image of the cross-section being observed by the sensors. This will provide for instance, measurements of two-phase flow boundaries in pipes with applications to multiphase flow measurements.

According to Bolton et al. (1998), the objective of ECT is to provide images of phase distribution by exploiting differences in electrical permittivity between the phases of a multiphase flow mixture within a process vessel or pipeline. To facilitate measurements throughout the sensing zone, multiple electrodes are arranged around the boundary of the zone. The capacitance electrodes are usually made from thin copper films, and are attached to the outside of an insulated section of the process vessel or pipeline, resulting in electrodes that are truly non-invasive and non-intrusive. Typically, the sensor consists of 8 or 12 electrodes mounted symmetrically around the sensing zone (Wang et al. (1995) and Yang (1996)). Capacitance measurements are taken between all independent pairs of electrodes. In this study, the number of sensor consists of 8 electrodes. An essential requirement of the imaging system is that the measuring circuit should only measure the capacitance between the selected pair of electrodes and that it should be insensitive to stray capacitance between the measuring electrodes and earth. Therefore, to satisfy these requirements a stray immune capacitance measuring circuit, which uses switched-capacitor charge transfer, is used, (Xie et al. (1992)).

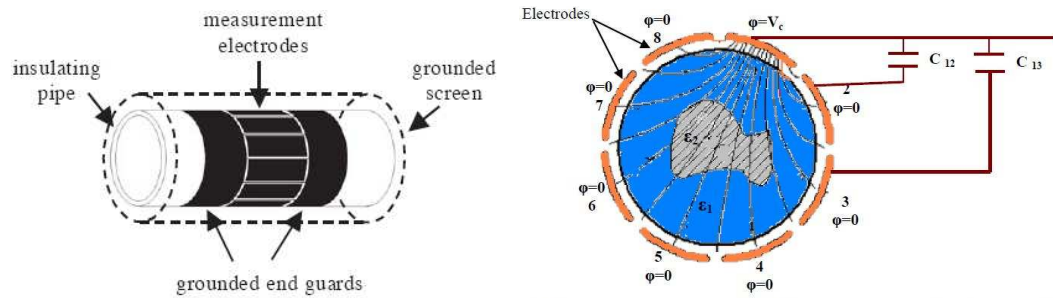


Figure 3.14: The electrical capacitance tomography (ECT) sensor. The ECT uses capacitance data measured between any two of a multiple set of electrodes mounted at the periphery of the pipe of a two-component flow to be imaged. An image reconstruction algorithm then translates the measurement data into the cross-sectional data into the cross-sectional concentration map. Adapted from Huang et al. (1989).

The electrical capacitance tomography (ECT) system used in this work is a PTL-300 system, supplied by Process Tomography Limited. It consists of a data processing unit PC, DAM-200 data acquisition unit and a capacitance sensor. The PC runs the ECT 32 program and the twin-plane ECT software designed for the PTL-300 system, and runs under the Windows XP operating system. The ECT 32 program allows one or two ECT sensor planes to be controlled either independently or simultaneously, the data are captured and can be played back at different frame rates. The measurement data can be displayed as permittivity images, normalised capacitances or a combination of both.

The DAM-200 unit hosts the twelve-channel inlets for the single and twin-plane arrangements, and must be connected to the PC at all times. If communications between the PC and the DAM-200 are interrupted, the PC will enter an indeterminate state and it will be necessary to reboot the system to resume operation.

3.5.7.2.1 Image Reconstruction Model:

For the configuration shown in Figure 3.14, the capacitance between electrodes 1 – 2, 1 – 3, 1 – 4 until 1 – 8, then 2 – 3, 2 – 4, until 2 – 8, etc can be measured sequentially with appropriate sensor electronics, providing a total number of 28 measurements.

Each of these measurements has a unique sensitivity weighting over the cross-section of the imaging volume, and hence is independent of the others. Alternatively, for an N-electrode sensor Huang et al. (1989), the number of independent measurements can be determined by the combination formula:

$$M = \frac{1}{2} N(N - 1) \quad (3.14)$$

As shown in Figure 3.14, the M measurements are obtained via appropriate electronics and sent to the image reconstruction computer. The computer controls the data-acquisition process and generates a tomographic image of the dielectric distribution from the measurements and their corresponding sensitivity distribution.

Since, there are 28 independent capacitance measurements between any of the 8 electrodes in all possible combinations, the value of the i_{th} capacitance C_i can be expressed according to Huang et al. (2003) as

$$C_i = \iint_D \varepsilon(x, y) S_i(x, y, \varepsilon(x, y)) dx dy, \quad i = 1, 2, \dots, 28 \quad (3.15)$$

Where

D is the cross-sectional diameter of the pipe (image area),

$\varepsilon(x, y)$ is the dielectric (permittivity) distribution function which corresponds to the phase component distribution of two-phase flow, because a different phase component distribution of two-phase flow results in a different dielectric (permittivity) distribution

S_i is the sensitivity distribution function of C_i .

The aim of image reconstruction is to solve the inverse problem of equation (3.15) and determine $\varepsilon(x, y)$ from a limited number of measurements (Huang et al. (2003)). It is worth mentioning that it is very difficult to solve the inverse problem with only 28 measurements, because the relationship between the capacitance and the dielectric (permittivity) distribution is complex and non-linear Huang et al. (2003). This therefore suggests that the more the number of electrodes, the better the image reconstruction would be. To obtain an approximate solution therefore, the following assumption is introduced to simplify the inverse problem.

Research works have proved that the effect of the dielectric distribution on the sensitivity is insignificant, if the difference between the dielectric constants of the constituent materials of two-phase flow (such as gas/oil flow) is relatively small Huang et al. (2003). It is assumed that the dielectric distribution $\varepsilon(x, y)$ is independent of the sensitivity function S_i . Thus, equation (3.15) can be simplified to

$$C_i = \iint_D \varepsilon(x, y) S_i(x, y) dx dy, \quad i= 1, 2, \dots, 28 \quad (3.16)$$

When high permittivity material (silicone oil) is introduced into a low permittivity background (air) within the sensing zone the capacitance measurements between electrode pairs will increase. An ECT system measures these capacitance changes and reconstructs a cross-sectional image from the capacitance data. It is common practice to convert capacitance measurements to normalized capacitance data for image reconstruction. The common approach to image reconstruction is based on a parallel capacitance model. This can be explained by considering the ideal parallel plate capacitor, with an air-silicone oil system, shown in Figure 3.15.

To represent the mathematical model for this process, assume that the capacitances when the whole sensor is completely filled with the low and the high permittivity materials are C_{oi} and C_{mi} , respectively. If the capacitance plate area is assumed to be unity and the mixture of air and silicone oil between the plates has a silicone oil fraction of Cr_i (Bolton et al. (1998)). As capacitance is proportional to capacitor plate area, the capacitance due to the silicone oil (high permittivity) filled part of the sensor is $C_{mi}Cr_i$ and the capacitance due to the air (low permittivity material) filled part of the sensor is $C_{oi}(1 - Cr_i)$ (Bolton et al. (1998)). The air and silicone oil are in a parallel arrangement as shown in Figure 3.15 and therefore the total parallel capacitance C_i is equal to the sum of these two capacitances, i.e.

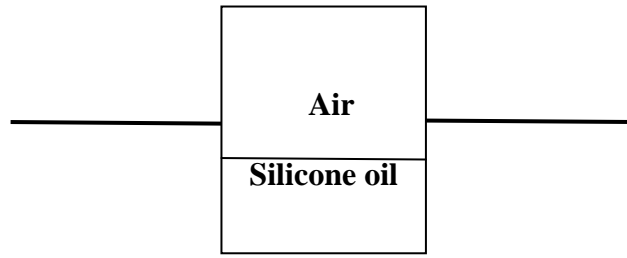


Figure 3.15: parallel capacitance model

$$C_i = C_{mi}Cr_i + C_{oi}(1 - Cr_i) = C_{mi}Cr_i + C_{oi} - C_{oi}Cr_i = Cr_i(C_{mi} - C_{oi}) + C_{oi} \quad (3.17)$$

$$C_i - C_{oi} = Cr_i(C_{mi} - C_{oi})$$

Rearranging this gives the normalised capacitance measurements Cr_i ,

$$Cr_i = \frac{C_i - C_{oi}}{C_{mi} - C_{oi}}, i = 1, 2, \dots, 28 \quad (3.18)$$

As capacitance is proportional to material permittivity (Bolton et al. (1998)), it is possible to substitute permittivity for capacitance as follows:

$$Cr_i = \frac{\varepsilon_{mi} - \varepsilon_o}{\varepsilon_m - \varepsilon_o} \quad (3.19)$$

Where

C_{oi} is the i_{th} measured capacitance when the pipe is filled with gas. In this case, $\varepsilon(x, y) = \varepsilon_o$, and according to equation

$$(3.16) C_{oi} = \iint_D \varepsilon_o(x, y)S_i(x, y)dxdy.$$

C_{mi} is the value of the i_{th} capacitance when the pipe is completely filled with oil.

$$\text{In this case, } \varepsilon(x, y) = \varepsilon_m, \text{ and } C_{mi} = \iint_D \varepsilon_m(x, y)S_i(x, y)dxdy.$$

ε_o is the dielectric constant (permittivity) of gas

ε_m is the dielectric constant (permittivity) of oil

Thus, equation (3.18) can be written as

$$Cr_i = \frac{\iint_D \varepsilon(x, y)S_i(x, y)dxdy - \iint_D \varepsilon_o S_i(x, y)dxdy}{\iint_D \varepsilon_m S_i(x, y)dxdy - \iint_D \varepsilon_o S_i(x, y)dxdy} \quad (3.20)$$

$$Cr_i = \frac{\iint_D \left(\frac{\varepsilon(x, y) - \varepsilon_o}{\varepsilon_m - \varepsilon_o} \right) S_i(x, y)dxdy}{\iint_D \left(\frac{\varepsilon_m - \varepsilon_o}{\varepsilon_m - \varepsilon_o} \right) S_i(x, y)dxdy} = \frac{\iint_D \left(\frac{\varepsilon(x, y) - \varepsilon_o}{\varepsilon_m - \varepsilon_o} \right) S_i(x, y)dxdy}{\iint_D S_i(x, y)dxdy} \quad (3.21)$$

Since an 8-electrode capacitance tomography system has 28 independent pairs of electrodes it follows that there are 28 independent values of Cr_i for one set of measurements. Each independent pairing of electrodes has a unique sensing zone comprising some of the pixels that make up the image. The presence of high permittivity material in one of these pixels in a background of low permittivity material will have a unique impact on the capacitance measurement between the pair of electrodes. This information for all pixels and all electrode pairs is known as the sensor sensitivity map and is approximated by a finite model (Bolton et al. (1998)). It is combined with the normalized capacitance data to reconstruct an image of the phase distribution within the sensing zone. The most common algorithm used to reconstruct images from capacitance data is based on a simple back-projection method Huang et al. (1989), which is as follows

$$p_i = \iint_D f(x, y)S_i(x, y)dxdy, i = 1, 2, \dots, 28 \quad (3.22)$$

$$f(x, y) = \frac{\varepsilon(x, y) - \varepsilon_o}{\varepsilon_m - \varepsilon_o} \quad (3.23)$$

Because p_i reflects the information from the void fraction of two-phase flow and its distribution, it can be regarded as the projection data of the ECT system. $f(x, y)$ is the grey-level function of the image and corresponds to the component distribution.

The measurement capacitance C_i can be expressed as the linear combination of the contribution of each digital image pixel by the linear approximation Huang et al. (2003).

$$C_{oi} = \iint_D \varepsilon(x, y) S_i(x, y) dx dy \approx \sum_{j=1}^M \varepsilon_j S_{ij} A_j = \sum_{j=1}^M \varepsilon_j w_{ij} \quad (3.24)$$

Where,

ε_j is the equivalent dielectric constant (permittivity) of the mixture of two-phase flow of the j^{th} pixel

A_j is the area of the j^{th} pixel,

M is the number of pixels

S_{ij} is the sensitivity of the j^{th} pixel to C_i

w_{ij} is the weight coefficient and $w_{ij} = S_{ij} A_j$. w_{ij} can be regarded as a kind of sensitivity which includes the effect of the area of the j^{th} pixel to C_i

On the basis of equation (3.24), p_i can be written as

$$p_i = \left(\sum_{j=1}^M w_{ij} \right) C_{r_i} = \sum_{j=1}^M f_j w_{ij} \quad (3.25)$$

Where,

$$Cr_i = \frac{\iint_D f(x, y)S_i(x, y)dxdy}{\iint_D S_i(x, y)dxdy} = \frac{\sum_{j=1}^M f_j w_{ij}}{\sum_{j=1}^M w_{ij}} \quad (3.26)$$

where f_j is the grey level of the j th pixel. The value of f_j represents the oil concentration in the area.

Thus, the mathematical model of image reconstruction can be written in matrix form

$$P = WF \quad (3.27)$$

Where

P is the vector of measurement projection data, $P = [p_1, p_2, \dots, p_N]^T$

W is the weight matrix whose entries are $w_{i,j}, i = 1, 2, \dots, N, j = 1, 2, \dots, M$. The values of w_{ij} are obtained by the finite-element method (FEM). The FEM is not discussed in this study but, can be found in Huang et al. (1989).

N is the number of measurements (projection data), for the 8-electrode ECT system, with $N = 28$.

M is the number of pixels

F is the vector of grey level, $F = [f_1, f_2, \dots, f_N]^T$.

3.5.7.2.2 Calibration procedure:

The usual calibration for an ECT system involves filling the sensor with the low permittivity material and taking a complete set of measurements followed by

filling the sensor with the high permittivity material and taking a complete set of measurements. This sets the lower and upper limits for all subsequent measurements.

It can be seen from equation (3.19) that when the sensor is full of low permittivity material the high permittivity material volume fraction will be zero and when it is full of high permittivity the volume fraction will be one. When the sensor contains both low permittivity and high permittivity material the volume fraction C_{r_i} is calculated by assuming it is a linear function between the lower and upper limits set during calibration. This method has been successfully applied to a number of process engineering applications including a stratified gas/oil flow model Huang et al. (1992), fluidized bed rig Wang et al. (1995) and Azzi et al. (2010), gas/liquid flow in pipes Azzopardi et al. (2010). The silicone oil used in this study has a relative permittivity value of 2.7.

3.6 Methodology during an experimental run:

As part of this study the design of an experimental data acquisition system to monitor the gas-liquid flows behaviour in vertical and horizontal pipes attached to 90° bends were constructed. Also the exploration of the factors affecting the evolution of slug flow was undertaken. The experimental conditions to be studied were predetermined for a corresponding set of gas and liquid flow rates. Firstly, an inlet flow condition was set, and then the condition was maintained until the end of that run. Once the full series of experiments was completed, an analysis of the corresponding data was conducted to determine that consistent and reliable flow phenomena were obtained and if not, the experiments were repeated to identify the cause of the errors. The analysis involved making plots of times

series of void fraction, PDF of void fraction and average void fraction against gas superficial velocity. The same procedure is repeated until all the entire matrix of inlet flow conditions had been tested.

During the experiments the pressure drop, void fraction and or/liquid holdup and corresponding time intervals were recorded. This process was repeated until all of the planned experiments were completed for both of the cases of the vertical and horizontal 90° bends.

3.7 Hazard analysis of experimental facility:

A hazard assessment of the experimental facility was conducted prior to the execution of the experimental programme. Where hazards were identified, necessary modifications were implemented to prevent the occurrence of any unexpected events. Some of the modifications instigated are described below.

An emergency shutdown button was located on the rig to isolate the power delivered to the oil pump, the heater and the gas flow delivered to the rig. In the course of carrying out experimental campaign at high gas flow rates, mists were observed escaping out of the cyclone (separator). To eliminate this problem, a special filter shown in Figure 3.4e was installed on top of the separator. Subsequent observation of the flow showed that this filter was successful in eliminating the mist being discharged from the cyclone.

3.8 Uncertainty analysis of the experimental measurements:

The purpose of the experimental measurements was to obtain the performance of the rig and the instrumentation in a digital/numerical format. This specification is in itself uncertain because the experimenter is in doubt about the accuracy of

these measurements. There is and will always be an error inherent in all measurements. Error is defined as the difference between the measured value and true value. The true value of a quantity is rarely known and therefore, the error is not known. According to Holman (2002) “uncertainty estimates the limits of error with some confidence”. Uncertainty analysis therefore, is a method of estimating the limits of error and describing the quality of experimental data.

There are two types of error, random error (precision error) and systematic error (bias error). Random errors are caused by random fluctuations inherent in a measurement system. Random uncertainty estimates the limits of random errors. Systematic error is the difference between averaged measured value and the true value. Systematic errors are caused by calibration errors, scale reading errors, and data acquisition errors. Systematic uncertainty estimates the limits of systematic errors.

Some parameters like gas and liquid superficial velocities were not measured directly from the experiment, it was therefore deemed necessary to perform the propagation of uncertainty to calculate the uncertainty of these parameters. Further explanations for random, systematic and propagation of uncertainty are presented below.

3.8.1 Random uncertainty:

N number of points in the population are obtained when a parameter is measured N times. The sample standard deviation of this population of measurements is evaluated as follows:

$$\sigma_x = \sqrt{\frac{\sum_{i=1}^N (X_i - \bar{X})^2}{N-1}} \quad (3.28)$$

Where σ_x and \bar{X} are the standard deviation or scatter and average of the N data points, respectively. However, it is more convenient to find the scatter of the mean values. Therefore, the standard deviation of the population average is calculated from the following equation:

$$\sigma_{\bar{x}} = \frac{\sigma_x}{\sqrt{N}} \quad (3.29)$$

$\sigma_{\bar{x}}$ is the relative standard deviation about the mean.

3.8.2 Systematic uncertainty:

Experimental data cannot be used for systematic uncertainty; systematic errors tend to remain consistent from measurement to measurement. Systematic errors are usually due to imperfections in measuring equipment, improper or biased observations, or by the presence of additional physical effects. Estimation of systematic uncertainty for liquid holdup and/or void fraction measurements could not be made, as there was no information about systematic uncertainty.

3.8.3 Uncertainty propagation:

When a parameter is not directly measured, but calculated from two or more directly measured parameters, the uncertainty in the derived parameter must be determined from the uncertainties in the measured parameters from which it is calculated. This is the concept of propagation of uncertainty. Uncertainty of a measured value is an interval around that value such that any repetition of the measurement will produce a new result that lies within this interval. Due to the fact that only one experiment was performed for each run, a reasonable estimate

of the measurement uncertainty due to random errors is based on the least count approach. Figures 3.16 and 3.17 presents estimate error in each of the measurements carried out in the experiments presented in this work. Appendix B provides the details of the calculation, including propagation error in calculable variables. Uncertainty propagation analysis was performed for liquid, gas and mixture superficial velocities in this study. Experiments were repeated when the data obtained is doubtful. Figure 3.16 present the plot of percentage error (uncertainty) against liquid and gas superficial velocities while Figure 3.17, the plot of % error (uncertainty) against mixture superficial velocity.

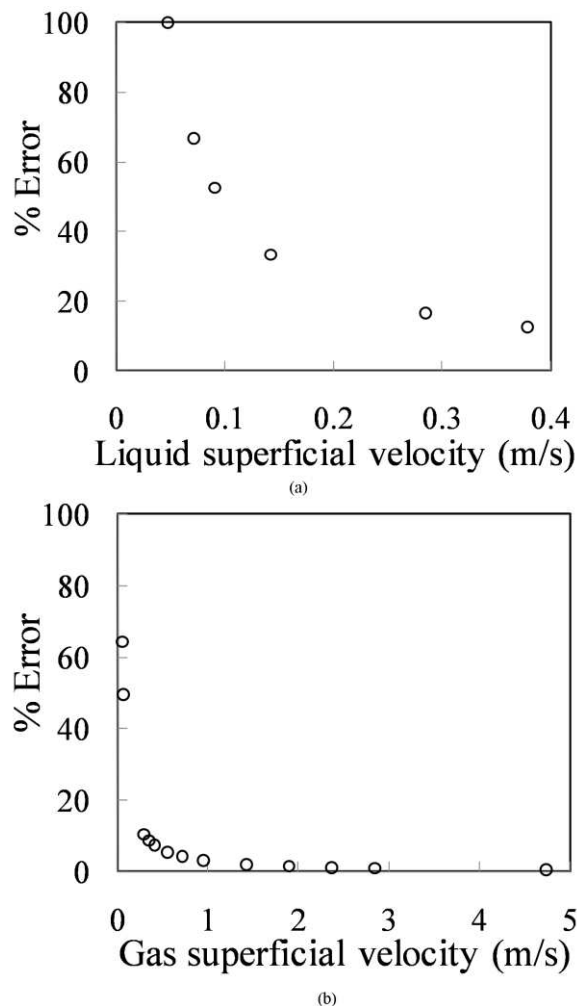


Figure 3.16: % error (uncertainty) against (a) gas superficial velocity and (b) liquid superficial velocity

Figure 3.16a shows that the % error decreases exponentially from 100–13 with an increase in liquid superficial velocity. On the other hand, the % error decreases exponentially from about 64 to 0.64 with an increase in gas superficial velocity as depicted on Figure 3.16 b.

The relationship between % error and mixture superficial velocity is shown in Figure 3.17. The same trend observed for the plot of % error against gas superficial velocity is also seen here. It shows that the maximum and minimum % errors are recorded at liquid superficial velocity of 0.05 and 0.38 ms^{-1} , respectively. It can be concluded that the % error decreases exponentially with an increase in liquid and gas superficial velocities. This therefore necessitated greater caution whilst recording data at these low flow rates giving rise to high errors.

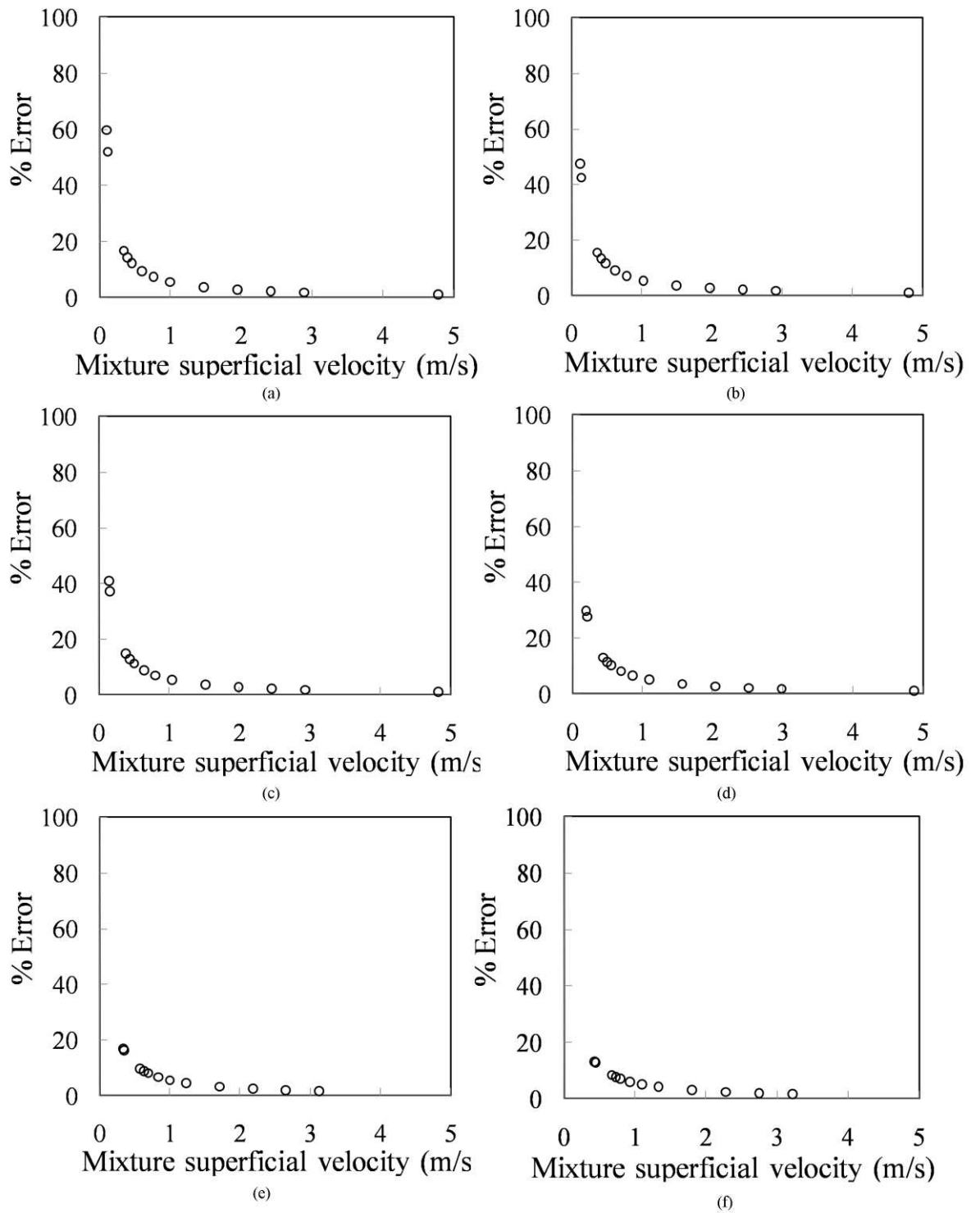


Figure 3.17: % error (uncertainty) against mixture superficial velocity for different liquid superficial velocity (ms⁻¹): (a) 0.05 (b) 0.07 (c) 0.09 (d) 0.14 (e) 0.28 and (f) 0.38

3.9 Summary

This chapter has presented both the experimental facility and instrumentation used for measurements. The later includes the measurement of liquid holdup and/or void fraction and pressure drop. The experimental design has taken into account modifications to the existing inclinable rig, the possibility of hazards when the rig is operated and also uncertainty analysis of experimental measurements. It also took into account all considerations mentioned by the previous researchers such as suggestions, advantages and limitations of equipment and flow conditions. Thus, the next two chapters provides new data for slug flow in a vertical riser and the effect that the installation of 90° bend on the outlet to the test pipe section may have on the air-silicone oil flows observed.

Gas-Liquid Flow in a Vertical 67 mm Pipe

During the course of carrying out the experimental campaign, it was observed that the most dominant flow pattern in both the vertical and horizontal pipes is slug flow. Also, due to the inherent unsteadiness typified by the slug flow pattern as it approached the 90° bends, it was decided to explore a more detailed and fundamental understanding of the behaviour of slug flow. In addition, serious vibrations were observed on the rig as the liquid slugs approached the bend. This is due to the momentum of the gas and liquid dominated packages being significantly different. To give foundation to these studies it was decided to conduct a review of the literature concerned with slug flow phenomena. However, the results of this exercise concluded that there were no peer reviewed published studies that had addressed slug flow in a vertical riser using air and low surface tension liquid (silicone oil) as the working fluid. The available work on slug flow in a vertical riser was concerned with other working fluids, water and glucose among others employing either conductance or capacitance probes. Consequently there is a need to conduct further experimental studies involving air-choice of viscosity flows in a vertical riser using more advanced instrumentation.

This chapter therefore reports the collection, analysis and discussion of new experimental data obtained from the output of the ECT measurement transducer as detailed in Chapter 3. The data was used to determine: the velocities of the Taylor bubbles and liquid slugs, the slug frequency, the lengths of the liquid slugs and Taylor bubbles, the void fractions in the liquid slugs and Taylor bubbles as well as the liquid film thickness. This was achieved via a time series analysis of the liquid holdup obtained from the two planes of the ECT. A differential pressure cell was used to measure the pressure drops along this length of the riser. This enabled the determination of the variation of pressure drop with flow rates to be studied. Also the experimental results against those obtained from model predictions and the results of these correlation studies are reported.

4.1 Slug flow in the vertical riser:

The resultant flow patterns created for the range of air-silicone oil injection flow rates were recorded using electrical capacitance tomography (ECT). In this study, a ring of electrodes were placed around the circumference of the riser at a given height above the injection portals at the bottom of the 6 m riser section. This enabled the measurement of the instantaneous distribution of the phases over the cross-section of the pipe. The use of two such circumferential rings of sensor electrodes, located at a small distance apart (also known as twin-plane sensors), enabled the determination of the rise velocity of any observed Taylor bubbles and liquid slugs. The twin-plane ECT sensors were placed at a distance of 4.4 and 4.489 m upstream of the air-silicone oil mixer injection portal located at the base of the riser.

The average of two ECT output data was used in this study. The two ECT output data were obtained at two locations: (1) WMS placed downstream of the ECT and (2) WMS moved after the bend. A comparison between the two ECT output data was then made for two reasons: to check measurement repeatability and to find out if the WMS placed first downstream of it and afterwards moved after the bend had significant effect on the data obtained. The average standard deviation of the data is $\pm 2\%$.

The experimental data reported here refer to conditions in which the rise velocity of the bubble is determined solely by liquid inertia. According to Wallis (1969), this regime corresponds to $E_o > 100$ and $N_f > 300$. The physical properties of the air-silicone oil system and the values of the dimensionless numbers, E_o , N_f and Mo are presented in Table 4.1.

A flow chart of the various experimental measurements recorded and the parameter calculations performed to characterise the observed slug flows are presented in Table 4.2.

Table 4.1: Properties of the fluids and dimensionless numbers

Fluid	Density (kgm^{-3})	Viscosity ($\text{kgm}^{-1}\text{s}^{-1}$)	Surface tension (Nm^{-1})
Air	1.18	0.000018	
Silicone oil	900	0.0053	0.02
Dimensionless numbers			
Eotvos number	$E_o = 1981.67$		
Dimensionless inverse viscosity	$N_f = 9311.72$		

Morton's number	$Mo = 1.035 \times 10^{-6}$		
------------------------	-----------------------------	--	--

Table 4.2: Table of Flowchart for experimental measurement used to obtain the parametric characterisation of the slug flow regime

Direct measurement	physical	Data processing method	Parametric Output 1	Parametric Output 2
Instrument	Data			
ECT	Time series of void fraction	PDF of void fraction PSD – Power Spectral Density Cross-correlation Image reconstruction	Flow pattern, $\epsilon_{gs}, \epsilon_{TB}$, frequency Frequency Structure velocity Contours of phase distribution	Lengths of liquid slug and Taylor bubble 3D structures
Differential Pressure Cell	Time series of pressure drop	Total pressure drop between the two tappings of the differential pressure cell	Frictional pressure drop	

4.2 Determination of the characterisation parameters:

4.2.1 Rise velocity of a Taylor bubble (Structure velocity):

A cross-correlation was performed between the time varying void fraction data measured by the twin ECT-planes located at 4.4 and 4.489 m above the mixer section at the base of the riser. This allows the determination of the time for individual slugs to travel between the two ECT-planes, and hence the calculation of the structure velocity, U_N . The cross-correlation operation gives the degree of

linear dependence between two time series data sets, a and b. It was calculated as the average product of $a - \mu_a$ and $b - \mu_b$. This average product defined in equation (4.1) gives the covariance of a and b in the limit as the sample size approaches infinity.

$$\sigma_{ab} = E[(a - \mu_a)(b - \mu_b)] = \lim_{N \rightarrow \infty} \frac{1}{N} \sum_{i=1}^N (a_i - \mu_a)(b_i - \mu_b) \quad (4.1)$$

For any time delay τ , the covariance function between a (t) and b (t) is:

$$C_{ab} = E[\{a(t) - \mu_a\}\{b(t + \tau) - \mu_b\}] = \lim_{T \rightarrow \infty} \frac{1}{T} \int_0^T [\{a(t) - \mu_a\}\{b(t + \tau) - \mu_b\}] dt = R_{ab}(\tau) - \mu_a \mu_b \quad (4.2)$$

Where the cross-correlation function between a(t) and b(t), $R_{ab}(\tau)$ is defined as

$$R_{ab}(\tau) = \lim_{T \rightarrow \infty} \frac{1}{T} \int_0^T a(t)b(t + \tau) d\tau \quad (4.3)$$

The correlation coefficient function is defined as:

$$\rho_{ab}(\tau) = \frac{C_{ab}(\tau)}{\sqrt{C_{aa}(0)C_{bb}(0)}} = \frac{R_{ab}(\tau) - \mu_a \mu_b}{\sqrt{(R_{aa}(0) - \mu_a^2)(R_{bb}(0) - \mu_b^2)}} \quad (4.4)$$

Details may be found in Bendat and Piersol (1980). These equations were then programmed as a computational MACRO program to determine the structure velocity of the Taylor bubble and liquid slug body, U_N .

4.2.2 Liquid film thickness:

The expression proposed by Fernandes et al. (1983) to describe the thickness of the falling liquid film in the Taylor bubble region,

$$\delta = \frac{D}{2} (1 - \sqrt{\varepsilon_{TB}}) \quad (4.5)$$

was used to determine the liquid film thickness, where δ is the liquid film thickness in mm, D is internal pipe diameter in mm and ε_{TB} is the experimental measured void fraction in Taylor bubble.

4.2.3 Slug frequency:

The slug frequency is defined as the number of slugs passing through a defined pipe cross-section in a given time period. To determine the frequency of periodic structures (slugs), the methodology of Power Spectral Density (PSD) as defined by Bendat and Piersol (1980) was applied. The Power Spectral Density, PSD, is a measure of how the power in a signal varies over a range of frequency and therefore, it describes how the power (or variance) of a time series is distributed with frequency. Mathematically, it is defined as shown in equation (4.6) as the Fourier Transform of the autocorrelation sequence of the time series. The method presents the power spectrum density functions in terms of direct Fourier Transformations of the original data.

$$S_{ab}(f) = \int_{-\infty}^{+\infty} R_{ab}(\tau) e^{-j2\pi f\tau} d\tau \quad (4.6)$$

Equation (4.6) is the cross-spectral density function between $a(t)$ and $b(t)$. For the special case where $a(t) = b(t)$,

$$S_{ab}(f) = \int_{-\infty}^{+\infty} R_{bb}(\tau) e^{-j2\pi f\tau} d\tau \quad (4.7)$$

Equation (4.7) represents the power spectral density (PSD) function.

4.2.4 Lengths of the slug unit, the Taylor bubble and the liquid slug:

Khatib and Richardson (1984) determined the lengths of the liquid slug and Taylor bubble as follows:

$$L_{SU} = L_{TB} + L_S \quad (4.8)$$

They took a volume balance over the slug unit

$$L_{SU} \varepsilon_g = L_{TB} \varepsilon_{TB} + L_S \varepsilon_{gs} \quad (4.9)$$

$$L_{SU} \varepsilon_g = (L_{SU} - L_S) \varepsilon_{TB} + L_S \varepsilon_{gs}$$

$$L_{SU} \varepsilon_g = L_{SU} \varepsilon_{TB} - L_S \varepsilon_{TB} + L_S \varepsilon_{gs}$$

$$L_{SU} \varepsilon_g - L_{SU} \varepsilon_{TB} = L_S \varepsilon_{gs} - L_S \varepsilon_{TB}$$

$$L_{SU} (\varepsilon_g - \varepsilon_{TB}) = L_S (\varepsilon_{gs} - \varepsilon_{TB}) \quad (4.10)$$

$$\frac{L_S}{L_{SU}} = \frac{\varepsilon_g - \varepsilon_{TB}}{\varepsilon_{gs} - \varepsilon_{TB}} \quad (4.11)$$

Equation (4.11) above is the equation for determining the overall length of the liquid slug based on the knowledge of the overall velocity of the slugs. However, the interest is in determining the lengths and velocities of individual slugs. This therefore necessitated a new method of achieving this. The following section will look at determining the lengths of individual slugs.

A slug unit is a Taylor bubble and the following liquid slug. The length of a slug unit is determined from the knowledge of the rise velocity of the Taylor bubble and the slug frequency. The length of the slug unit was obtained as shown in

equation (4.13). The lengths of the different zones of the individual slug unit have been determined for a range of different liquid and gas flow rates. The time of passage of the individual slug unit, Taylor bubble and liquid slug have been determined from an analysis of the output time series from the twin-planes of the ECT signals. The time of passage for the slug unit, the Taylor bubble and the liquid slug, were then assumed to be proportional to the lengths of the slug unit, Taylor bubble and liquid slug, respectively. Relationships were then obtained to estimate the lengths of the individual Taylor bubble and the liquid slug as described below. Equations (4.13), (4.20) and (4.21) are employed to determine the lengths of the slug unit, liquid slug and Taylor bubble, using parameters evaluated from the recorded measurements.

$$U_N = \frac{L_{SU}}{\theta} \quad (4.12)$$

where, θ is a time for a slug unit to pass the probe. If the slug/Taylor bubble are uniform $\theta = \frac{1}{f}$. Where, f is the slug frequency.

Therefore,

$$L_{SU} = \frac{U_N}{f} \quad (4.13)$$

For an individual slug unit, assuming steady state so that the front and back of the slug have the same velocity

$$L_{SUi} = kt_{SUi} \quad (4.14)$$

$$L_{TBi} = U_{Ni} t_{TBi} \quad (4.15)$$

$$L_{Si} = U_{Ni} t_{Si} \quad (4.16)$$

Dividing equation (4.15) by (4.16) yields the expression

$$\frac{L_{TBi}}{L_{Si}} = \frac{kt_{TBi}}{kt_{Si}} = c \quad (4.17)$$

$$L_{TBi} = cL_{Si} \quad (4.18)$$

However,

$$L_{SUi} = L_{TBi} + L_{Si} \quad (4.19)$$

Substituting equation (4.18) into (4.19) and rearranging yields the expressions

$$L_{Si} = \frac{L_{SUi}}{c + 1} \quad (4.20)$$

$$L_{TBi} = L_{SUi} - L_{Si} \quad (4.21)$$

4.3 Results and discussion: Slug flow in a vertical riser

Khatib and Richardson (1984) and Costigan and Whalley (1997) proposed that twin peaked probability density function (PDFs) of recorded void fractions represented slug flow as shown in Figure 4.1. The low void fraction peak corresponds to liquid slug while the high void fraction peak is for the corresponding Taylor bubble. Following the PDF approach, it has been determined that the experimental flow rates that create a slug flow regime within the riser are: a liquid superficial velocity of 0.05 to 0.38 ms⁻¹ and a gas superficial velocity of between 0.42 ≤ U_{SG} ≤ 1.35ms⁻¹.

The structure velocity, liquid film thickness, slug frequency, lengths of liquid slug, Taylor bubble and slug unit, determined using the methods above, were

arranged over the total number of slugs for the given experimental conditions. Plots of the structure velocity to mixture superficial velocity, and the void fractions in liquid slug and the Taylor bubble to gas superficial velocity, and the total pressure and frictional pressure drops to the gas superficial velocity are shown in Figures 4.4 to 4.10, respectively. Plots of the slug frequency to gas superficial velocity and dimensionless Strouhal number to the liquid quality, and the Lockhart-Martinelli parameter and the dimensionless lengths of liquid slug, Taylor bubble and slug unit to the gas superficial velocity are shown in Figures 4.10 to 4.14, respectively.

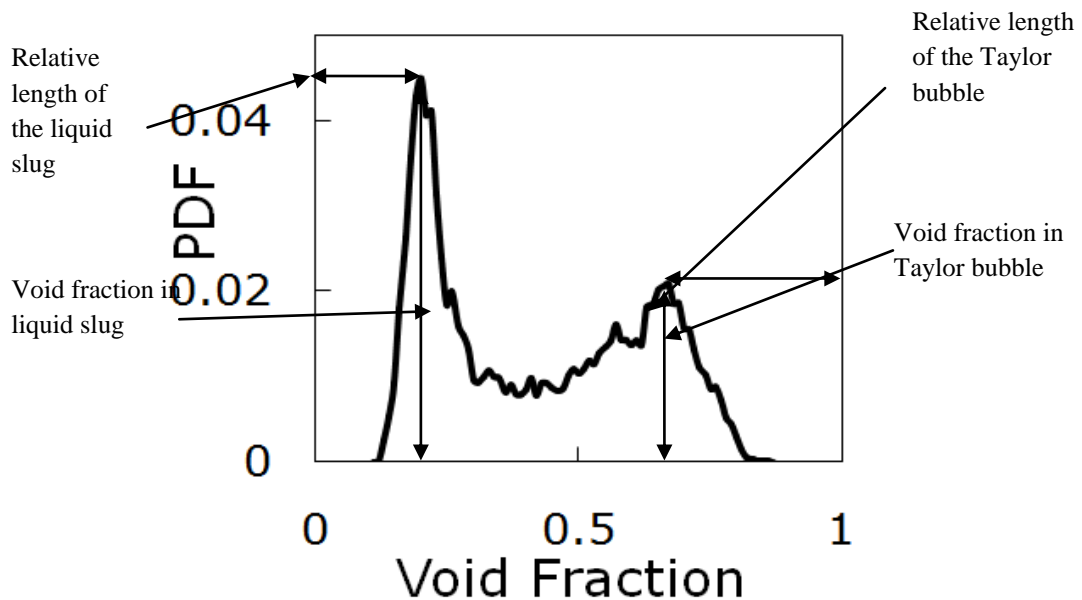


Figure 4.1: PDF of cross-sectional average void fraction for the case of slug flow measured from the experiments using air-silicone oil. The location of the peak in the low void fraction region represents the average void fraction in liquid slug, while its height represents the relative length of the liquid slug section.

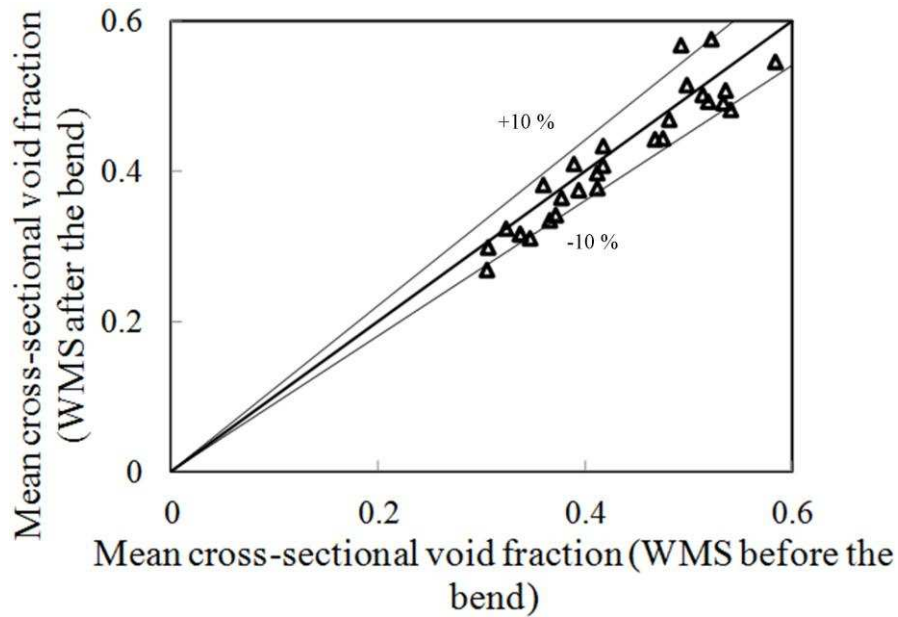


Figure 4.2: Comparison between the cross-sectional void fractions obtained from the ECT when the WMS sensor was placed before and after the vertical 90° bend.

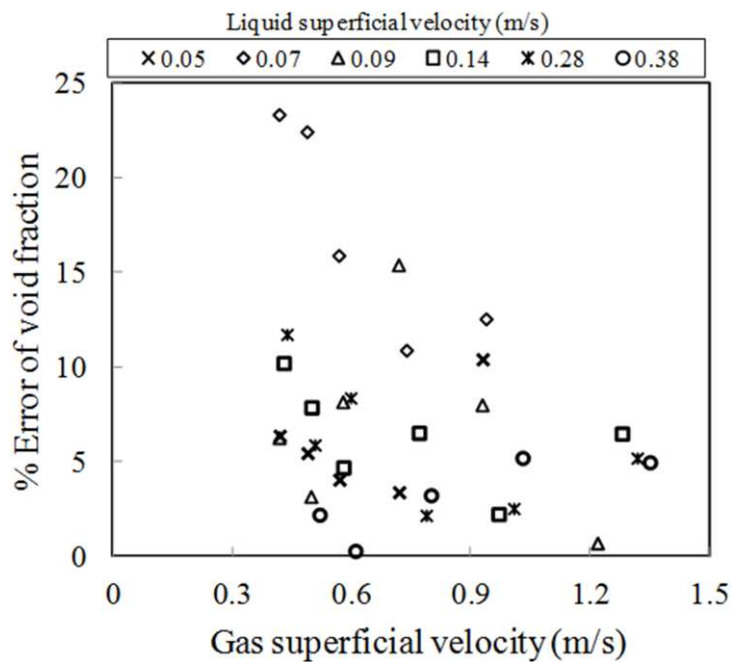


Figure 4.3: Variation of % error of void fraction with gas superficial velocity
 Figure 4.2 shows the plot of average cross-sectional void fraction obtained from the output of the ECT with the: (1) WMS placed downstream of the ECT and (2) WMS placed after the vertical 90° bend. It can be observed from the plot that error is within $\pm 10\%$. The question that will be answered shortly is: what can be done to reduce the error?

In order to reduce the error, it is first important to identify the source of the error and then decide what action to take. In order to find out if the errors observed from the plot are actually systemic or due to human error, an error analysis was performed. This was achieved by making a plot of % error against gas superficial velocity with liquid superficial velocity as a parameter. This plot is presented in Figure 4.3.

At a liquid superficial velocity of 0.05 ms^{-1} , the % error of void fraction decreases almost linearly with gas superficial velocity as shown in Figure 4.3. The decrease in % error is from 12 to 2.5. With an increase of the liquid superficial velocity to 0.07 ms^{-1} , the % error also decreases almost linearly with an increase in gas superficial velocity. The decrease is from about 23 to 10 %. The effect can be attributed to the presence of the WMS measurement transducer: the WMS interacts with the liquid rather than the gas and as a consequence provokes a great influence on the liquid holdup. At these low liquid superficial velocities, the liquid does not have enough momentum to pass through the WMS. An interesting observation made in this study is that at gas superficial velocity of 0.72 ms^{-1} , both the % error observed from liquid superficial velocities of 0.05 and 0.07 ms^{-1} increased with gas superficial velocity. It can be concluded that there is a liquid superficial velocity (0.07 ms^{-1}) at which the error becomes a maximum. After this point there is a drop off in the error.

For higher liquid superficial velocities of between, 0.09 - 0.38 ms^{-1} , there is no noticeable trend between the % error and gas superficial velocity. This therefore suggests that the WMS has no effect on the flow behaviour at higher liquid flow rates and that the error is negligible and therefore not important.

To study the characteristics of slug flow in a vertical pipe, the data of the ECT without either the WMS or bend placed downstream of it should be considered only. Otherwise, it cannot be established whether any difference in the result is due to the bend or the WMS. To address the issue of reducing the error observed, the average of the two data from both cases will be used in characterising the slug flow in the vertical pipe.

4.3.1 Structure velocity of the Taylor bubble:

The translational velocity (structure velocity) of the Taylor bubble is considered to be made up of two main components, namely, the maximum mixture superficial velocity in the slug body and the drift velocity. Figure 4.4 shows a plot of the structure velocity as a function of the mixture superficial velocity. As expected, a linear relationship is obtained between them. The drift velocity for the experimental data can be taken as the y-intersection of a line that fits the data, while the distribution coefficient is given by the slope of the line. The empirical equations proposed by Nicklin et al. (1962) and Mao and Dukler (1985) are also plotted in Figure 4.4.

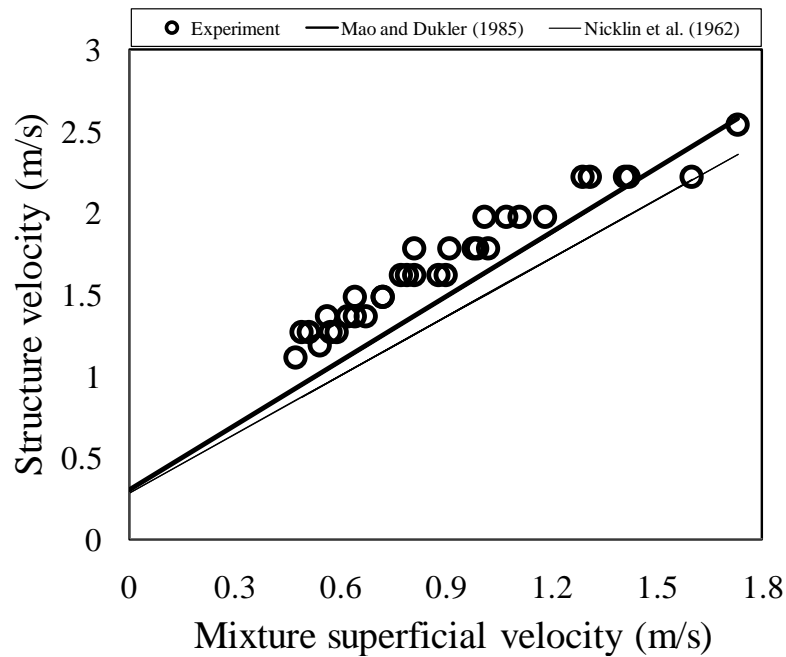


Figure 4.4: Experimentally measured structure velocity vs. mixture superficial velocity. The empirical equations proposed by Nicklin et al. (1962) and Mao and Dukler (1985) were recalculated using the physical properties of air and silicone oil.

It can be observed that the Nicklin et al. (1962) relation, with distribution coefficients of 1.2, under predicts the Taylor bubble velocity over the range of flow conditions of the present work. From the present data, the value obtained for the distribution coefficient is 1.16. However, the experimental drift velocity is higher than the values predicted by the correlations. This could be due to the assumptions made by Nicklin et al. (1962) regarding the condition of single Taylor bubble moving in static liquid which is in contrast with the situation in the present experiment, where continuous moving liquid has been used. In addition, the drift velocity obtained by them did not consider the effect of surface tension and viscosity. The predictions of Mao and Dukler (1985) also differ from the present experimental results, but over predict the distribution coefficient as compared to that of Nicklin et al. (1962). This can be because Mao and Dukler

(1985) have considered that the liquid slug in front of the Taylor bubble is aerated, and coalescence takes place between the small bubbles and the Taylor bubbles, as the Taylor bubbles move through them at a higher velocity. Therefore, this results in an increase in the rise velocity of the Taylor bubble. Mao and Dukler (1985) also did not consider the role of surface tension and viscosity in obtaining their drift velocity.

4.3.2 Void fraction in liquid slug, Taylor bubble and liquid film thickness:

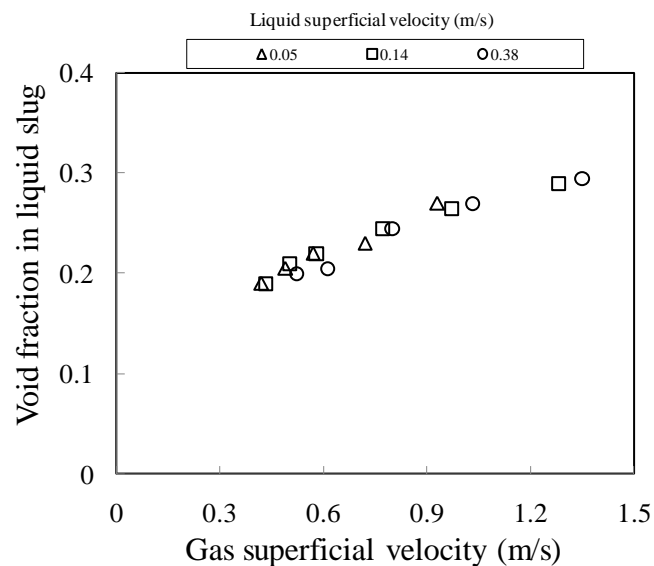


Figure 4.5: The determined mean void fractions in the liquid slug at different liquid and gas superficial velocities.

The plot in Figure 4.5 shows that the void fraction in the liquid slug increases linearly with an increase in the gas superficial velocity for a constant liquid superficial velocity. This may be explained by the fact that an increase in the gas flow rate may increase bubble production, thereby bringing about an increase in the void fraction. This is similar to the conclusion reported by other authors such as Mao and Dukler (1991) and Nicklin et al. (1962). However, it is also observed that the liquid flow rate has a less noticeable effect on the void fraction in the liquid slug.

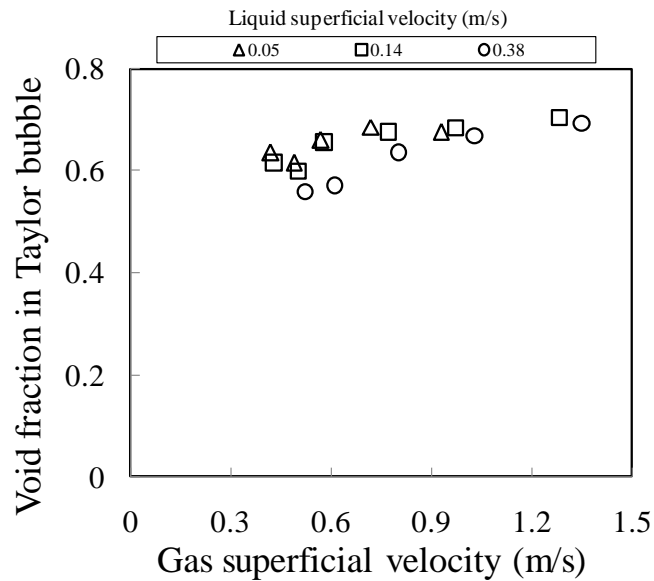


Figure 4.6: The determined mean void fractions in the Taylor bubbles at different liquid and gas superficial velocities

Figure 4.6 presents a plot of the void fraction in the Taylor bubble against the gas superficial velocity. It is observed that the void fraction in the Taylor bubble increases as the gas velocity increases. At liquid superficial velocities of between 0.14 - 0.38 ms^{-1} , an exponential relationship is established between the void fraction in the Taylor bubble and the gas superficial velocity. Contrary to this, at a liquid superficial velocity of 0.05 ms^{-1} , the void fraction in the Taylor bubble decreases a little and then increase from 0.62 to 0.68 ms^{-1} , until the terminal gas superficial velocity is reached and then it drops to about 0.67 ms^{-1} . As the gas flow rate is increased, there is an increase in the bubble population observed in the liquid slug, which may then coalesce with the Taylor bubble. It is proposed that this phenomenon may be responsible for the increase in the void fraction of the Taylor bubble. The drop in the void fraction in the Taylor bubble may be explained by a collapse of the Taylor bubble and may then be regarded as a transition towards a spherical cap bubble.

Since, the measured void fractions in the liquid slugs and Taylor bubbles have been found to increase with an increase in gas superficial velocity for a constant liquid superficial velocity, the liquid film thickness, shown in Figure 4.7, gets consequently thinner.

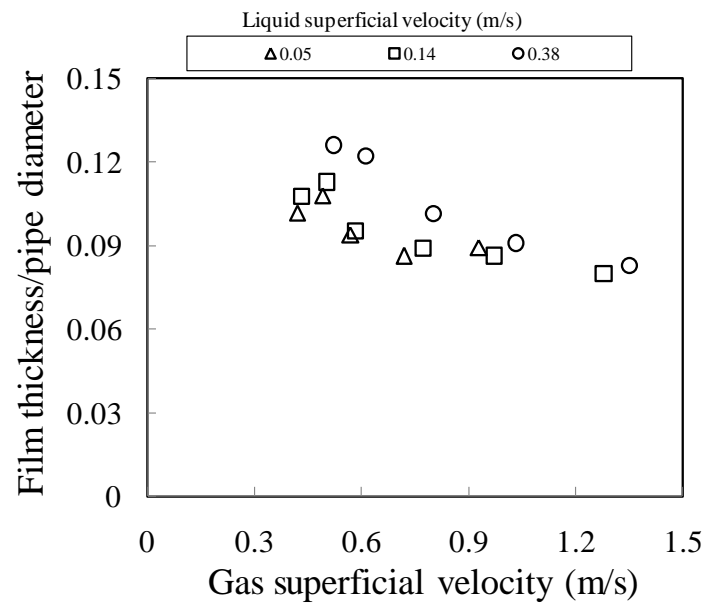


Figure 4.7: The determined dimensionless film thickness at different liquid and gas superficial velocities.

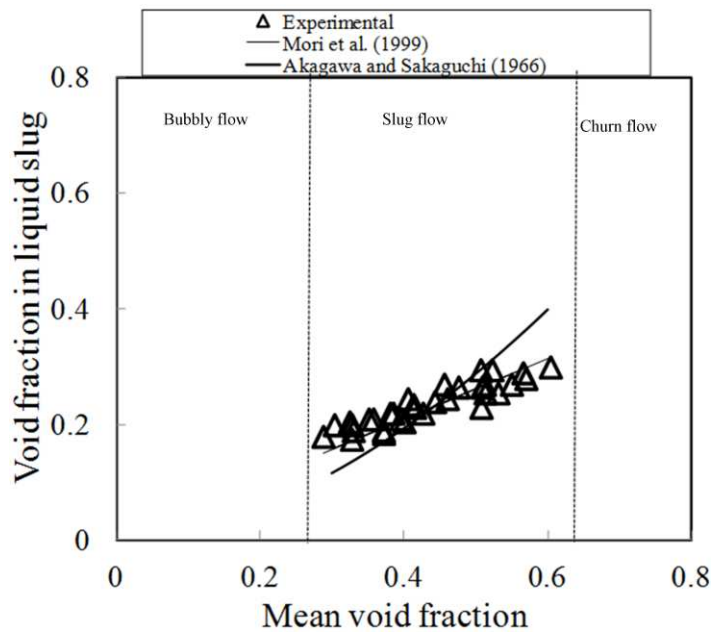


Figure 4.8: A plot of the relationship between the void fraction in the liquid slug and the mean void fraction

Figure 4.8 shows a plot of the void fraction in the liquid slug against the mean void fraction. The values of the mean void fractions were obtained by averaging the time-series of the cross-sectional void fraction recorded by the ECT. A comparison of this data with the data measured by Akagawa and Sakaguchi (1966) and Mori et al. (1999) concludes that the current experimental data shows good agreement with the model proposed by Mori et al. (1999). However, the data does not fit well the empirical model proposed by Akagawa and Sakaguchi (1966) for medium mean void fractions, whilst the experimental data are greater than those predicted by the empirical models for the lower mean void fractions, and lower than the higher mean void fractions.

It is interesting to observe from the plot that for $0 \leq \bar{\varepsilon} \leq 0.25$, the flow pattern is bubbly flow whilst for $0.25 \leq \bar{\varepsilon} \leq 0.65$ and $0.65 \leq \bar{\varepsilon} \leq 0.80$, the flow patterns are slug and churn flows, respectively.

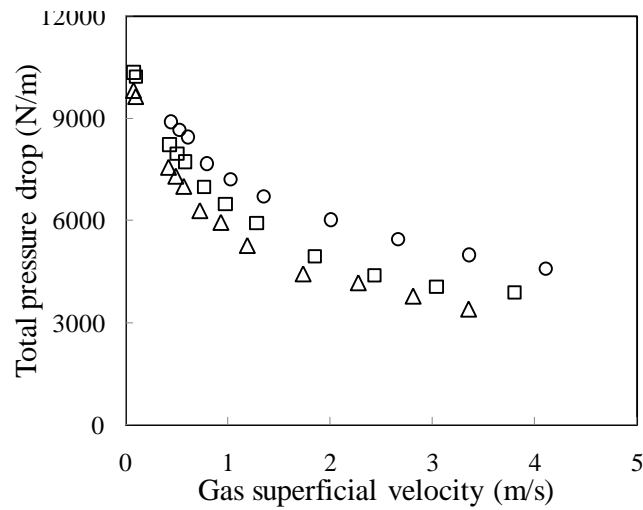
4.3.3 Total pressure and frictional pressure drop:

The total pressure drop was measured with a differential pressure cell whose taps were placed around the twin-plane ECT, whilst the frictional pressure drop was obtained by subtracting the gravity term from the measured total pressure drop. The separation distance between the DP cell tappings was 0.86 m. Figures 4.9a shows a decrease in the total pressure drop due to an increase in gas superficial velocity. On the contrary, in Figure 4.9b the frictional pressure drop is observed to increase.

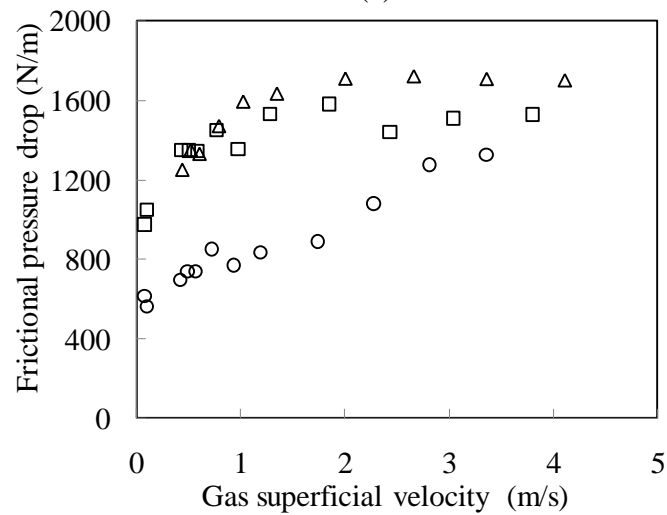
The observed decrease in the total pressure drop can be explained by the fact that the flow in the riser is gravity dominated, i.e., the major contributor to total

pressure drop in a vertical pipe is static pressure drop ($\rho_m g$). In addition, an increase in gas superficial velocity, will promote an increase in the void fraction, thereby reducing the mixture density as a consequence of a decrease in the liquid hold up. However, the velocities encountered are not high enough to cause high frictional pressure drops. Consequently, the total pressure drop decreases with an increase in gas superficial velocity.

On the other hand, the frictional pressure drop increases with gas superficial velocity, but the rate of increase at higher gas superficial velocities is lower compared to that at lower gas superficial velocity. These observations support the phenomena recently reported by Mandal et al. (2004), who worked on a vertical 51.6 mm internal diameter pipe using an air-non-Newtonian liquid system in co-current downflow bubble column. It is also interesting from Figure 4.9b that lower pressure drops are observed at higher liquid superficial velocities for the same gas superficial velocity. These phenomena may be explained by considering the increasing drag experienced by the bubbles and the coalescence of gas bubbles. At higher liquid superficial velocities, comparatively larger bubbles are observed to form due to coalescence, which causes a decrease in the true liquid velocity because of higher liquid holdup. A similar observation and conclusion was previously reported by Mahalingam and Valle (1972) (liquid-liquid system), Friedel (1980) (gas-liquid system), Godbole et al. (1982) (liquid-liquid system), and Mandal et al. (2004) (gas-liquid system).



(a)



(b)

Figure 4.9: the influence of the gas superficial velocity on the total and the frictional pressure drop. The total pressure drop was measured with a differential pressure cell connected around the twin-plane ECT. (Liquid superficial velocity (ms^{-1}): $\triangle = 0.05$; $\square = 0.14$; $\bigcirc = 0.38$)

It is concluded that the lower the mixture density, the lower will be the measured total pressure drop. It is further concluded that the rate of increase in the frictional pressure drop at lower gas superficial velocities is much higher than that recorded within the higher gas superficial velocity region. This increase can be explained by the fact that an increase in gas superficial velocity causes higher

production of gas bubbles, which in turn increases the true liquid velocity due to a decrease in the liquid holdup.

4.3.4 Frequency:

The slug frequency is found to increase with the liquid superficial velocity, Figure 4.10. Slug frequency varies between 3.2 to 1.4 Hz. The liquid superficial velocity strongly affects the frequency of the periodical structures in intermittent flows such as spherical cap bubbles and Taylor bubbles.

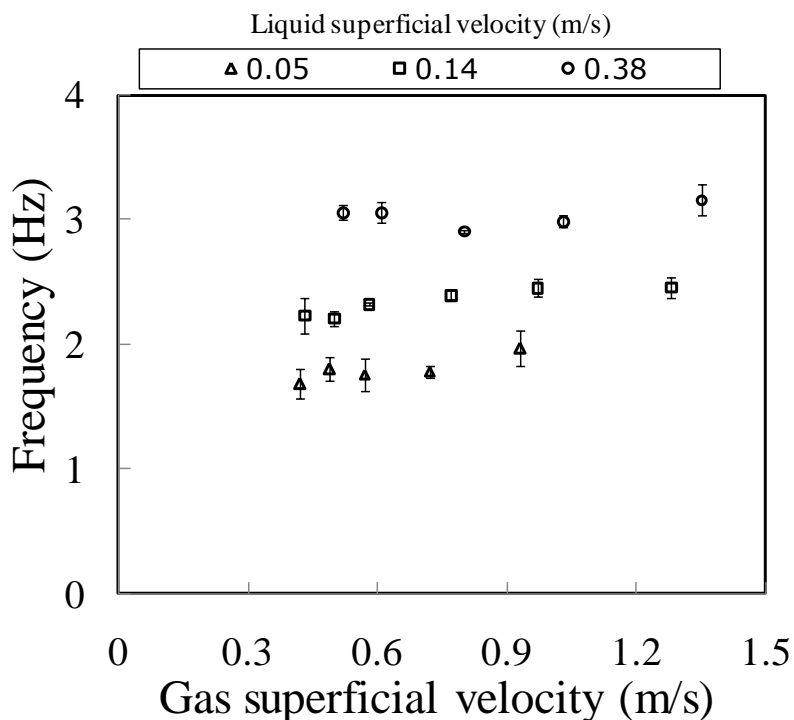


Figure 4.10: Variation of slug frequency with mixture velocity at different liquid superficial velocities. The error bar represents standard deviation.

For the lowest liquid superficial velocity, the frequency increases slightly with gas superficial velocity. Then as the liquid superficial velocity is increased to 0.14 ms^{-1} , the frequency is observed to show a low influence of gas superficial velocity. However, at the highest liquid superficial velocity, the frequency decreased and then increased a little, having a minimum at 0.8 ms^{-1} , gas

superficial velocity. This behaviour might be attributed to the observed changes in the flow pattern associated with a change in the liquid superficial velocity. These observations supported the findings of previous studies in horizontal gas-liquid flow including Hubbard (1965), Taitel and Dukler (1977), Jepson and Taylor (1993), Manolis et al. (1995).

For the analysis of oscillating unsteady fluid flow dynamics problems, a dimensionless value useful is the Strouhal number. It represents a measure of the ratio of inertial forces due to the unsteadiness of the flow to the inertia forces due to changes in velocity from one point to another.

The Strouhal number, St , in terms of liquid superficial velocity can be expressed as:

$$St = \frac{fD}{U_{SL}} \quad (4.22)$$

In Figure 4.11a, the Strouhal number based on the liquid superficial velocity is shown as a function of liquid quality on a log-log plot. The liquid quality is defined as the ratio of liquid superficial velocity to mixture superficial velocity.

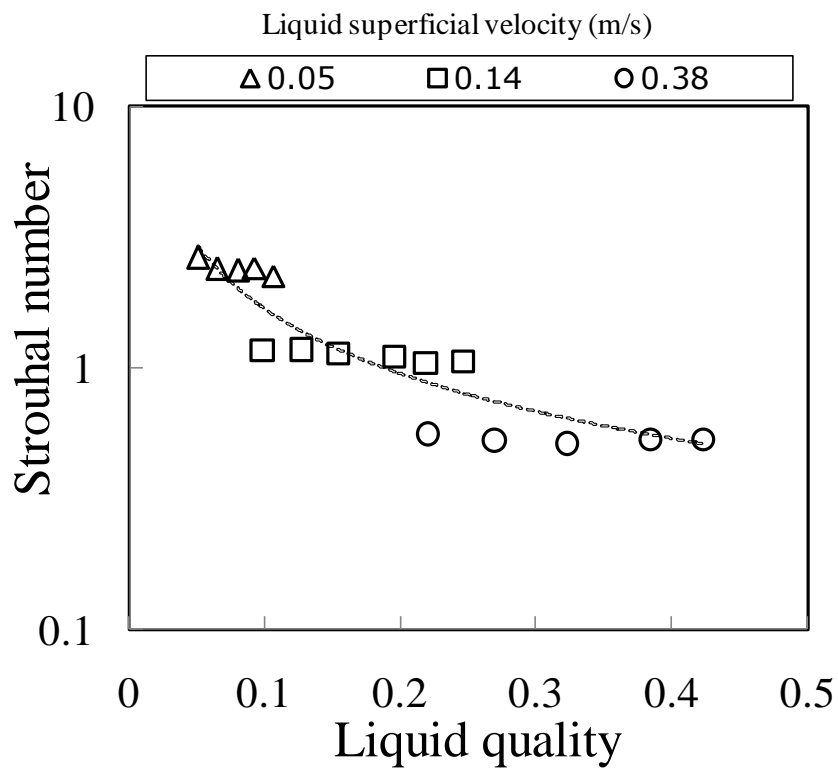
$$\text{Liquid quality, } q = \frac{U_{SL}}{U_{SL} + U_{SG}} \quad (4.23)$$

The relationship between Strouhal number and the Lockhart-Martinelli parameter is shown in Figure 4.11b again on a log-log plot. The Lockhart-Martinelli parameter is defined as the square root of the pressure drops for the liquid part of the flow flowing alone in the pipe divided by that for the gas and it is

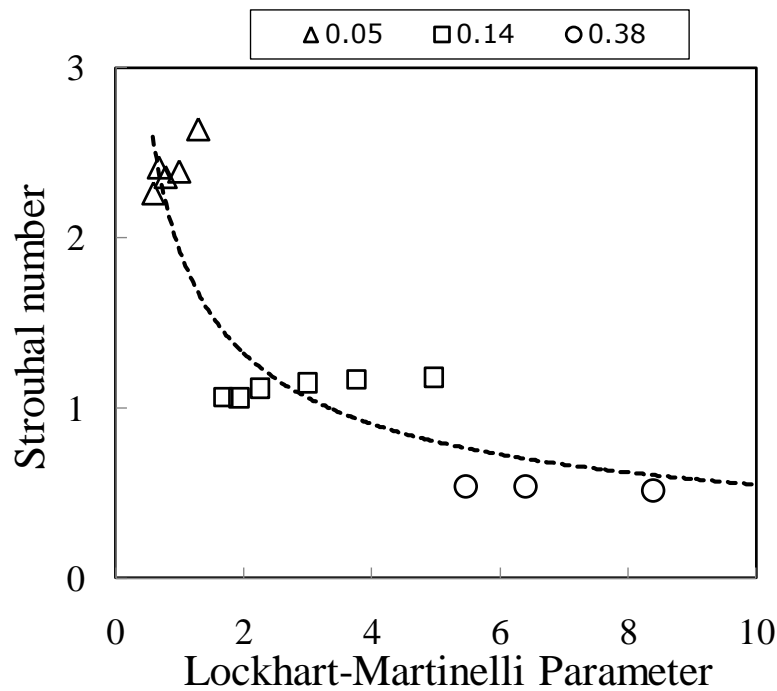
approximately equal to the ratio of liquid and gas superficial velocities times the square root of the liquid to gas density ratio:

$$\text{Lockhart-Martinelli parameter, } X = \sqrt{\frac{\rho_L}{\rho_G}} \frac{U_{SL}}{U_{SG}} \quad (4.24)$$

Each plot exhibits a decrease in the Strouhal as the liquid quality or the Lockhart-Martinelli parameter increases. Figure 4.11a shows the existence of three distinct regions of the Strouhal number for different values of the liquid quality in the range $0.1 < \text{liquid quality} < 0.5$. The lower frequency Strouhal number is attributed to the large scale instability of the liquid slug region. The higher frequency Strouhal number is caused by small scale instabilities from the separation of the shear layer. The same trend can be observed for the variation of Strouhal number with the Lockhart-Martinelli parameter as shown in Figure 4.11b.



(a)



(b)

Figure 4.11: Log-log plot of the dimensionless Strouhal number vs (a) the liquid quality (b) the Lockhart-Martinelli parameter.

4.3.5 Lengths of the liquid slug, the Taylor bubble and the slug unit:

The length of each Taylor bubble has been calculated from the measured velocities and slug frequencies. The resulting lengths have been averaged for each set of gas and liquid superficial velocities. The lengths of the Taylor bubble and the slug unit are found to increase with a corresponding increase in the gas superficial velocity, for a constant liquid superficial velocity. Conversely, the lengths of the liquid slug do not exhibit a definite trend with an increase in gas superficial velocity.

The average lengths of the liquid slugs as a function of the gas superficial velocity at various liquid flow rates are shown on Figure 4.12. It is concluded that there is no clearly defined trend between the variation of the liquid slug length

and the gas superficial velocity. Although, for a liquid superficial velocity of between $0.05 - 0.14 \text{ ms}^{-1}$, the lengths of the liquid slug are observed to decrease with an increase in the gas superficial velocity. However, it is interesting to note that at liquid superficial velocity of 0.38 ms^{-1} , the length of the liquid slug increases from approximately 6 to 9 pipe diameters and then finally decreases to a length of about 6 pipe diameters. The qualitative shape of the best fit curve is an arc, with a maximum at the top. The stable liquid slug length is reported to be between 10 to 20 D (Moissis and Griffith (1962); Akagawa and Sakaguchi (1966); Fernandes (1981); Barnea and Shemer (1989) and Van Hout et al. (2003)) for air-water system in a vertical pipe. The shorter liquid slug lengths observed may be attributed to the bigger pipe diameters used in these experiments. It has been reported that the slug flow pattern tends to disappear as the pipe diameter increases, Omebere-Iyari et al. (2008). It is concluded that for a particular flow condition, the length of the slug is changing constantly due to the constant interaction between the phases at the tail of the Taylor bubble. Consequently, different velocities can be obtained for individual Taylor bubbles.

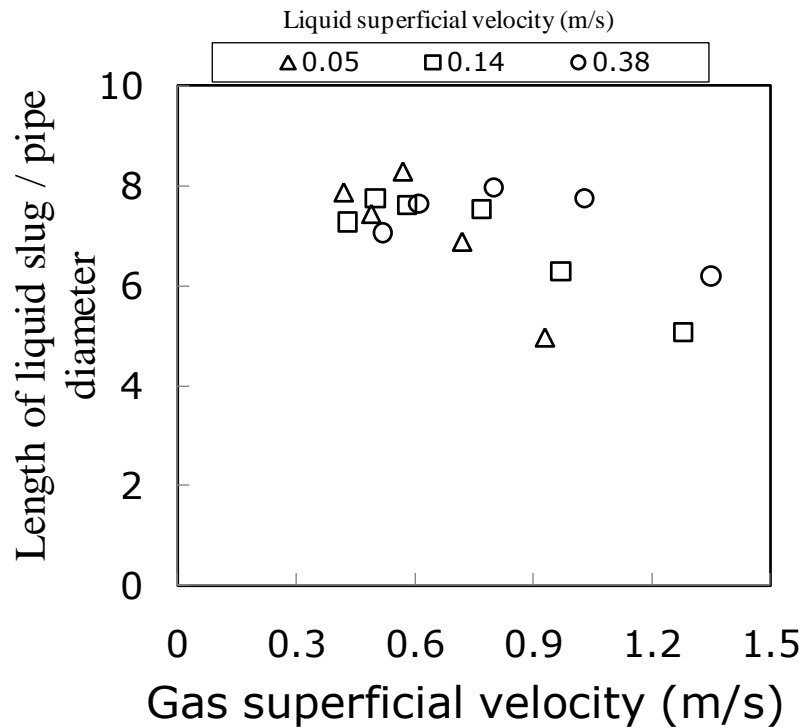


Figure 4.12: The determined length of liquid slug at different liquid and gas superficial velocities.

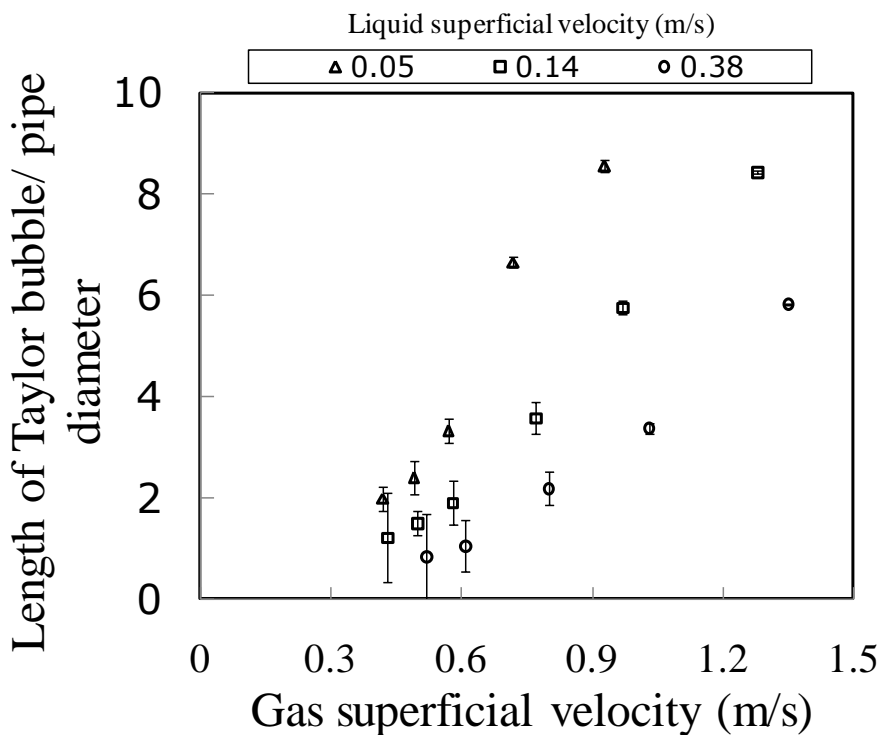


Figure 4.13: Influence of gas superficial velocity on the ratio of average lengths of the Taylor bubble to pipe diameter. The error bar represents standard deviation. These lengths were determined for an experimental measurement averaging period of 60 seconds.

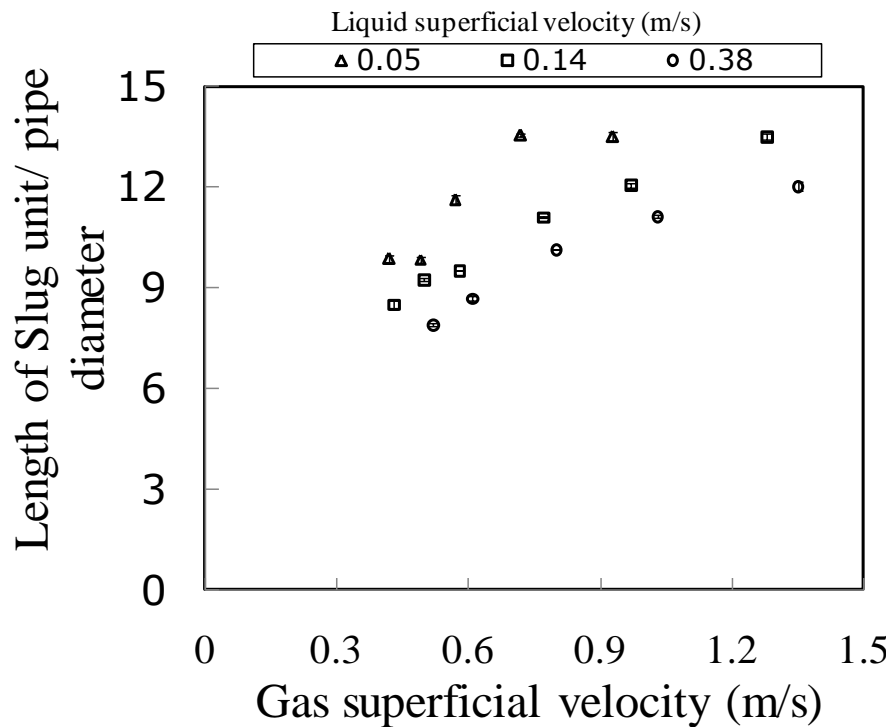


Figure 4.14: Influence of gas superficial velocity on the ratio of average lengths of the slug unit to pipe diameter. The error bar represents standard deviation. These lengths were determined for an experimental measurement averaging period of 60 seconds.

From an analysis of the data presented on Figure 4.13, it is concluded that at certain liquid flow rates an almost linear relationship seems to exist between the Taylor bubble length and the gas superficial velocity. Furthermore, an increase in the gas superficial velocity leads to a proportional increase in Taylor bubble length. The increase in the observed Taylor bubble length could be due to an increase in bubble coalescence as a consequence of an increase in gas flow rate.

The length of the slug unit on the other hand can be observed to increase with gas superficial velocity. But, it can be observed that the length of the liquid slug becomes shorter with an increase in gas superficial velocity. This is due to the fact that the frequency of the slugging increases with an increase in the gas superficial velocity. A similar observation was made by Hernandez-Perez (2008).

4.3.6 Comparison of length of liquid slug with the Khatib and Richardson (1984) method:

A comparison between the experimental data and the Khatib and Richardson (1984) method (equation (2.22)) for determining the length of liquid slug has been made and is presented on Figure 4.15. The under-prediction of the Khatib and Richardson method could be attributed to the simple empirically derived model they derived.

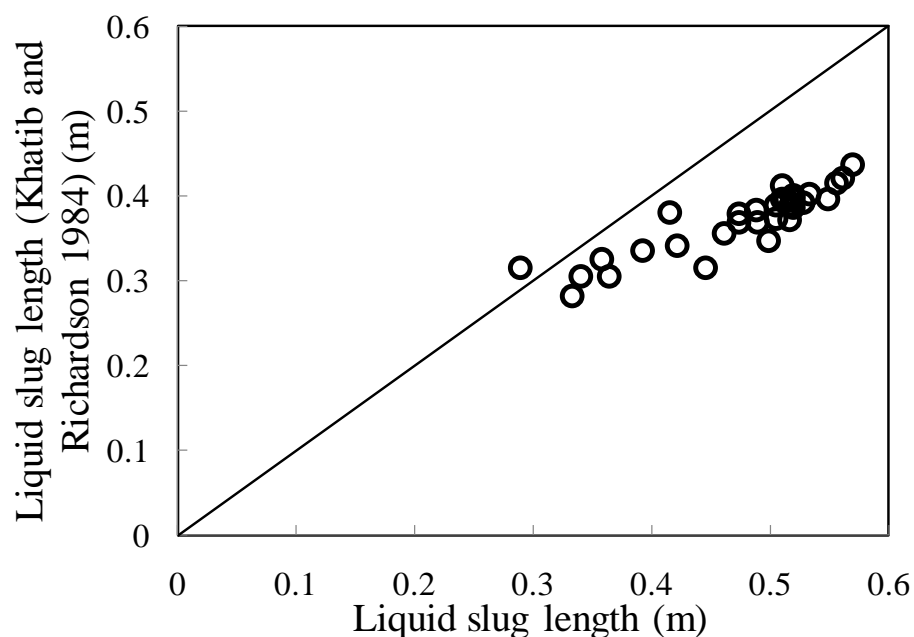


Figure 4.15: Comparison between the experimental data and the Khatib and Richardson method (1984).

4.4 Summary

This chapter has presented an analysis and discussion of the experimental results obtained to characterise the slug flow produced within a riser when known quantities of air and silicone oil are injected at the base of the riser. The flow characteristics were measured and characterised using non-intrusive instrumentation, including electrical capacitance tomography (ECT) and a differential pressure cell. The following conclusions may be drawn:

(1) To study the characteristics of slug flow in a vertical pipe, the data of the ECT without either the WMS or bend placed downstream of it should be considered only. Otherwise, it cannot be established whether any difference in the result is due to the bend or the WMS.

(2) A linear relationship was obtained between structure velocity and mixture superficial velocity. A comparison of this data with the empirical relationships proposed by Nicklin et al. (1962) and Mao and Dukler (1985) showed good qualitative agreement. The best quantitative agreement was obtained with the relationship proposed by Nicklin et al. (1962).

(3) The drift velocity discussed in the literature was developed by consideration a static liquid column and also using potential flow analysis which assumes no surface tension and viscosity effects on the drift velocity. The experimental results reveal that a continuous liquid, surface tension and viscosity are significant parameters for drift velocity. Drift velocity for an air-silicone oil flow is higher than that of air-water system.

(4) For a given liquid flow rate, as the gas flow rate was increased, the experimental average void fractions in the liquid slug and the Taylor bubble were found to increase, whilst the liquid film thickness was found to decrease. The liquid superficial velocity has no significant influence on the void fractions in the liquid slug and the Taylor bubble. These findings were found to agree well with those made by previous published studies.

(5) The total pressure drop along the riser was found to decrease as the gas superficial velocity increases, whilst the measured frictional pressure drop was found to increase.

(6) The slug frequency increased with an increase in the liquid superficial velocity, whilst the dimensionless Strouhal number was found to decrease with corresponding increases in the liquid quality and the Lockhart-Martinelli parameter.

(7) The dimensionless lengths of the Taylor bubbles, and the slug units were found to increase with an increase in the gas superficial velocity. However, the length of the liquid slug was found to be changing due to a coalescence of the dispersed bubbles from the wake of a Taylor bubble with the Taylor bubble. This is in agreement with the result obtained by Akagawa and Sakaguchi (1966); Fernandes (1981) and Van Hout et al. (2002)

(8) An adequate agreement was found between the experimental liquid slug length and the Khatib and Richardson method (1984) after considering the influence of the void fraction in liquid slug.

This study has provided a more fundamental insight into the physical phenomena that govern the behaviour of slug flows and the way these parameters behave under various flow conditions.

Gas-Liquid Flow in Bends of Different Orientations

In this chapter, the results of the experiments carried out in an inclinable 67 mm internal diameter and 6 m high rig attached to a 90° bend will be presented using the experimental facility and measurement techniques described in Chapter 3. In this study, only the experimental results obtained from a vertical and horizontal orientation of test pipe flow section will be presented, analysed and discussed. Experiments involving air-silicone oil flows have been performed to interrogate the effect of 90° bends on the two-phase flow and to develop appropriate boundary conditions at bends to validate computational fluid dynamics (CFD) models.

In the experiments performed, measurements of the void fraction were obtained from the ECT and WMS measurement transducers. Two bend orientations were investigated: (1) vertical bend (upstream-vertical riser/downstream-horizontal flowline) and (2) horizontal bend (horizontal flowlines upstream and downstream) for a wide range of flow rates. The flow patterns were determined by analyzing the Probability Density Function (PDF) of the time series of the void fraction. The resultant statistical patterns of this recorded data were analysed in the pipe sections immediately before and after the bends. Supporting evidence

for flow pattern identification was obtained from visual observations obtained from the analysis of high speed video stills. A flow pattern map was constructed to summarize the range of the flow patterns observed in both the vertical and horizontal 90° bends. A comparative analysis of this data was performed to determine the effects that different gas and liquid superficial velocities have on the mean cross-sectional void fraction distributions, both before and after the vertical and horizontal 90° bends. Finally, a comparative analysis of the present experimental results with the work of Gardner and Neller (1969) was made based on the use of a modified Froude number.

5.1 Testing of instruments:

Advanced instrumentation, including ECT and WMS measurement transducers use tomographic imaging methods to manipulate data from remote sensors to obtain precise quantitative information from inaccessible locations. The need for this instrumentation is analogous to the medical need for body scanners, which has been met by the development of computer-aided tomography.

In this study, the WMS measurement transducer was used to give detailed information about air-silicone flows whilst the ECT transducer was used to measure the void fractions within the flow. Experimental measurements have been recorded with the aid of the above instrumentation at liquid superficial velocities across the range of 0.05 - 0.38 ms⁻¹ and for air flow rates in the range 0.05 - 4.73 ms⁻¹. The electronics governing the WMS measurement transducers was arranged to trigger the ECT transducer measurements to enable simultaneous recordings. The sampling frequencies of the ECT and WMS measurement transducers were set at 200 and 1000 Hz, respectively. A great deal of information

may be extracted from an examination of the time series of the cross-sectionally averaged void fractions. In particular, the probability density function (PDF) of the observed void fractions can have characteristic signatures. The results of the PDFs of the void fraction were confirmed by the cross-sectional slice view of void fraction obtained from the WMS measurement transducers. Figure 5.1 shows a 3-D plot of the PDF of the void fractions recorded by the ECT and WMS measurement transducers. The data presented on the figure illustrates the good agreement between the two methods of measurements. Some of the minor differences may be due to the fact that the ECT measures over larger axial distances than that of the WMS.

5.2 Comparison of PDFs of void fraction for the ECT and WMS for the riser before the vertical 90° bend:

Figure 5.1 present a comparison between the 3-D plot of PDFs of void fraction for the ECT and WMS for same flow conditions in a vertical riser. The plots show that at a liquid superficial velocity of 0.05 ms^{-1} and a gas superficial velocity of $0.05 - 0.29 \text{ ms}^{-1}$, both the ECT and WMS identify the flow regimes as spherical cap bubble. However, the ECT provides a higher peak value while the WMS predicts higher void fraction. An increase in the gas superficial velocity from 0.34 to 0.95 ms^{-1} (whilst maintaining same liquid velocity of 0.05 ms^{-1}) results in a characteristic signature of slug flow regimes by both the ECT and WMS measurement transducers. It may also be observed that the ECT provides a higher PDF for the void fraction than that recorded by the WMS but with a lesser range compared to at gas superficial velocity of 0.05 ms^{-1} while the WMS provide a higher void fraction. At a gas superficial velocity of between $1.23 - 4.73 \text{ ms}^{-1}$,

the ECT and WMS both defined the flow patterns as churn flow. It is interesting to note that both the PDF of the void fraction for ECT and WMS show almost same peak at a gas superficial velocity of 4.73 ms^{-1} . The degree of agreement both in the length of the PDF and the void fraction improves with an increase in the gas superficial velocity. The result therefore shows that both instruments predict similar flow regime signatures.

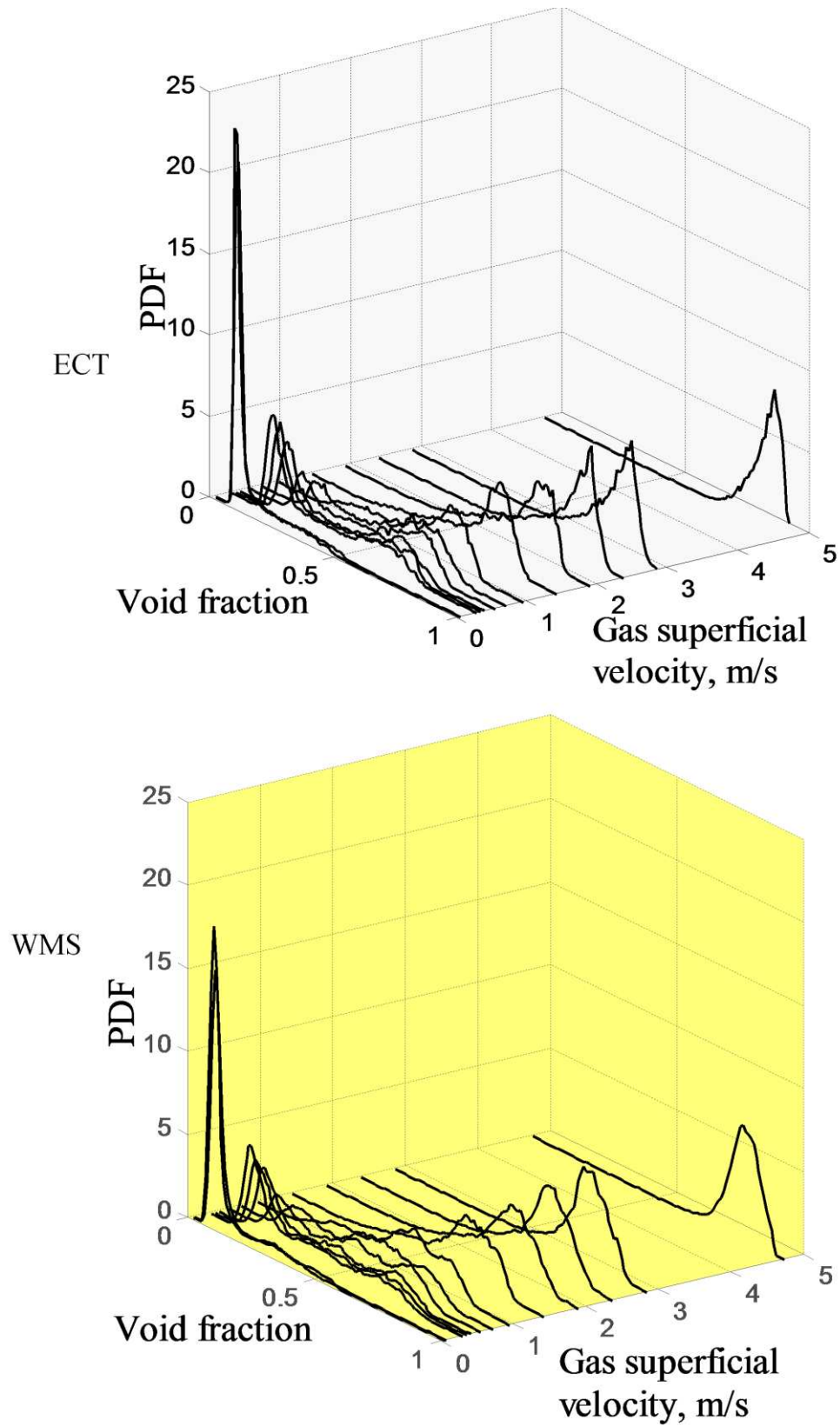


Figure 5.1: Comparison of 3-D plot of PDFs of void fraction before the vertical 90° bend obtained from the ECT and WMS. Liquid superficial velocity = 0.05 ms^{-1}

5.2.1 Reconstructed images of the two-phase flow before the vertical 90° bend as depicted by the WMS:

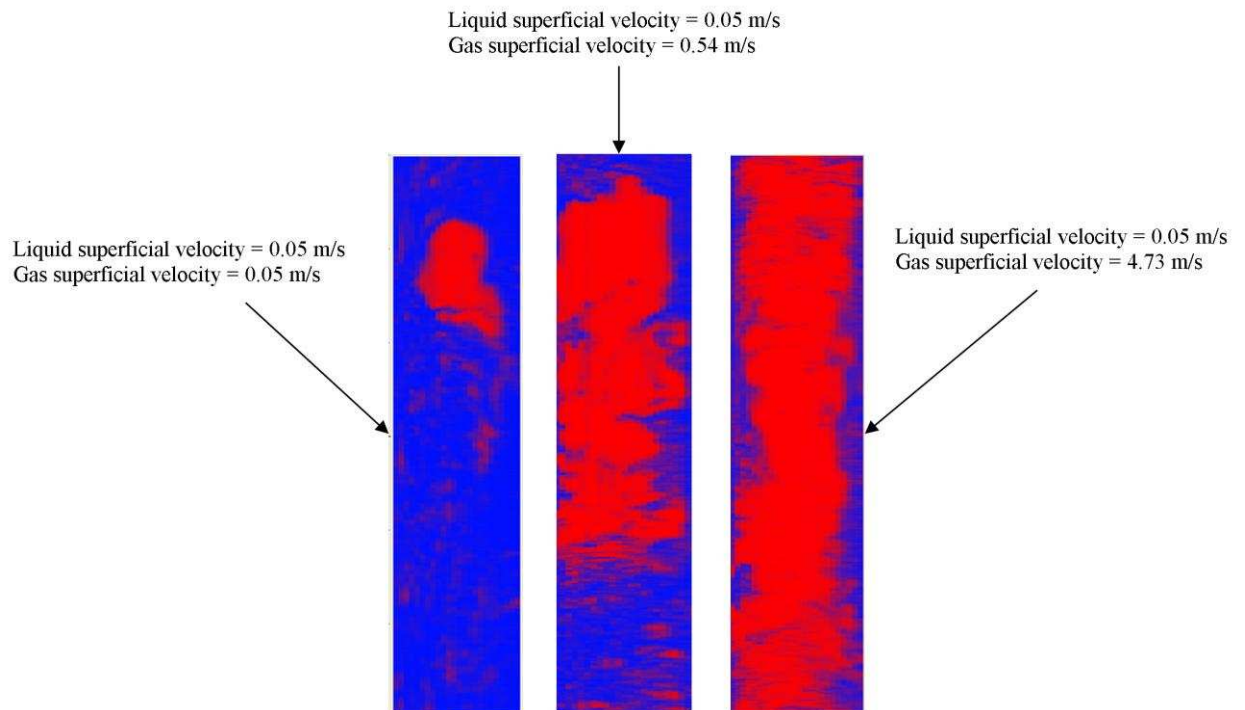


Figure 5.2: Reconstructed images of the two-phase flow transition from spherical cap bubble to churn flow.

Figure 5.2 (a – c) show 2 dimensional slice views of the void fractions observed for different gas superficial velocities. It is concluded that these results support the result presented on Figure 5.1(a – b). At a gas superficial velocity of 0.05 ms^{-1} , there are still bubbles of large size, but not as big as the pipe diameter. These are often described as spherical cap bubbles. When the gas velocity is increased to 0.54 ms^{-1} , the coalescence of these cap bubbles starts to lead towards creating a slug flow. At a critical gas superficial velocity of 4.73 ms^{-1} , the slug flow is observed to change to churn flow. These results are in good agreement with the results presented in Figure 5.1(a – b).

5.3 Comparison of PDFs of void fraction before and after the bend using the WMS:

This section compares the flow patterns observed both before and after the vertical and horizontal 90° bends position using the probability density function (PDF) representations of the void fraction. On the top plot presented in Figure 5.3, the PDF for the riser before the vertical bend (the dark curve) are compared with that for the flowline before the horizontal bend (the light curve) for the same gas and liquid inlet flow conditions. The bottom plot gives the same comparison for the flow regime experienced after the bend.

A PDF is the variation of the probability that the void fraction values lie within a certain range ($\varepsilon \pm \delta\varepsilon$) versus void fraction. The PDF was determined by counting the number of data points in data bins of width 0.01 centred on void fractions from 0.005, 0.015 ...0.995, and then dividing each sum by the total number of data points. They confirm the dominant void fractions which are observed for each flow condition.

The PDFs of time varying void fractions has been used to classify the flow patterns in the same manner as Costigan and Whalley (1997) and Omebere-Iyari and Azzopardi (2007). The PDFs of the void fraction data obtained at liquid superficial velocity of between 0.05 to 0.38 ms⁻¹ and variable gas superficial velocities of between 0.05 to 4.73 ms⁻¹ are shown in Figure 5.3.

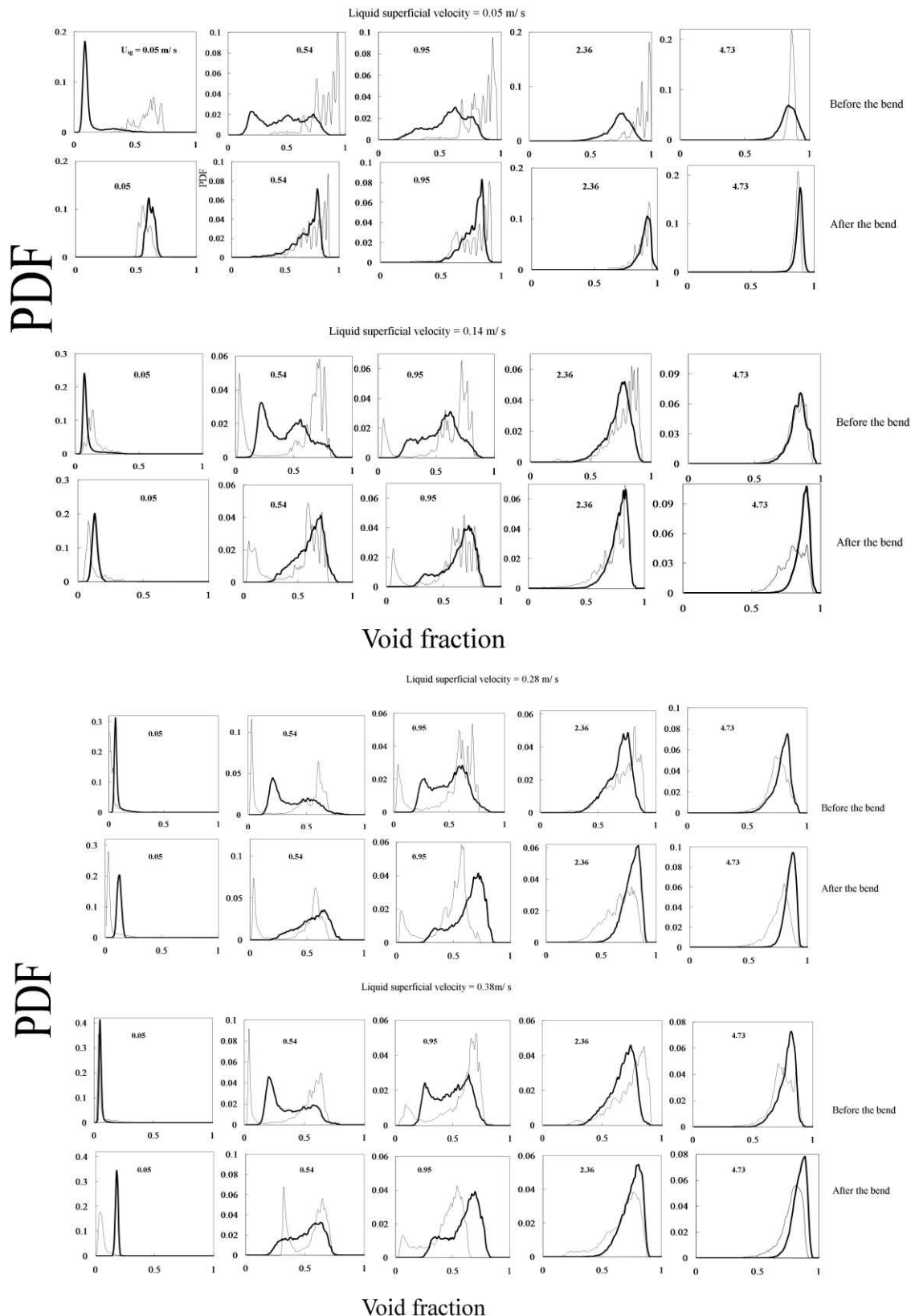


Figure 5.3: PDF of void fraction before and after the bend. The top plot, PDF before the bend, the dark curve represents the flow patterns before the vertical 90° bend whilst the light ones are for the horizontal 90° bend. The bottom plot gives the same comparison for the PDF after the bend (flow pattern)

One interesting observation is that over the range of liquid flow rates studied, the liquid flow rate has little observable effect on the two phase flow behaviour for the upstream section of the vertical 90° bend. Indeed the observed flow patterns are substantially the same (cap bubble, slug, unstable slug and churn flows) irrespective of an increase in the liquid superficial velocity as shown in Figure 5.3. However, there might be small differences in the gas flow rates at which these transitions occurred. In contrast, for the horizontal 90° bend, the liquid flow rate has a noticeable effect on the two phase flow behaviour. The flow patterns observed at low liquid flow rate, i.e., stratified wavy and annular flows changed to plug and slug flows when the liquid superficial velocity is increased. This is not surprising results as the amount of liquid present in the pipe at low liquid superficial velocity is too small for plug or slug flows to exist and as a result, stratified wavy or annular flows are formed. But as the liquid flow rate is increased, plug and slug flows begin to form.

On the other hand, within the downstream pipe flow of both the vertical and horizontal 90° bends, the same annular flow patterns are observed for both the lowest liquid superficial velocity (0.05 ms^{-1}) and highest gas superficial velocity (4.73 ms^{-1}) as illustrated in Figure 5.3. This is supported by direct visual observations made from an analysis of the high speed video stills. This behaviour is a result of the impact of the air-silicone oil flow on the bend that transfers some of the liquid to the top and bottom of the internal pipe sections. Unfortunately, the pipe flow section beyond the Wire Mesh Sensor (WMS) was opaque, but it was expected that the flow would subsequently settle to a stratified wavy flow.

At liquid superficial velocity of 0.14 ms^{-1} and low gas flow rate (gas superficial velocity = 0.05 ms^{-1}), the PDF for the vertical riser flows presents a single peak of the void fraction value at about 0.06 with a broadening tail extending to a higher value of about 0.35. This defines a spherical cap bubble flow, as described previously by Costigan and Whalley (1997) with a velocity higher than the velocity of the small bubbles. This flow pattern has also been confirmed by an analysis of the images of high speed video stills as shown in Figure 5.5. The gas bubbles are confirmed to exhibit spherical cap shapes. When the upstream flow pipe was horizontal, the PDF of the measured void fraction at the same flow rate shows a dominant peak at 0.14 with a wide base spanning from 0 to 0.36, which is a typical feature of a plug flow. The elongated gas bubbles are separated by sections of continuous liquid moving downstream along the top part of the pipe with almost zero void fraction in the liquid. The variation of the void fraction reflects the different size of the gas bubbles and the continuous liquid phase. After the bend, the PDF for the horizontal pipe in the riser shows a single peak, the signature of a bubbly flow. A following broad tail present in the PDF of the riser does not exist in the PDF after the bend. The big cap bubbles are observed to break up in the bend due to an imbalance in the centrifugal and surface tension forces. Thereafter the bubbles become more uniform. For the horizontal arrangement, the PDF after the bend move to the lower void fraction values with the dominant peak frequency at the void fraction of 0.08. There is little change in the size of the wide base compared with that before the bend. With the same mechanism the elongated bubbles break in to smaller bubbles when passing through the bend. However, the observed flow patterns remain as a characteristic plug flow though.

When the gas flow rate increases to 0.54 ms^{-1} , the cap bubbles coalesce into bullet-shaped Taylor bubbles and a slug flow regime is formed. The PDFs of the void fraction within the riser records two main peaks at the values of 0.22 and 0.55, respectively for ($U_{SL}=0.14 \text{ ms}^{-1}$). These peaks are the signature of the aerated liquid slugs and the Taylor bubbles of different sizes. The Taylor bubbles are as yet not fully developed. This is confirmed by an analysis of the fast video stills images as shown in Figure 5.6. Similar to that for the riser, the PDFs for the horizontal flowline has one narrow peak at the value of 0.02 and one wide peak with fluctuations at around 0.7. With an increase in the gas superficial velocity from 0.05 to 0.54 ms^{-1} , the elongated bubbles are observed to grow and coalesce into bullet-shaped Taylor bubbles. The flow pattern, thus changes from plug flow to slug flow. According to Simmons and Hanratty (2000), slugs are formed when waves on the surface of a stratified liquid layer, intermittently, grow to reach the top of the pipe. The liquid then fills the whole cross-section, to produce highly aerated masses of liquid that propagate down the pipeline at a velocity close to that of the gas phase. After the bend, the PDFs of the void fraction in the flowline for the riser exhibit a “hill” shape. Within this zone stratified wavy flow were observed. For the horizontal flow line before the bend, the recorded PDFs exhibit a lower void fraction peak that moves to the higher void fraction values and more peaks appear at the void fractions 0.5 - 0.8. This may be attributed to the collapse of the larger Taylor bubbles as they pass through the bend. However, the flow pattern remains as slug flow.

When the gas flow rate reaches a critical value of 0.95 ms^{-1} , again two peaks appear on the PDF plots of the void fractions in the riser. However, the height of

the lower void fraction peak decreases by 53 %, whilst the PDF of the higher void fraction increases by 42 %, as compared to those recorded at a gas flow rate of 0.54 ms^{-1} . An increase in the gas superficial velocity leads to a corresponding increase in the length of the Taylor bubbles and a shrinkage of the length of the liquid slugs. Consequently, more and more bubbles are entrained into the liquid slugs. This pattern is defined as unstable slug flow by Costigan and Whalley (1997). For the case of the flowline arrangement, the height of the lower void fraction peak also decreases significantly. The PDF curve moves to the higher void fraction values with the increase of the gas superficial velocity. After the bend for the riser setup, with the increase of gas superficial velocity from 0.54 to 0.95 ms^{-1} , the stratified wavy flow in the flowline becomes a developing slug flow, which is recognised by a small peak on the PDF superimposed on a big peak with a wide base. With an increase in the gas superficial velocity from 0.54 ms^{-1} , the observed waves becomes stronger and as consequence more bubbles being trapped inside. At a certain critical point Taylor bubbles are formed. For the horizontal setup, no significant difference is present in the PDF observed before and after the bend except the significant reduction in the height of the peak at the high void fraction (~ 0.72).

At gas superficial velocity of 2.36 ms^{-1} , the PDF of the observed void fraction for the riser has a single peak at about 0.76 with tails down to 0.2 and 0.9, which are typical of churn flows. An increase in the gas superficial velocity escalates the instability of the liquid slugs. When the speed of the gas core reaches a critical point, the liquid slugs will be penetrated and the integrity of the Taylor bubbles will be compromised. This leads to the transition of the flow regime to a churn

flow. For the horizontal setup, the liquid released from the collapsed slugs accumulates at the bottom part of the pipe which forms a strong wave in the direction of the gas that travels along the upper part of the pipe. Consequently a stratified wavy flow is formed. After the bend, the PDF of the void fractions for the riser significantly shifts to the higher values compared with that before the bend. The dominant void fraction of 0.75 increases to 0.83 an increase of 42 %. The churn flow observed before the bend changes to a semi-annular flow after the bend. This has subsequently been confirmed by an analysis of fast video stills. However, the liquid films are erratic and exhibit disturbances with void fractions down to about 0.5. For the horizontal arrangement, no significant flow pattern change was observed, as it maintains the same stratified wavy flow after the bend.

At the highest gas flow rate of 4.73 ms^{-1} examined, the PDFs of void fractions observed in the riser has very similar shape to those at a lower value of 2.36 ms^{-1} but with a much narrower tail. The peak moves towards the higher void fraction. The flow pattern is still classified as a churn flow, but moves very close to the transition zone leading to a semi-annular flow. For the horizontal pipe flow layout, with an increase in the gas flow rate from between 2.36 to 4.73 ms^{-1} , the liquid film becomes gradually more uniformly distributed around the pipe wall. This is mirrored by the PDF curve whereby the peak becomes narrower and exhibits less fluctuation. The annular flow regime is approached when the gas superficial velocity is large enough to distribute the liquid evenly across the pipe wall. After the bend, semi-annular flow is present in the flowline for the riser and stratified wavy appears in the flowline for the horizontal configuration.

A flow pattern map is presented in Figure 5.4, summarizing all the flow patterns

observed in both the vertical and horizontal 90° bends.

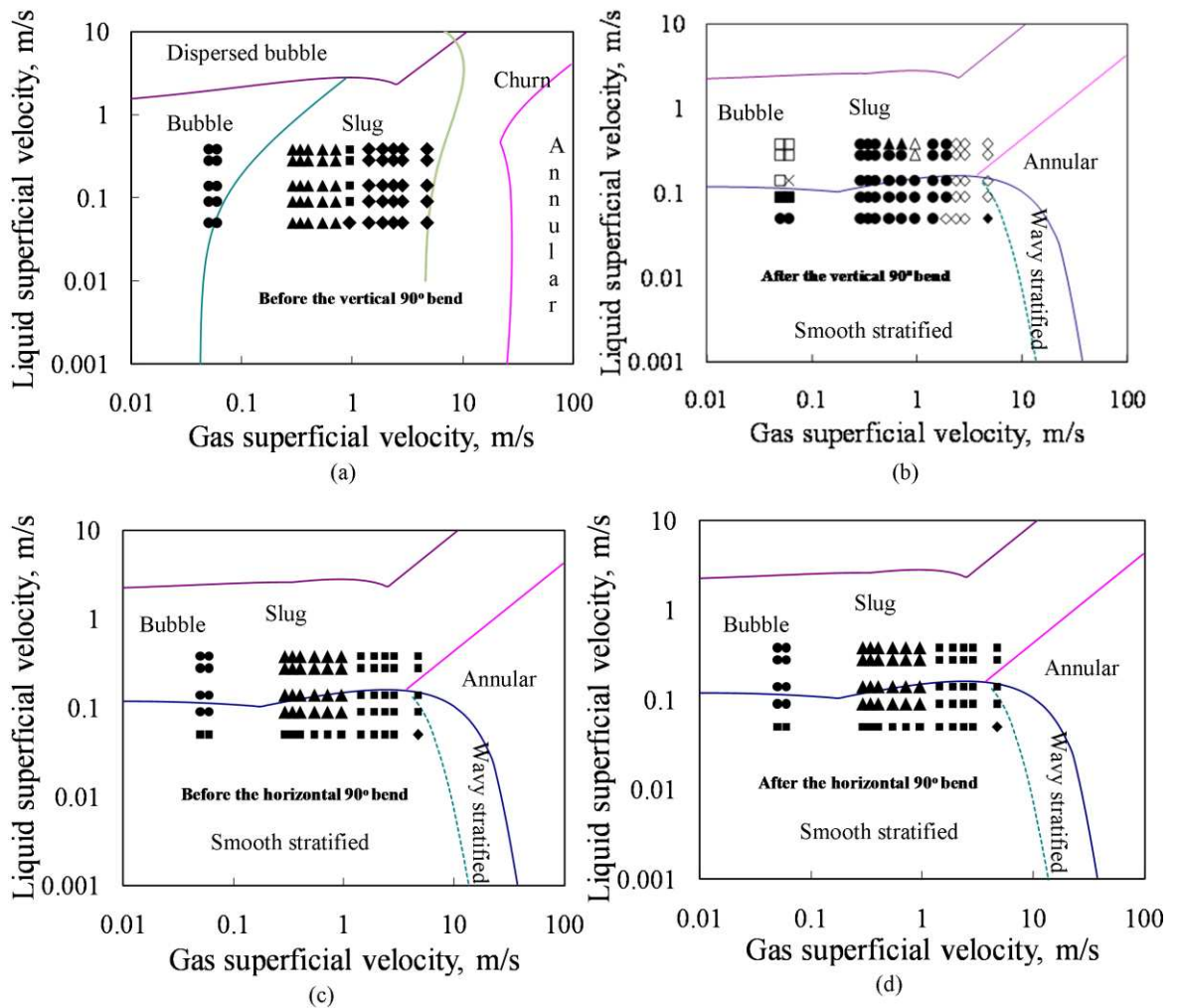


Figure 5.4: Shoham (2005) flow pattern maps for both the vertical and horizontal 90° bends. For the vertical 90° bend (a) upstream: ● = spherical cap bubble flow, ▲ = slug flow, ■ = unstable slug flow, ◆ = churn flow (b) downstream: □ = bubble flow, ■ = dispersed bubble flow, × = plug flow, ● = stratified wavy flow, ▲ = slug flow, △ = unstable slug flow, ◇ = semi-annular flow, ◆ = annular flow. For the horizontal 90° bend (c) upstream = (d) downstream: ● = plug flow, ■ = stratified wavy, ▲ = slug flow, ◆ = annular flow

5.4 Flow patterns identification using high speed video images:

The observation of the various phenomena occurring for two-phase flows may be made by visual inspection through a transparent pipe section. However, when the processes occur at high speeds the observer is unable to have a clear picture of

what is happening. The use of the high speed photography and high speed video film analysis techniques allows this problem to be overcome.

5.4.1 Flow regimes in vertical riser (vertical 90° bend):

In the following sections, descriptions of the various flow patterns are presented for constant liquid flow rates and increasing air flow rates:

Spherical cap bubble: As shown in Figure 5.5a, there may be swarms of small bubbles as the gas velocity increases. In time these bubbles may then form larger ones as shown in Figure 5.5b, but not big enough to cover the pipe diameter. The velocity of a bubble may differ substantially from that of the liquid phase. At this flow rate, both the bubble number density and the mean diameter of the bubbles increase. The inter-bubble space decreases and the movement of the bubbles become more irregular. Due to the collisions between bubbles, coalescence takes place and spherical cap bubble flow is formed. As a consequence of coalescence and velocity differences, the bubbles are no longer uniformly distributed along the pipe.

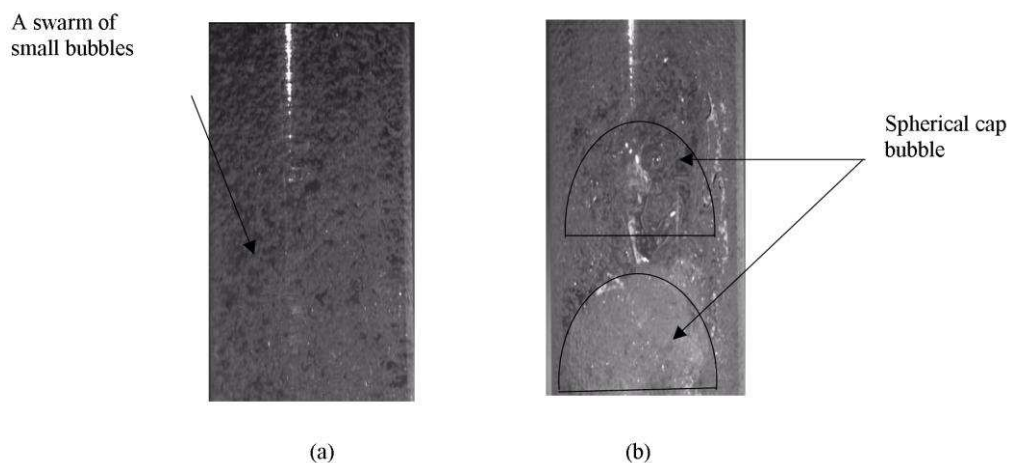


Figure 5.5: Video image of spherical cap bubble for a riser at liquid and gas superficial velocities of 0.14 and 0.05 ms⁻¹, respectively

Slug flow: As the spherical cap bubbles coalesce with one another and with other smaller bubbles to form bigger ones, which may almost fill the entire cross-section of the pipe resulting in higher void fraction. Consequently, the void fraction and bubble size at various places in the riser may become so high that bullet-shaped Taylor bubbles are formed as observed in Figure 5.6 separated by slugs of silicone oil with some gas entrained in it as small bubbles. There are significant quantities of small bubbles in the liquid film surrounding the Taylor bubble.

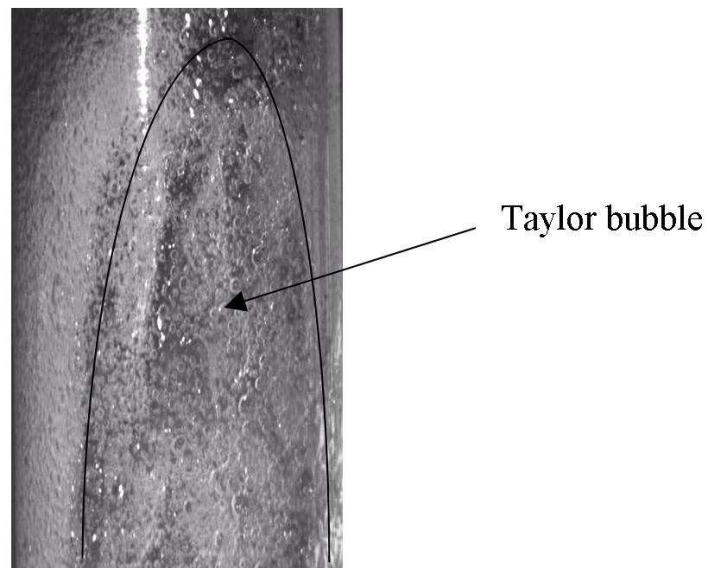
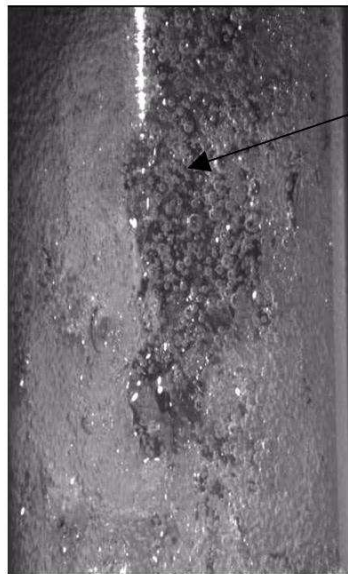


Figure 5.6: Video image of slug flow for a riser at liquid and gas superficial velocities of 0.14 and 0.54 ms^{-1} , respectively

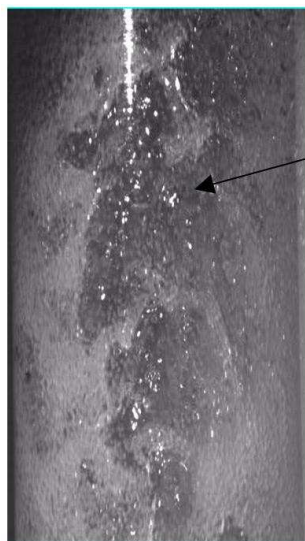
Unstable slug: the flow pattern shown in Figure 5.7 obtained at higher gas flow rates represents the transition to churn flow. An increase in the small gas bubble coalescence in the liquid slug as a consequence of an increase in gas flow rate may result in an oscillation of the liquid slug, which may eventually lead to a collapse of the liquid.



Unstable slug flow
(showing a transition
to churn flow)

Figure 5.7: Video image of unstable slug flow at liquid and gas superficial velocities of 0.14 and 0.95 ms^{-1} , respectively

Churn flow: as the gas flow rate increases further as shown in Figure 5.8, the unstable slug flow regime ceases to exist as a result of a breakdown of all of the liquid slugs. The broken down slugs are now distributed in the form of waves on an annular film.



Churn flow

Figure 5.8: Video image of churn flow for a riser at liquid and gas superficial velocities of 0.14 and 2.36 ms^{-1} , respectively

5.4.2 Flow regimes in bend (vertical 90° bend):

The two dominant factors governing the flow structure of a two-phase flow mixture as they travel around 90° bends, were the flow patterns as the mixture enters the bends, come under the combined influence of changing gravitational and centrifugal forces.

When the flow pattern of the mixture entering the bend is a spherical cap bubble with the size of the bubbles almost occupying the entire cross-section of the pipe, on entering the bend the bubbles migrate to and follow the outside path of the bend whilst the liquid moves to the inside path of the bend as observed in Figures 5.9a to 5.9c. Consequently, bigger bubbles are created due to higher levels of mixing. Some of the created bubbles are as a result of the immediate collapse of bubbles that have low surface tension forces.

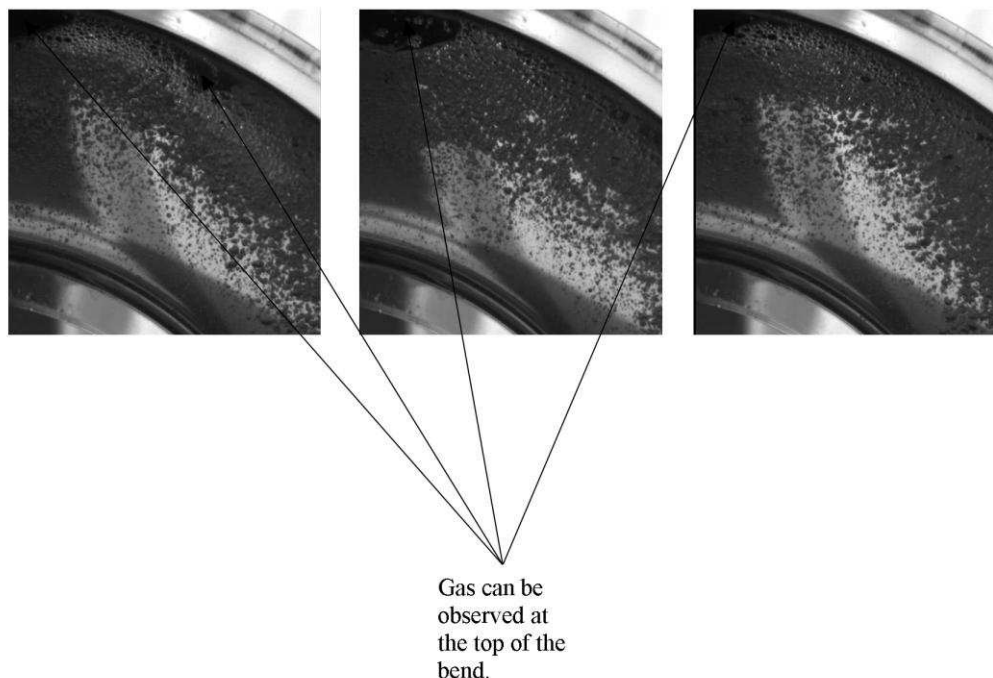


Figure 5.9: Video image of spherical cap bubble flow passing through a vertical 90° bend at liquid and gas superficial velocities of 0.14 and 0.05 ms⁻¹, respectively

Slug and unstable flows: here the gravitational force dominates and the liquid moves to the inside of the bend whilst the Taylor bubbles migrate to the outside of the bend as observed in Figure 5.10a. As the Taylor bubble and the liquid slug move along the bend, the liquid film in the annulus and the liquid in the liquid slug start to drain out and fall to the bottom of the bend. The falling liquid at the bottom of the bend that possesses a high momentum move in a forward direction, whilst the fluid with less momentum moves backward counter to the normal direction of the gas flow due to the shape of the curvature of the bend. The collapsed slug flow regime may create an internal pipe surface dry patch. This region illustrated on Figure 5.10b may be wetted periodically. According to Oshinowo and Charles (1974) unless there is a quick replenishment of the liquid plug as shown in Figures 5.10c and 5.10d, the bend is liable to dry out, especially at the upper wall surface.

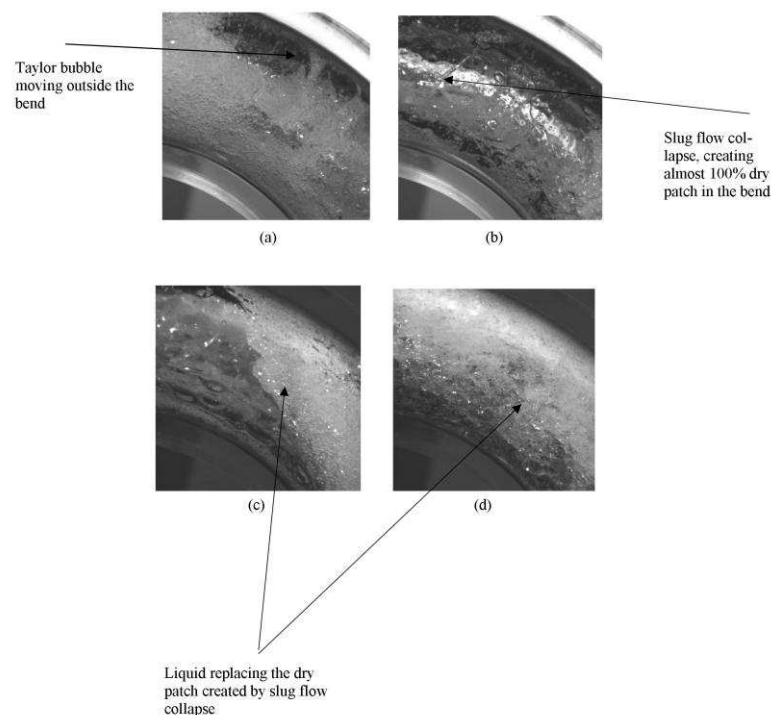


Figure 5.10: Video image of stable slug flow passing through a vertical 90° bend at liquid and gas superficial velocities of 0.14 and 0.54 ms⁻¹, respectively

Churn flow: A different mechanism could be taking place during both the slug and churn flows. The centrifugal force dominates in this case, and the gas moves to the inside of the bend. Because of the high shearing action of the gas on the gas-liquid interface, it will transfer some of the liquid downwards and deposits this at the bottom of the bend and create some droplet entrainment in the main gas core. As a consequence of this liquid will exist at both the top and bottom of the bend as observed in Figure 5.11. However, some of the liquid at the top of the bend may be observed to drain down to the bottom of the bend. However, there is no dry patch observed for this flow regime.

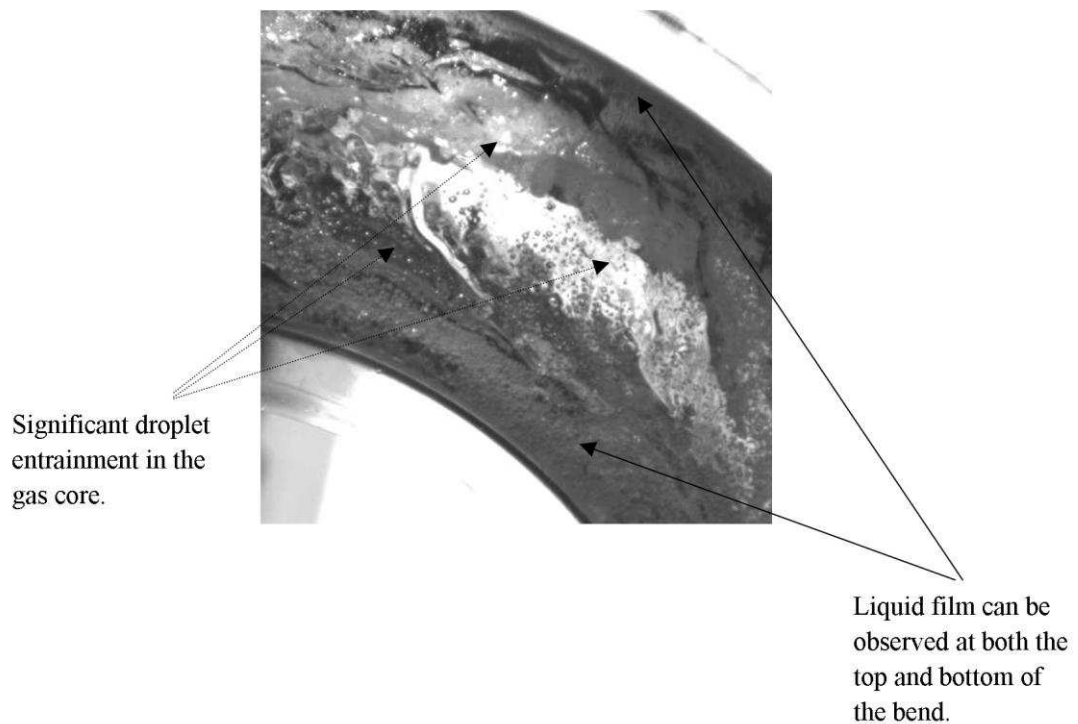


Figure 5.11: Video image of churn flow passing through a vertical 90° bend at liquid and gas superficial velocities of 0.14 and 2.36 ms⁻¹, respectively

Flow patterns just downstream of the bend can also be observed in the output of the WMS as illustrated in Figure 5.12

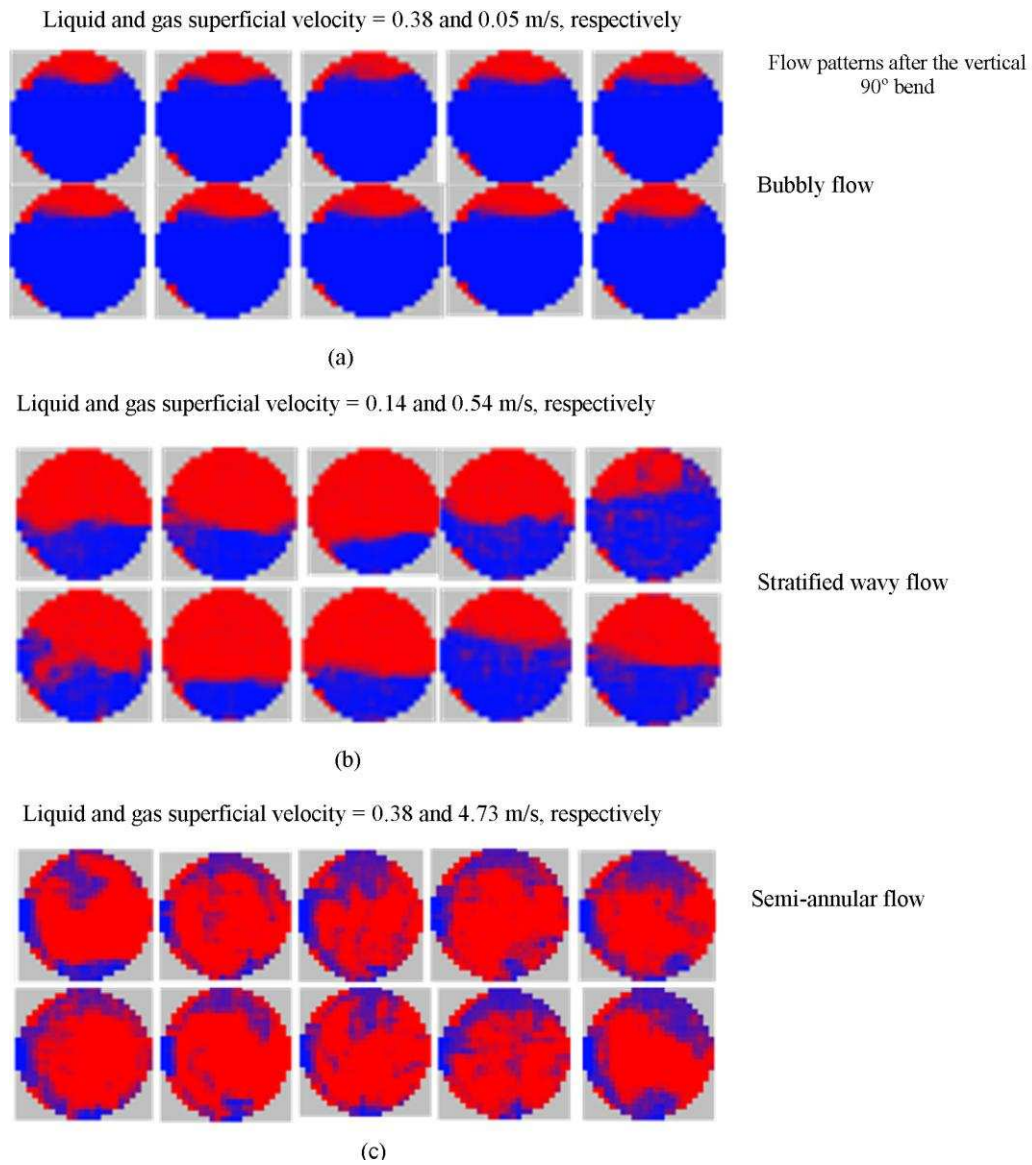


Figure 5.12: Sequence of frames at 1 ms intervals showing the location of the gas, top and bottom of the pipe.

5.4.3 Flow patterns in the upstream flowline (horizontal 90° bend):

For the horizontal test pipe flow line configuration, a different flow regime classification has to be established; since gravity introduces an asymmetry to the resultant flows: whereby the density difference between the two phases will cause the liquid to travel preferentially along the bottom of the pipe. These flow patterns are described below in order of increasing gas flow rate.

Plug flow: the effect of gravity cause the gas plugs to move along the top of the pipe. The level of liquid in the pipe is usually higher than half the diameter of the pipe.

Slug flow: this regime is characterized by the intermittent appearance of slugs of liquid which bridge the entire pipe section and move at almost the same velocity as the gas. It is typified by the occurrence of significant pressure fluctuations. The length of the large bubble decreases with increasing gas flow rate for a given constant liquid flow rate.

Stratified wavy flow: at higher gas velocities within this flow pattern, the shearing action of the gas at the interface generates large amplitude waves on the liquid surface. Liquid is torn from the surface of these waves giving rise to liquid droplets entrained in the gas region. These drops may partially deposit at the top of the pipe.

5.4.4 Flow patterns in the bend (horizontal 90° bend):

Plug flow: the gas bubbles initially migrate towards the inner radius of the bend under the influence of centrifugal force, but subsequently are forced outwards due to the increasing effect of gravity.

Slug flow: at higher gas flow rate, the centrifugal force moves the liquid to the outside of the bend whilst moving the gas to the inside of the bend. The gravity force then takes the liquid to the inside of the bend and the gas to the outside of the bend. Only a little amount of liquid film drains downward to the bottom of the bend. This behaviour is contrary to that observed for the slug flow in the vertical 90° bend.

Stratified wavy flow: the level of liquid in the pipe drops to less than half the diameter of the pipe with an increase in gas flow rate leading to collapse of bigger bubbles existing in the bend.

5.5 Cross-sectionally averaged void fraction:

A mean void fraction across a pipe section was determined by averaging the cross-sectional void fraction data over an interval of 60 seconds at a data acquisition frequency of 1,000 Hz. This parameter is a good indicator for the general picture of phase distribution. The change of flow patterns may be qualitatively revealed by evaluating the variation in the parameters.

A. The effect of gas superficial velocity:

The effect of the gas superficial velocity on the mean void fraction for the riser and the flowline, before the vertical and horizontal 90° bends, respectively is presented in Figure 5.13. The mean void fraction increases monotonically with the gas superficial velocity. However, the increase at the lower gas superficial velocity is much sharper than that at the higher gas superficial velocity. For a liquid superficial velocity of 0.05 ms⁻¹, the increase of the mean void fraction with gas superficial velocity for the horizontal flowline is substantially higher than experienced for the vertical riser. At this flow condition, the flow patterns observed for the horizontal flowline are different for the riser as highlighted in earlier sections.

However, for liquid superficial velocities of between 0.14 – 0.38 ms⁻¹, there is little difference in the mean void fraction for both the vertical riser and horizontal flowlines at the lower and higher gas superficial velocities. This is not surprising because under these conditions the riser and flowline have more or less similar

flow patterns as discussed in previous sections. In the intermediate gas flow rates (gas superficial velocity = $1\sim 3\text{ ms}^{-1}$) slight differences are observed due to the development of the different flow patterns in the two rig configurations.

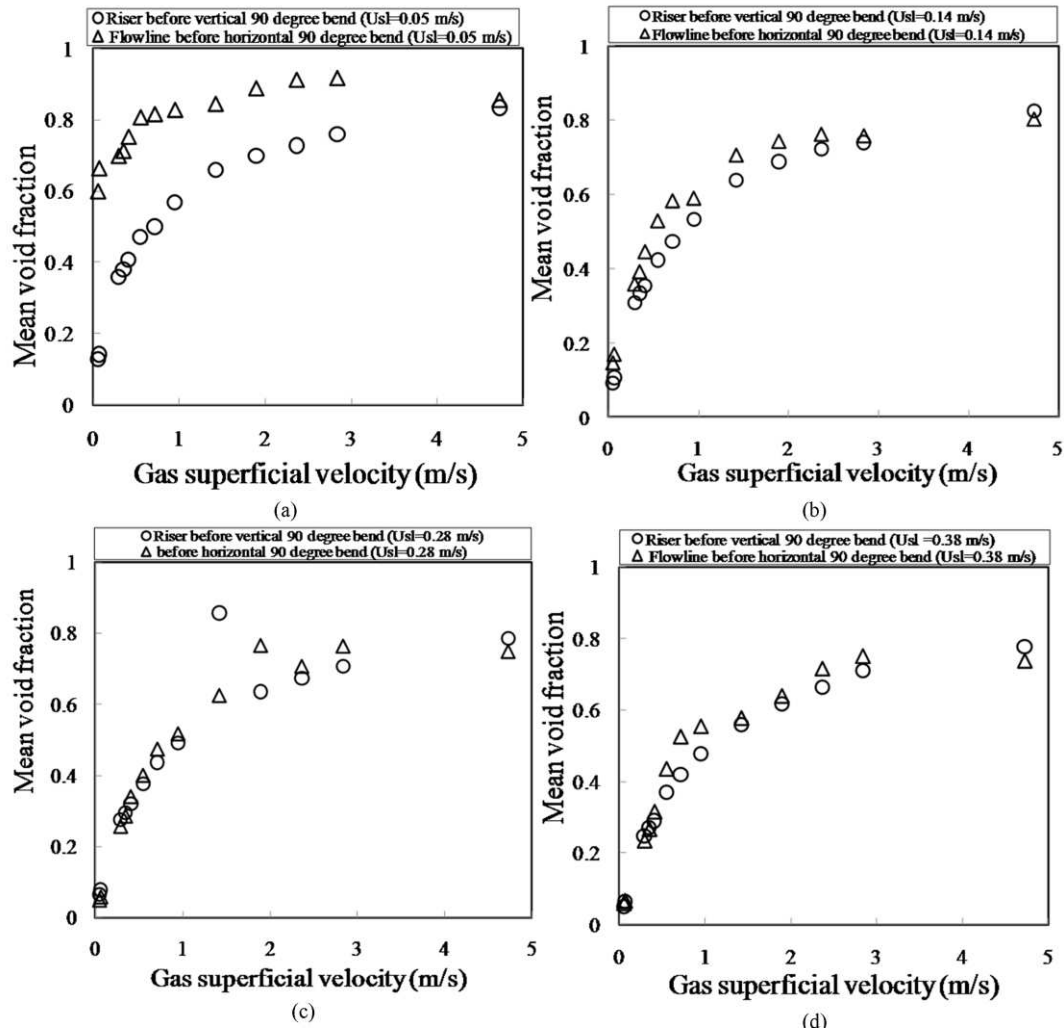


Figure 5.13: Influence of gas superficial velocity on mean void fraction before the vertical and horizontal 90° bends at liquid superficial velocity of (a) 0.05 (b) 0.14 (c) 0.28 and (d) 0.38 ms^{-1}

However, this is not the case for the bend. The mean void fraction after the bend for the vertical and horizontal 90° bends configurations are shown in Figure 5.14. Clearly the flowline, after the vertical 90° bend arrangement has considerably higher mean void fractions than those of the horizontal configuration, after the

horizontal 90° bend over the range of liquid flow rates. The liquid flow rates are over the range of 0.14 – 0.38 ms⁻¹. The dominant flow pattern after the horizontal 90° bend is the stratified wavy flow regime, whilst the slug, stratified and semi-annular flow are observed after the vertical 90° bend. The different flow patterns are represented by the different mean void fractions.

However, for a liquid superficial velocity of 0.05 ms⁻¹, there is little difference in the mean void fraction for both the riser and the horizontal flow line and different gas superficial velocities. This is not surprising as under these conditions the vertical riser and horizontal flowline have more or less similar flow patterns as discussed in the previous sections.

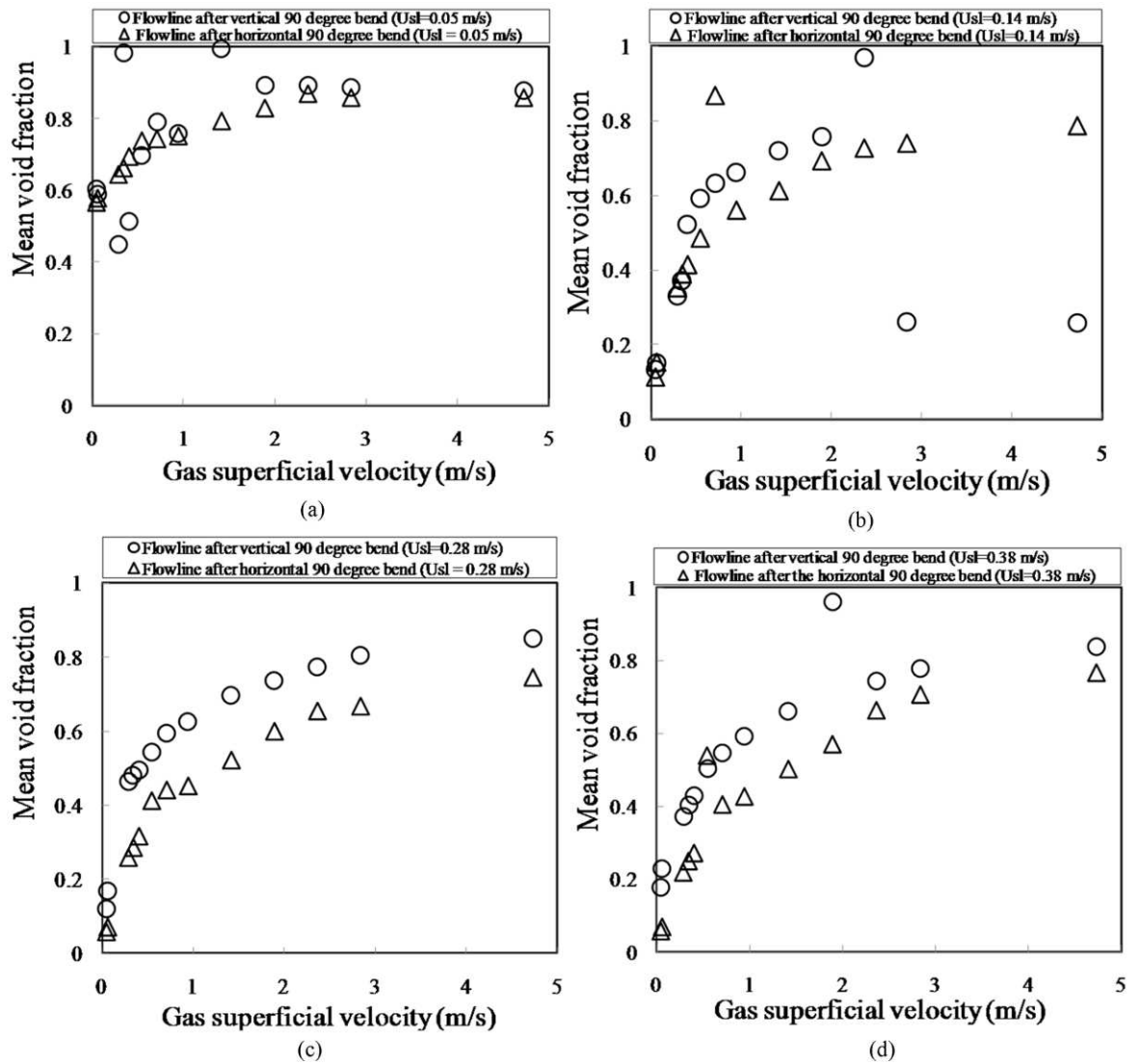


Figure 5.14: Influence of gas superficial velocity on mean void fraction after the vertical and horizontal 90° bends at liquid superficial velocity of (a) 0.05 (b) 0.14 (c) 0.28 and (d) 0.38 ms⁻¹

B. The effect of liquid superficial velocity:

Figure 5.15 presents a plot of the experimental data that shows the effect of liquid superficial velocity on the mean void fraction in the vertical riser and horizontal flowline, before the vertical and horizontal 90° bends. Generally, the mean void fractions in both the vertical riser and the horizontal flowline decrease with an increase in liquid superficial velocity except at the higher gas superficial velocity

(2.36 and 4.73 ms^{-1}) in the flowline where the mean void fraction slightly increases. The mean void fractions before the horizontal 90° bend at the lower liquid superficial velocity drop more significantly than those before the vertical 90° bend and then they become closer at the higher liquid superficial velocity. This is probably because in the examined range of gas superficial velocity, the influence of the liquid superficial velocity on the flow patterns is limited.

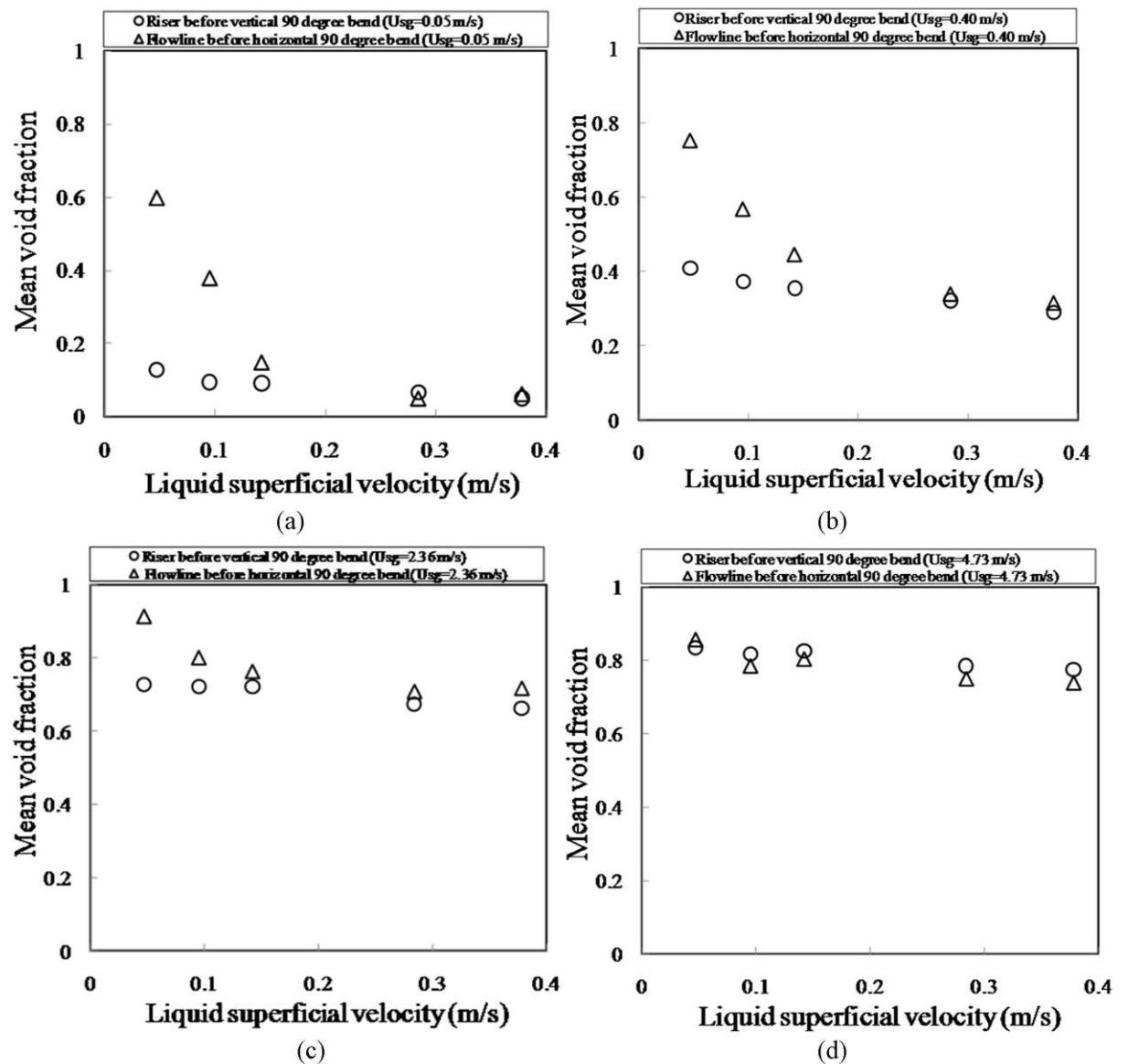


Figure 5.15: Influence of liquid superficial velocity on mean void fraction before the vertical and horizontal 90° bends at gas superficial velocity of (a) 0.05 (b) 0.4 (c) 2.36 and (d) 4.73 ms^{-1}

The effect of liquid superficial velocity on the mean void fractions after the vertical 90° bend is different from that after the horizontal 90° bend as shown in Figure 5.16. The dependence of the mean void fractions after the vertical 90° bend on liquid superficial velocity is strongly influenced by gas superficial velocity. At low gas superficial velocity (0.05 ms⁻¹), the mean void fraction decreases, changes a little and then increases with an increase in liquid superficial velocity. The opposite trend is shown for a gas superficial velocity of 0.40 ms⁻¹, the mean void fraction increases, changes a little and then decreases with an increase in liquid superficial velocity from the examined liquid superficial velocity range. The trend for gas superficial velocity at 2.36 ms⁻¹ was similar to that for 0.40 ms⁻¹, but the mean void fraction decreases more sharply with an increase of liquid superficial velocity at the intermediate liquid superficial velocity. At a gas superficial velocity of 4.73 ms⁻¹, the decrease in mean void fraction with an increase in liquid superficial velocity is almost linear. A generally monotonic decrease was observed for the mean void fraction after the horizontal 90° bend with an increase in the gas superficial velocity. These differences may be attributed to the change of flow patterns that result as a consequence of different gas and liquid superficial velocities but more detailed analysis is needed to draw a more general conclusion.

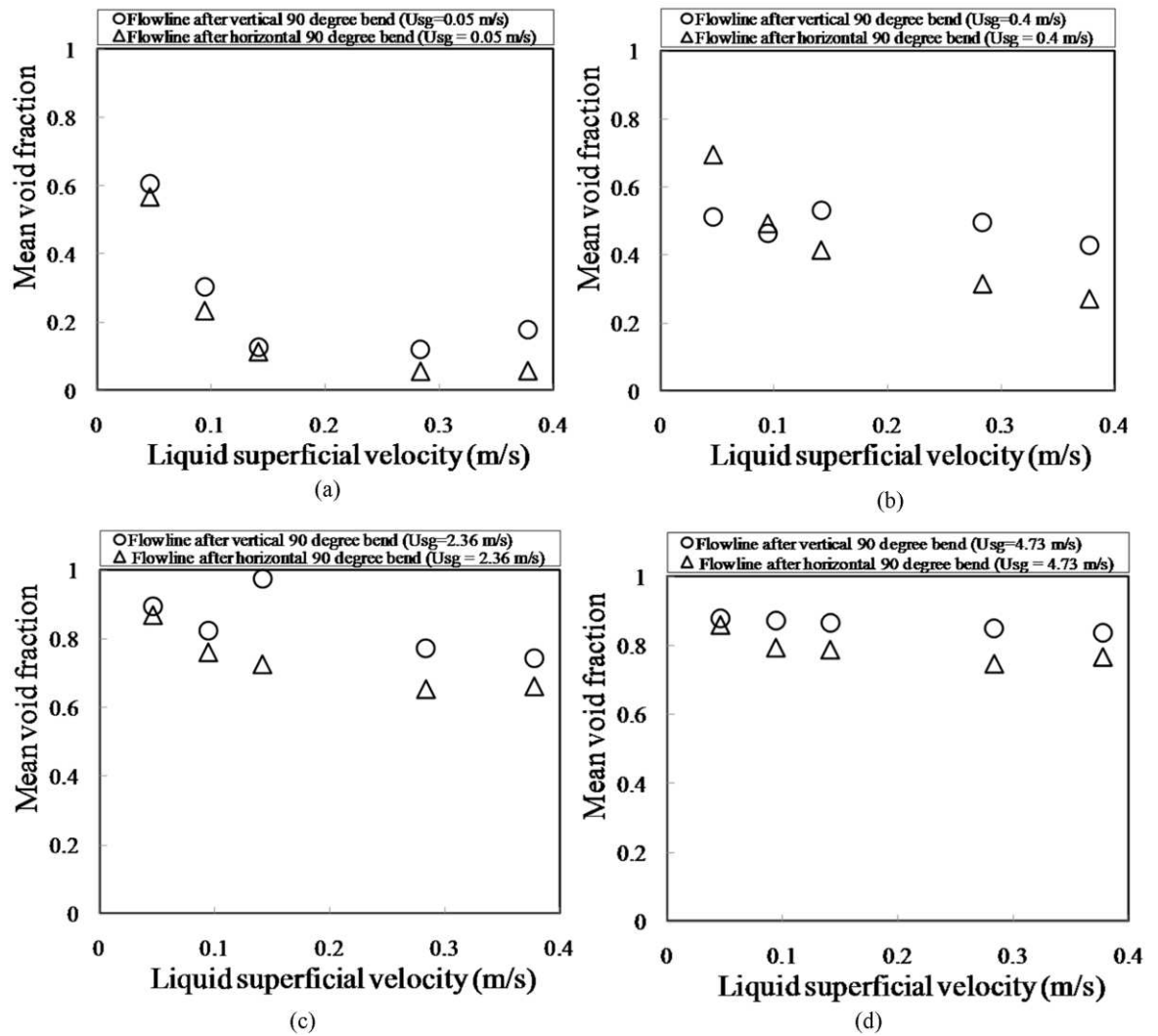


Figure 5.16: Influence of liquid superficial velocity on mean void fraction after the vertical and horizontal 90° bends at gas superficial velocity of (a) 0.05 (b) 0.4 (c) 2.36 and (d) 4.73 ms^{-1}

5.6 Competition between centrifugal and gravitational forces:

Gardner and Neller (1969) proposed a criterion based on a modified Froude number, Fr , (equation (2.23)) to determine stratification effects experienced after a bend. According to their proposed criterion, when Fr is greater than unity, the air will hug the inside of the bend whilst for Fr less than unity, the air will move to the outside of the bend. The validity of this criterion will be discussed here.

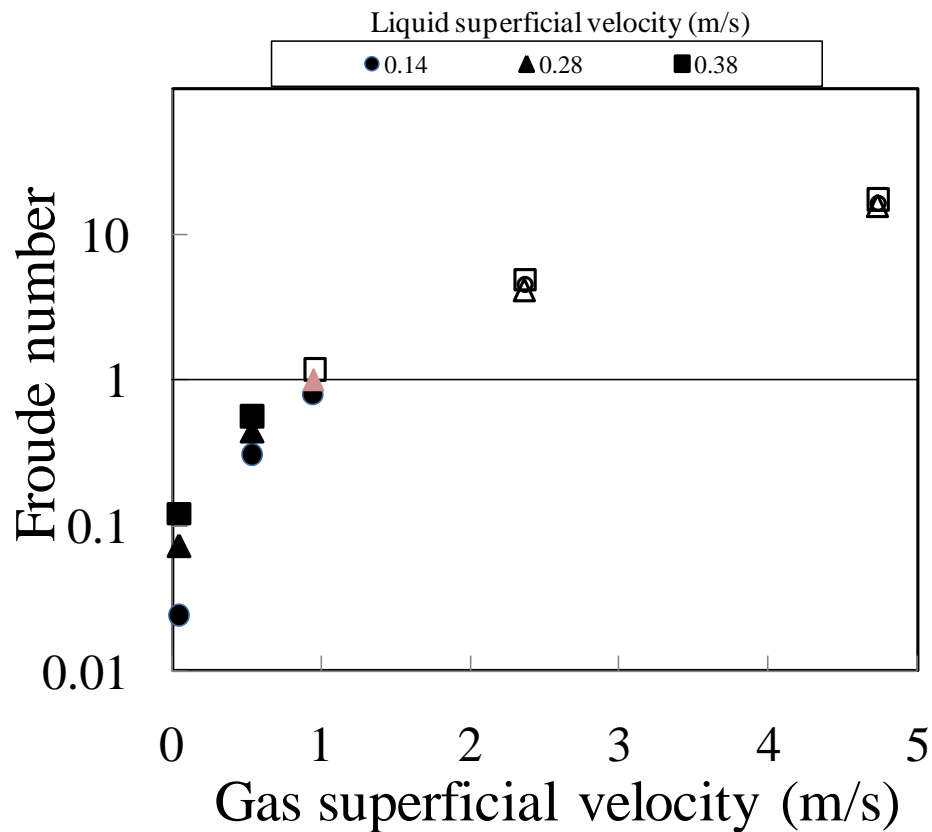


Figure 5.17: Influence of gas superficial velocity on the modified Froude number with liquid superficial velocity as the constant known parameter. Closed symbols-liquid on inside of the bend; open symbols-liquid on outside of bends; grey symbols transition case liquid goes to inside and/or outside of bend.

The conditions that govern whether the liquid goes to the outside or inside of the bend are identified in Figure 5.17 as the Froude number plotted against gas superficial velocity with liquid superficial velocity as the constant known parameter. There was one combination of flow rate where it was not clear whether it was liquid or gas which was on the outside of the bend. For flow rates which give a low Froude number, the flow patterns in the vertical pipe approaching the bend are spherical cap bubble, slug and unstable slug flow. The gas superficial velocity is slightly greater than that for the liquid. As the liquid density is much greater than that for the gas and since $gR\sin\theta > U_m^2$, gravity dominates and we would expect the liquid to move to the inside of the bend, as in

fact observed in Figures 5.9, 5.10 and 5.12(a – b). In contrast, for churn flow, the gas superficial velocity is much greater than that for the liquid. Again the liquid density is much greater than that for the gas, the modified Froude number is greater than 1 and we would expect the liquid to move to the outside of the bend, as in fact observed in Figures 5.11 and 5.12 c. The situation is further complicated by the fact that the centrifugal force acting on the fluid depends not only on the fluid velocity but also on the fluid density.

5.7 Summary

As shown above the effect of 90° bends on air-silicone oil flows has been successfully interrogated using the ECT and WMS measurement transducers. The characteristic signatures of the Probability Density Function derived from the time series of cross-sectionally averaged void fraction data were used to identify the flow patterns. Flow patterns for the vertical and horizontal 90° bends are shown on the diagram of the gas superficial velocity versus liquid superficial velocity. The results were validated by a comparative analysis with simultaneously recorded high speed video image stills taken of the flow around the bend. In this section a summary of the key findings is presented:

- The ECT and WMS measurement techniques produced same flow pattern signatures.
- An increase in the gas superficial velocity from 0.05 to 4.73 ms⁻¹ resulted in spherical cap bubble, slug, unstable slug and churn flows being observed in the vertical riser whilst in the horizontal flowline: plug, slug, stratified wavy and annular flows were formed. Buoyancy force plays an important role in the formation of the different flow patterns.

- Bends have significant effect depending on the gas superficial velocity on the gas-liquid flow regimes. In both the vertical riser and horizontal 90° bends the gravitational force tends to move the liquid to the inside of the bend whilst the gas migrates to the outside of the bend. Some big spherical cap bubbles and Taylor bubbles break up in the bends due to the any imbalance in the centrifugal and the surface tension forces. The bubbles become more uniform. Dry patches in the bend were observed in the slug and unstable slug flows. As a result, after the vertical bend the spherical cap bubble flow became bubbly flow, stable and unstable slug to stratified wavy flows and the churn flow turn to stratified wavy and semi-annular flows. The horizontal bend has less effect on the flow patterns compared with the vertical bend.
- At low liquid and high gas superficial velocities, both the vertical and horizontal 90° bends have the same effect on the two-phase air-silicone oil flow, the flow pattern downstream of the bend is annular.
- No slug flow was observed at low liquid flow rate both for the upstream and downstream sections of the horizontal 90° bend.
- In general, the mean void fraction was found to monotonically increase with gas superficial velocity both before and after the bend. Little difference in the mean void fractions for the vertical riser and horizontal flowline before the bend were detected, whilst the mean void fractions after the vertical bend were significantly higher than those after the horizontal bend. The effect of the liquid superficial velocity on the mean void fraction

is more complicated. More work is required before any concrete conclusion can be drawn on the flow regimes created by this rig configuration.

- The validity of the criterion proposed by Gardner and Neller (1969) which is based on a modified form of Froude number ($Fr_e = U_m^2 / Rg \sin \theta = 1$) has been confirmed by the results of the current experimental studies for a liquid of a different surface tension and viscosity different to those used by Gardner and Neller.

Chapter 6

Experimental design

This chapter presents a description of the construction of the experimental rig used to study air-water flow behaviour in a 127 mm pipe connected to a vertical 180° return bend. The purpose of these studies was to provide new experimental data for film fraction and liquid film thickness around the bend. The experiments were carried out on a large scale closed loop facility, available within the L3 laboratories of the Department of Chemical and Environmental Engineering at the University of Nottingham. A series of experiments were carried out in this study to measure the film fraction and liquid film thickness simultaneously around the bend using different measurement techniques. The results of these experiments are presented and discussed in Chapter 7. In all of these experiments, air and mains tap water at a temperature of 25°C were used as the test fluids. The liquid and gas superficial velocities employed were in the ranges from 0.02 to 0.2 ms⁻¹ and 3.5 to 16.1 ms⁻¹, respectively. The experiments were carried out at a pressure of 2 barg. The flow patterns recorded for this range of input flow conditions were churn and annular flows. From an analysis of the data presented in Figure 6.1, the transition lines were determined using the mechanistic models suggested by Shoham (2005) and the slug/churn transition of Jayanti and Hewitt (1992). From an analysis of the observations it is concluded that for the churn/annular flow transition, the Shoham transition line is less reliable and in fact under predicts the conditions examined. On the other hand, the Jayanti and Hewitt transition line

performs better, but under predicts the transition from slug/churn flow at higher liquid and lowest gas superficial velocities.

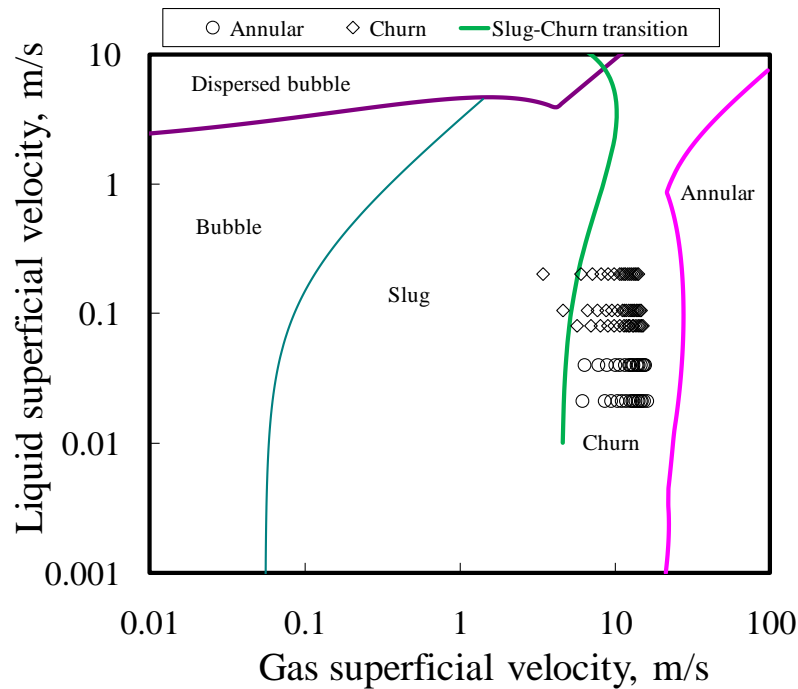


Figure 6.1: Flow pattern map for the range of flow rates in the present study

An overview of the experimental facility and the choice of the working fluids are presented in Sections 6.1 and 6.2, respectively. Sections 6.3 and 6.4 briefly describe the film fraction and liquid film thickness instrumentation and their calibration, respectively. Section 6.5 describes the acquisition software used and finally, Section 6.6 summarises an analysis of the hazards and safety features of the experimental rig.

6.1 Overview of the experimental facility:

The facility used in the present study has been previously used by in the reported and published studies of Omebere-Iyari (2006), Van der Meulen et al. (2009) and Zangana (2011). A summary of this previous work is shown schematically in

Figure 6.2. The rig is located within the L3 Engineering Laboratories of the Department of Chemical and Environmental Engineering at the University of Nottingham. The key components of the facility are shown in Figure 6.3. The test flow channel, constructed from PVC plastic pipes of a 127 mm internal diameter, comprises a riser, a 180° return bend and a downcomer. The bend has a radius of curvature of 381 mm ($R/D = 3$), and the riser and downcomer lengths are 11 and 9.6 m, respectively. The 180° return bend was made by bolting together two slabs of transparent acrylic resin (Perspex) in the surface of each circular groove with an accurate semi-circular cross-section had been machined. The bend is of a modular construction and a probe can be inserted at radial positions of 45°, 90° or 135° around the bend as shown in Figure 6.3c. Care was taken to ensure that there are no discontinuities in diameter at each joint. The probe consists of a pair of metal rings separated by an acrylic resin ring.

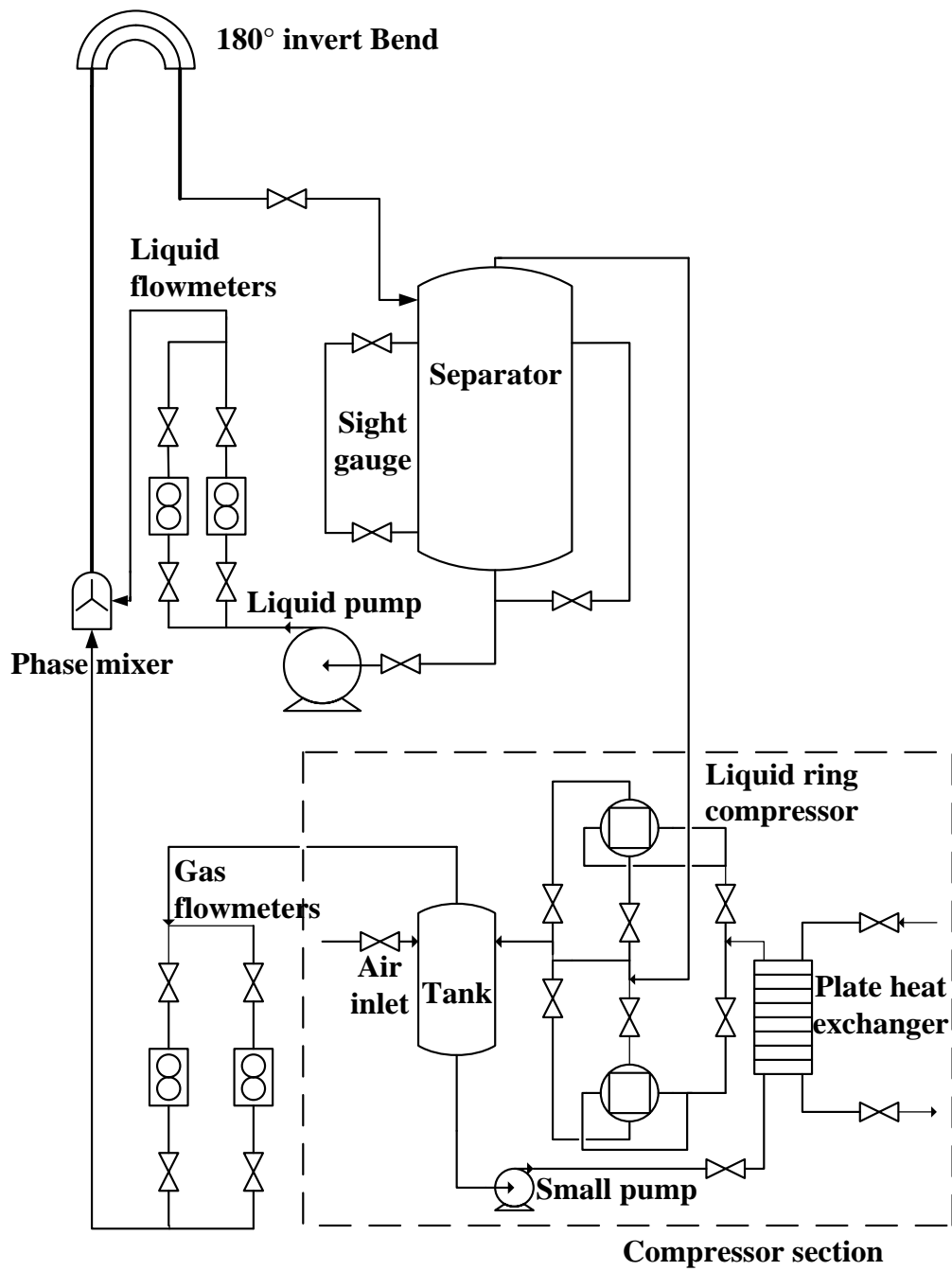


Figure 6.2: Schematic diagram of the experimental facility

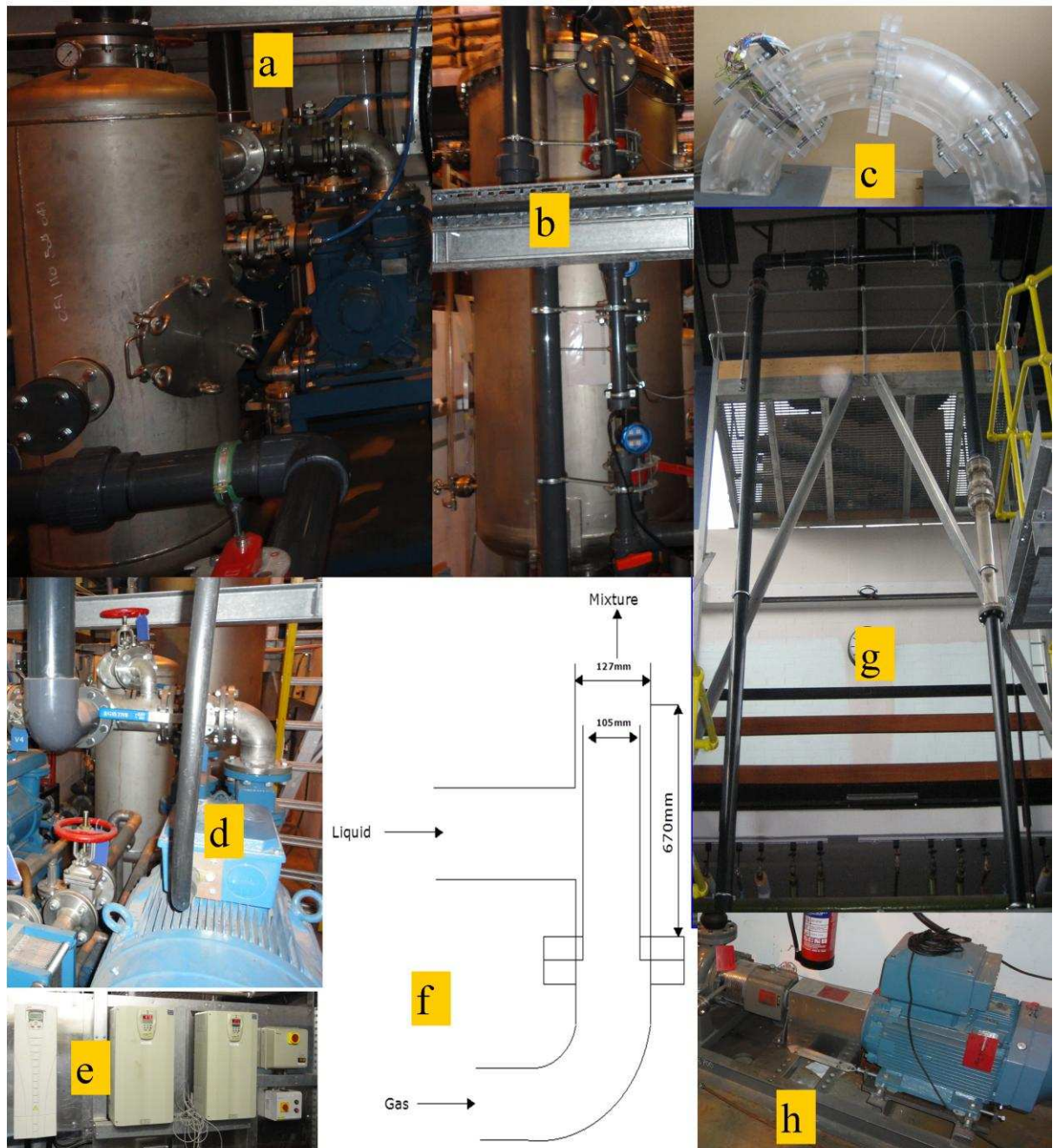


Figure 6.3: The major constituent components of the rig (a) the pressure tank (b) the separator/liquid tank (c) 180° return bend (d) the compressor motor (e) the calibrated vortex and turbine meters (f) the diagram of the air-water mixing section (g) the riser section and, (h) the liquid centrifugal pump

The water is stored in a tank (the bottom part of the separator). The liquid phase was delivered to the mixer injection by the centrifugal pump (ABB IEC 60034-1) at a volumetric flow rate of about $68 \text{ m}^3\text{hr}^{-1}$. The separator is a cylindrical stainless steel vessel of 1m in diameter and 4m high with a capacity of 4,000

litres. In this work, the vessel was filled to a volume 1,600 litres. The liquid collected at the bottom of the separator is recycled to the test section. Air was used as the gas phase. The valve located on the gas return line exiting the separator is used to control the air supply to the compressor section. The gas flow rate can be regulated by varying the speed of the motors (up to 1500 rpm) together with the valves just below the gas flow meters that are used to regulate the pressure in the pipe flow test section.

6.1.1 The Experimental procedure:

Before the start of the experiments, the flow loop was pressurised to 2 barg using compressed main air. Two liquid ring pumps with 55 kW motors were employed to compress and deliver the air to the mixer. In the mixer, the supplied air combines with the water drawn from the two phase separator/supply tank by means of the centrifugal pump. The mixing device (Figure 6.3f) consisted of a 105 mm diameter tube placed at the centre of the 127 mm internal diameter test section, termed an annular injection method. Water enters the main pipe from the periphery to form a uniform film on the pipe wall whilst the air passes along the central pipe. The gas was introduced first to avoid the flooding of the air line with water. The flow rates of the air and water were measured using calibrated vortex and turbine meters, respectively. The temperature and pressure of the system were taken close to the liquid and gas flow meters and at the base of the riser. This allowed the inlet flow rates to the test section for both phases to be determined accurately. The maximum uncertainties in the liquid and gas flow rates according to Omebere-Iyari (2006) are 0.5 and 2.9 %, respectively.

Downstream of the mixer, the two-phase mixture travels for 11m along a 127 mm internal diameter vertical pipe in which annular or churn flow is established. Small inaccuracies in the alignment of a vertical pipe can cause significant asymmetry in the velocity and liquid distribution profiles of multiphase flows Gill et al. (1963). Consequently, great care was taken to ensure that this tube was true vertical. Indeed, the maximum measured lateral deviation was recorded as little as 1.5 mm over the mm. Along the length of the riser, the time varying cross-sectional film fractions are measured using three identical conductance ring probes (Figure 6.4) placed at distances of 8.1, 8.4 and 8.5 m above the mixer/injection section. These locations correspond to, 64.0, 65.0 and 66.6 pipe diameters above the mixer/injection section.

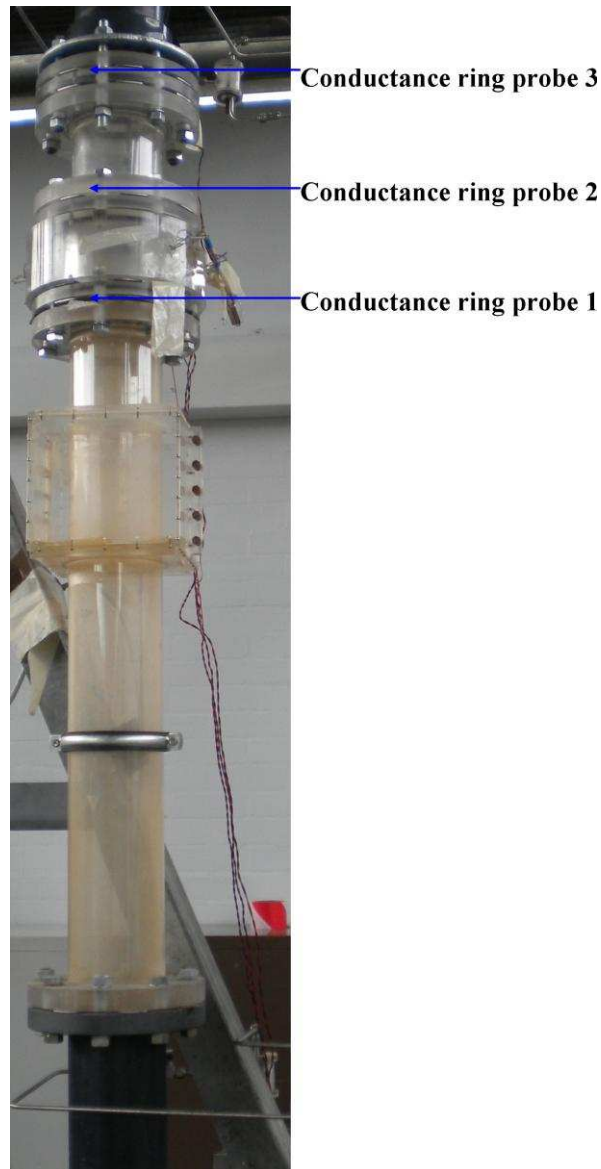


Figure 6.4: The locations of the measurement of film fraction on the transparent test section of the riser

The test bend, mounted on top of this section, is also of a 127 mm internal diameter. Provision was made for the measurement probe to be inserted at every 45° around the bend. Time varying cross-sectional film fraction and local liquid film thickness measurements were recorded simultaneously at the three measurement locations in the bend: 45° , 90° , and 135° , using a conductance pin and parallel wire probes. The conductance pin probes were used to measure very

thin films outside the bend whilst the parallel wire probes for thick film measurements inside the bend.

Beyond the bend, the air-water flow mixture travels a further 9.6 m vertically downwards and 1.5 m horizontally to the separator where the gas and the liquid are separated and directed back to the compressors and the pump respectively, to create a double closed loop. As the flow enters the downcomer through the bend, time varying cross-sectional film fractions data is measured using a conductance ring probe placed at 2667 mm (21 pipe diameters) downstream of bend.

6.2 The working fluids

The working fluids were selected as air and water for several reasons. Firstly, the materials were readily available, cheap and neither being toxic or flammable. Secondly, air-water has been used by many other previous research workers so that direct comparisons could be made with their work. Thirdly, in this investigation the measurement of the film fraction and liquid film thickness were a major objective, and established techniques exist for film fraction and liquid film thickness measurements for water.

The properties of the two fluids used in the experiments are shown in Table 6.1.

Table 6.1: Properties of the fluids at a pressure of 3 bar (absolute) and at the operating temperature of 20°C

Fluid	Density (kgm^{-3})	Viscosity ($\text{kgm}^{-1}\text{s}^{-1}$)	Surface tension (Nm^{-1})
Air	3.55	0.000018	
Water	998	0.00089	0.072

6.3 Experimental apparatus and calibration procedures:

The aim of this section is to present a description of the instrumentation used to study the air-water flow behaviour in a 127 mm pipe connected to a vertical 180° return bend. The instrumentation for film fraction measurement and its calibration procedure is given in Section 6.3.1. Section 6.3.2 briefly describes the types of instrumentation and their calibration for the liquid film thickness used in this study.

6.3.1 Film fraction measurement:

The film fraction of a gas-liquid flow is a fundamental quantity used to describe the flow pattern; it is the fraction of the pipe cross-sectional area occupied by the liquid phase. Its determination is of great importance in a variety of engineering applications. One of the most common techniques to study the form and the extension of the phase interface consists in measurement of the electrical impedance of the two-phase gas-liquid area close to a system of electrodes. In such a way, once the relationship between the electrical impedance of the medium and the phase distribution is obtained, the average cross-sectional film fraction can be inferred, dependent upon the extension of the measuring region, Conte (2000).

Many studies have been carried out on this subject: the main conclusion from these investigations is that the measured electrical impedance across an electrode pair immersed in a conducting liquid is essentially resistive when the frequency of the a.c. excitation signal is sufficiently high (for tap water, 10~100 kHz) Fossa (1998). For higher frequencies (above a megahertz) the behaviour of the electrolyte becomes essentially capacitive: for this reason impedance methods

are usually classified as either conductance or capacitive methods. With reference to the conductance method, Coney (1973) has reported the theoretical behaviour of flat electrodes wetted by a liquid layer, and Hewitt (1978) has presented a comprehensive critical review of the technique.

In the present work the conductance technique is applied to study the two-phase distribution using flush mounted ring probes. The non-intrusive nature of the ring probes is the main reason why this technique has been very attractive to researchers. In addition, its ability to detect a small impedance and low mechanical difficulty during the construction in comparison to any other type of probes, makes it a more practical and cost effective technique, Zangana (2011). Air-water mixtures were considered. An a.c. carrier voltage of 10 kHz frequency was applied across each pair of electrodes whilst an electronic device, especially designed for this purpose, converted the a.c. signal into a d.c. signal proportional to the impedance of the two-phase test section. The frequency was checked to give the resistive behaviour of the water by measuring both the amplitude and phase shift of the applied voltage signal. A detailed description of the design of the probe rings used in the present study has previously been given by Omebere-Iyari (2006). They were identical both in shape and size. Each probe consists of a pair of stainless steel electrodes of 3 mm thickness (s) and spacing (D_e) of 25 mm; this gives an electrode width to pipe diameter ratio (s/D) of 0.024 and the electrode spacing to pipe diameter ratio (D_e/D) of 0.2. The probes were insulated using non-conducting acrylic resin. The probes were flush mounted with the pipe wall and they were designed to have the exact diameter as the test section.

The parallel conductance ring probes employed in the present study were calibrated by Omebere-Iyari (2006) for both bubble and annular flow patterns.

The latter type of flow is simulated by placing a non-conducting cylindrical plastic rod with a known diameter inside the pipe and filling the annulus between the rod and pipe wall with a conducting liquid. By repeating this procedure with plastic rods of different diameters, void fraction/dimensionless conductance relationship were obtained, Zangana (2011). Following the same procedure the probes were re-calibrated by Van der Meulen et al. (2009). However, in the latter approach the effect of gas bubbles in the liquid film was taken into account. The gas bubbles in the liquid film were simulated by adding a known volume of spherical glass beads with different diameter ranging from 3 to 6 mm to the annulus between the non-conducting rod and the pipe wall. For further details on the role of the glass beads during the calibration see Van der Meulen et al. (2009). The calibration curve for annular type of flow based on the Van der Meulen et al. (2009) approach is shown in Figure 6.5. Emphasis was placed on to the repeatability of the measurements and calibration procedures.

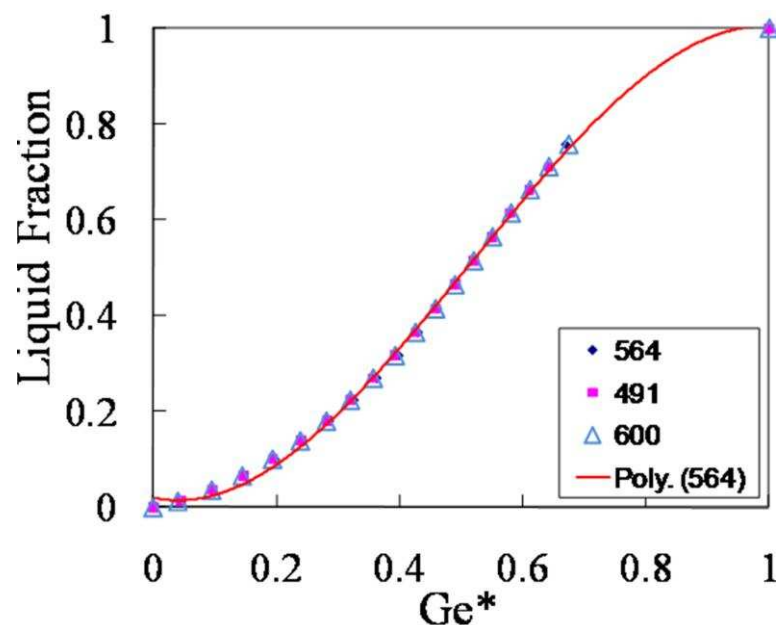


Figure 6.5: Calibration curve for the conductance ring probes for annular flow with respect to different liquid conductivities. Ge^* is the dimensionless conductance of the two-phase flow (after Van der Meulen et al. (2009))

6.3.2 Liquid film thickness measurement:

For gas-liquid annular flows in which the liquid is electrically conducting, the conductance measurements are the most widely used technique to measure the liquid film thickness. The technique is based upon measurements of the electrical conductance between two electrodes in contact with the liquid film. Different types of electrodes such as needle probes, parallel wire probes and flush mounted pin probes have been reported by researchers over the last decades, e.g., Koskie et al. (1989), Fossa (1998), Conte and Azzopardi (2003), Belt (2006) and Geraci et al. (2007).

The type of probe employed in this study was chosen on the basis of the range of their operability. The liquid film in annular flow was observed to be asymmetrical with a thick pool at the bottom and a thin liquid film at the top. Liquid film thickness measurements were carried out using a conductance technique, which employed either flush mounted or parallel wire probes. The first type was used for the almost entire section of the pipe. The second type, suitable for higher liquid film thickness, was used only for the bottom section of the bend.

(a) A parallel wire

Wire probes have been mainly used by Hanratty and his co-workers, Miya (1970), Miya et al. (1971) and Tatterson (1975). These probes according to Brown et al. (1978) give a linear response versus liquid film thickness and allow a more localised measurement to be carried out. Possible objections come from the perturbation which may be induced in the flowing film by the wires and from modifications to the shape of the liquid surface due to the wetting of the wires by liquid. However, in a static film the meniscus which can be observed around thin

platinum wires is very small if compared with the liquid film thickness to be measured. A more significant disturbance might occur when the probe has to work in a wavy film. When the liquid height decreases, a thin liquid layer sticks to the probe which may indicate a liquid level higher than the actual level, thus introducing a certain amount of lag in the dynamic response of the probe. This phenomenon has been experimentally investigated by Pearlman (1963) who reports these errors to be negligible and the response of the probe almost instantaneous. Finally Brown et al. (1978) advised that the disturbances in the flow caused by stationary wires can be minimised by the use of very thin wires.

The parallel wire-pair probes used to measure liquid film thickness at the bottom of the bend are the same type employed by Rea and Azzopardi (2001), Conte (2000), Conte and Azzopardi (2003) (Figure 6.6) and Geraci et al. (2007). The parallel wires shown in Figure 6.7 may also be referred to as a harp arrangement. In this methodology, five pairs of stainless steel wires are stretched along chords of the pipe cross-section and the resistance between pairs measured. According to Miya et al. (1971), Brown et al. (1978), Koskie et al. (1989) and Conte and Azzopardi (2003), the electrodes are two parallel thin wires stretched across a channel or along chords of the pipe or protrude from the wall supported only at one end. The spacing between the two wires of each pair is of 5 mm and the distance between pair is 25 mm, with the central pair placed symmetrically about a vertical diameter. Wires based on the recommendations of Pearlman (1963) have a diameter of 0.33 mm and are stretched across an acrylic resin ring 25 mm deep. To ensure proper tension of each wire, plastic screws are inserted in a threaded hole at each end to keep the wires taught. Particular care had to be taken

to avoid the wires snapping on the sides of the metallic screw when they were fitted. Because the flow patterns investigated in this study were either annular or churn, precaution had to be taken to eliminate the route for current at the top of the main pipe, across the thin film. For this reason, the top 15 mm of the wires were insulated with a synthetic waterproof coating to prevent errors being caused by the liquid film at the top of the bend. As the liquid height varies, the surface of active electrode increases and so the resistance decreases because of the larger area of passage for the electric current. The output depends on the geometrical dimensions and on the conductivity of the medium (liquid). The liquid height (liquid film thickness)/output relationship is obtained by calibration. The response of this system is fairly linear and may be successfully used for thick films. However, for thin films according Conte and Azzopardi (2003), it is a less reliable method because of its intrusive nature, i.e., the formation of a meniscus due to surface tension effects. Also, the local character of measurement depends on the distance between the wires.

The electronic circuit to apply voltage and filtering is the same as used by Rea and Azzopardi (2001), Conte (2000) and Conte and Azzopardi (2003). An a.c. carrier voltage of 10 kHz frequency was applied across each pair of electrodes. In this frequency range, measures are strictly reproducible and stable. For details of the electronic circuits and calibration procedure, the reader is referred to Rea and Azzopardi (2001). The calibration lines of the five pairs of parallel wires used in this study are shown in Figure 6.8. Figure 6.9 shows the calibration lines of probe C for different conductivities. The measurement accuracy of the wire probes according to Brown et al. (1978) is within 10 % error.

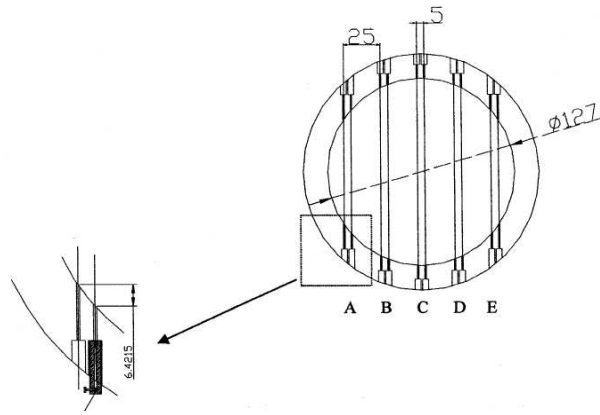


Figure 6.6: Sketch of the test section for liquid film thickness at the bottom of pipe. Adapted from Conte and Azzopardi (2003)

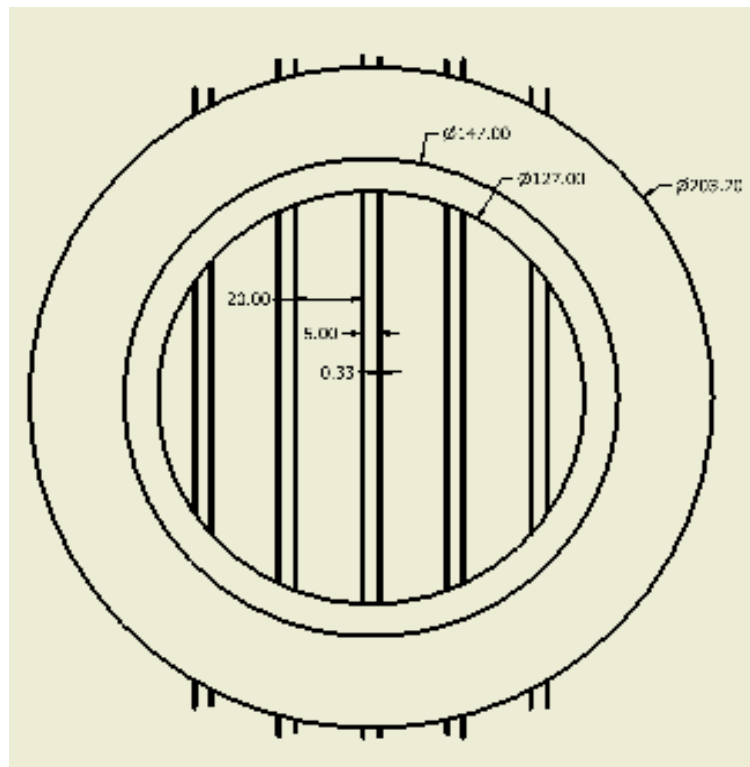


Figure 6.7: Sketch of the test section for liquid film thickness at the bottom of pipe. Present study

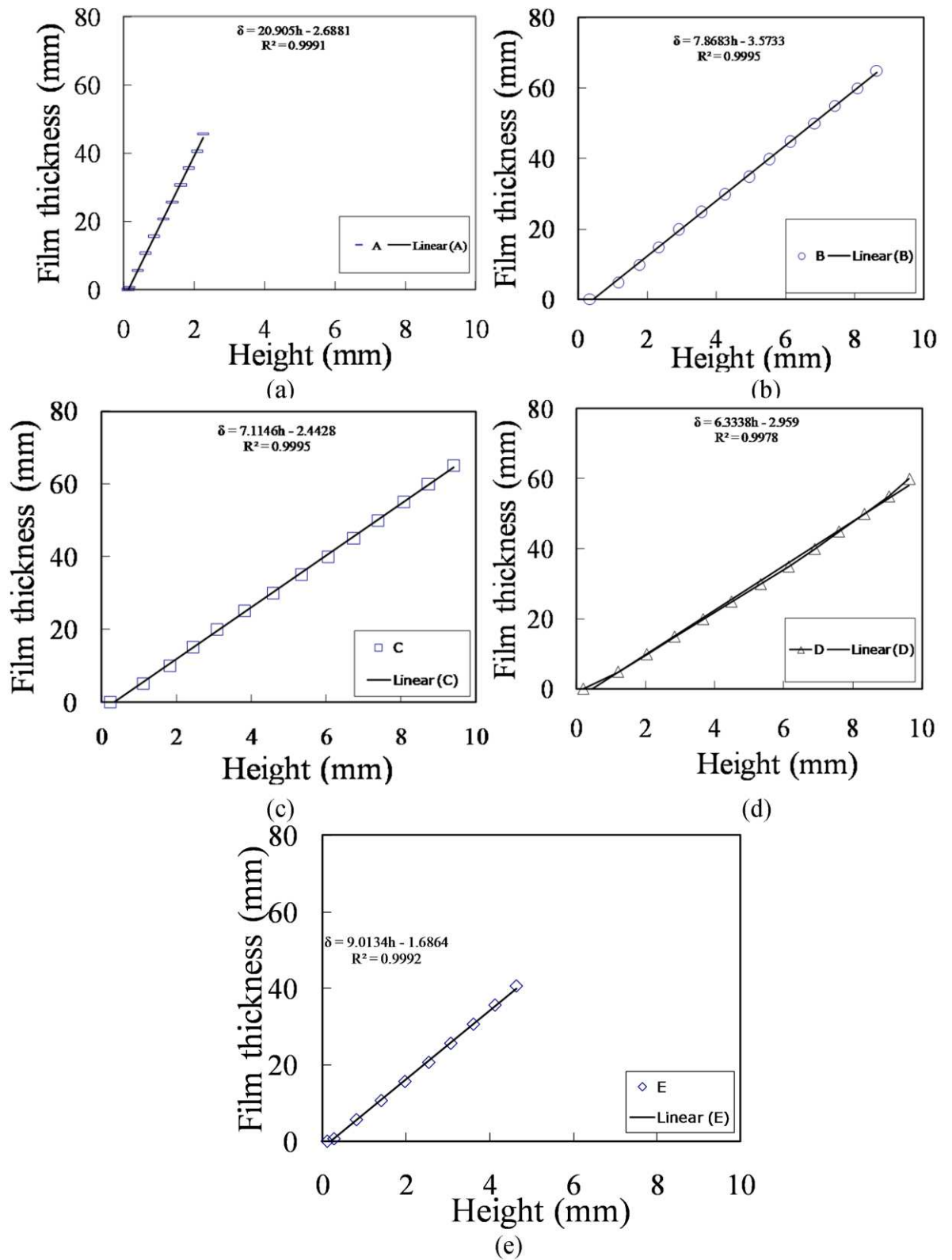


Figure 6.8: Calibration curves for the five parallel wire probes

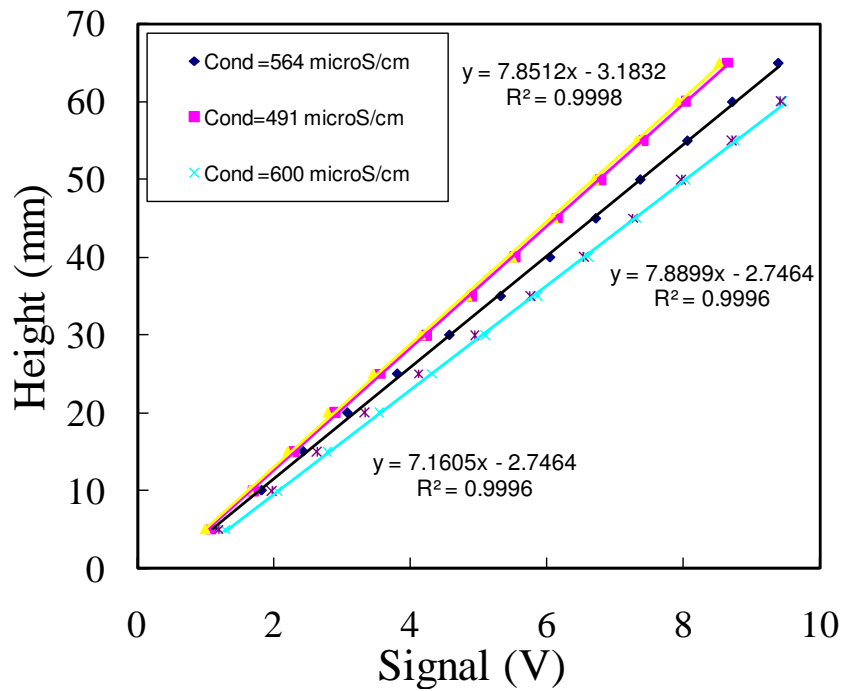


Figure 6.9: Calibration lines of probe C for different liquid conductivities

(b) Flush mounted pin probes

This method is used for very thin liquid films, typically up to 2.5 mm. In this case, each electrode is a pin mounted flush with the pipe surface and coupled to another electrode close to it as shown in Figures 6.10, 6.11 and 6.12. If care is taken in the mounting of probes, the method is virtually non-intrusive. The electric field is very weak away from the pipe surface and has a negligible contribution to the passage of current. The response is initially linear close to the pipe wall (typically up to 2 mm) and then asymptotically flattens to a uniform value. To enlarge the range of measurement, the diameter and separation of pins needs to be increased. However, the greater the spacing, the more averaged is the result over space. To obtain an optimum measurement of the liquid film thickness therefore, a balance must be struck between range of operability and local character of the measurement. The measured liquid film thickness is assumed to be the value at the mid-point between the centres of the electrodes.

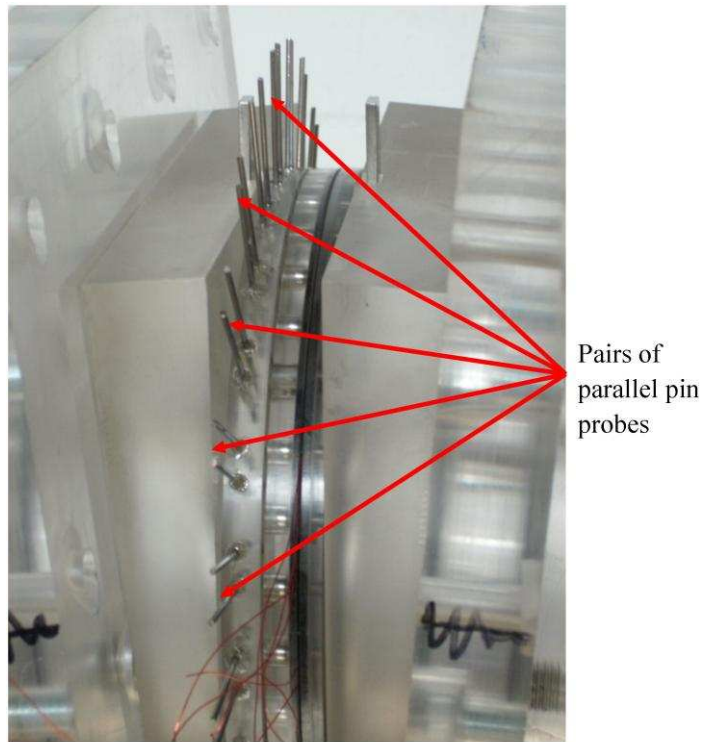


Figure 6.10: Picture of the flush mounted pin probes in modular sections

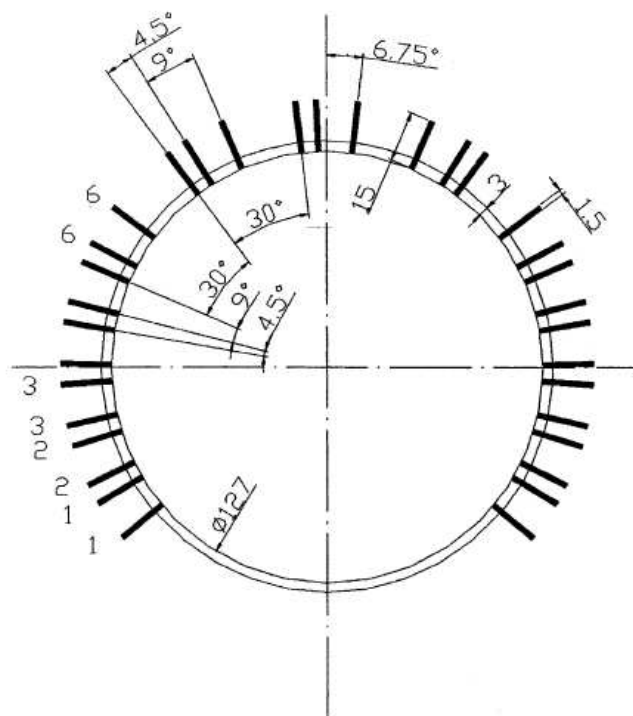


Figure 6.11: Cross-sectional view of the test section for liquid film thickness measurements at the top of the pipe. Dimensions are in mm. Adapted from Conte and Azzopardi (2003)

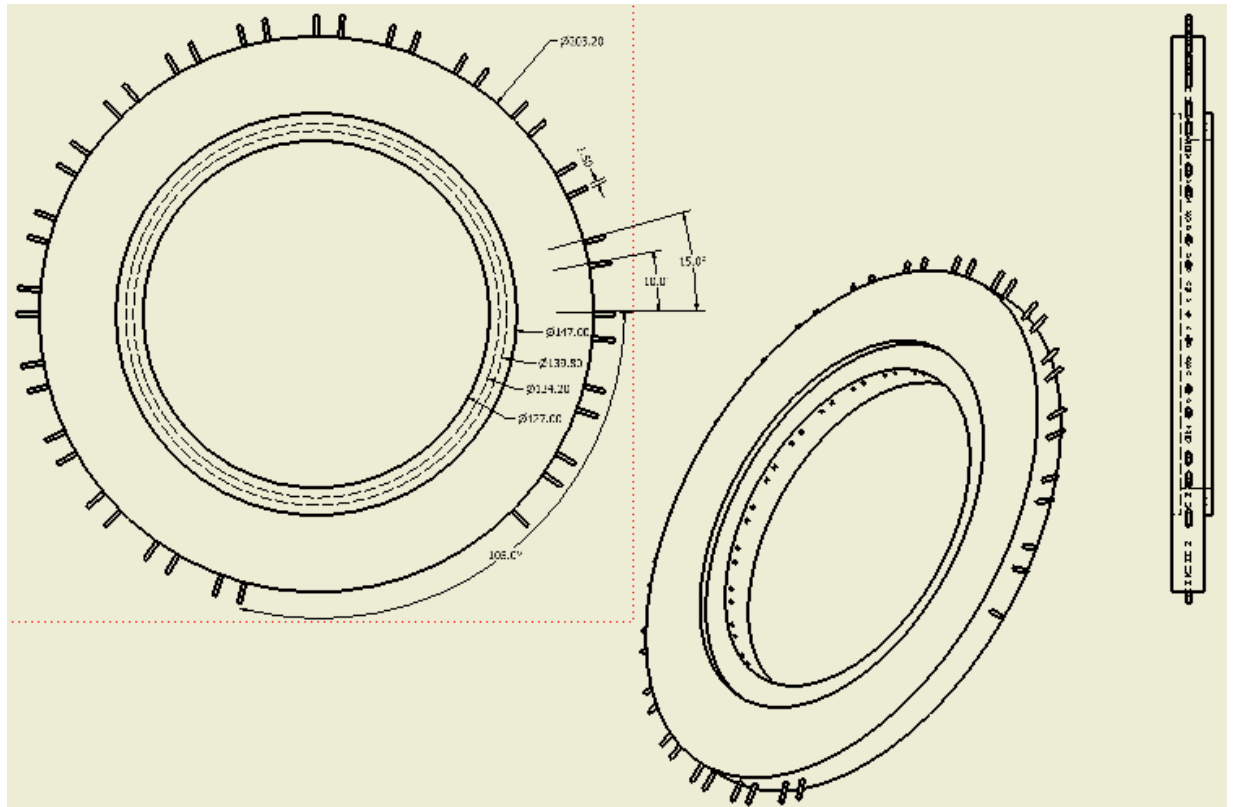


Figure 6.12: Cross-sectional view of the test section for liquid film thickness measurements at the top of the pipe. Dimensions are in mm. Present study

In the present study, Figure 6.12 shows the configuration for the test section to locally measure the liquid film thickness on the outside wall without disturbing the flow. The electrodes were spaced by every 10° from each other and 11.84° from the closest wire probe assembly. The probes were made from 1.5 mm diameter welding rods, made of stainless steel to avoid problems of corrosion. The probes were positioned onto the test section by inserting each pair of the electrodes through a cylindrical Perspex rod of 10 mm diameter to ensure accurate location of the probes without causing any damage to the test section. Particular consideration was paid to the different hardness of steel and Perspex so as to avoid jamming of the lathe and disruption of the test section. This became necessary in order to ensure that the probes were perfectly flush with the inner diameter of the test section. On each side of the test section, 20 pairs of electrodes

were located as shown in Figures 6.11 and 6.12. The sequence is shown on the figure, (1-2, 2-3, 3-4, 4-5, 5-6...6-7). The voltage was applied by an electronic box designed and previously used by Conte (2000) and Conte and Azzopardi (2003); the probes were driven by 10 kHz current. According to Belt (2006), the flow of electrical current from a transmitter in one probe to the neighbour receivers and transmitters (cross-talk) will decrease the spatial resolution of the sensor and increase the measurement errors of the liquid film thickness. To prevent cross-talking, the 20 pin probes were categorized into 4 groups. The first group classified as A is made up of pins 1, 5, 9, 13 and 17 while pins 2, 6, 10, 14 and 18, as group as B. On the other hand, group C is made up of pins 3, 7, 11, 15 and 19 and finally the fourth group classified as D is made up of pins 4, 8, 12, 16, and 20. Moreover all the probes from the four groups were calibrated simultaneously in the same position as they were located in the test section and with the same signal acquisition as has been used during the experiments.

During the calibration of the local liquid film thickness using the 20 pairs of pin probes, a high level of care was taken as dealing with a thin film of liquid. The pin probes were calibrated simultaneously as they were employed during measurements of liquid film thickness in vertical 180° return bend. It is not possible to calculate the response of the instrument. Calibration by simulating the exact geometry of the system is therefore necessary. For this purpose a non-conducting solid rod (PVC) with the same inside and outside diameter as the flow pipe was therefore used for the calibration procedure. Starting from one extremity, the diameter of the rod was reduced progressively by cutting 0.37, 0.62, 1.5, 2, 2.43 and 2.78 mm off the original surface in the radial direction.

This was done to produce a static film of liquid on the wall of the test section by filling the annulus between the PVC rod and the pipe wall with a conductive liquid (water). The diameter of the rod was measured with an accuracy of better than $10\ \mu\text{m}$ Zangana (2011). The rod was centred correctly at the bottom and the top of the test section using a plastic insert made specifically for that purpose. The calibration was repeated several times and with different rotations as an extra check. The probes were calibrated with three different conductivities (491, 564 and $600\ \mu\text{Scm}^{-1}$). The conductivity of the liquid was kept constant during the calibration over temperature changes of less than 0.5°C . The output voltage as a function of liquid film thickness was recorded and as a result the calibration curve for each group of pin probes was obtained. The calibration curve of the four arrangements is shown in Figure 6.13.

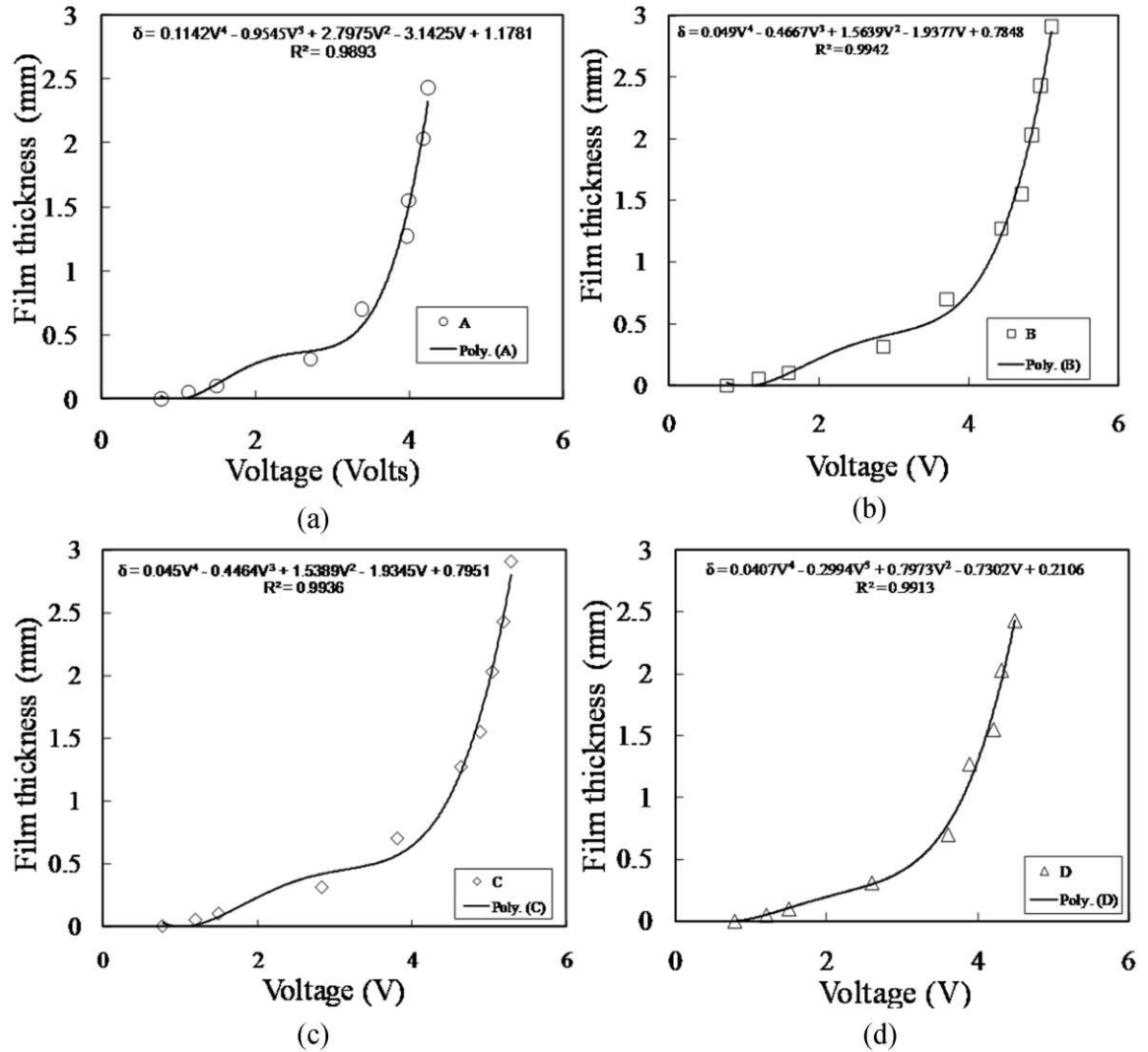


Figure 6.13: Calibration curves for the parallel pin probes

In conclusion, tap water, which was used in the experiments, was found to have conductivity between 491 and 600 μScm^{-1} . If not replaced the water quickly became contaminated and mineral deposits began to show, mostly on the wires. To avoid large variations of conductivity within the same experimental run and to reduce fouling of the electrodes, fresh water was fed continuously to the separator/storage tank and discharged to drain. The conductivities determined during the measurement were used to interpolate between the calibrations curves to obtain the liquid film thickness relationship. Calibrations were repeated

periodically without a cleaning of the electrodes. It was observed that the variations of the calibration curves caused changes in the liquid film thicknesses, which were well within experimental error. The largest discrepancy recorded was 4.5 %. From the gradient of the signal/liquid film thickness curve and the accuracy of the signal measurement, the uncertainty in liquid film thickness at the top of the pipe is about 11 %. The value for thicker liquid films at the bottom of the bend is much lower.

6.4 Cross checking of conductance ring data with those from the liquid film thickness probes

In order to check the data obtained with the conductance ring probes, a comparison was performed against the data from the liquid film thickness probes. Here, the liquid film thickness probes constitutes the pin and wire probes. In order to carry out the comparison, liquid film thickness had to be converted into film fraction so that a direct comparison can be made. Film fraction was obtained from the liquid film thickness measurement by integrating over the cross-sectional area as shown below:

$$(1-\varepsilon) = \frac{\int_0^{2\pi} y d\theta}{\frac{\pi D^2}{4}} = \frac{4}{\pi D^2} \int_0^{2\pi} y d\theta \quad (6.1)$$

Where,

$(1-\varepsilon)$ is the film fraction and y is the liquid film thickness and θ is the circumferential angular position in the bend.

Before the comparison of the two methods, it is worth mentioning here again that the local pin probes can measure the liquid film thickness accurately up to 2 mm while the wire probes can cope with very thick liquid films. A typical comparison between the average film fraction obtained from the ring probes and the liquid film thickness probes is presented in Figure 6.14. As expected, the data from both instruments show similar trend: a decrease in average film fraction as a consequence of an increase in gas superficial velocity. The best degree of agreement is observed at the 90 and 135° bends and at the higher gas superficial velocities whilst the least at the 45° bend. The calculated maximum and minimum % error for the 45, 90 and 135° are respectively, (53, 22 and 17) and (43, 3.1 and 0.23). Though, there is a marked variation between the results obtained from both methods at the lowest gas superficial velocity. The probable explanation for the variations are: (1) for the 90° bend, the pin probes were not able to pick up the thick liquid films outside the bend and as a consequence, under predicts the value of the film fraction. (2) the film outside the 135° bend is not as thick as those of the 45 and 90° bends, that's why the deviation here is the least. (3) At the 45° bend which suffers from the most significant variation in film fraction, the effect of the centrifugal force on the liquid is greatest. The liquid is thrown to the outside of the bend and as earlier explained the pin probes could not detect the expected thick films and as a consequence became saturated. This is evidenced from the polar plot of liquid film thickness (Figure 7.10); some of the liquid film thickness values had to be omitted based on the fact that they were saturated.

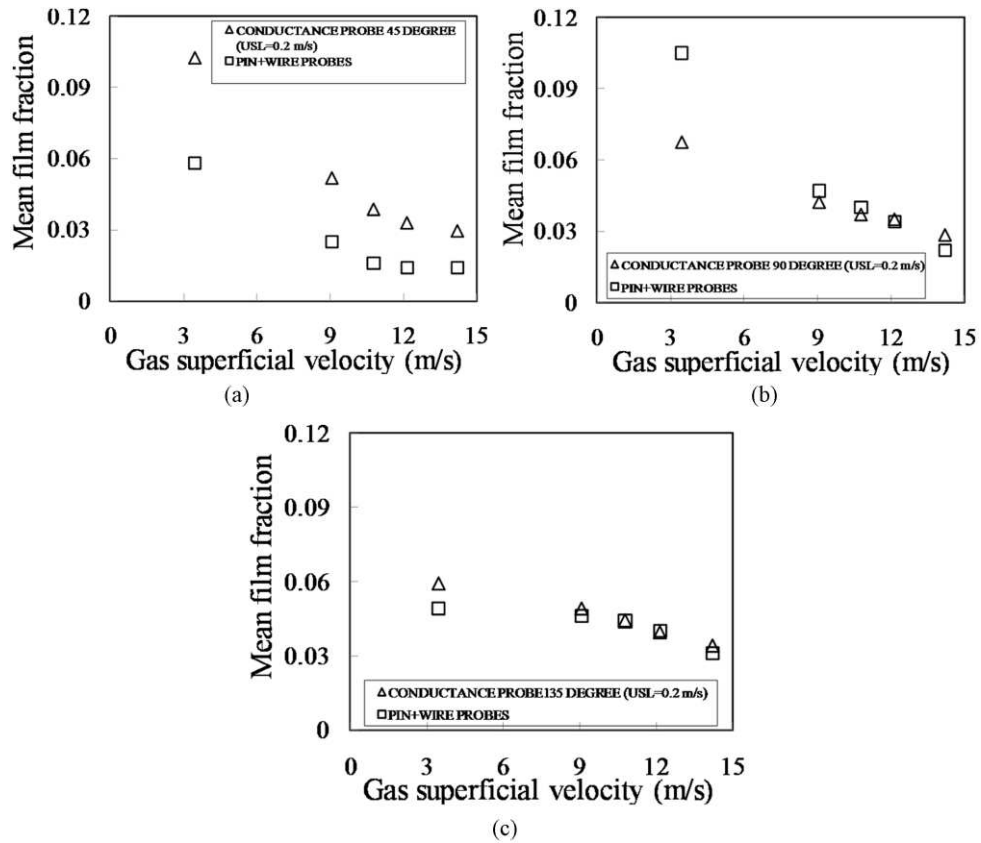


Figure 6.14: Typical comparison between the film fraction obtained from the ring and liquid film thickness probes. Liquid superficial velocity = 0.2 ms^{-1} .

Another justification for the instruments is a plot of average liquid film thickness for the second 5 seconds and third 5 seconds against the first 5 seconds. As expected, when the system is steady, this plot should give a straight line as indeed observed in Figure 6.15. There are exceptions for the data taken at low gas superficial velocities and for the highest liquid superficial velocity of 0.2 ms^{-1} . This is probably due to the fact at those conditions; the values of the liquid film thickness obtained from the pin probes became saturated at some time interval and as a consequence gave slight discrepancies.

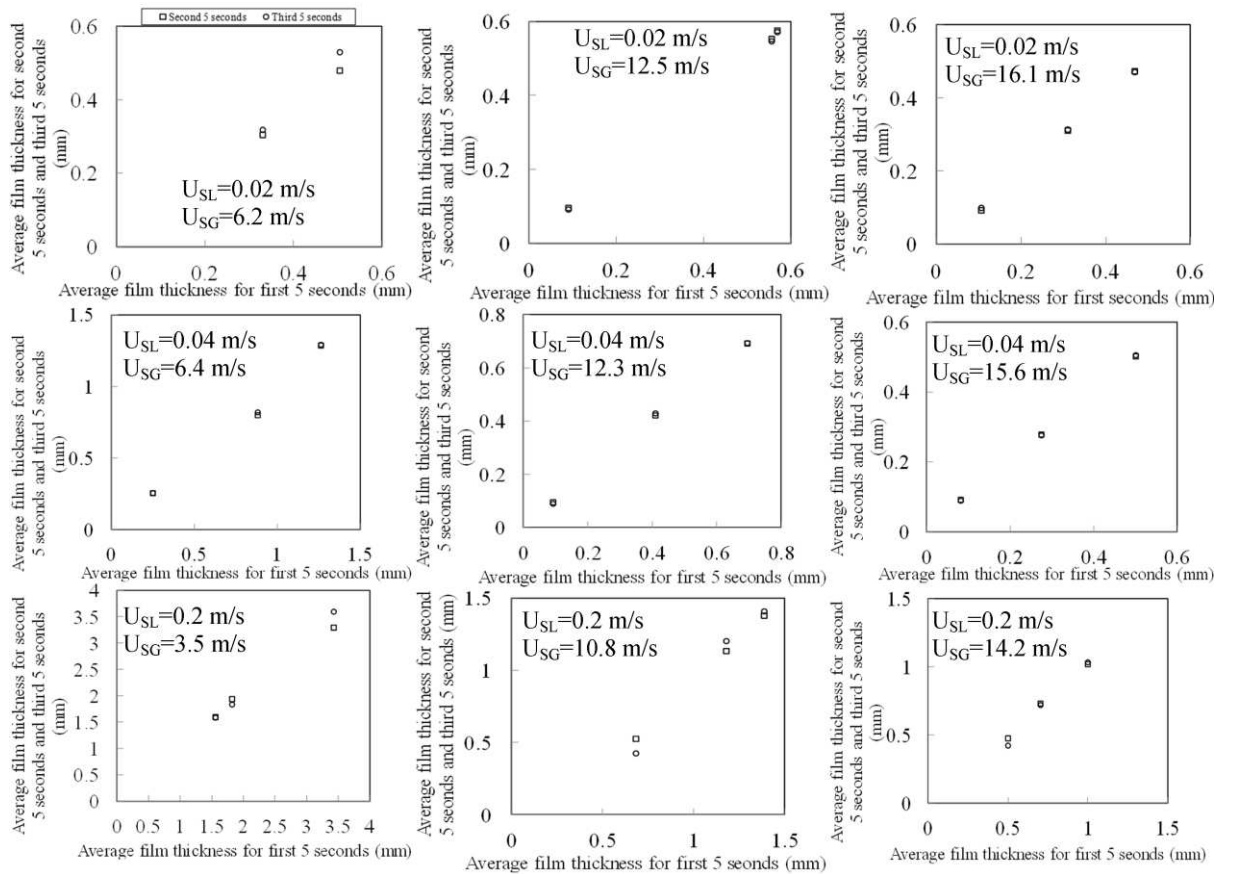


Figure 6.15: variation of averaged film thickness for the second 5 seconds and third 5 seconds against first 5 seconds.

6.5 Data acquisition:

The signals from the instruments described in the previous sections were saved into a personal computer through a 32 channels DAQ card from National Instruments in addition to DAQ hardware, and LABVIEW 7 and 8.6 software, again from National Instruments. The data acquisition rate was controlled using the built-in functions within the software package. The data were recorded every 0.001 seconds over 15 seconds for each experimental run. The signals from the sensors were obtained simultaneously and saved on a PC as EXCEL files. The block diagram that outlines how the current data acquisition was carried is shown on Figure 6.16.

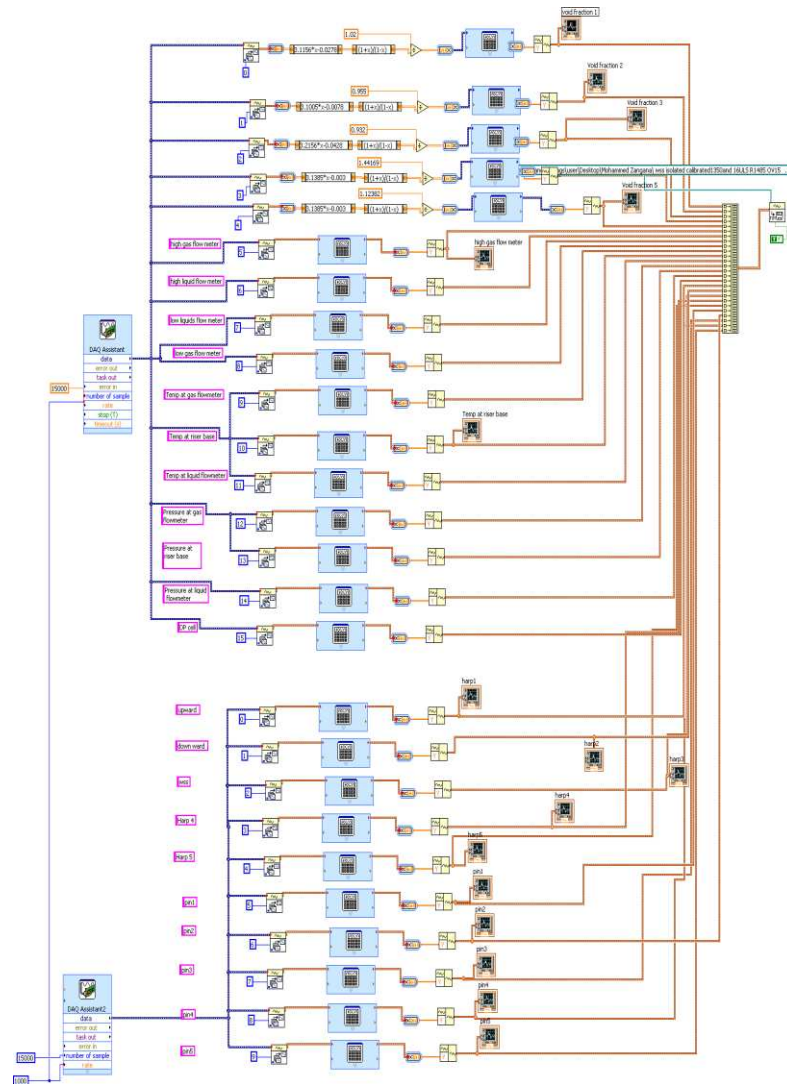


Figure 6.16: Block diagram of the LABVIEW program for data acquisition

6.6 Safety features:

Emergency stop buttons for the power to the air compressor and the water pump are located on all three levels of the experimental facility. The tank in the compressor section and the air-water separator are fitted with a relief valve and bursting disc respectively, for emergency pressure relief. The pressure limit for the pressure relief valve is 5 bars. Air/water mixtures at low pressures present no toxic hazards.

6.7 Summary:

A comparative analysis of the experimental results obtained from the conductance ring probes and the liquid film thickness probes measured in the bend test sections correlated very well except at the 45° bend where a significant variation was observed. This deviation was ascribed to the fact that the pin probes that were meant to measure the liquid film thickness outside the bend could not detect the expected thicker liquid films within that vicinity and as a result it under predicted the true values of the film fraction.

The next chapter provides new data for film fraction and liquid film thickness around a large internal diameter vertical 180° return bend.

Gas-Liquid Flow in a 127 mm Pipe and Bend

In Chapter 5, the experimental studies summarised used advanced measurement instrumentation to record the air-silicone oil flow around 90° bends attached to feeder and exit pipes set at different orientations. The conclusions drawn from such studies is not directly applicable to the design of heat exchangers, reboilers and chemical plants as these tend to employ 180° return bends. The 180° return bend flow involves a combined action of centrifugal and gravity forces, which tend to produce complicated multiphase flow phenomena, due in part to:

- 1) A centrifugal force, which acts at right angles to the main flow, would move the gas toward the zone of smaller curvature radius of the bend, and moves the liquid toward the outer zone.
- 2) A gravitational force that tends to pull the liquid toward the inner wall of the bend and rise the gas toward the outer wall.

These forces according to Usui et al. (1983) may result in a separation of the phases. Furthermore, the change of direction from the upflow to down flow through the curved bend would have a major effect on the flow. The flow structure in the bend would also be influenced by the flow patterns as the mixture

enters the bend. These effects would bring unique characteristics not only on the flow behaviour, but also on the local void fraction and local liquid film thickness distributions. In addition, where the flow is annular, there will be considerable disturbance to the liquid flow in the pipe. If the flow conditions before the bend were such that the fractions of entrained liquid were low then there is a strong possibility that a dry patch may develop on the outside of the bend. However, it is noted that these observations were made from research that employed pipes of small internal diameter. Additional experimental data is therefore necessary to improve the current fundamental understanding of the mechanisms involved in the formation of the flow regimes within large diameter 180° return bends. This is essential for current prediction methodologies to be enhanced and for accurate modelling and simulation to be achieved.

This chapter reports the results of a series of studies conducted to investigate the multiphase air water flows experienced around a 180° return bend. The parameters which were measured are the the film fraction in both upward and downward flows, as well as at 45, 90 and 135° around the bend. The circumferential local liquid film thickness distribution was also measured at the 45, 90 and 135° around the bend. The ranges of the independent variables, the gas and liquid flow rates, expressed as superficial velocities are given in Table 7.1. In total, 102 runs were carried out for each of the 45, 90, and 135° positions.

Table 7.1: The range of variables

u_{gs} (ms^{-1})	u_{ls} (ms^{-1})	Re_{gs}	Re_{ls}
3.5-16.1	0.02-0.2	86413-402,000	2535-25350

The gas flow rates were chosen such that in all cases the flow in the vertical riser before the bend was either annular or churn. In order to understand the influence of 180° return bend on the film fraction and liquid film thickness distributions, the flow patterns in the upstream, downstream and at the bend sections are deduced. Typical time series and probability density functions (PDF) of dimensionless liquid film thickness encountered at upstream, downstream, and within the bend are shown and discussed. The effect of gas superficial velocity on average film fraction is illustrated. The axial variations of average film fraction are shown and discussed. Others are: The location of the liquid and gas in the bend based on a modified form of the Froude number; the flow pattern map of Usui et al. (1983). A comparison between the results of the present work based on mean film fraction and that of Hills (1973); the relationship between the average cross-sectional liquid film thickness and its locations in the bend; the liquid film thickness distribution in the bend is; a comparison between Computational Fluid Dynamics (CFD) and experiments.

7.1 Film fraction:

The question that is going to be addressed here is “ what is the right parameter to use involving churn-annular flow, void fraction or film fraction? When high void fraction values are considered in two-phase flow (0.8 - 0.99), then it becomes a very sensitive problem. In this range void fractions cannot undergo significant variations even if the actual two-phase flow structure changes. In annular flow for instance, if a plot of mean void fraction is made against gas superficial velocities, because the values are very close to one another, there will be no noticeable difference between them. Thus, if calculations are aimed at describing the two-

phase structure, the void fraction is not the right parameter to be considered. Film fraction is more significant from this point of view. For example, a significant effect of specific mass flow rate and geometry can be evidenced on film fraction, which this effect would never have been seen if void fraction were considered instead of film fraction.

7.1.1 Flow development:

Measurements of film fraction obtained from the conductance probes located at the riser were examined to determine the extent of flow development. A fully developed flow is one when the flow pattern does not change with the distance downstream. To achieve this, a comparison of time series, Probability Density Function (PDF) and Power Spectral Density (PSD) of film fraction are shown in Figure 7.1. Details of the PDF and PSD functions are given in Chapter 4.

An examination of Figure 7.1 (b-c) shows a striking similarity between the shape of the PDF distribution and location of the frequency in the PDF and PSD plots of the three probes at liquid and gas superficial velocities of 0.2 and 14.2 ms⁻¹, respectively. The plot of the time series of film fraction (Figure 7.1 a) for the three locations also did not yield any significant differences. Therefore, there is an indication that equilibrium has been reached and that the flow is fully developed at 64 pipe diameters for the flow condition considered. Interestingly, this is consistent with the results of Omebere-Iyari (2006); he measured the void fraction at various points under similar conditions at 3.5, 30.9, 62.7, 63.8 and 65.5 pipe diameters downstream of the mixer. He found that the variation in the void fraction characteristics at 64.0 and 65.5 pipe diameters were small and concluded that the flow was fully developed at 64.0 pipe diameters.

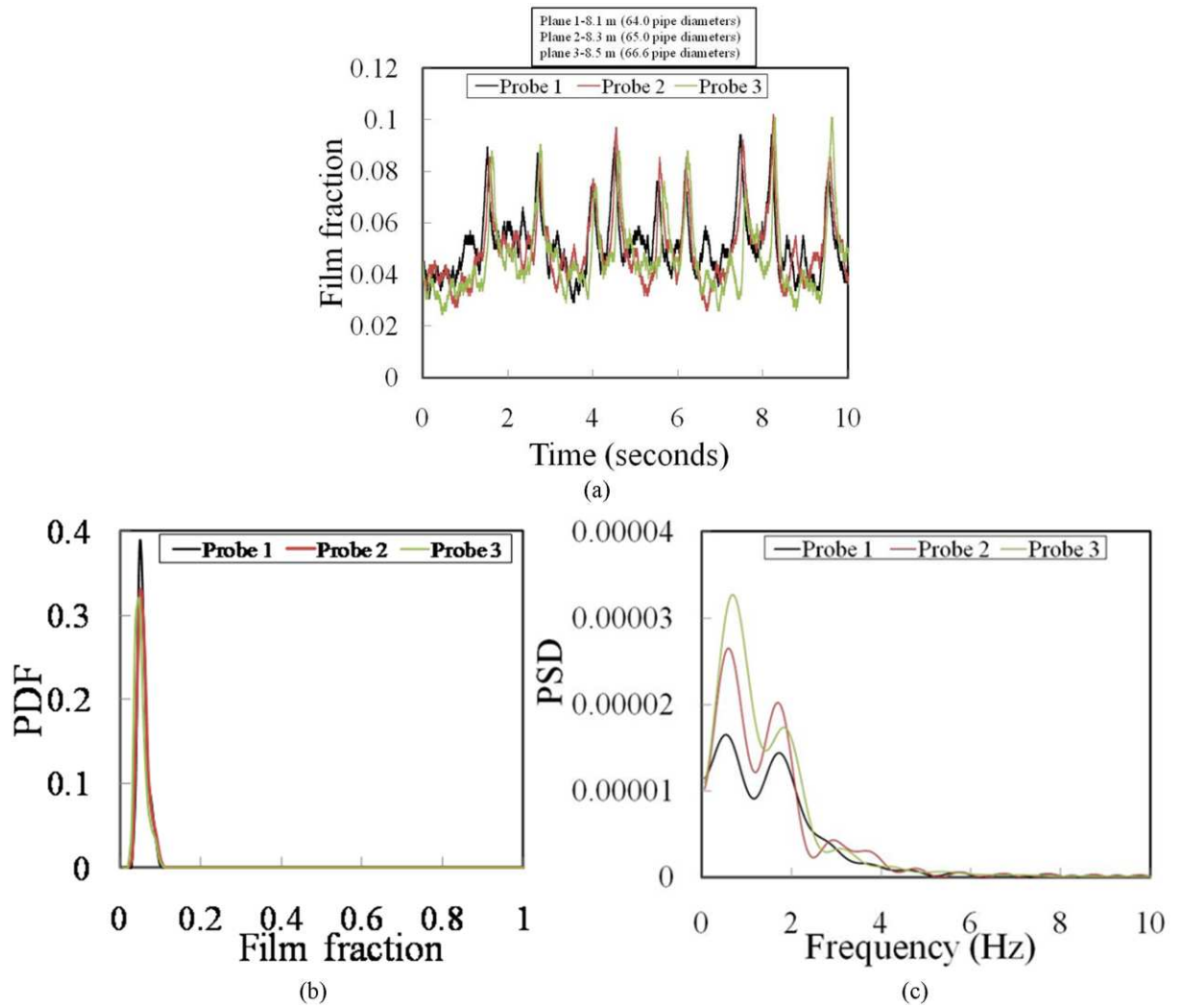


Figure 7.1: a typical comparison between the (a) time series of film fraction (b) PDF of film fraction and (c) Power spectral density (PSD) of film fraction obtained at three measurement locations: probes 1, 2 and 3 for liquid and gas superficial velocities of 0.2 and 14.2 ms⁻¹, respectively.

7.1.2 Time series and PDF of dimensionless liquid film thickness, before, around and after the 180° return bend:

The time series of dimensionless liquid film thickness was obtained with the aid of ring conductance probes flush mounted on the pipe. The dimensionless liquid film thickness was obtained from film fraction using equation (7.1) below:

$$\frac{\delta}{D} = \frac{1}{2} [1 - (1 - \epsilon_F)^{0.5}] \quad (7.1)$$

where,

ε_F is the film fraction and $\frac{\delta}{D}$ is the dimensionless liquid film thickness.

The probes were located at various sections of the pipe: 17 and 21 pipe diameters, upstream and downstream of the bend, respectively, and at 45, 90, and 135°. This enabled the determination of the PDF of dimensionless liquid film thickness to be obtained.

A typical time series and PDF of dimensionless liquid film thickness before, around and after the 180° return bend at liquid and gas superficial velocities of 0.2 and 14.2 ms⁻¹, respectively are presented in Figure 7.2. From an analysis of the time series and PDF of dimensionless liquid film thickness, the flow pattern upstream of the bend is confirmed to be churn flow. This was also verified by visual observation. On entering the 45° bend, the centrifugal force displaces the liquid to the outside of the bend, whilst the gas migrates to the inside of it. Gravity on the other hand, drains part of the liquid to the inside of the bend. The flow pattern within this vicinity is annular flow. However, the gas-liquid interface is wavy as shown from the time series of dimensionless liquid film thickness (Figure 7.2). As the air-water flow enters the 90° bend, the orientation of the flow changes from the vertical to horizontal and hence gravity slows them down and drains more of the liquid to the bottom of the bend. From an analysis of the time trace of the dimensionless liquid film thickness as shown in Figure 7.2, it is concluded that the liquid film is very thick and unstable. Although more waves appear on the gas-liquid film interface, the flow pattern still remains annular. According to Hills (1973) annular flow in horizontal tubes depends on a high

level of entrainment to replenish the liquid film at the top of the tube which in turn implies a film of sufficient thickness for entrainment to occur. At the 135° bend, the flow pattern is still annular. On reaching the downcomer, the gas is now at the centre of the pipe whilst the liquid moves to the walls of the pipe. Here, the liquid film is thick due to the fact that the effect of gravity on the two-phase flow is greatest: both gravity and flow are in the same direction whilst buoyancy is in the opposite direction. However, the flow pattern is still annular.

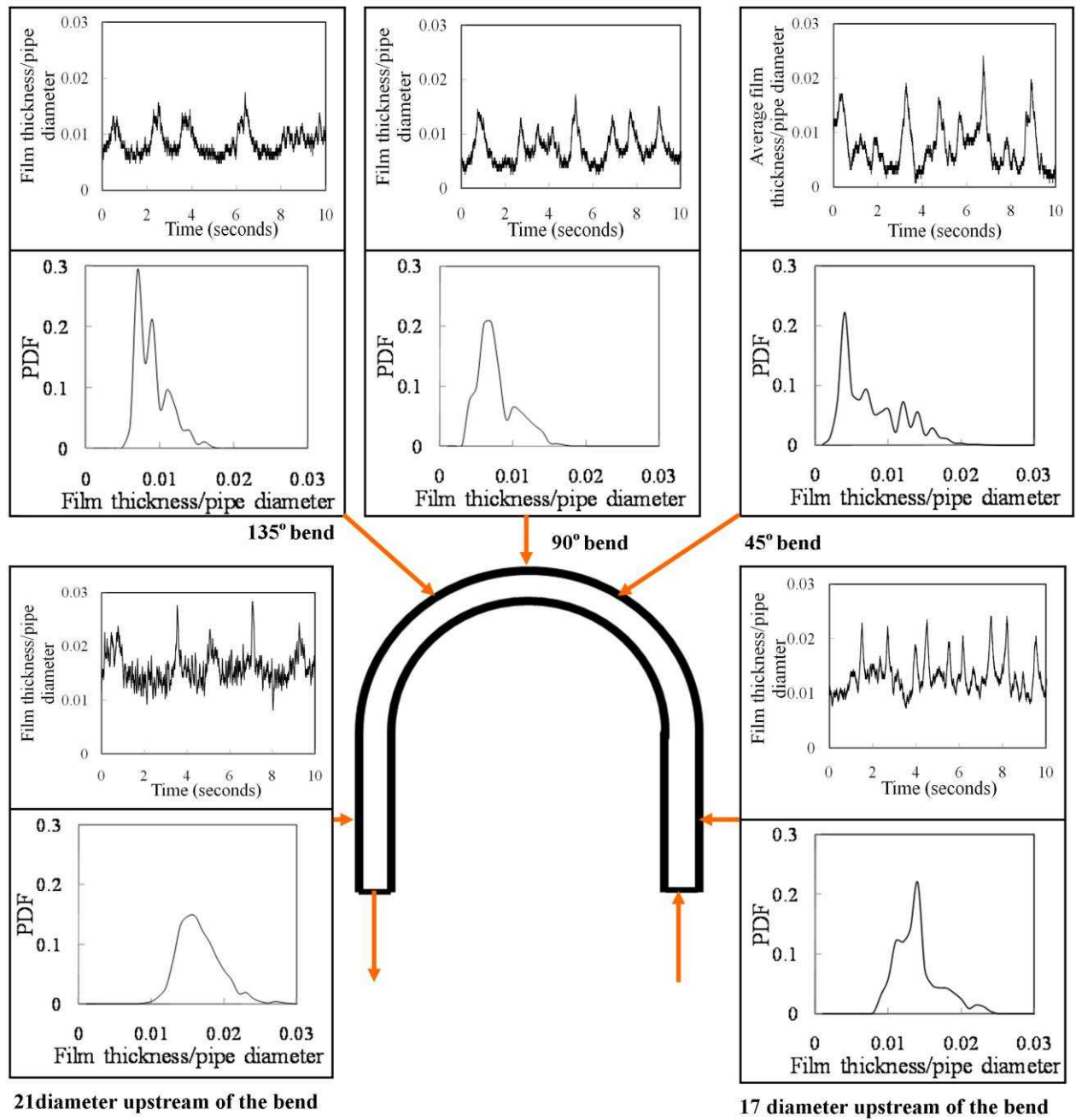


Figure 7.2: a typical time series and PDF of dimensionless liquid film thickness around the 180° return bend for liquid and gas superficial velocity of 0.2 and 14.2 ms^{-1} , respectively.

An analysis of the plots of the time series of dimensionless liquid film thickness for the riser, 45, 90, 135° and downcomer show that:

- a) Riser: fifteen peaks may be seen in the 10 second sample illustrated. These can be interpreted as waves on a base film. These waves are created due to the high gas shear stress acting at the gas-liquid interface. The waves are able to remain on the gas liquid interface because the gas inertia is able to overcome the gravitational force which may want to collapse them. The peaks of the average film thickness have a maximum value of 0.024 D whereas the base liquid film thickness is 1.03 mm. Therefore, the ratio of wave height to average liquid film thickness is 1.74.
- b) Some of the waves at the 45° bend position merge with one another and so create larger ones. However, the probability value of the peaks of the waves remained the same, 0.024 D. However, the number of visible waves in the 10 seconds sample goes down to 10. It is interesting to observe from the plot that the ratio of the wave height to the average liquid film thickness is now 3.24. This is close to the value of 4 to 6 obtained by Hewitt and Nicholls (1969). The mean height of the liquid film is now 0.02 mm. The drop in the liquid film thickness suggests that some of the liquid could not climb up the bend due to the influence of gravity and as a consequence falls back into the riser (back flow).
- c) Moving from the 45 to 90° position shows that there is an increase in the coalescence of waves leading to larger ones. The probability values of the peaks of the waves have now decreased further to 0.0172 D, whilst the height of the liquid film has increased to 0.48 mm. The ratio of the wave height to the average liquid film thickness has now decreased to 2.39.
- d) The mean liquid film thickness at 135° has increased to 0.70 mm. The number of peaks has decreased to four. It is interesting to note that the waves are very

thick having a maximum peak of 0.018 D with a large base superimposed on the dimensionless liquid film thickness traces. The thick liquid film observed is due to the accumulation of liquid at the bottom of the pipe. The ratio of wave height to average liquid film thickness has decreased further to 2.03.

- e) Due to the force of gravity acting in the same direction as the flow, some of the waves are being broken down on entering the downcomer. The appearance of the waves in the downcomer is not as clear as compared to others. However, the height of the liquid film is 1.10 mm, whilst the height of the peak is 0.026. The ratio of the wave height to the average liquid film thickness is almost same as for the riser, 1.71.

7.1.3 Variation of average film fraction with gas superficial velocity:

Following these studies attempts have been made to understand the effect of 180° return bend on the film fraction. Figure 7.3 (a – e) shows the variation of the average film fraction with the gas superficial velocity for different liquid superficial velocities. A comparison of the outputs of the conductance ring probes are made for the five different locations, riser, 45°, 90°, 135° and the downcomer. It can be concluded that there is a general trend that the average film fraction over the cross-sectional area for the bend flow is lower than that for an upward vertical flow. This is because at the bend the slip is less than that of a straight pipe. Similar observation was also reported by Usui et al. (1983) who worked on an inverted 180° bend using air-water as the model fluids. The average film fraction is found to decrease slightly for gas superficial velocity from 6 to 10 ms⁻¹, and above 10 ms⁻¹ becomes practically constant regardless of the measurement

location. The study also found out that the average film fraction for the riser was generally greater than for the downcomer at low gas superficial velocity. The difference between the values of the average film fractions, riser and downcomer decreases as the gas superficial velocity increases. This is to be expected since in downward flow (downcomer) the buoyancy force is acting on the gas phase in a direction opposite to the main flow, while in upflow it complements the main flow. The effect is such that the actual gas velocity is mostly greater in upward flow than in downward flow. This results in a higher film fraction for upward flow (riser) for the same liquid and gas superficial velocities.

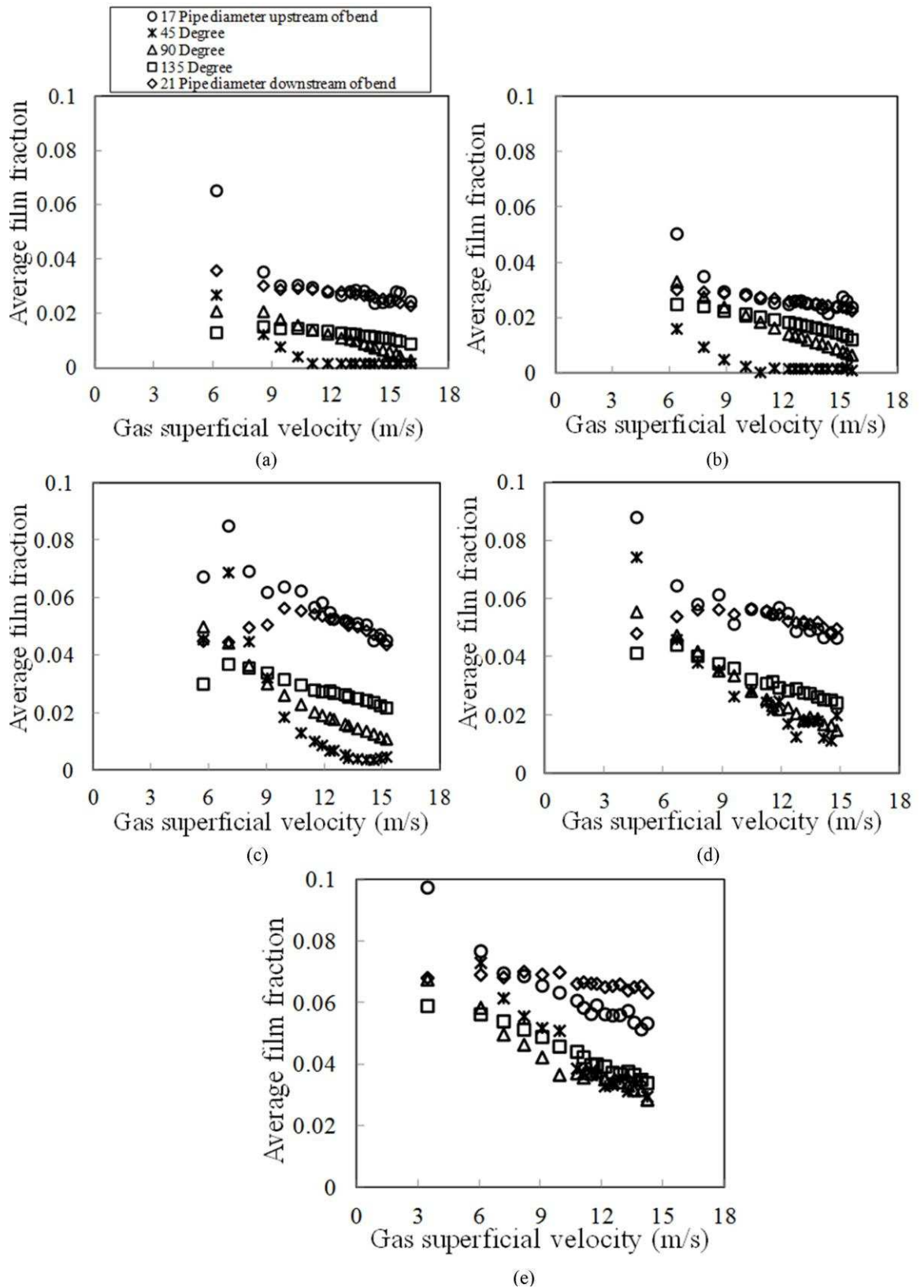


Figure 7.3: Variation of average film fraction with gas superficial velocity around the 180° return bend at liquid superficial velocity of (a) 0.02 ms⁻¹ (b) 0.04 ms⁻¹ (c) 0.08 ms⁻¹ (d) 0.1 ms⁻¹ and (e) 0.2 ms⁻¹

It can be observed in Figure 7.3 that at liquid superficial velocity of 0.02 ms^{-1} , a maximum average film fraction of 0.062 is obtained for the riser at gas superficial velocity of 6.2 ms^{-1} . However, the maximum value obtained decreased to a minimum at the 135° bend due to entrainment of droplets arising from the shearing off of the crest of waves. It is interesting to observe that as the gas superficial velocity is increased from 6.2 to 9 ms^{-1} , the value of the average film fraction for both the riser and downcomer become the same and continued in that manner throughout the remaining gas superficial velocities studied. This shows that the film fraction is less sensitive to the flow direction in those regions. Therefore, this signifies that the gas superficial velocity of 9 ms^{-1} may be regarded as the critical gas velocity, for the direction of flow to be insignificant. For the bend pipe section, at the higher gas superficial velocities, the maximum and minimum average film fractions are observed at the 135 and 45° bend locations, respectively. It is interesting to observe that the average film fraction for the 45° at gas superficial velocity of 10.5 to 15 ms^{-1} and liquid superficial velocity of 0.02 ms^{-1} is almost zero, suggesting that there is a film breakdown within the vicinity. The film breakdown (burn out) phenomenon is clearly the result of a total loss of water from the liquid film by evaporation and entrainment. This is similar to the observation reported by Balfour and Pearce (1978) and Poulson (1991) with regards to film breakdown. This is also in agreement with the works of Hewitt and Lacey (1965) and Hills (1973) who investigated the breakdown of thin liquid films in climbing film flow. They concluded that with low liquid rates the film can exist in a metastable condition and that if breakdown is induced artificially then the dry patch so formed will not re-wet unless the liquid flow rate is increased considerably.

If the liquid superficial velocity is doubled at a gas superficial velocity of 6.4 ms^{-1} , the maximum average film fraction is observed at the riser whilst values at the 45° into the bend are the smallest. The (riser and downcomer) and the 45° bend are observed to have the maximum and minimum average film fractions, respectively at higher gas superficial velocities. The same observation made for the case of liquid superficial velocity of 0.02 ms^{-1} is also seen here with regards to the riser and downcomer; at gas superficial velocity of 9.2 to 15.6 ms^{-1} , the average film fraction becomes almost the same. Also observed here is the film breakdown within the 45° bend at higher gas superficial velocities.

At liquid superficial velocity of 0.08 ms^{-1} , the point of convergence of the riser and downcomer moved to about 12 ms^{-1} . The minimum average film fraction is observed for the 45° followed by the 90° bend. This is due to the fact that some of the liquid films are not able to move into the bend. This is because gravity has a significant effect on the liquid film; the liquid becomes thicker within that vicinity and as a consequence result in a backflow. A similar trend is observed when the liquid superficial velocity is increased to 0.1 ms^{-1} . Though, there is an absence of film breakdown in the 45° bend at higher gas superficial velocities.

When the liquid superficial velocity is increased to 0.2 ms^{-1} and at gas superficial velocity of 6.2 ms^{-1} , the value of average film fraction is almost the same for both the riser and the downcomer. Though, initially, the value of the average film fraction was higher in the riser than the downcomer at gas superficial velocity of 3.5 ms^{-1} . It can be concluded that at liquid and gas superficial velocities of 0.2 and 6.2 ms^{-1} , respectively, the 180° return has no effect on the flow. An interesting observation made in this study is that as the gas superficial velocity is

increased to about 9 ms^{-1} , the average film fraction starts to diverge; the point of maximum average film fraction is shifting from the riser to the downcomer. It is this shift in the location of the maximum average film fraction from maximum to minimum that is called film inversion. The film inversion becomes apparent at higher gas superficial velocities. This seems to suggest that the influence of flow direction and entrainment are becoming significant. This is because we have more gas entrainment in the riser than in the downcomer. The location of the minimum average film fraction in the bend however, is not very clear. The maximum average film fraction is observed to be in the 135° bend, followed by the 45° then the 90° bend. The explanation for this is: large droplets with a velocity similar to that of the gas and with a density similar also to that of water moving at the gas speed are deposited at the outside of the bend by centrifugal forces. When these droplets hit the outside of the bend, they are converted into liquid film and spread in different directions, including the downcomer and 135° into the bend. This could explain why we have thickening of liquid film in the 135° bend.

Although this presentation is useful for giving an idea of how, in a mean sense, the liquid film varies with the gas superficial velocity before, within and after the bends, it is not easy to quantify the information. For this reason, the experimental average film fraction data will be presented in terms of axial distance.

7.1.4 The effect of gas superficial velocity on average film fraction:

Figure 7.4 shows the effect of gas superficial velocity on average film fraction at different axial distance. On the plot, -2159 mm, -299 mm and 0 mm represents 17 pipe diameters upstream of the bend, 45° and 90° , respectively. On the other

hand, 299 mm and 2667 mm correspond to 135° and 21 pipe diameters downstream of the bend. Here, the axial distance expressed in mm has a negative sign for upstream of the bend, and a positive sign for downstream of it. For the sake of clarity, the points belonging to the same liquid and gas superficial velocities are joined by dash lines. In order to check the effect of gravity on flow, a straight line is used to join the average film fraction obtained at the riser and the downcomer positions. The figure shows the location of the maximum and minimum average film fractions around the bend.

One interesting observation made in this study is that gravity has no effect on the flow at the highest gas superficial velocities over the range of liquid superficial velocities studied 0.02-0.2 ms⁻¹. This is based on the fact that the average film fraction for the riser and downcomer are almost same.

At liquid and gas superficial velocities of 0.02 and 6.2 ms⁻¹, respectively, the average film fraction decrease linearly from (0.0653 to 0.012) with axial distance (-2159 to 299 mm). It then increased to 0.0359 at 2667 mm. As the gas superficial velocity is increased to 8.6 ms⁻¹, the position of minimum average film fraction shifts to -299 mm whilst the location of maximum average film fraction is still at -2159 mm. Contrary to this at gas superficial velocity of 13.3 ms⁻¹, the minimum average film fraction is obtained at -299 mm. This suggests that further proportions of gas as the fluid moved from the -2159 to -299 mm in relation to liquid flow rate led to the occurrence of film inversion.

When the liquid superficial velocity is doubled and at gas superficial velocity of 6.4 ms⁻¹, the locations of minimum and maximum values of average film fraction are 299 and -2159 mm, respectively. At gas superficial velocity of 8.9 ms⁻¹, the

average film fraction decreased from 0.03 at -2159 mm to 0.005 (-299 mm). It recovered to 0.0239 at 0 mm, dropped a little at the 299 mm before finally increasing to 0.0289 at 2667 mm. At the maximum gas superficial velocity of 15.6 ms^{-1} , the minimum and maximum average film fractions are observed at the -299 and -2159 mm, respectively. It then increased linearly to 0.0122 at 299 mm before finally increasing to 0.0289 at 2667 mm.

The positions of the minimum and maximum average film fraction at liquid and gas superficial velocity of 0.08 and 5.7 ms^{-1} respectively, are at -2159 and 299 mm, respectively.

It can be concluded that the maximum average film fraction is observed at the lowest gas superficial velocity for different liquid superficial velocities except at liquid superficial velocity of 0.08 ms^{-1} , where the value is obtained at the second lowest gas superficial velocity, 8 ms^{-1} . The location of maximum average film fraction is observed contrary to the -2159 mm to be at -299 mm for the highest liquid superficial velocity. This shows that the liquid has strong influence in the flow behaviour.

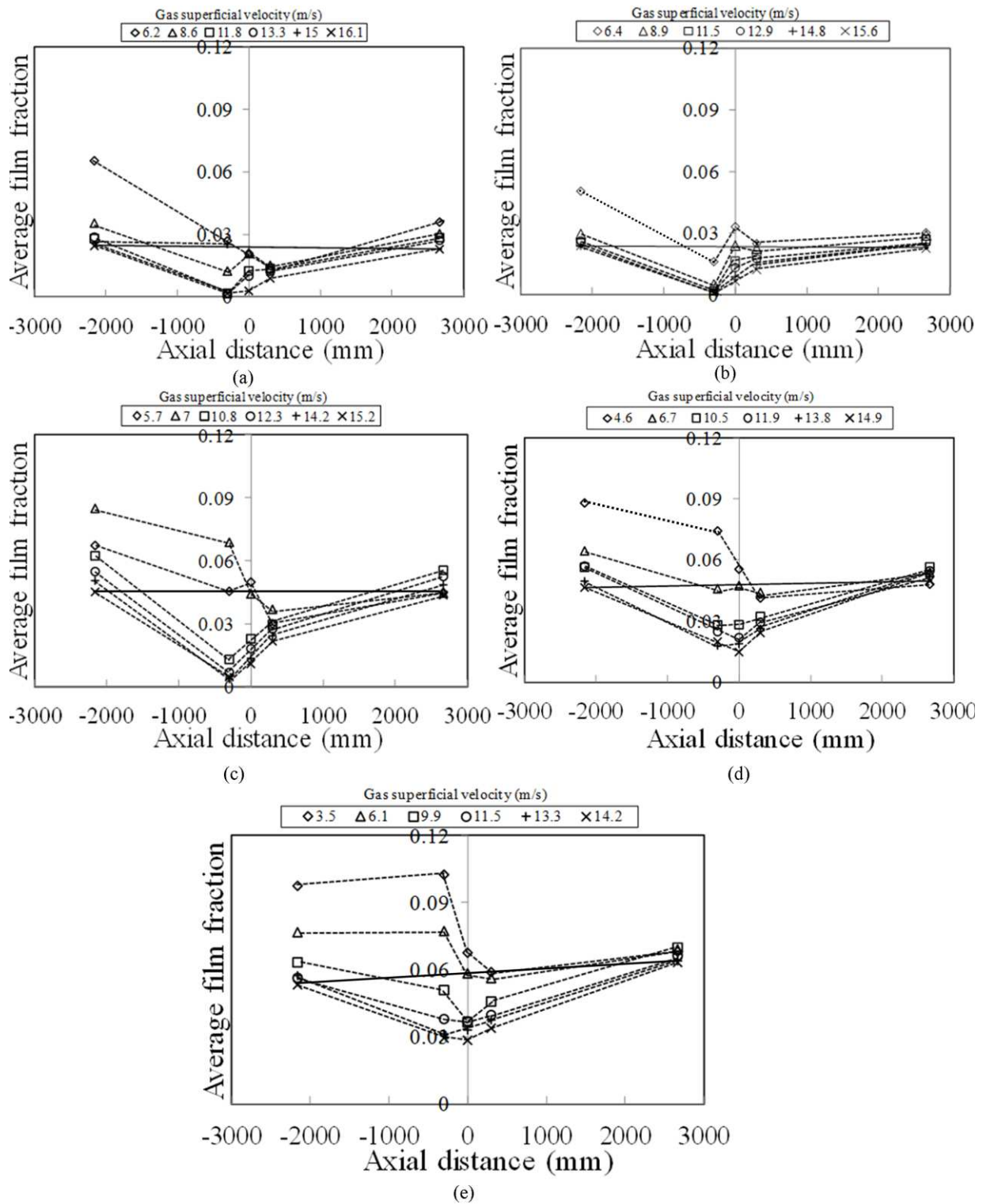


Figure 7.4: Variation of average film fraction with axial distance before, around and after the 180° return bend at liquid superficial velocity of (a) 0.02 ms⁻¹ (b) 0.04 ms⁻¹ (c) 0.08 ms⁻¹ (d) 0.1 ms⁻¹ and (e) 0.2 ms⁻¹. Lines are provided to guide the eye within each data set.

In general it can be concluded that the liquid and gas flow rates, gravity and centrifugal forces have a strong effect on the flow behaviour in a 180° return bend.

7.1.5 Competition between gravitational and centrifugal forces:

Oshinowo and Charles (1974) and Usui et al. (1983) proposed a criterion based on a modified form of Froude number, Fr , (equation 2.37) to determine positions of the liquid within the 180° return bend. According to their proposed criterion when Fr is greater than 1, the liquid will move outside the bend whilst for Fr less than unity, the liquid will hug to the inside of the bend. The validity of the criterion will be discussed here based on the fact that the test bend is located in a vertical plane so that the flow passes from vertical upflow to vertical downflow. It is worth mentioning that in the present study the densities of the liquid and gas are 998 and 3.55 kgm⁻³, respectively. Based on the densities of both phases, the ratio of the gas and liquid superficial velocities was determined as follows:

The centrifugal force needed to confine unit volume of fluid to move in a circular path or radius of bend R for both the liquid and air, F_l and F_g , respectively can be, represented as:

$$F_l = \frac{\rho_{\text{Liquid}} u_{ls}^2}{R} \quad (7.2)$$

$$F_g = \frac{\rho_{\text{Gas}} u_{gs}^2}{R} \quad (7.3)$$

At equilibrium, $F_l = F_g$

$$\frac{\rho_{\text{Liquid}} u_{\text{ls}}^2}{R} = \frac{\rho_{\text{Gas}} u_{\text{gs}}^2}{R} \quad (7.4)$$

Where,

u_{gs} and u_{ls} , the gas and liquid superficial velocities, respectively.

$$\rho_{\text{Liquid}} u_{\text{ls}}^2 = \rho_{\text{Gas}} u_{\text{gs}}^2 \quad (7.5)$$

But,

$$\frac{u_{\text{gs}}}{u_{\text{ls}}} = \sqrt{\frac{\rho_{\text{Liquid}}}{\rho_{\text{Gas}}}} = \sqrt{\frac{998}{3.55}} = 16.8$$

Therefore,

$$u_{\text{gs}} = 16.8 \times u_{\text{ls}} \text{ ms}^{-1} \quad (7.6)$$

Equation (7.6) therefore represents the ratio of gas and liquid superficial velocities. This means that the liquid will have a higher momentum flux than the gas unless the velocity of the latter is 16.8 times greater.

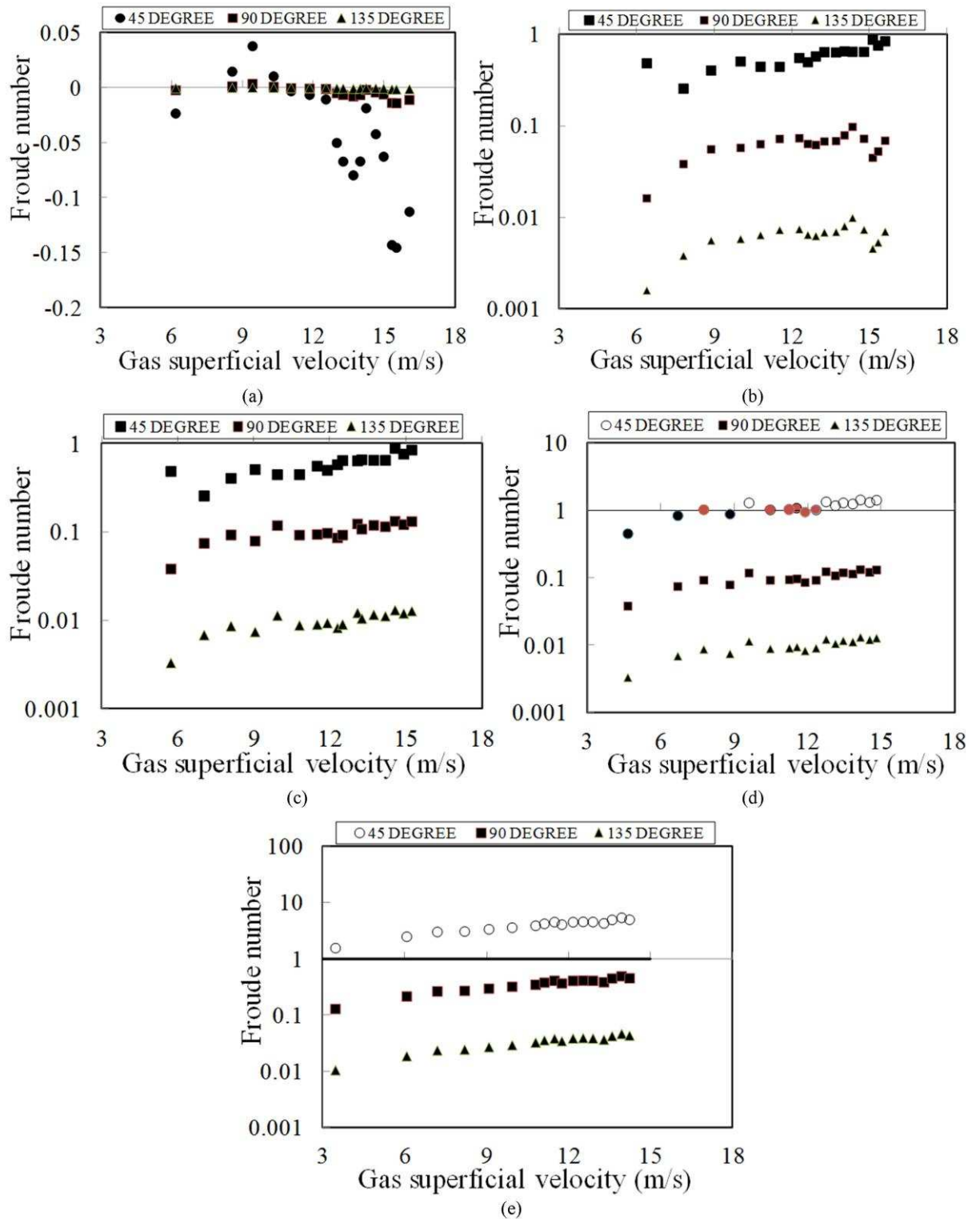


Figure 7.5: Influence of gas superficial velocity on the modified form of Froude number for different liquid superficial velocities: (a) 0.02 ms⁻¹ (b) 0.04 ms⁻¹ (c) 0.08 ms⁻¹ (d) 0.1 ms⁻¹ and (e) 0.2 ms⁻¹. Closed symbols-liquid on inside of the bend; open symbols-liquid on outside of bends; grey symbols transition case liquid goes to inside and/or outside of bend.

The condition for which the liquid goes to the outside or inside of the bend are identified in Figure 7.5 as modified form of Froude number plotted against gas superficial velocity with liquid superficial velocity as a parameter. There was one combination of flow rate (Froude number equals to 1) where it was not clear whether it was liquid or gas which was on the outside of the bend. For flow rates which give a low Froude number, the flow patterns in the riser approaching the 135° bend through the 45 and 90° bends is annular flow. The gas superficial velocity is greater than that for the liquid. As the liquid density is much greater than that for the gas, gravity dominates and we would expect the liquid to move to the inside of the 45, 90 and 135° bends, as in fact observed. Conversely, when the modified form of Froude number is negative it tells us that the liquid is being driven to the inside of the bend independently of gravity. For churn flow, the gas superficial velocity is much greater than that for the liquid. Again the liquid density is much greater than that for the gas, the modified form of Froude number is > 1 and we would expect the liquid to move to the outside of the 45° bend, as in fact observed. As both the two-phase mixture move from the 90 to the 135° bend through the 45° bend, gravity slows them down and throws the liquid to the bottom of the bend and the gas to the outside.

7.1.6 Comparison of the present work with that of Usui et al. (1983) flow pattern map:

Usui et al. (1983) developed a flow pattern map for an inverted 180° bend based on the basis of visual observation. They claimed that the flow patterns which were observed in the bend were generally similar to those for the C-shaped bend flow except the ways of the gas and liquid distributions and the shape of the

bubbles. The map is shown in Figure 7.6, indicating the form of the flow observed at various combination of liquid and gas superficial velocities. According to the transition boundary lines shown on the map, the flow pattern is annular mist flow for liquid superficial velocity of 0.04 ms^{-1} and gas superficial velocity above 15.6 ms^{-1} . On the other hand, for higher liquid superficial velocities, $0.08\text{-}0.2 \text{ ms}^{-1}$, annular flow except at the lower and intermediate gas superficial velocities. From the map also, the region above the 90° and 135° lines would correspond to the case where the liquid moves to the outside of the bend, the air shifting to the inside, and the region below the lines would give the opposite. However, they did not show on the map the line for the 45° bend. They concluded that the inverted 180° bend has the effect of extending the region of annular flow toward much lower gas velocities.

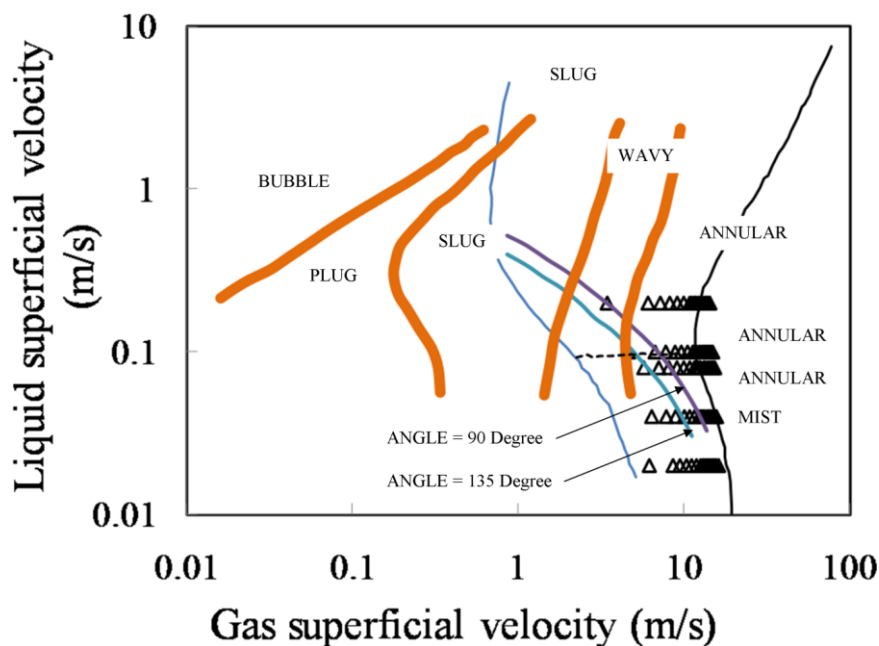


Figure 7.6: Flow pattern map of Usui et al. (1983). The two lines represent the average void fraction along the 90° and 135° bend positions. The region above the lines corresponds to the case where the liquid moves to the outside of the bend and the region below the lines give the opposite.

Contrary to the Usui et al.'s flow pattern transition boundaries, at liquid superficial velocity of $0.02-0.04 \text{ ms}^{-1}$, the flow pattern is annular whilst there is a good agreement with the other liquid flow rates, $0.08-0.2 \text{ ms}^{-1}$ except at the high gas superficial velocities. The two lines depicted in the map corresponding to the 90 and 135° are in contradiction to the present work: at the 90 and 135° the liquid moves to the inside of the bend for all liquid and gas flow rates considered.

7.1.7 Comparison between present study and that of Hills (1973):

A comparison between the present study and that of Hills (1973) will be made based on mean film fraction at 45 , 90 , and 135° bends. Hills carried out experimental work on a 180° return bend with pipes of an internal diameter of 25.4 mm . The radius of curvature was 305 mm and the fluids employed were air and water at a system pressure of 1.5 bar absolute. The results of the comparison presented in Figure 7.7 were carried out at the same liquid superficial velocity of 0.04 ms^{-1} . The plot shows the same tendency, though the values of mean film fraction obtained from the work of Hills are higher than those of present study. This might be due to the fact that the amount of entrainment of liquid drops in the gas core in large diameter pipe is greater than that of smaller pipes. Therefore there is less liquid in the film in the large diameter case.

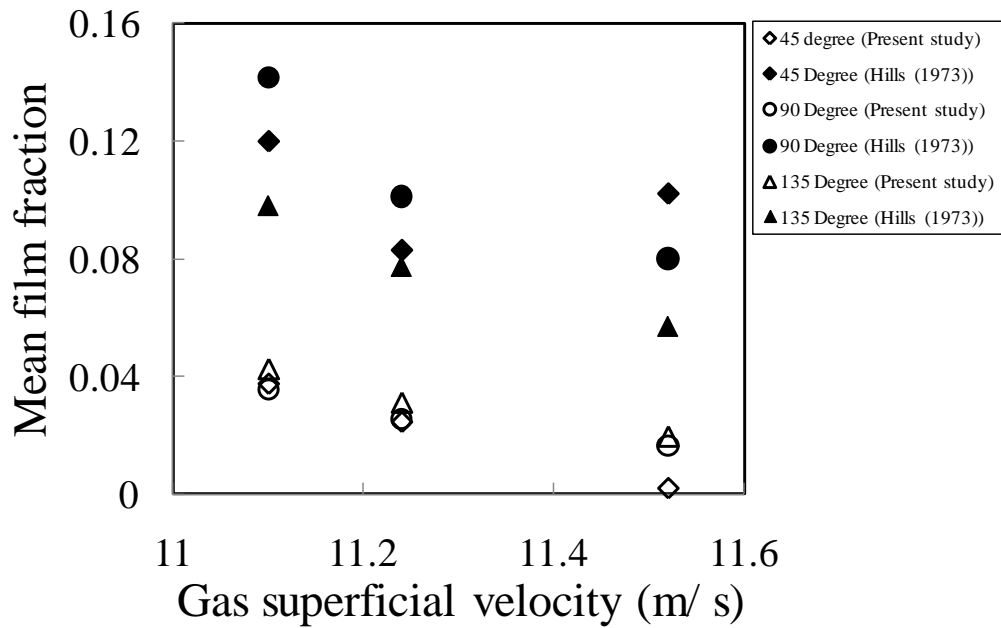


Figure 7.7: Comparison of mean film fractions (present study) with those of Hills (1973). Liquid superficial velocity = 0.04 ms^{-1}

7.2 Summary of the film fraction distribution around the 180° return bend:

The experimental study on the influence of a large diameter 180° return bend which is needed in the aspects of operational design and safety of the fired reboiler has been carried out. The observation of two-phase churn-annular flow behaviour and average film fraction around the bend yielded the following conclusions:

- 1) A remarkable similarity was observed between the shape of the time series of film fraction, PDF distribution and location of the frequency in the PDF and PSD plots of the three probes. This therefore, is an indication that equilibrium has been reached and therefore confirms the results reported in the literature that the flow is fully developed at 64 pipe diameters from the mixer.
- 2) The plot of the time series of dimensionless liquid film thickness at high liquid flow rate revealed the merging and collapsing of waves as they move from the

riser to the downcomer through the bends. The waves are created due to the high gas shear stress acting on the gas-liquid interface. The waves are able to remain on the gas-liquid interface because the gas inertia is able to overcome the gravitational force which may want to collapse them. Because of the wavy nature of the liquid film they lead to surface tension differentials and as a consequence disrupt it.

- 3) The average film fraction is found to be higher in the straight pipes than in bends. This is because at the bend the slip is less than that of the straight pipes and as a consequence results in a lower film fraction.
- 4) The study also found that at low gas superficial velocities that the average film fraction for the riser was generally greater than for the downcomer. This is because in downward flow (downcomer) the buoyancy force is acting on the gas phase in a direction opposite to the main flow, while in upflow (riser) it complements the main flow. The effect is such that the actual gas velocity is mostly greater in upward flow than in downward flow. This results in a higher film fraction for upward flow for the same liquid and gas superficial velocities.
- 5) For low liquid flow rates and high gas superficial velocities, film break down (burn out) occurs at the 45° position around the bend. The burn out phenomenon was clearly the result of total loss of liquid from the liquid film by evaporation and entrainment. This is confirmed by the liquid film thickness measurement.

- 6) The study found that the effect of gravity is insignificant at the highest gas superficial velocity. This is because the average film fraction for the riser is almost same as for the downcomer.
- 7) The condition for which the liquid goes to the outside or inside of the bend can be identified based on a modified form of Froude number, a proposal first made by Oshinowo and Charles (1974). A plot of the modified form of Froude number against gas superficial velocities was used to locate position of the liquid in the bend. From the plot, there was one combination of flow rate (Froude number equals to 1) where it was not clear whether it was liquid or gas which was on the outside of the bend. For flow rates which gave a low Froude number, the flow patterns in the riser approaching the 135° bend through the 45 and 90° bends was annular flow. For annular flow, since the gas superficial velocity is greater than that for the liquid and on the other hand the liquid density is much greater than that for the gas, gravity therefore dominates and the liquid moved to the inside of the 45, 90 and 135° bends. When the modified form of Froude number is negative it tells us furthermore that the liquid is being driven to the inside of the bend independently of gravity. For churn flow, the modified form of Froude number is > 1 and we would expect the liquid to move to the outside of the 45° bend, as in fact observed. As both the mixture move from the 90 to the 135° bend through the 45° bend, gravity slows them down and throws the liquid to the bottom of the bend and the gas to the outside.
- 8) The plot of liquid superficial velocity versus gas superficial velocity using the Usui et al. (1983) did not give a reasonably good agreement. At higher gas

superficial velocities, the two lines depicted in the map corresponding to the location of the liquid in the 90° and 135° bend positions are in contrast with the present study. Based on the present study, the liquid is inside the 90° and 135° bend locations for all the gas flow rates considered. In addition, Usui et al. (1983) did not present the 45° bend location in the map.

- 9) The comparison between the results of the plot of mean film fraction obtained from the present study and those of Hills (1973) showed the same tendency. Though, the values of mean film fraction obtained from the work of Hills are higher than those of present study. This might be due to the fact that the amount of entrainment of liquid drops in the gas core in large diameter pipe is greater than that of smaller pipes. Therefore there is less liquid in the film in the large diameter case.

7.3 Liquid film thickness:

Having concluded the film fraction distribution around the bend, this section will focus on the liquid film thickness distribution within the bend. It is worthy of mention that obtaining an estimation of the film fraction from the conductance ring probes will lead to an oversimplification of the results. This is because using the film fraction results to obtain liquid film thickness will be based on the assumption of an ideal annular flow in which the liquid flows as a smooth thin film on the pipe wall with the gas in the centre. However, in practice the liquid film is not smooth but is covered by a complex system of waves. These waves according to Hewitt and Whalley (1989) and Azzopardi and Whalley (1980) are very important as the sources of the droplets that are entrained in the gas core. According to Hills (1973) such waves will have large effects on the flow patterns

in the gas core and may interfere with the establishment of the secondary flow. Azzopardi et al. (1983) reported that the waves in large diameter pipes are circumferentially localised instead of being coherent around the circumference as observed by Hewitt and Lovegrove (1969) for smaller pipes.

In bends, the direction of the liquid film depends on the relative magnitude of the pressure, interfacial shear, centrifugal and gravity forces. The combined action of these components is to induce a secondary flow in the liquid film. In addition, the flow pattern is further complicated by entrainment from the liquid film into the gas phase and deposition of entrained droplets onto the film. The rate of entrainment depends on the liquid film thickness which is not uniform around the pipe wall. According to Hills (1973), centrifugal and secondary flow of the gas assist the transfer of droplets from the lower to the upper wall of the pipe.

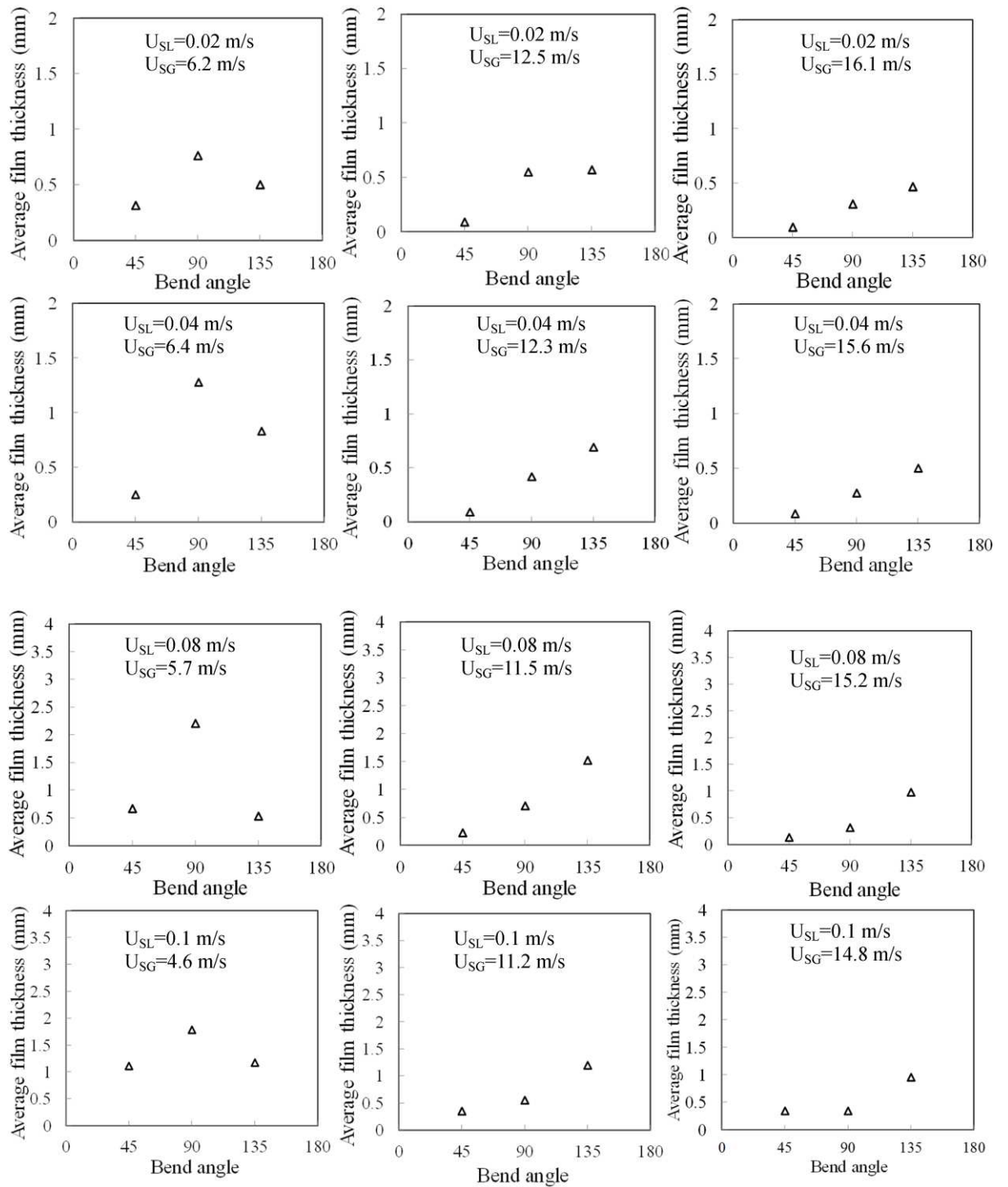
The averaging effect of the conductance rings can therefore result in differences in the time-varying data, as some details of the asymmetric nature of the liquid film thickness profiles can be affected. Therefore, the time varying results from the conductance ring probes might not represent accurately the roughness of the film that actually passes through bend. Therefore, conductance pin and parallel wire probes were used to measure liquid film thickness. Twenty pairs of conductance pin probes (round the circumference, mainly on the outside of the bend) and 5 pairs of wire probes (around the inside of the bend) were therefore used to measure the local values of liquid film thickness in the bend.

The following sections will focus on the liquid film thickness distribution in the bend and to confirm if conclusions drawn from smaller diameter pipes can hold true for larger ones.

7.3.1 Time averaged cross-sectional liquid film thickness in the 180° bends:

Figure 7.8 shows a plot of averaged liquid film thickness against bend angle for different liquid and gas superficial velocities. From the figure, the abscissa represents the bend angles considered in this study, 45, 90 and 135° while the averaged liquid film thickness is the ordinate. The averaged liquid film thickness was obtained by integrating over the cross-sectional area of the local film thickness. The description of the pin and wire probes may be found in Chapter 6.

One interesting observation made in this study is that over the range of liquid flow rates studied, the liquid flow rate has a significant effect on the liquid film thickness distribution in the bend. At the lowest gas and liquid superficial velocities, the position of the average liquid film thickness in the bend is like a scalene triangle. Here, the altitude which is at the 90° bend corresponds to the location of the thickest liquid film. This is not surprising because at the 90° bend position, gravity is dominant and as a consequence draining liquid from the top to the bottom of the pipe. Due to shear forces becoming more dominant than gravity at higher gas superficial velocities, the position of the average liquid film thickness in the 45, 90 and 135° bends is shifting from a triangular relationship to a linear one. Conversely, at the highest gas superficial velocity, the relationship between the average liquid film thickness and the bend angle is now linear. Though, more experimental data is required to substantiate this argument. Also, the linear relationship between the averaged liquid film thickness and the bend angle occurred sooner at higher liquid superficial velocities. This is because at higher liquid flow rates, entrainment is expected to be high, thereby provoking thickening of the liquid film around the 45 and 135° bends.



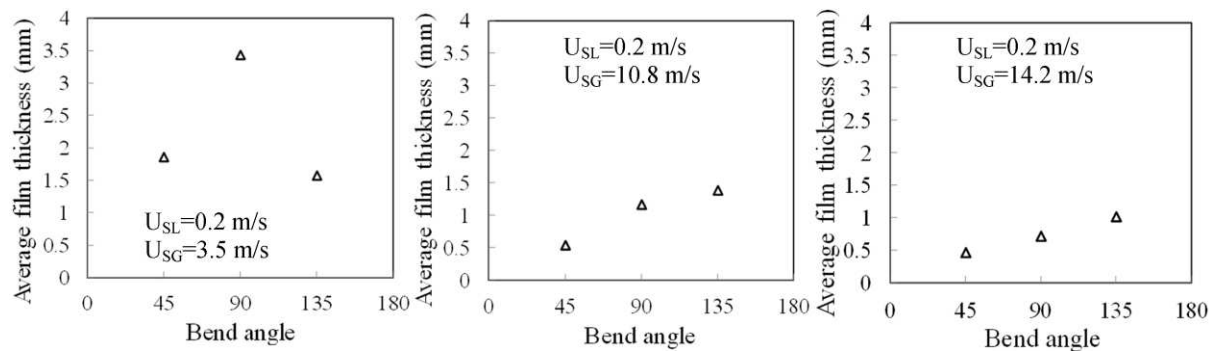


Figure 7.8: Variation of averaged liquid film thickness with the bend angle

At liquid and gas superficial velocities of 0.02 and 6.2 ms^{-1} , the relationship between the averaged liquid film thickness and the bend angle is like a scalene triangle and the 90° bend is the location of the maximum value. This is due to the fact that at this location the effect of gravity is more pronounced and as such drains the liquid to the bottom of the pipe. There is a gradual shift in the location of the maximum average liquid film thickness in the bend, from 90 to the 135° bend position as the gas superficial velocity is increased to 12.5 ms^{-1} . This is as a consequence of shear forces overcoming gravity and as a result more droplets are deposited at the walls (45 and 135° bends) supplied with liquid. The end result is that the liquid film at these locations becomes thick. However, because there are more droplets deposited at the 135° bend, the liquid film is thickest here. The entrainment/deposition theory also received some support from the experiments of Laurinat et al. (1985) using two horizontal pipes with internal diameters of 95.3 mm and 25.4 mm using air-water as the model fluid. They concluded that for the large diameter pipe, entrainment/deposition is the mechanism that maintains the liquid film at the top of the pipe. In addition, they observed waves only at the bottom of the pipe. On the other hand, for the smaller pipe, they concluded that the entrainment/deposition is a dominant factor only for liquid superficial

velocities lower than 0.015 ms^{-1} . At the highest gas superficial velocity, there is a linear relationship between the average liquid film thickness and the bend angle.

When the liquid superficial velocity is doubled to 0.04 ms^{-1} , and at gas superficial velocity of 6.4 ms^{-1} , the same trend that was observed for liquid and gas superficial velocities of 0.02 and 6.2 ms^{-1} , respectively is also seen here. The variation of average liquid film thickness with bend angle again is like a scalene triangle. Interestingly, the linear relationship between the average liquid film thickness and the bend angle took place much sooner than at the lowest liquid superficial velocity. This is because at higher liquid flow rates, entrainment is high thereby provoking thickening of the film at the 45 and 135° bends positions.

At a liquid superficial velocity of 0.08 ms^{-1} and gas superficial velocity of 5.72 ms^{-1} , as observed earlier, there is a triangular relationship between the average liquid film thickness and the bend angle. The 90° bend still remains the location of the maximum liquid film thickness. For gas superficial velocity of $9.9\text{-}13.1 \text{ ms}^{-1}$, the relationship between average liquid film thickness and bend angle is almost linear. At the highest gas superficial velocity, the tendency towards linear is diminishing.

When the liquid superficial velocity is increased to 0.1 ms^{-1} and gas superficial velocity of 4.6 ms^{-1} , the triangular relationship that was observed for liquid superficial velocities of $0.02\text{-}0.08 \text{ ms}^{-1}$ and lowest gas superficial velocities is also seen here. For higher gas superficial velocities, similar trends that were observed for the case of 0.08 ms^{-1} , liquid superficial velocity is also seen here.

At the highest liquid superficial velocity of 0.2 ms^{-1} and gas superficial velocity of 3.5 ms^{-1} , the relationship between the average liquid film thickness and the

bend is like a scalene triangle as indeed observed for the other liquid superficial velocities considered. As the gas superficial velocity is increased further, there is a gradual shift in the position of the film in the bend. At the highest gas superficial velocity, the relationship between the average liquid film thickness and the bend angle is linear.

7.3.2 Movement of the liquid film in the bend:

In Figure 7.2, the plot of dimensionless liquid film thickness with time revealed the merging and collapsing of waves as they move from the riser to the downcomer through the bends. The data, film fraction was obtained from conductance ring probes. The film fraction data was converted to dimensionless liquid film thickness to track the movement of the liquid around the bend. However, the drawback of the ring probes is that they provide cross-sectional averaged information and also assume that the liquid film is smooth as discussed in Section 7.3.

To investigate the movement of the waves with liquid and gas flow rates, some further analysis was carried out using the pin and wire probes. These two probes provide localised liquid film thickness distribution information. The analysis involved splitting the data into 1/15 seconds. This enabled the average liquid film thickness to be determined for every second. Below is a typical plot (Figure 7.9) of averaged liquid film thickness in the bend over an interval of 15 seconds. Here, the abscissa represents time in seconds and the ordinate represents the liquid film thickness averaged over an interval of every one second. The green, blue and red curves represent respectively, a trace of the average liquid film thickness for the 45, 90 and 135° bends. A close examination of the data shown on the plot shows

the movement of waves with time, and in particular the merging and collapsing of waves in the bend. Within an interval of 2 seconds, the liquid film (waves) at the 45° bend is greater than that at the 90° bend. The waves coming from the 45° bend merge with the one at the 90° bend and become much thicker after a duration of 3 seconds. Due to the high relative momentum of the liquid droplets at the 45 and 135° bends, the waves (films) within this vicinity are much thicker than at the 90° bend after an interval of 4 to 5 seconds.

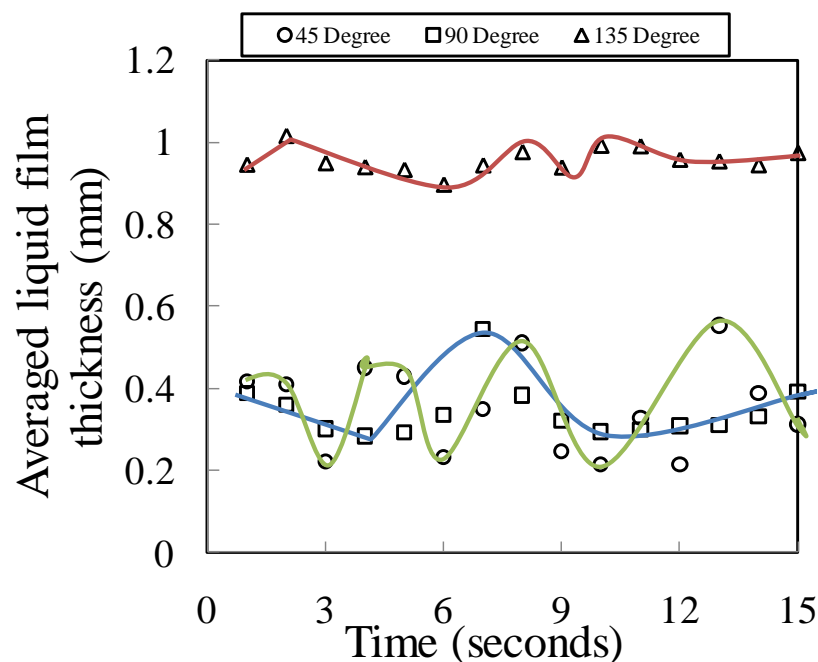


Figure 7.9: a typical average liquid film thickness distribution in the bend over 15 one second at liquid and gas superficial velocities of 0.1 and 14.8 ms⁻¹, respectively.

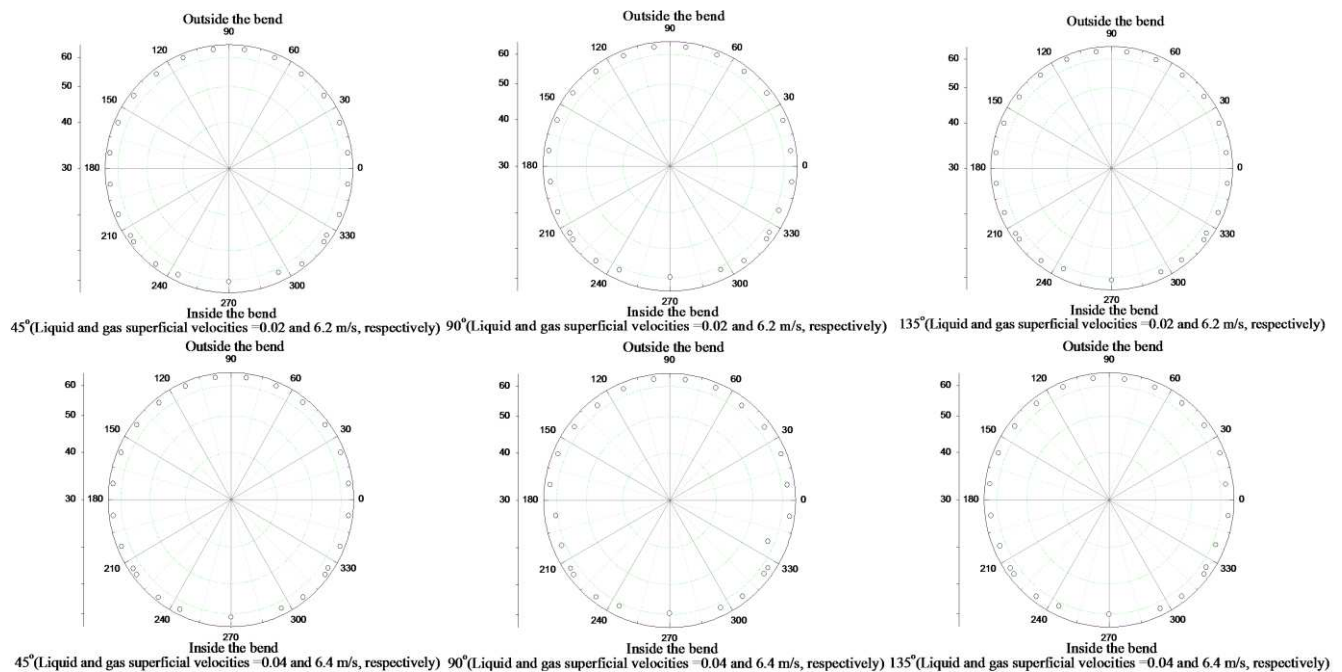
For 6 to 7 seconds, due to the merging wave's mechanism, the waves coming from the 45° meet with those at the 90° bend and as a consequence become thicker than the film at the 45° bend. A second later, because of the action of gravity part of the liquid film is drained at the 90° bend and some of it is collected at both the 45 and 135° bends. That is why the liquid film at the 45° bend is

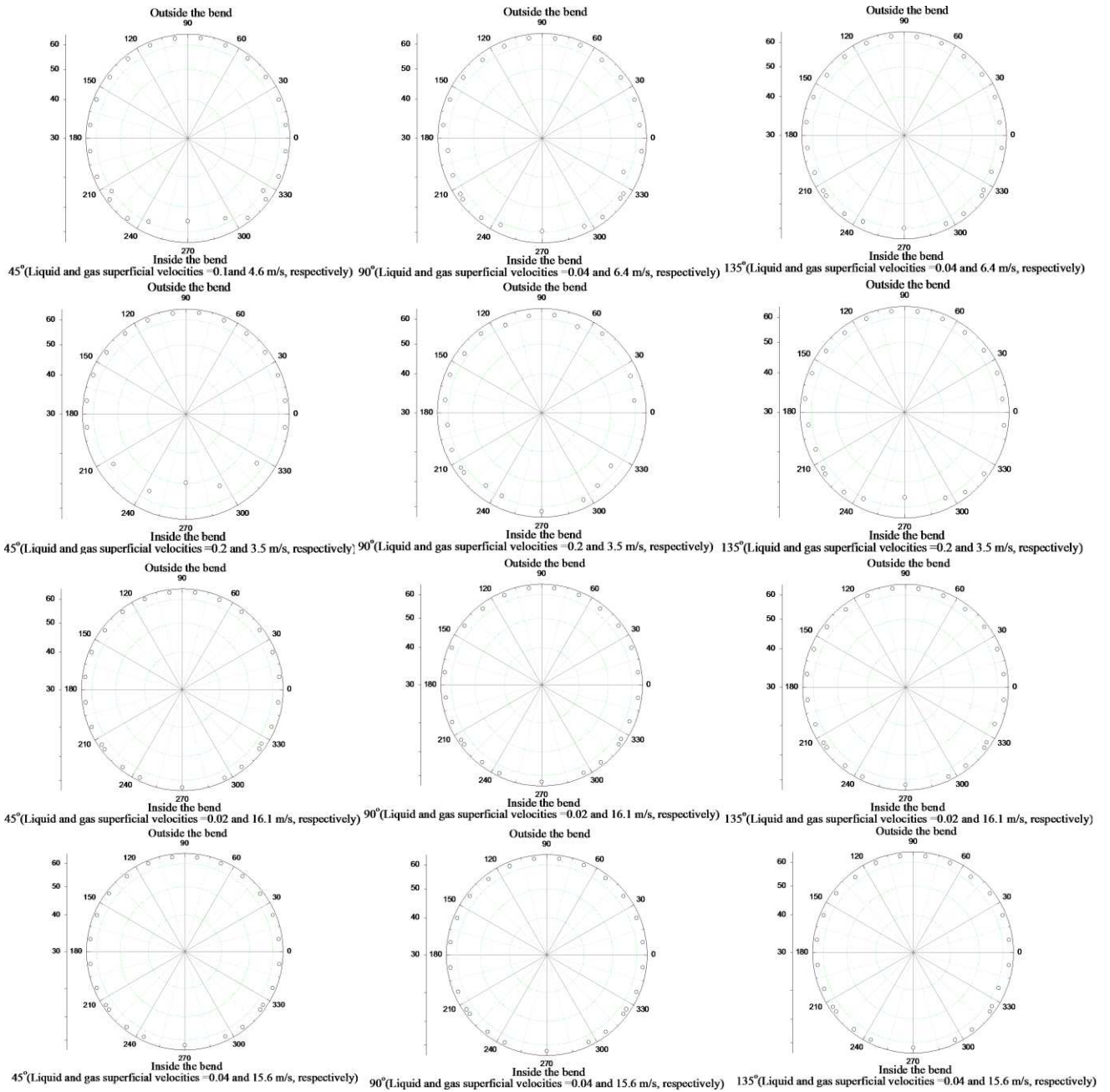
thicker than the 90° bend. However, the liquid film at the 90° bend becomes thicker than the 45° within the next 2 seconds. This trend seems to repeat itself, to follow a merging and collapsing of waves. It is the variation in the direction of these waves that could be the explanation for the observed shift in the average film thickness in the bend. According to Hills (1973), it is the effect of these disturbance waves projecting into the gas core which will break up the secondary flow pattern which is responsible for the asymmetry of the liquid film. The gas core will also be subject to a non-uniform shear stress from the varying liquid film thickness round the pipe, which will affect the position of the maximum velocity.

7.3.3 Circumferential liquid film thickness variation in the bend:

The variations of the liquid film thickness with four liquid flow rates (0.02, 0.04, 0.1 and 0.2 ms⁻¹) are shown in Figure 7.10. The form of the profiles varies with the liquid and gas superficial velocities. Here, the polar plots show that at lower liquid and gas superficial velocities, the liquid film distribution is not symmetrical for the three bend angles. However, at the highest gas superficial velocity, the liquid film is almost uniformly distributed around the bend. This is due to a balance between gravity, shear and circumferential drag forces. But at higher liquid superficial velocities, the liquid film becomes much thicker at the bottom and is significantly asymmetrical. The plots at the higher liquid flow rate show that the profile of the liquid film thickness changes significantly when the bend angle is increased from 45° to 135°. At the 45° bend position, the liquid film is thick at the inside of the bend. The thick film becomes a source of new droplets

and at the inside of the 90° bends location; the liquid film is thinner than at the 45° bend designation. At the inside of the 135° bend position, the liquid film is thicker than at the 90° but less than at the 45° bend. This may be due to deposited droplets falling down due to gravity drainage as a liquid film at the inside of the 135° bend position. Though, a thickening of the liquid film outside the three bends is also visible, most especially at the 90° and 135° positions. Because the ratio of average liquid film thickness to pipe diameter is very small, the variation of liquid film thickness cannot be seen clearly. It is in view of this development that subsequent results will be displayed in Cartesian coordinates. Figure 7.11 shows the variation of the time averaged liquid film thickness that occurs in the bend. Here, the abscissa is the circumferential angular position of the probes and the 90 and 270° are the top and bottom of the pipe. 0 and 180° represents the side of the bend.





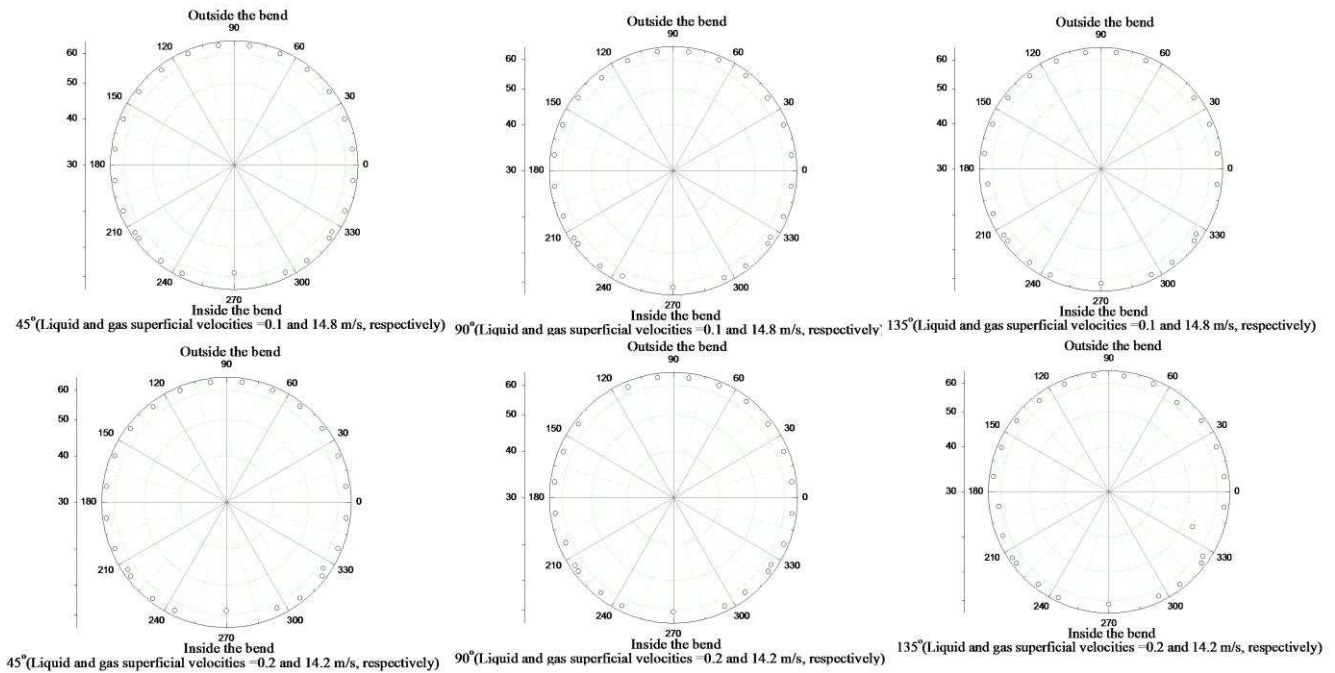
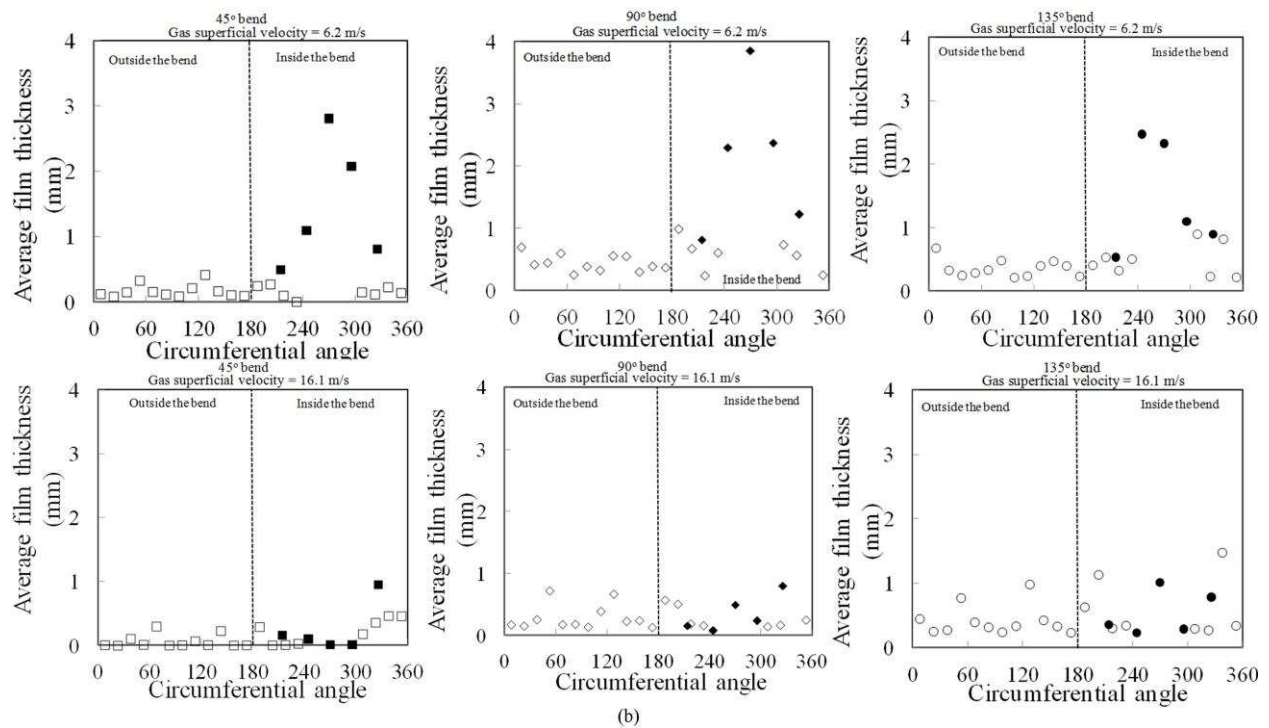


Figure 7.10: Polar plots of average liquid film thickness in the bend for different liquid and gas superficial velocities. Some points were omitted as shown in some plots based on the fact that they became saturated, most especially at higher liquid flow rates.

7.3.4 Spatial variations of the average liquid film thickness in the bend:

The average liquid film thickness profiles are presented in Figure 7.11 that were measured for the 45, 90 and 135° bends. The data collected can be used to understand the variation of liquid film thickness distribution with gas and liquid superficial velocities. Comparison of these profiles shows that the general form of these is greatly influenced by both the gas and liquid superficial velocities. The liquid film thickness inside the bend decreases with increasing gas superficial velocity as the increased interfacial shear produces liquid entrainment in the gas core. In spite of this decrease there are fewer tendencies for film breakdown to occur at higher gas rates except at the 45° bend. The same tendency, according to Hills (1973), has been observed for straight pipe horizontal flow with low liquid

rates where at higher gas rates stratified flow gives way to annular flow. A double peak attached to the maximum film thickness inside the 45, 90 and 135° bends was observed for all liquid flow rates. This double peaked liquid film thickness distribution is also exhibited by the data of Anderson and Hills (1974), Maddock et al. (1974) and Tkaczyk (2011). The appearance of these two peaks according to Tkaczyk (2011) results from the interaction between the secondary flow in the gas phase and the liquid film. The secondary flow takes the form of two concentric vortices. The gas phase is moving towards the inner part of the bend close to the liquid film and moves it towards the the outer part of the bend. Though, the peaks are more noticeable at the highest liquid superficial velocity. There amplitude decreases with an increase in gas superficial velocity.



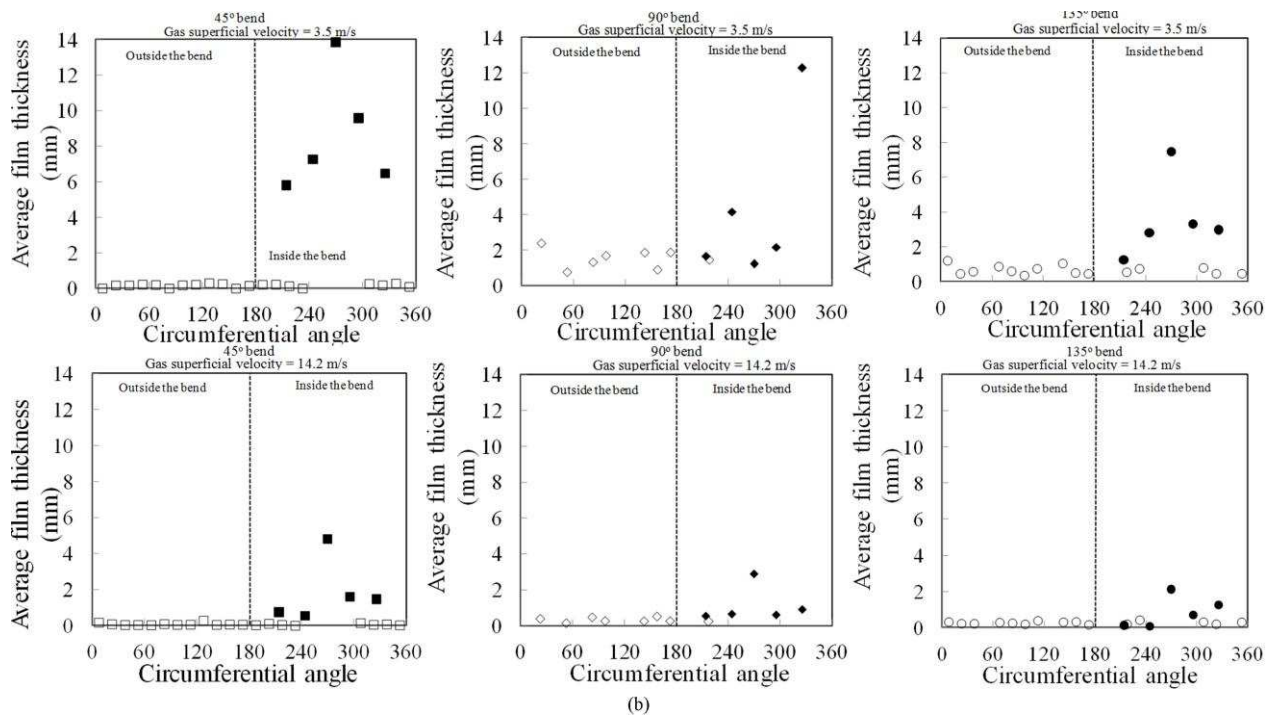


Figure 7.11: Spatial liquid film thickness distribution at liquid superficial velocity of (a) 0.02 ms^{-1} and (b) 0.2 ms^{-1} . Closed symbols-wire probes; open symbols-pin probes.

At low liquid superficial velocity of 0.02 ms^{-1} , the liquid film thickness inside the bend decreases with an increase in gas superficial velocity as shown in Figure 7.11 (a). In contrast, for the outside of the bend, the liquid film thickness increases and then remains almost constant with an increase in gas superficial velocity. Though, the liquid films are wavy. The decrease in liquid film thickness on the inside of the bend can be attributed to the high interfacial shear stress, bringing about an increase in liquid entrainment in the gas core. The increase on the other hand for the outside of the bend is a result of an increase in droplet deposition outside the bend. This is in agreement with the observations reported by Flores et al. (1995). Flores et al. (1995) confirmed that a secondary flow exists in horizontal annular flow using a twin axial vorticity meter. They concluded that at low gas velocity the major factor which transports liquid into the upper part of

the tube causing the transition from stratified to annular flow is the circumferential secondary flow in the gas core. That at higher gas velocities, the deposition of entrained liquid is a significant factor in transporting liquid to the top of the tube. In addition, the observations made here supports the arguments presented in Figure 7.8. At gas superficial velocity of 12.5 ms^{-1} , the location of liquid film inside of the bend in ascending order are 45° , 90° and 135° while for the outside also in the same order are 45° , 135° and 90° . It is worth mentioning that at higher gas flow rates, the film both inside and outside the 45° bend can be observed to thin out, suggesting that this could be a dryout region. The observation here supports the arguments presented in Figure 7.4 with regards to dry out occurring at the 45° bend at low liquid and higher gas superficial velocities. At higher gas superficial velocities (14 and 16.1 ms^{-1}) also, the location of the maximum and minimum liquid film thickness both inside and outside the bend shifts to the 135° and 45° bends, respectively. Though, the change in the magnitude of the liquid film thickness outside the bend is insignificant with an increase in gas superficial velocity.

As the liquid superficial velocity is doubled (Appendix C), a similar behaviour observed for liquid superficial velocity of 0.02 ms^{-1} is also seen here. The locations of the maximum and minimum liquid film thicknesses inside the bend at gas superficial velocity of 6.4 ms^{-1} are at the 90° and 45° bends. But as the gas superficial velocity is increased, the position of the former shifted to the 135° bend while the latter remained at the 45° bend. For the outside of the bend, the liquid film thickness decreases a little and then remained almost constant with an increase in gas superficial velocity. However, one interesting observation made

here is that at higher gas superficial velocities, the liquid film outside the 90 and 135° bends are greater than those inside the bend. Contrary to the results of Hills (1973) and Anderson and Hills (1974), it can be concluded that at liquid superficial velocity of 0.04 m/s and highest gas flow rate, the liquid film is thicker outside the 90 and 135° bends than the inside. This discrepancy may be attributed to the fact that they both used a bend with a curvature ratio 4 times that of the present study and as a consequence they observed more liquid been drained from the top to the bottom of the bend. According to Conte and Azzopardi (2003), the mechanism which provides liquid at the top of the pipe against the draining action of gravity is different in small and larger pipes.

For the highest liquid superficial velocity (0.2 ms^{-1}), the maximum liquid film thickness for the inside and outside of the bend are found at respectively, 45 and 90° as shown in Figure 7.11b. For the 45° bend, because liquid flow rate is high, the centrifugal force therefore has a greater influence and acts on it like a cyclone: throwing the liquid to the outside of the bend. Gravity on the other hand, drains the liquid to the bottom of the pipe. In addition, some of the liquid that is meant to move up to the 90° bend due to its lower momentum and curvature of the bend return back (back flow) to the 45° bend. These two scenarios could be the explanation for why the observed liquid film at the bottom of the 45° bend is thicker than the other locations, 90 and 135° bends. This observation supports the arguments made in Figure 7.5 with regards to the modified form of Froude number. Some of the liquid at the bottom and top of the 90° bend due to the action of gravity and shape of the curvature of the bend, drain down to the bottom of the 135° bend and accumulate there. Also the droplets that impinged on the

wall also deposit at the 135° bend. These could be the reason why the liquid film is thicker here than at the 90° bend. For the outside of the bend scenario, the liquid film is thickest at the 90°, followed by the 135° and thinnest at the 45° bend. The film is wavy. This is an indication that more liquid is drained from the top of the 45° bend. As a consequence of this drainage, the liquid film at the outside of the 45° bend thins out and become more uniformly distributed around it. The uniformity of the liquid film could be due to a balance of circumferential drag, shear and gravity forces. Another possible explanation could be that the pin probes that are meant to cope with thin liquid films could not see the expected thick films outside the 45° bend. As the gas superficial velocity is increased to 10.8 ms⁻¹, the locations of the maximum and minimum liquid film thickness remains unchanged. Though, the locations of the maximum average liquid film thicknesses inside the bend corresponding to the 45, 90 and 135° bends decreased by 65, 46 and 23 %, respectively. Interestingly, the position of maximum liquid film thickness inside the 90° bend shifted from 270° to 240°. At higher gas superficial velocities, 12.2 to 14.2 ms⁻¹, as expected the location of the liquid film inside the bends in increasing order are 135°, 90° and 45°, respectively. This therefore suggest that the reverse flow of liquid that was observed for the 90° bend at the lower gas superficial velocity is not seen here: most of the liquid is able to climb up into the bend and accumulate there. For the outside of the bend, most of the liquid at higher gas flow rate are being drained to the bottom of the bend and as a consequence the liquid thins out in the 3 bends.

It can be concluded that contrary to the observations reported by Hills (1973) and Anderson and Hills (1974), with regards to liquid film distribution at higher

liquid flow rates and lower gas flow rates, the liquid film thickness on the inside of the bend is indeed thicker than on the outside. Three reasonable explanations suggest themselves: (1) Anderson and Hills (1974) used a bend with a curvature ratio 4 times that of the present study and the implication is more liquid film is drained from the top to the bottom of the bend. (2) The ratio of surface tension to pipe diameter (drag force) in this study is small, experiments therefore suggest that the effect of gravity has overcome the circumferential drag and as a result the liquid film drains to the bottom of the bend. (3) The pin probes could not cope with thicker films > 2 mm and became saturated as consequence suggests a thinning of the liquid film. As the gas superficial velocity is increased further, the film at the outside of the bend drains out almost completely. The prevailing flow pattern therefore in the 3 bends is stratified flow.

7.4 Comparison between Experiments and Computational Fluid Dynamics (CFD) based on spatial liquid film thickness variation in the bend:

Some disagreements were observed in the data reported by Hills (1973), Anderson and Hills (1974) and the present experimental study with regards to liquid film distribution in the bend. The reason can be argued to be because the pipe diameter and radius of curvature are different. In order to actually find out if the present data is consistent, there was a need to compare experimental data against similar pipe configuration. Hitherto, no such experimental data was found available in the literature. The next option was to carry out CFD simulation exercise to address the discrepancy. The aim of this section therefore is to compare and verify whether CFD calculations are consistent with the experimental observations discussed earlier (Section 7.2 above). The CFD

calculations were carried out by Tkaczyk (2011) using similar pipe configuration and dimensions, fluid properties and operating conditions to the experiment. He handled the gas-liquid flow as a continuum gas field, continuum liquid film and as liquid droplets of varying diameters. He accounted for the dynamics of the droplet flow in the gas core and the interaction between them. He also solved explicitly the liquid film using a modified Volume of Fluid (VOF) method. He traced the droplets using a Lagrangian technique. The liquid film to droplet and droplets to liquid film interactions were taken into account using sub-models to complement the VOF model. He took into cognizance the fact that in free surface flows, a high velocity gradient at the gas/liquid interface results in high turbulence generation. In order to overcome this shortcoming, he implemented a correction to the VOF model based on the work of Egorov (2004). Full details can be found in Tkaczyk (2011). The model gives a reasonably good prediction of the liquid film thickness in the bend. Figure 7.12 shows the comparison between the Tkaczyk (2011) simulation results with experiment.

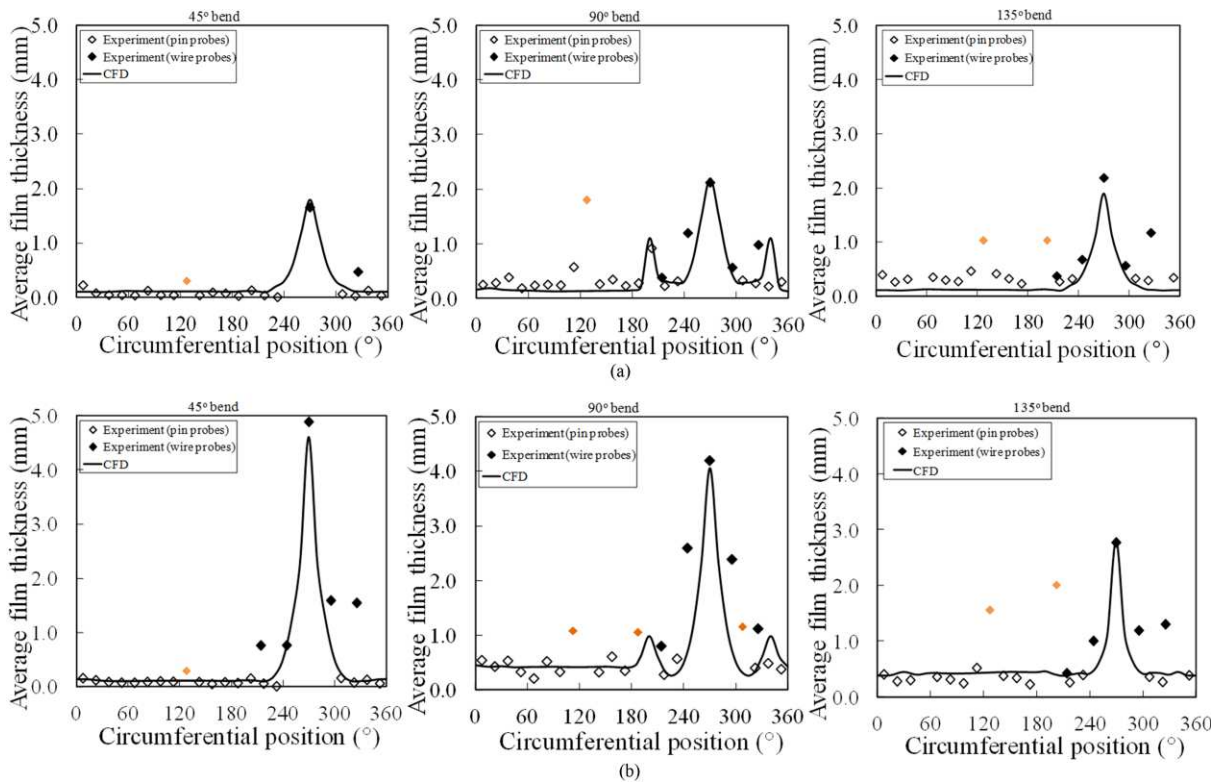


Figure 7.12: The distribution of liquid film thickness in the bend at (a) liquid and gas superficial velocities of 0.1 and 11.24 ms^{-1} , respectively and (b) liquid and gas superficial velocities of 0.2 and 12.5 ms^{-1} , respectively. Closed symbols-wire probes; open symbols-pin probes; grey symbols represents film thickness measurement with less confidence.

At liquid and gas superficial velocity of 0.1 and 11.24 ms^{-1} , respectively the model under predicts the film thickness outside the 90 and 135° bends. It also under predicts the maximum film thickness inside ($\theta = 270^\circ$) the 135° bend. Here the % error is 13.2. It is interesting to note that the model is able to predict the maximum film thickness inside the 45 and 90° bends. It is also able to predict the film thickness outside the 45° bend. Though, the error is 8.3 %. Another interesting observation made here is that the double peak found on the film thickness which Adechy and Issa (2004) made an effort to replicate without success is correctly predicted. Adechy and Issa (2004) used a Lagrangian/Eulerian approach to simulate annular flow in a T-junction. They

represented the liquid film as a thin film model based on the assumption that the liquid film is thin and behaves like a boundary layer, so that the dominant derivatives are in the direction normal to the flow. Although, the first and second peaks separated by the maximum film thickness are shown to occur respectively at a position 200° and 340° . The former occurring at 2.5° less than that found experimentally while the latter 14.2° more.

At the highest liquid superficial velocity of 0.2 ms^{-1} and gas superficial velocity of 12.5 ms^{-1} , the model is able to predict the maximum film thickness inside and outside the 135° bend except for some few points outside. The model under predicts the maximum film thickness inside the 45° and 90° bends. The % error of the former is 5.7 whilst for the latter, 3.3. However, it is able to predict the film thickness outside the 45° bend well.

It can be concluded therefore that the present experimental data have been used to validate models for the prediction of spatial film thickness variation in the bend.

7.5 Summary of liquid film thickness distribution in the bend:

A comprehensive set of measurements has been taken to study the effect of bend on the liquid film thickness distribution at various gas and liquid flow rates. The liquid film thickness distribution in the bend has been measured with pin and wire probes. With the former for measuring very thin films outside the bend while the latter for very thick liquid films inside the bend. These measurements have been supplemented by visual observation.

- For the lowest liquid and gas superficial velocities, the relationship between the average liquid film thickness and the bend angle is like a

scalene triangle with the position of the maximum value at the 90° bend. This is because at these flow rates and at the 90° bend, the effect of gravity is great and as a result, liquid films accumulate there. As the gas superficial velocity is gradually increased, the triangular relationship begins to diminish and tends towards linear. This is as a result of shear forces overcoming gravity and as a result the thickness of the liquid film at the 90° decreased while it increased at the other locations. At the highest gas superficial velocity, the relationship between them is linear. At higher liquid superficial velocities because of high degree of entrainment in the gas core, the tendency towards a linear relationship occurred much sooner than at the lowest liquid flow rate.

- Deposition of entrained droplets, which has a higher momentum than the gas which carries them, keeps the film on the outside of the bend supplied with the liquid. This is consistent with the observations reported by Flores et al. (1995). This will be of vital importance in applications where it is desirable to maintain a liquid film on the pipe wall.
- At higher liquid flow rates, although the liquid film thickness is always relatively high on the inside of the bend due both to the lower interfacial shear stress and to gravity drainage of the liquid film to the bottom of the pipe. The liquid film thins out in the three bends location. Gravity appears to be the main cause of this breakdown. The flow pattern is stratified flow.
- The comparison between CFD and experiment showed a very good agreement. The double peak found on the liquid film thickness which

Adechy and Issa (2004) made an effort to replicate without success is correctly predicted by Tkaczyk (2011).

CFD–Modelling and Solution Methodology

A considerable amount of research has been devoted to the study of this two-phase slug flow regime. Slug flow has received much attention from research workers: (Dumitrescu (1943); Moissis and Griffith (1962); Nicklin et al. (1962); White and Beardmore (1962); Brown (1965); Akagawa and Sekoguchi (1966); Wallis (1969); Collins et al. (1978); Fernandes et al. (1983); Mao and Dukler (1985); Mao and Dukler (1991); Barnea and Brauner (1993); DeJesus et al. (1995); Pinto and Campos (1996); Clarke and Issa (1997); van Hout et al. (2002); Brauner and Ullmann (2004); Taha and Cui (2006) among others. A critical review of this topic is given by Fabre and Line (1992). However, there remains much to be investigated and understood about that flow pattern. In particular, deeper investigation is needed to attain a thorough understanding of the internal structure of slug flow. Moreover, reports on slug flow behaviour with fluids which are relevant to the industry are limited. Empirical correlations and mechanistic models have been presented in the literature. These are mainly one-dimensional approaches that cannot fully characterise the flow. The limitations of one-dimensional models may be addressed by the use of Computational Fluid Dynamics (CFD). The applications of CFD to investigate multiphase flow are highly dependent on the flow pattern under study, as different closure models are

needed for different flow regimes. These models require to be validated to gain confidence in their use. The validation of CFD models requires experimental data that characterise the important flow parameters and over a wide range of values.

In this chapter, a description of the CFD model and the results obtained will be presented and discussed. Different slug flow characteristics (e.g. void fraction in liquid slug and Taylor bubble, lengths of liquid slug and Taylor bubble, slug frequency, structure velocity) are determined using the results of experiments and the solutions to the CFD models. In order for the simulation to be useful, the results that it yields must be a realistic representation of a fluid in motion. Therefore, the simulation was run under similar conditions as those used in the experiments so that a proper comparison between experiments can be performed. The agreement is found to be both qualitatively and quantitatively satisfactory.

Although it is true that CFD modelling cannot be a complete substitute for real experimental works, it however offers many opportunities which would not have been possible with physical experiments. CFD makes it possible to simulate different flow conditions and environments without the rigours and expenses required for real life experiments. It is worth mentioning that each type of modelling can profit from union with the other. Once a CFD model of a particular flow scenario has been validated as being of reasonable accuracy (by comparing with real experimental results), the parameters governing the fluid flow can then be varied to suit different flow conditions using CFD simulations.

8.1 Overview of Computational fluid dynamic (CFD)

8.1.1 Computational fluid dynamic (CFD)

Fluid flows and related phenomena are described by non-linear partial differential equations which, for most engineering problems, are impossible to solve analytically. It is however possible to obtain approximate numerical solutions to these equations by using a discretization method. This method approximates differential equations by a system of algebraic equations and the algebraic equations are then solved using a computer Ferziger and Peric (2002). This approach at solving engineering flow problems is the subject matter of Computational Fluid Dynamics.

Computational Fluid Dynamics (CFD) is a technique based on the numerical solution of the fundamental equations that govern fluid motion. According to Versteeg and Malalasekera (2007), computational fluid dynamics is the use of computer-based simulations to analyse fluid flow, heat and mass transfer and associated phenomena. This involves solving the mathematical equations that govern these processes, by using a numerical algorithm, which is provided on a computer. The solutions provided by this computational method have been found to be quite accurate in most cases, while at the same time providing greater insight into the physics of fluid flow. The use of CFD backed up by the great computing power available today is therefore having great impact on the understanding of fluid mechanics.

This branch of fluid dynamics called computational fluid dynamics complements experimental and theoretical fluid dynamics by providing an alternative cost-effective means of simulating real flows. As such it offers the means of testing

theoretical advances for conditions unavailable experimentally as noted by Fletcher (1991).

According to Fletcher (1991), CFD provides five major advantages compared with experimental fluid dynamics:

- Lead time in design and development is significantly reduced;
- CFD can simulate flow conditions not reproducible in experimental model tests;
- CFD provides more detailed and comprehensive information;
- CFD is increasingly more cost-effective than wind-tunnel testing;
- CFD produces lower energy consumption.

Presently, there are many software codes used for CFD simulations. The choice of any particular software would depend on such factors as: availability, cost, ease of use, computing speed and the application to the flow problem. The commercial CFD package Star-CD and/or Star-CCM+ are one of the codes that are widely used in the industry and were used in this research work. Star-CD provides comprehensive modelling capabilities for a wide range of fluid flow problems and has the ability to perform either steady-state or transient analyses Star-CD (2009).

8.1.2 Equations Governing Fluid Flow:

$$\frac{\partial(\rho u \phi)}{\partial x} + \frac{\partial(\rho v \phi)}{\partial y} + \frac{\partial(\rho w \phi)}{\partial z} = \Gamma \left(\frac{\partial^2 \phi}{\partial x^2} + \frac{\partial^2 \phi}{\partial y^2} + \frac{\partial^2 \phi}{\partial z^2} \right) + S_\phi \quad (8.1)$$

The term ϕ represents the transported property, the parameter Γ is the diffusion coefficient for scalar ϕ and S_ϕ represents the source term.

The above equations are the fundamental equations of motion for an incompressible fluid and are generally known as the Navier-Stokes (N-S) equations. With the Star-CD CFD code, discretization of the transport equation is done using finite volume formulation. In the finite-volume approach, the integral form of the conservation equations are applied to the control volume defined by a cell, to get the discrete equations for the cell (Versteeg and Malalasekera (2007)).

8.2 CFD Simulation Process:

There are three basic steps which are required of all CFD simulations. These are:

- Pre- processing: this step involves the definition of the geometry of the computational domain; grid generation and; the specification of appropriate boundary conditions.
- Solution: this is where the equations governing the fluid flow are solved by discretization and series of iterations, using a CFD code. This step also involves the definition of fluid properties and the selection of flow models.
- Post-processing: this involved interpreting and analysing the results obtained from Step 2 above

8.2.1 CFD Pre-Processing: Domain Discretization and Meshing:

Discretization is the process by which the partial differential or integral equations governing the fluid flow are replaced by a system of algebraic equations. These algebraic equations are then solved for the value of the flow field variable across a discrete network of grid points or cells.

In discretizing the computational domain, there are three main techniques for numerical solutions (Versteeg and Malalasekera (2007)). These are: the Finite

Difference, the Finite Element and the Spectral methods. While any of the three methods can be adopted in CFD modelling, the Star-CD code however uses the Finite Volume method, which is a special finite difference formulation used by most CFD codes.

The first step in the finite volume method is to define the computational domain and divide the domain into discrete control volumes or cells. This process is known as grid generation or meshing. This is followed by the specification of the appropriate conditions at cells which coincide with or touch the domain boundary.

The sizes and shapes of the generated grids have a significant impact on the accuracy of the CFD predictions. When the configuration to be modelled is complex, there may be challenges to satisfactorily discretize the computational domain. For complex geometry and configuration, an approach based on unstructured mesh was proposed by Kim and Boysan (1999). They stated that this approach enables CFD users to economically model complex geometry and complex flow phase. However, for relatively simple geometry, a structured mesh is generally adopted.

The geometry and grid generation process is carried out using specialized computer-aided drawing (CAD) software codes. All major CFD codes such as FLUENT, PHONENICS, CFX/ANSYS and Star-CD are equipped with their own CAD-style interface or provide the facilities to import data from proprietary surface modellers and mesh generators, (Versteeg and Malalasekera (2007)).

8.2.2 CFD Solution and Post-processing:

The CFD code Star-CD, uses the finite volume discretization technique to numerically solve the equations governing the fluid flow. The numerical algorithm adopted by the solution method consists of the following steps Versteeg and Malalasekera (2007):

- i. Integration of the fluid flow over the finite control volumes of the domain.
- ii. Discretization - This is the process of conversion of the resulting integral equations into algebraic equations.
- iii. Solution of the algebraic equations by an iterative method.

The solution process involves the selection of fluid properties, the specification of boundary conditions and the selection of the turbulence model to be used for the simulation.

CFD modelling can be applied to all types of fluid flow, either laminar or turbulent. While laminar flows could be said to be quite straight forward and easy to analyse, turbulent flow modelling do require some special considerations. For turbulent flows, the CFD codes use turbulence models to simulate the flows and solve the governing flow equations. The Star-CD code provides different choices of turbulence models which include: the Spalart-Allmaras Model; $k-\varepsilon$ model, $k-\omega$ model (k = turbulence kinetic energy, ε = turbulence dissipation rate, ω = specific dissipation rate); the v^2-f (velocity-mixture fraction) model; the Reynolds Stress Model; Detached Eddy Simulations (DES) model and; Large Eddy Simulations (LES) model Star-CD (2009). The choice of turbulence model will therefore depend on its applicability to the particular flow situation.

The solution of the equations governing fluid flow involves a number of assumptions and approximations that can have significant effect on the quality of the CFD prediction. The accuracy of CFD solutions for turbulent flows is dictated by the satisfactory choice of the turbulence model, especially for flows around structures because of the complex features of the resultant flow regimes. It has been recognized by CFD users that, the choice of turbulence models used to represent the effect of turbulence in the time-averaged mean-flow equations represents one of the principal sources of uncertainty of CFD predictions (Pope (2000) and Versteeg and Malalasekera (2007)).

In engineering applications, the most widely used turbulent models are the $k-\varepsilon$ turbulence models. These models are based on the Reynolds Averaged Navier Stokes (RANS) equations and have been used efficiently in the simulation of practical engineering flows (Versteeg and Malalasekera (2007)). However, their predictions may not always be completely satisfactory. For instance, the standard $k-\varepsilon$ model has been found to sometimes perform unsatisfactorily by over predicting results and therefore prompted the pursuit of better alternatives such as the Renormalization Group (RNG) and the Realizable $k-\varepsilon$ models Kim and Boysan (1999). The dissatisfaction with RANS models coupled with the increasing computing power has therefore made Large Eddy Simulation (LES) models more attractive to some CFD users. However, the $k-\varepsilon$ models still continue to enjoy wide usage and produce good results for many applications.

Also for the purpose of discretization, a differencing scheme is specified depending on whether the implicit or explicit scheme has been adopted and the order of solution accuracy required. A differencing scheme is required to

calculate the value of the transported fluid property at control volume faces and its convective flux across the boundaries which are stored in the cell centres Ferziger and Peric (2002). The different schemes which are used include: Central Differencing scheme, Upwind Differencing scheme, Power Law Differencing scheme, Quadratic Upstream Interpolation for Convective Kinetics (QUICK) Differencing scheme. The choice of differencing scheme will also depend on the type of model. Full explanations of the applications of these schemes are available in many CFD literatures (Versteeg and Malalasekera (2007)).

The results of the CFD simulations are presented as contours and vectors as well as path lines of the different flow properties such as velocity, pressure, temperature and turbulence. The analysis and interpretation of these results, and the application to real life flow situations is undoubtedly the main purpose of computational fluid dynamics.

8.3 Description of the problem:

Before presenting and discussing the relevant results in section 9.1 some basic features of the simulations will be stated in this section and the particular features for each individual case (inlet flow condition) will be shown in the subsequent sections. Two slug flow cases involving the riser and vertical 90° bend were simulated in this study using the commercial CFD code Star-CD and Star-CCM+ in order to solve the governing equations.

8.3.1 Computational domain:

The experimental arrangements were described in Chapter 3. The geometries for the case studies modelled are illustrated in Figures 8.1 and 8.2. Figure 8.1 is a 67

mm internal diameter pipe and 6 m long riser while Figure 8.2 is a vertical 154.4 mm radius of curvature 90° bend connected to the riser arrangement (Figure 8.1). In order for the simulation to produce meaningful results, it was important to ensure that the geometry of the flow domain faithfully represented the experimental arrangement. Hence, a full 3-Dimensional flow domain, as shown in Figure 8.1, was considered based on the fact that the flow simulated has been found to be axisymmetric according to the conclusions of the previous experimental studies of Azzopardi et al. (2010) and Hernandez-Perez et al. (2011). These investigations employed conductance wire mesh sensor (WMS) to look at the flow distribution in a 67 mm internal diameter and 6 m length vertical pipe. They concluded that the classical Taylor bubble shape is rarely obtained in that pipe diameter. For the slug flow in a vertical riser study, three CFD measurement sections were located at positions similar to those of the experimental work, namely, at distances of 4.4 m, 4.489 m and 4.92 m above the base of the riser. Here, the locations 4.4 m and 4.489 m represent the two electrical capacitance tomography (ECT) planes, whilst 4.92 m the wire mesh sensor (WMS). On the other hand, for the slug flow in a vertical 90° bend case, the location of the measuring instrument (ECT and WMS) upstream of the bend is same as for the riser case. However, only the WMS was used after the bend, and it was placed at 0.21 m downstream of the bend. These measurement positions are also similar to those of the experimental work. Air and silicone oil are injected at the inlet section of the pipe, then the two-phase mixture flows upwards through the vertical riser pipe, finally discharges through the outlet at atmospheric pressure. The relevant fluids properties are shown in Table 3.1.

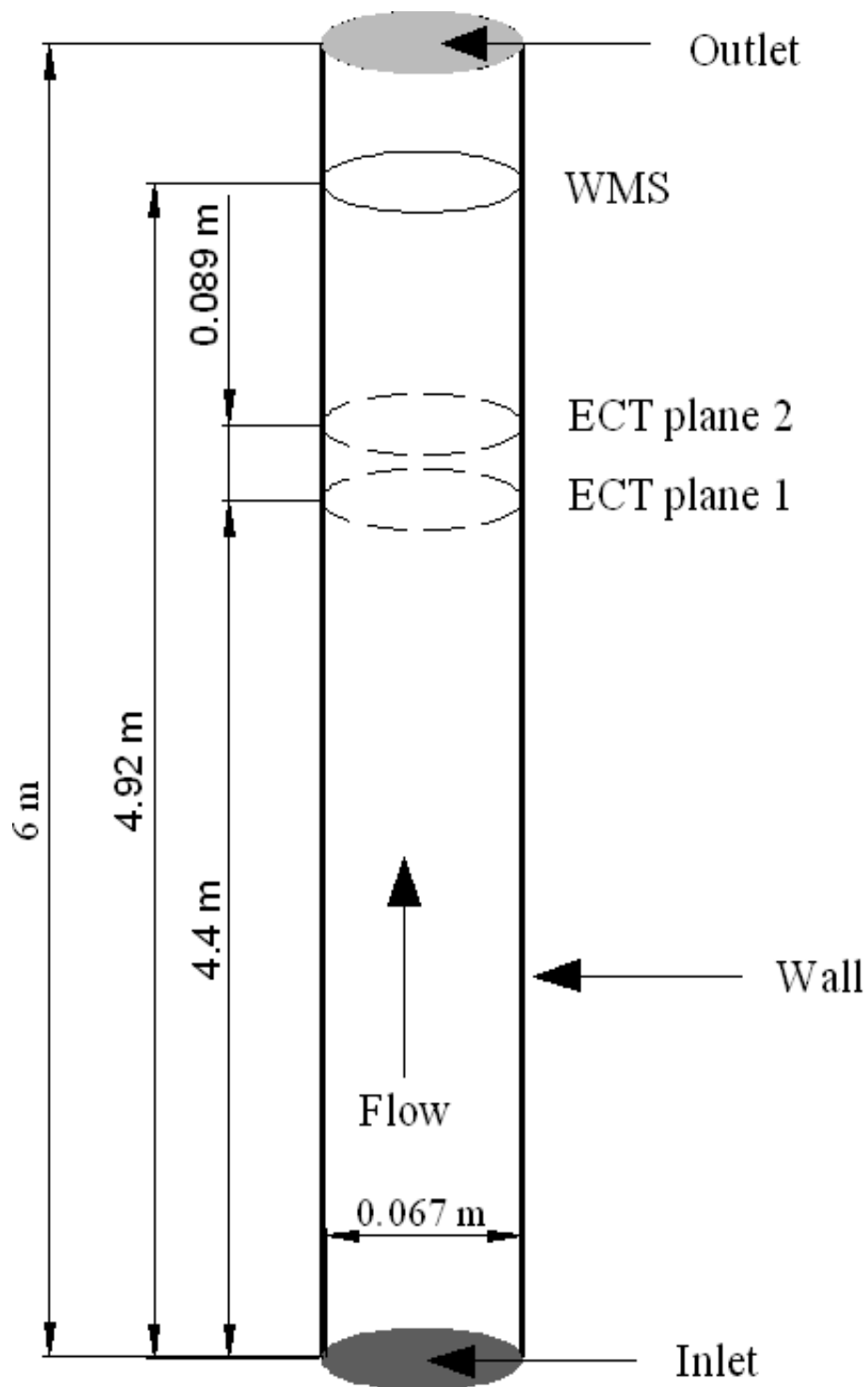


Figure 8.1: 3-D geometry of the computational flow domain showing the location of the recording sections that correspond to the locations of the experimental measurement transducers.

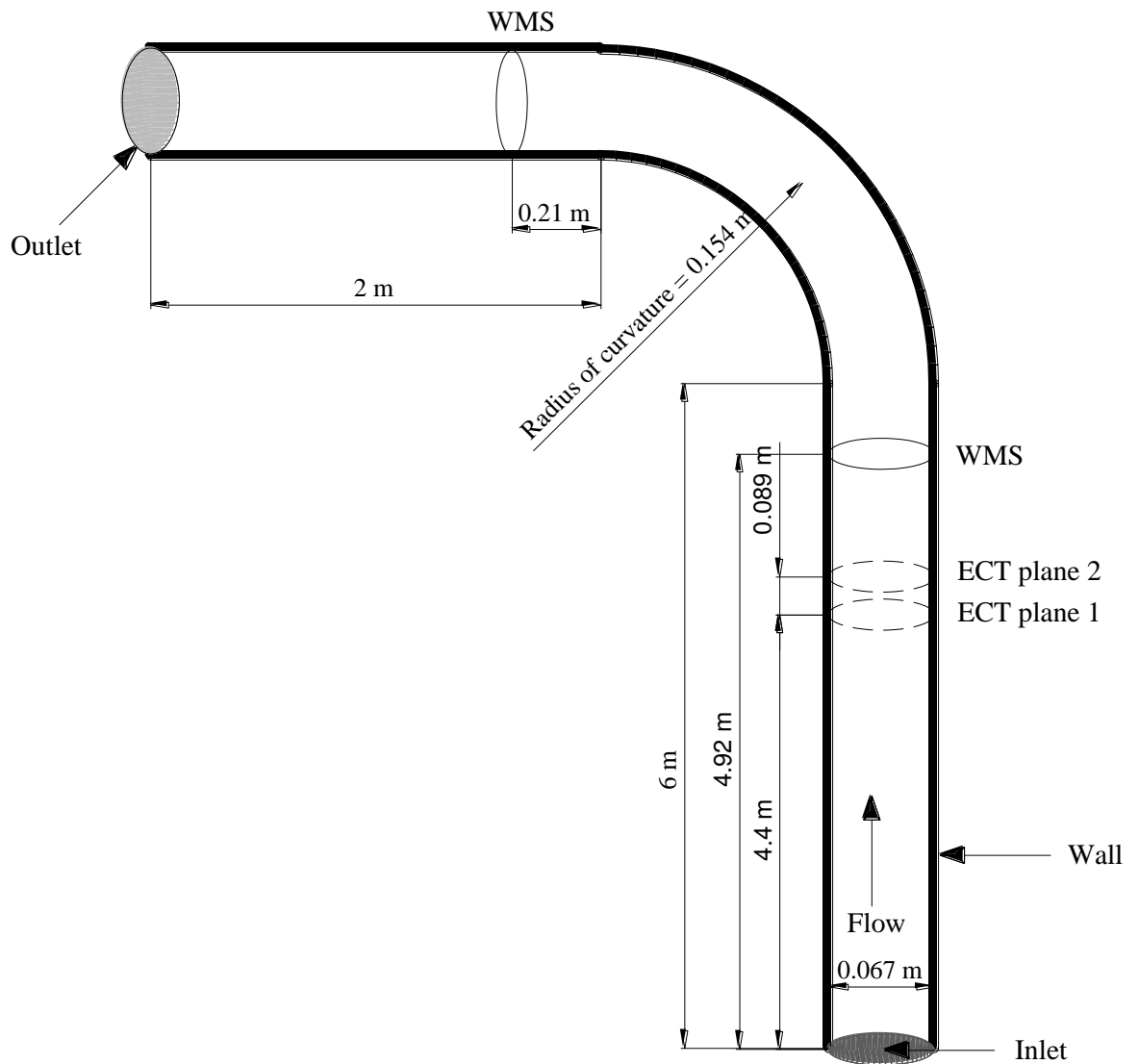


Figure 8.2 3-D geometry of the computational domain showing the measurement locations and instrumentation

8.3.2 Boundary conditions:

Once the mesh was generated, the boundaries of the computational domain were specified. Boundary type specifications define the physical and operational characteristics of the model at those topological entities that represent model boundaries. It is worth mentioning that the imposition of boundary conditions depends on the physics of the problem and have to be treated with care. Hence, the boundary conditions were chosen based on the experimental setup described

in Chapter 3. These conditions are summarized below.

The summary of the boundary specifications is as follows:

Inlet (Velocity inlet) Dirichlet Boundary condition $\hat{n} \cdot \bar{v} = U_o$

Outlet (Pressure outlet) Dirichlet Boundary condition $P = P_o$

Wall.....Wall $\hat{n} \cdot \bar{v} = \hat{t} \cdot \bar{v} = 0$

Where $\hat{n} \cdot \bar{v} = \text{no penetration}$ and $\hat{t} \cdot \bar{v} = \text{no slip}$

All solid boundary walls were assumed to possess a non slip boundary condition, where $v = 0$. At the flow inlet at the base of the riser, a velocity-inlet boundary type is used in which the mixture superficial velocity and the liquid void fraction are specified. The velocity profile is assumed to be uniform. This approach according to Hernandez-Perez (2008) requires no additional experimental knowledge about the slugs in order to setup the numerical simulation. This is also similar to the way experimental work has been carried out (see Chapter 3 for details about the mixing section design). The inlet values for turbulent kinetic energy, k , and its dissipation rate, ε , are estimated using the following equations proposed by Launder and Spalding (1974):

$$k_{in} = \frac{3}{2} I^2 U_{in}^2 \tag{8.2}$$

$$\varepsilon_{in} = 2k_{in}^{3/2} / D \tag{8.3}$$

$$I = \frac{0.16}{Re^{1/8}} \tag{8.4}$$

Where I is the turbulence intensity for fully developed pipe flow.

The walls of the pipe are assumed to be rigid and impermeable, in which the wall roughness was set as a smooth wall. A no-slip condition is applied to the velocity

where there is contact at solid walls at any instant. Close to the wall, the standard wall function approach also based on the Launder and Spalding (1974) was employed to predict accurately the flow close to the walls. At the flow outlet at the top of the riser and top of the horizontal pipe (downstream of the vertical 90° bend), the remaining variables are transported out of the computational domain with zero average static pressure so that the mass flow balance is satisfied. The operating conditions were specified as being standard atmospheric pressure (101.3 kPa) and temperature 20°C. Gravity effects are accounted for and the acceleration due to gravity to be -9.81 ms^{-2} on the vertical.

8.3.3 Initial conditions:

At time $t = 0$ second all velocity components are set to 0 ms^{-1} ($t = t_0 \quad \hat{n} \cdot \bar{v} = V_0$).

For the liquid volume fraction, the specified initial condition depended on the case under study; for the riser pipe and vertical 90° bend flow cases the initial condition was the pipe full of air or silicone oil. These initial conditions ease the convergence process. In addition, an initial guess for the turbulent kinetic energy and the dissipation rate was applied in all the simulations studied.

8.3.4 CFD Model:

This software family, Star-CD and Star-CCM+ was used to simulate the motion of the Taylor bubbles rising in a flowing liquid through a vertical 67 mm internal diameter: (1) 6 m height riser and (2) 6m riser connected to a horizontal flowline via a vertical 90° bend. The Finite Volume method was employed to numerically discretize the computational flow domain. The movement of the modelled gas-liquid interface is tracked based on the distribution of, α_{G_i} , the volume fraction of

gas in a computational cell; where $\alpha_G = 0$, is a liquid cell and $\alpha_G = 1$ in a gas phase cell, Hirt and Nichols (1981). Therefore, the gas-liquid interface exists in the cell where α_G lies between 0 and 1.

8.3.5 Governing equations:

The motion of an incompressible two-phase slug flow under isothermal conditions has been considered as the flow scenario in the present work. The assumption of an isothermal flow is a reasonable approximation for pipes which have a large surface area to volume ratio and a constant temperature. The Volume of Fluid (VOF) method, based on the Eulerian approach, implemented in the commercial CFD package Star-CCM+ is used in the numerical simulation.

The VOF method is an interface tracking technique that captures the interface between the phases. This powerful tool according to Kvicinsky et al. (1999) allows the simulation of complex free surface flows with an arbitrary shape in any situation including folding or break-up. Rhee et al. (2004) concluded that as long as the interface resolution and conservation of mass, momentum, and energy flow is ensured by use of proper numerical technique, the VOF method is accurate enough to capture essentially flow features around the free surface. According to Hernandez-Perez (2008), it is possible to handle mass and heat transfer through the interface using the VOF method. It is important to keep in mind that the VOF method has its limitations. The fact that the two fluids are assumed to share the same momentum equations restricts the suitability of it for cases where the difference in the velocity between the two fluids is significant. Despite this, the VOF method is a very popular tracking algorithm that has proven to be a useful and robust tool since its development, and is therefore a

frequent choice in Eulerian models of interfacial flows DeJesus (1997). In addition, Star-CCM+ (2009) uses a High Resolution Interface Capturing Scheme (HRIC) based on the Compressive Interface Capturing Scheme for Arbitrary Meshes (CISCAM) introduced by Ubbink (1997) and enhanced by Muzaferija and Peric (1999). In the VOF method, the fields for all variables and properties are shared by the phases and represent volume-averaged values, as long as the volume fraction of each of the phases is known at each location, and to maintain the mass balance in the system the continuity equation is also solved. The body forces in the momentum equation consist of gravitational and surface tension forces. Surface tension along an interface arises as a result of attractive forces between molecules in a fluid. In the VOF method, surface tension is introduced by adding a momentum source. The momentum equation, equation (8.6), is dependent on the volume fractions of all phases through the properties ρ and μ .

The mass, momentum and volume fraction conservation equations for the two-phase flow through the domain are represented as:

$$\frac{\partial \rho}{\partial t} + \frac{\partial \rho u_i}{\partial x_i} = 0 \quad (8.5)$$

$$\frac{\partial \rho u_j}{\partial t} + \frac{\partial \rho u_i u_j}{\partial x_i} = -\frac{\partial P}{\partial x_j} + \frac{\partial}{\partial x_i} \mu \left(\frac{\partial u_i}{\partial x_j} + \frac{\partial u_j}{\partial x_i} \right) + \rho g_j + F_j \quad (8.6)$$

Where, P , g and F indicate, respectively, the pressure, the gravitational acceleration and the external force per unit volume. The momentum equation, shown above, is dependent on the volume fractions of all phases through the properties density (ρ) and viscosity (μ). For a two-phase flow system, if the phases are represented by the subscripts 1 and 2 and the volume fraction of the phase 2 is known, the ρ and μ in each cell are given by the following equation:

$$\rho = \alpha_2 \rho_2 + (1 - \alpha_2) \rho_1, \mu = \alpha_2 \mu_2 + (1 - \alpha_2) \mu_1 \quad (8.7)$$

The interface between the two phases can be traced by solving the continuity equation for the volume fraction function:

$$\frac{\partial \alpha_q}{\partial t} + \frac{u_i \partial(\alpha_q)}{\partial x_i} = 0 \quad (8.8)$$

Where u_i and x_i denote, respectively, the velocity component and the co-ordinate in the direction i ($i = 1, 2$ or 3), t , being the time; and through the resolution of the momentum equation shared by the two considered fluids.

The primary-phase volume fraction will be computed based on the prevailing condition: the volume fraction equation for the primary phase in equation (8.8) will be obtained from the following equation:

$$\sum_{q=1}^n \alpha_q = 1 \quad (8.9)$$

The continuum surface force (CSF) model proposed by Brackbill et al. (1992) was used to model the surface tension. The proposed model considers the surface tension as a volume force across an interface rather than as a free surface boundary condition. The use of the CSF model to introduce surface tension to the VOF model calculation results in the addition of a source term to the momentum equation (8.6).

The numerical solution of these sets of equations was performed using the software package Star-CCM+. A second order discretization scheme was used to determine the fluxes at the control volume faces required by the VOF model.

8.3.6 Turbulence model:

As the Taylor bubbles rises through the liquid, even at low flow rates, a developing liquid film is created around the bubble and a wake at its tail. Therefore, turbulence must be considered in the numerical simulation. The accuracy of CFD solutions for turbulent flows can be affected by turbulence modelling, the complex features of the flow. As documented by Pope (2000) and Versteeg and Malalasekera (2007), it is recognised that the choice of turbulence model used to represent the effect of turbulence in the time-averaged mean-flow equations represents one of the principal sources of uncertainty of CFD predictions. According to Pope (2000), turbulence effects are a major source of non-linearity in the discretised equations. In order to simulate turbulence, the standard k- ϵ model, Launder and Spalding (1974) was used for this study as suggested by the multiphase flow studies of Ramos-Banderas et al. (2005) and Cook and Behnia (2001). Since 1974, the k- ϵ model has become the most widely used turbulence model in the engineering industry DeJesus (1997).

The k- ϵ turbulence model assumes that the rate of production and dissipation of turbulent flows are in near-balance with energy transfer, so that the dissipation rate, ϵ , of the energy is given as,

$$\epsilon = \frac{k^{3/2}}{L} \quad (8.10)$$

Where k is the kinetic energy of the flow and L is the length involved. The dissipation rate, ϵ , is in turn related to the turbulent viscosity μ_t based on the Prandtl mixing length model

$$\mu_t = \rho C_\mu \frac{k^2}{\varepsilon} \quad (8.11)$$

Where C_μ is an empirical constant and ρ is the density of the flow.

The model is described by the following elliptic equations required as closure for the Reynolds Averaged Navier Stokes (RANS) equations:

The k-equation:

$$\frac{\partial(\rho k)}{\partial t} + \underbrace{u_i \frac{\partial(\rho u_j k)}{\partial x_j}}_{\text{Convection term}} = \underbrace{\frac{\partial}{\partial x_j} \left(\frac{\mu_t}{\sigma_\varepsilon} \frac{\partial k}{\partial x_j} \right)}_{\text{Diffusion term}} + \underbrace{\mu_t \frac{\partial u_i}{\partial x_j} \left(\frac{\partial u_i}{\partial x_i} + \frac{\partial u_j}{\partial x_j} \right)}_{\text{Production term}} \underbrace{\frac{\partial u_i}{\partial x_j}}_{\text{Destruction term}} - \rho \varepsilon \quad (8.12)$$

The ε - equation:

$$\frac{\partial(\rho \varepsilon)}{\partial t} + \underbrace{u_i \frac{\partial(\rho u_j \varepsilon)}{\partial x_j}}_{\text{Convection term}} = \underbrace{\frac{\partial}{\partial x_j} \left(\frac{\mu_t}{\sigma_\varepsilon} \frac{\partial \varepsilon}{\partial x_j} \right)}_{\text{Diffusion term}} + \underbrace{C_{\varepsilon 1} \frac{\varepsilon}{k} \mu_t \frac{\partial u_i}{\partial x_j} \left(\frac{\partial u_i}{\partial x_j} + \frac{\partial u_j}{\partial x_i} \right)}_{\text{Production term}} - \underbrace{\rho C_{\varepsilon 2} \frac{\varepsilon^2}{k}}_{\text{Destruction term}} \quad (8.13)$$

The inherent production of turbulence is what is responsible for the transfer of energy from the mean flow to the turbulence, and is counterbalanced by the interaction of the Reynolds stresses and mean velocity gradient. On the other hand, the destruction term represents the dissipation of energy into heat due to viscous nature of the flow Fokeer (2006).

In the above equations $\sigma_k, \sigma_\varepsilon, C_\mu$ and $C_{\varepsilon 1}$ and $C_{\varepsilon 2}$ are constants whose values are 1.0, 1.3, 0.09, 1.44 and 1.92 respectively, u_i is the i component of the fluid velocity u , x_j is the j spatial coordinate. The fluid viscosity must be corrected for

turbulence in the Navier-Stokes equations by employing an effective viscosity $\mu_{\text{eff}} = \mu + \mu_t$ where μ is the dynamic viscosity and μ_t is the turbulent viscosity.

8.3.7 Discretization and method of solution:

In order to numerically solve the system of governing partial differential equations, discretization of the equations has been carried out using a Finite Volume Method (FVM) with an algebraic segregated solver and co-located grid arrangement, as implemented in Star-CCM+(2009). Pressure and velocity are both stored at cell centres in this grid arrangement. Details of the discretization (FVM) can be found elsewhere (e.g. Versteeg and Malalasekera (2007)) and are hence omitted here. The continuity and momentum equations need to be linked based on the fact that the Star-CCM+ uses a segregated solver for the VOF model. To achieve the linkage, various techniques are reported in the literature. The Semi-Implicit Method for Pressure-Linked Equations (SIMPLE) algorithm, (Patankar and Spalding (1972)), is applied as it produces a fast and convergent solution. In addition, the iterative solver was further improved by the use of an Algebraic Multigrid (AMG) technique to yield a better convergence rate.

8.3.8 Solver controls:

All simulations in this work are performed under time dependent conditions. For a time dependent solution scheme, the main controlling factor is the time step chosen. This should be set to give as small a number of time steps as possible, whilst maintaining a smoothly converging solution. If too large a time step is chosen, then the solution may change too much and consequently may diverge. More information on the time step is discussed under stability constraints (see Section 8.3.10).

Within each solution time interval, iterations are carried out to solve the transport equations for that time step. For this iteration process to converge, it may be necessary to control the change of the variables from one iteration to the next. This is achieved by the use of under relaxation factors. Under relaxation factors of 0.3, 0.7 and 0.8 respectively, were applied on pressure, momentum and turbulence kinetic energy parameters, as recommended by Star-CCM+ (2009).

An assessment of the degree to which the solution has converged may be obtained by plotting the residuals errors for each equation at the end of each time step. The maximum permitted residual determined was set to be 10^{-4} .

8.3.9 Grid generation:

The first step in the finite volume method was to divide the flow domain into discrete control volumes. This is the process known as grid generation or meshing. In meshing the flow domain, a structured mesh approach was adopted. This was done in order to achieve the desired grid density at different parts of the flow domain. The flow domain was therefore divided into three different faces with each face meshed separately to achieve the desired results. It has been reported by Hernandez-Perez et al. (2011) and confirmed by this study that it is important to adopt high quality mesh generation standards to ensure the convergence and accuracy of the numerical simulation. The models, riser and vertical 90° bend flow geometries were built and meshed with Star-CD, then imported into Star-CCM+, where the computation and post-processing of the results were performed. The geometries of the mesh employed is the butterfly grid (O-grid), which has been successfully employed by Hernandez-Perez (2008),

Lo and Zhang (2009), Hernandez-Perez et al. (2011), and Tkaczyk (2011). Figure 8.3 shows the meshes for the riser and vertical 90° bend used for the CFD simulation. It uses a Cartesian mesh at the centre of the pipe combined with a cylindrical one around it. According to Hernandez-Perez (2008), the O-grid (butterfly grid) allows for a good representation of the boundary layer and it is adequately stretched along the longitudinal axis. It requires multiple blocks but generally has the best grid quality in terms of orthogonality and mesh density.

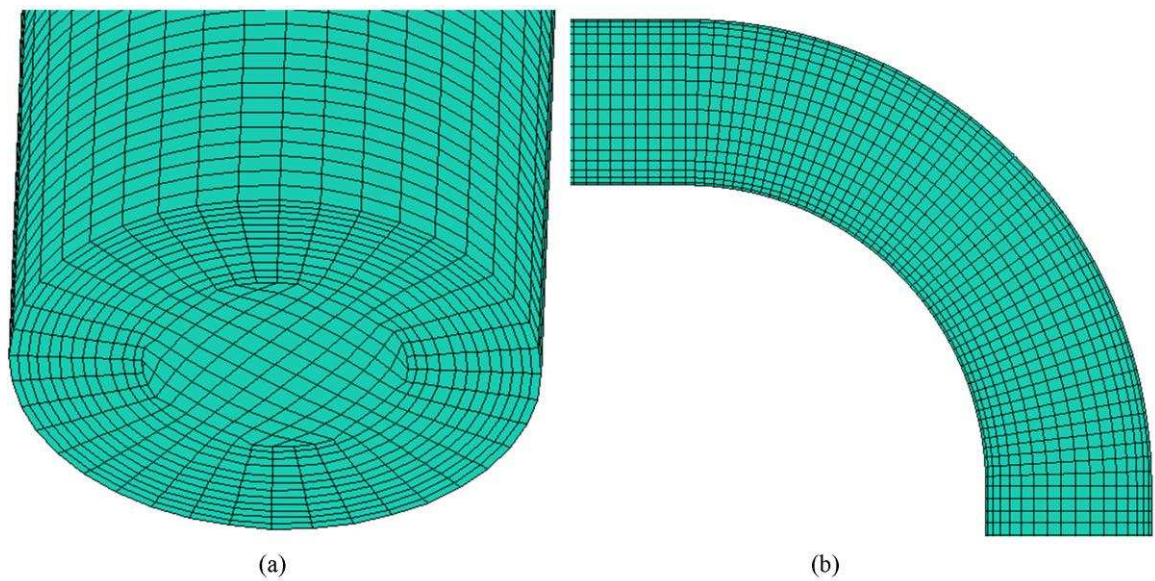


Figure 8.3: Computational mesh used for simulations (a) riser and (b) vertical 90° bend used for the CFD simulation.

The region near the wall is meshed finer than the rest of the cross-section, as it contains the maximum amount of gradients. It is imperative to know the distance of the first node above the wall $y(1)$ when using wall functions; this is to ensure that the normalized wall distance (y^+) values remain within 20-100. The following equation is used Star-CCM+ (2009)

$$y = y^+ L / \left(\text{Re} \sqrt{\frac{C}{2}} \right) \quad (8.14)$$

Here L is the characteristic length, diameter in case of a circular pipe,

$$\frac{C_f}{2} = \frac{0.039}{\text{Re}^{0.2}} \quad (8.15)$$

This gives an approximate idea of the value of y .

8.3.10 Stability constraint:

To prevent numerical instabilities, certain restriction must be observed in defining time step size. Many of the terms are evaluated explicitly DeJesus (1997). This incurs a penalty on the time step to be smaller than a critical value for prevention of undamped oscillations. Once a computational mesh has been specified, several restrictions are placed on the time step to ascertain that it remains below a critical value.

A condition for stability is that fluid should not advect through more than one cell in one time step because the difference equations assume fluxes only between adjacent cells. Thus, VOF and momentum advection are subject to a Courant condition. This is expressed as

$$C = \mathbf{u} \times \frac{\Delta t}{\Delta x} \quad (8.16)$$

Where Δx is the cell width in the flow direction and Δt is the time step

A linear stability analysis according to Hirt and Nichols (1981) requires that the Courant number be less than 1.0, but in practice it is set to less than 0.5 DeJesus (1997). The VOF method in the Star-CD recommends a value of 0.25 Star-CCM+ (2009).

8.3.11 Mesh independence study:

CFD simulations are computationally expensive. One of the most significant factors influencing the computation time is the size of the computational grid specified by the user. Mesh independence studies are conducted to establish the minimum mesh density required to ensure that the converged solution obtained from a CFD calculation is independent of the grid density. Thus, any increase in the number of mesh cells in the simulated flow would not change the flow solution and integrated quantities. In practice, mesh independence is indicated when further mesh refinement yields only small, insignificant changes in the numerical solution obtained.

In order to identify the minimum mesh density to ensure that the solution is independent of the mesh resolution, a mesh sensitivity analysis has been carried out in the construction and analysis of the CFD model. In the mesh independence study, a computational domain of 1m length was used as this length is sufficient to carry out a test on the performance of the mesh with quite reasonably computational effort. Six 3-Dimensional meshes were investigated in the present study as shown in Figure 8.4. The mesh sensitivity study is performed with a

constant ratio $\frac{\Delta t}{\Delta x} = 1 \times 10^{-4}$ and the mesh sizes of 24,000, 36,000, 54,600, 76,800,

84,000 and 102,600 cells. The meshes were tested with an inlet velocity ($U_{SL} = 0.05 \text{ ms}^{-1}$ and $U_{SG} = 0.34 \text{ ms}^{-1}$) flow condition of flow domain full of liquid was used. This is analogous to the simulation of a single Taylor bubble flowing in stagnant liquid. But in this case, an initial gas bubble was formed at the bottom of the liquid pipe by entering a continuous flow of gas and the two-phase flow

domain interaction allowed the development of the bubble over time until the terminal bubble rise velocity and shape were reached.

The velocity of the Taylor bubble, U_N is given by the relation of Nicklin et al. (1962):

$$U_N = 1.2(U_{SL} + U_{SG}) + 0.35\sqrt{gD} \quad (8.17)$$

A calculation was performed to compare the performance of these meshes. The time calculated for the bubble to reach the measurement section (0.5 m) turned out to be 0.66 seconds. The plot of the time history of the void fraction for the six meshes is shown in Table 8.1.

To determine the time series of the void fraction, the following procedure similar to that used by Hernandez-Perez (2008) was performed: a cross-sectional plane is defined across the measurement location and an area-weighted average value of the void fraction is calculated. The cross-sectional average void fraction is computed by dividing the summation of the product of the air volume fraction and facet area by the total area of the surface as follows:

$$\frac{1}{A} \int \varepsilon A = \frac{1}{A} \sum_{i=1}^n \varepsilon |A_i| \quad (8.18)$$

From Table 8.1, it can be observed that meshes 5 (84,000 cells) and 6 (102,600 cells) performs well as the time the Taylor bubble got to the measurement location is closer to the one predicted by the theoretical expression. Here, the % error is 1.4.

The % error is evaluated as follows:

$$\% \text{ error} = \left| \frac{X_{\text{measured}} - X_{\text{simulated}}}{X_{\text{measured}}} \right| \quad (8.19)$$

Where X is the time average of the variable for which the error is computed. The purpose of this is to compare the predictions once the code has reached a steady-state.

It can be concluded that for a given flow condition, the residence time of a fluid particle in a cell ($t=x/u$) decreases as the mesh density increases and that the finer the mesh is, the narrower the error between predicted (simulated) and analytical solution becomes.

An insight into the effect of mesh density can also be obtained from the probability density function (PDF) of void fraction that was successfully employed by Hernandez-Perez (2008) for his mesh independence studies. An examination of the plots of the PDF of void fraction shows that when the mesh is too coarse a refinement in the mesh can have a remarkable influence on the results, as depicted in Table 8.1. Therefore, it can be concluded that the mesh 5 with 84000 cells is adequate, as the change in the results produced is very small when the number of cells is increased to 102600, and it requires less computational effort than the 102600 cells.

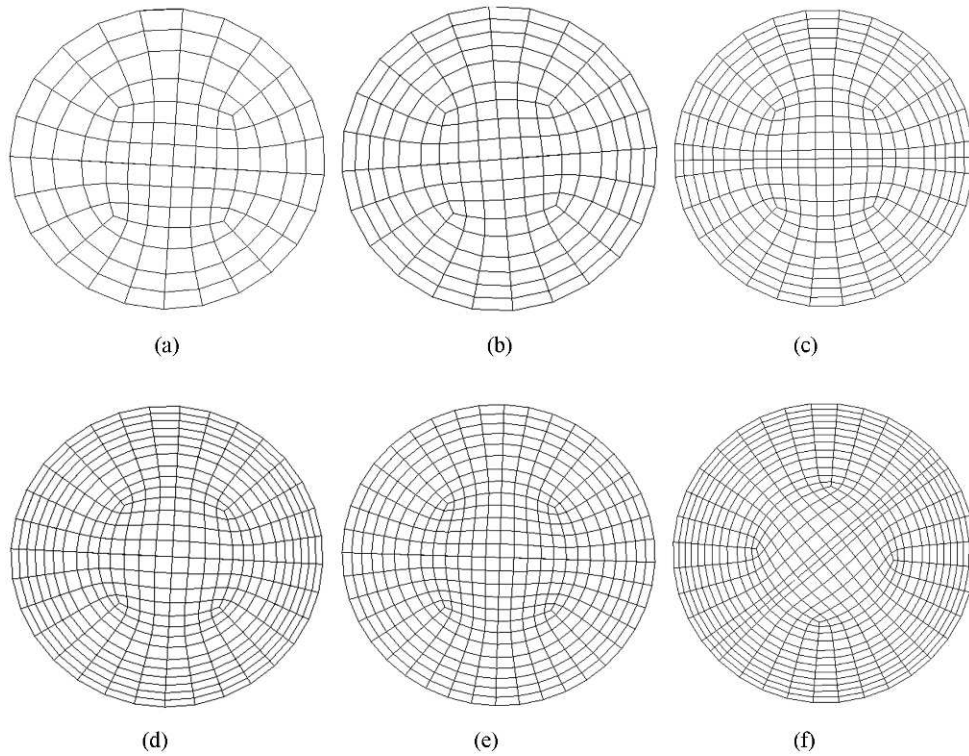
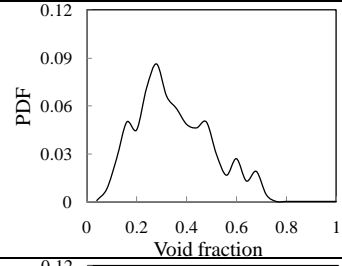
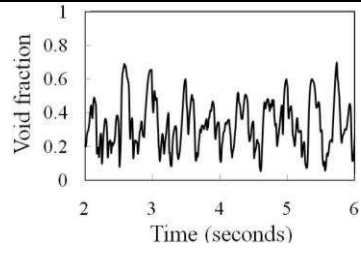


Figure 8.4: Cross-sectional view of different sizes of computational grid used for mesh independent study (a) 26400 cells (b) 36000 cells (c) 54,600 cells (d) 76,800 cells (e) 84,000 cells (f) 102,600 cells

Table 8.1: The results obtained from the CFD mesh independence studies

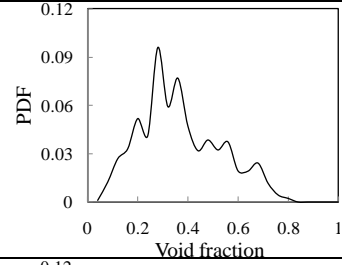
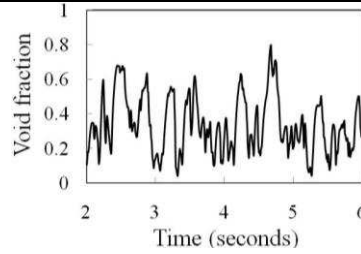
Number of cells	Time series of void fraction	PDF of void fraction	Time the Taylor bubble arrived the measurement location (seconds)
26400			0.737
36000			0.724

54600



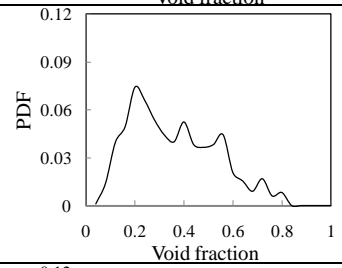
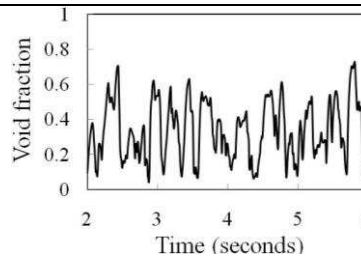
0.696

76800



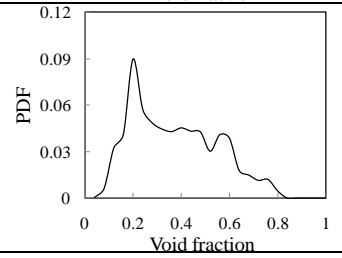
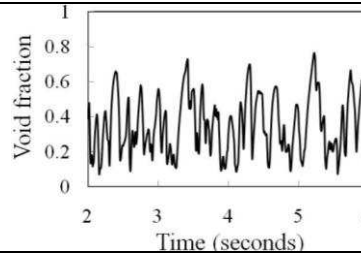
0.671

84000



0.669

102600



0.669

Modelling Slug Two-Phase Flow with CFD

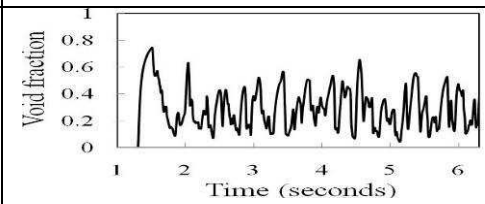
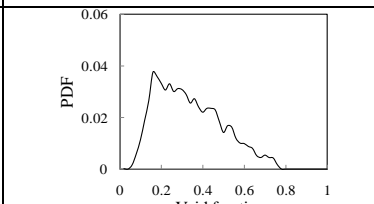
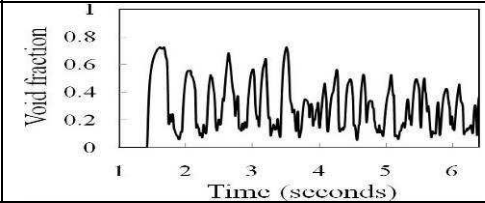
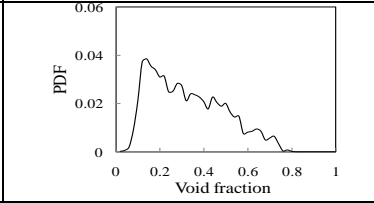
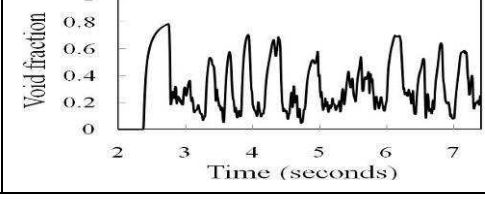
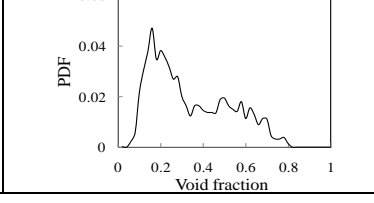
In order for the validation of the results of the CFD simulations be fair and objective, the comparison between the simulations and experiment will be based on quantitative parameters obtained under the same operating conditions. Here, operating conditions refers to pipe configuration, flow rates, fluid properties, temperature and pressure. In this chapter, two cases involving slug flow will be investigated, riser pipe and vertical 90° bend. Though, the study will begin by investigating the effect of the method of introducing liquid into the riser pipe flow domain. The number of cells used for the CFD calculation is 500,000 for both cases. The result of the investigation showed that the method of introducing the liquid into the flow domain ceases to be an issue once the flow reaches steady-state. And that the comparison between CFD and experiment when steady-state is reached is reasonably good. Thereafter, a detailed quantitative comparison was made based on the same method of introducing liquid into the flow domain: pipe full of liquid before introducing air into it. Here, again the comparison is reasonably good.

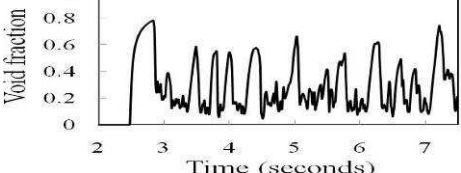
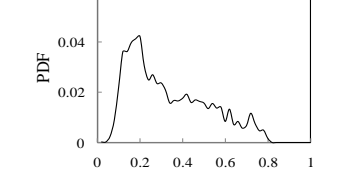
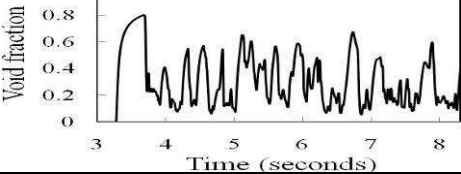
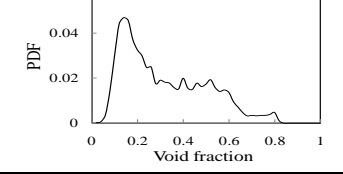
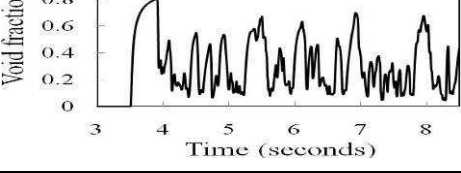
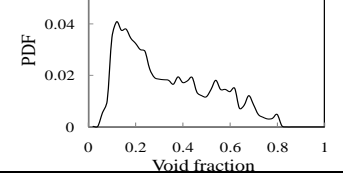
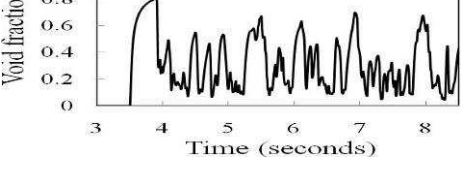
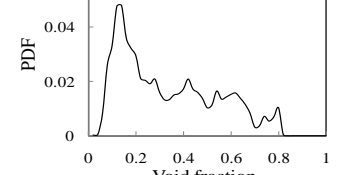
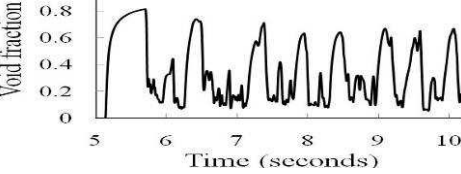
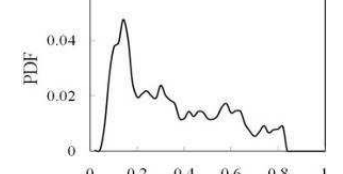
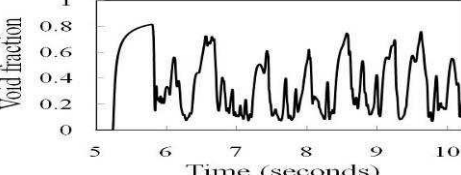
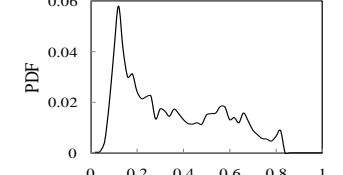
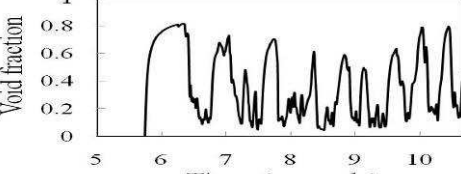
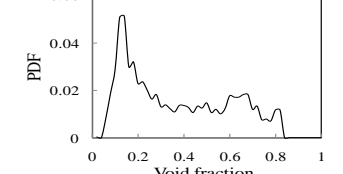
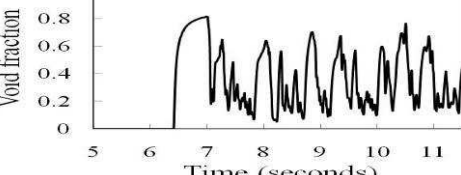
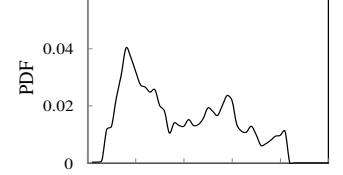
9.1 Flow development:

A fully developed flow is defined as one when the flow pattern does not change with the distance downstream. Flow development in the vertical riser was studied

using CFD and the results are presented and discussed. The advantage of the CFD simulation compared to the physical experiment is the possibility to record the void fraction time series at many measurement sections along the pipe. In addition, the flow pattern frequently depends upon the observation position along the test section. This has given rise to the concept of partially and fully developed flow regimes. However, the extent to which a compressible gas flowing with an incompressible liquid in a vertical pipe can ever be considered fully developed is debatable. Also, due to physical limitations in the length of the rig, the question that we are going to address here is whether a sufficient pipe length (often quoted in terms of pipe diameter) had been provided so that observations taken at the end of the pipe could be considered to be a true representation of a fully developed flow situation.

Table 9.1: Interrogating flow development in a vertical 67 mm internal diameter and 6 m long riser

Distance from the mixing section of the riser (m)	Time averaged void fraction	Probability density function (PDF) of void fraction
1.0 (15 pipe diameters)		
1.15 (17 pipe diameters)		
2.0 (30 pipe diameters)		

<p>2.1 (31.3 pipe diameters)</p>		
<p>2.8 (41.8 pipe diameters)</p>		
<p>3.0 (45 pipe diameters)</p>		
<p>4.0 (60 pipe diameters)</p>		
<p>4.4 (66 pipe diameters)</p>		
<p>4.489 (67 pipe diameters)</p>		
<p>4.92 (73 pipe diameters)</p>		
<p>5.5 (82 pipe diameters)</p>		

Time series of void fraction, and probability density function (PDF) of void fraction obtained from the CFD simulation are used to assess the change in flow characteristics with distance. Table 9.1 shows simulation results of time varying void fraction and PDF of void fraction derived from the eleven measurement locations at liquid and gas superficial velocities of 0.05 and 0.34 ms⁻¹, respectively. The simulations were performed within a flow domain of 6 m long vertical pipe (the same length as the one used in the experiment) with the measurement sections located as indicated in the table.

It can be observed from the time series of void fraction shown in Table 9.1 that the length of the large bubbles (Taylor bubbles) increases with axial distance. This can be explained by the occurrence of bubble coalescence. The PDF of the time series of void fraction at 1.0 m, just downstream of the two-phase mixing section, shows a single peak at low void fraction with a broadening tail down to higher void fraction. It also shows that the results obtained from 1.0 m are initially affected by entrance effects. This is further reinforced by the time trace of void fraction. With the time series of void fraction showing a maximum void fraction of 0.78 while the PDF of void fraction depicting a single peak at about 0.16, void fraction with a tail down to 0.8. The flow patterns begin to change to slug flow at a distance of about 2.8 m (42 pipe diameters) from the mixing section. At a distance of 2.8 m from the mixing section, both the time series and PDF of void fraction have taken the shape of slug flow. Though, it becomes more apparent at 4.0 m from the mixing section.

It is worthy of mention that at a distance of 4.0 to 5.5 m as depicted in Table 9.1, the PDF of void fraction show the traditional features of slug flow; a double peak.

One peak at lower void fraction represents liquid slug whilst the one at higher void fraction, Taylor bubble. On the other hand, the time series of void fraction also show large bubbles separated by smaller ones. It can be concluded that between, 4.0 to 5.5 m, that flow is fully developed based on the fact that the flow remains quite similar, i.e. not changing with distance from 4.0 to 5.5 m. This corresponds to approximately 60 to 82 pipe diameters. It can also be observed from the time series of void fraction that the average void fraction increases when the flow is developing; this means the liquid tends to accumulate at the bottom of the pipe until the liquid slug is formed. This result is in agreement with the work of Hernandez-Perez (2008) who worked on a 38 mm internal diameter and 6 m pipe at 45° inclined to the measurement section using air-water as the model fluid. It is in view of this development that we decided to locate our experimental measuring instruments at 4.4 (66 pipe diameters), 4.489 (67 pipe diameters) and 4.92 m (73 pipe diameters) corresponding to the ECT plane1, ECT-plane 2 and WMS.

9.2 The effect of the method of introducing liquid into the flow domain:

9.2.1 Qualitative comparison between CFD and experiment:

In this case an inlet flow condition of mixture superficial velocity ($U_{SL} = 0.05 \text{ ms}^{-1}$ and $U_{SG} = 0.34 \text{ ms}^{-1}$) and liquid volume fraction of 0.2 is used. The liquid and gas Reynolds numbers are 574 and 1462, respectively. Here, an initial condition of pipe full of liquid is used while for the experiment, the air was introduced before the liquid. The data for the CFD is obtained after an interval of 16 seconds.

However, the time simulated is enough to compare the time series of void fraction.

As a starting point, the raw experimental data will be plotted in the form of time series of void fraction, probability density function (PDF) of void fraction and power spectral density (PSD) of void fraction, see Figure 9.1. The data is collected at three measurement locations, ECT-plane 1, ECT-plane 2 and WMS. These locations correspond respectively to 4.4 m, 4.489 m and 4.92 m from the two-phase flow mixer. The data is obtained after an interval of 60 seconds.

It can be observed from the figure that the shape of the PDF and PSD of void fraction for both the CFD and experiment are similar. Both CFD and experimental PDF predict slug flow as the flow pattern, according to the definition of Costigan and Whalley (1997). According to them, slug flow is a flow pattern characterised by a PDF graph with two peaks, one at lower void fraction (liquid slug) and the other one at higher void fraction, Taylor bubble.

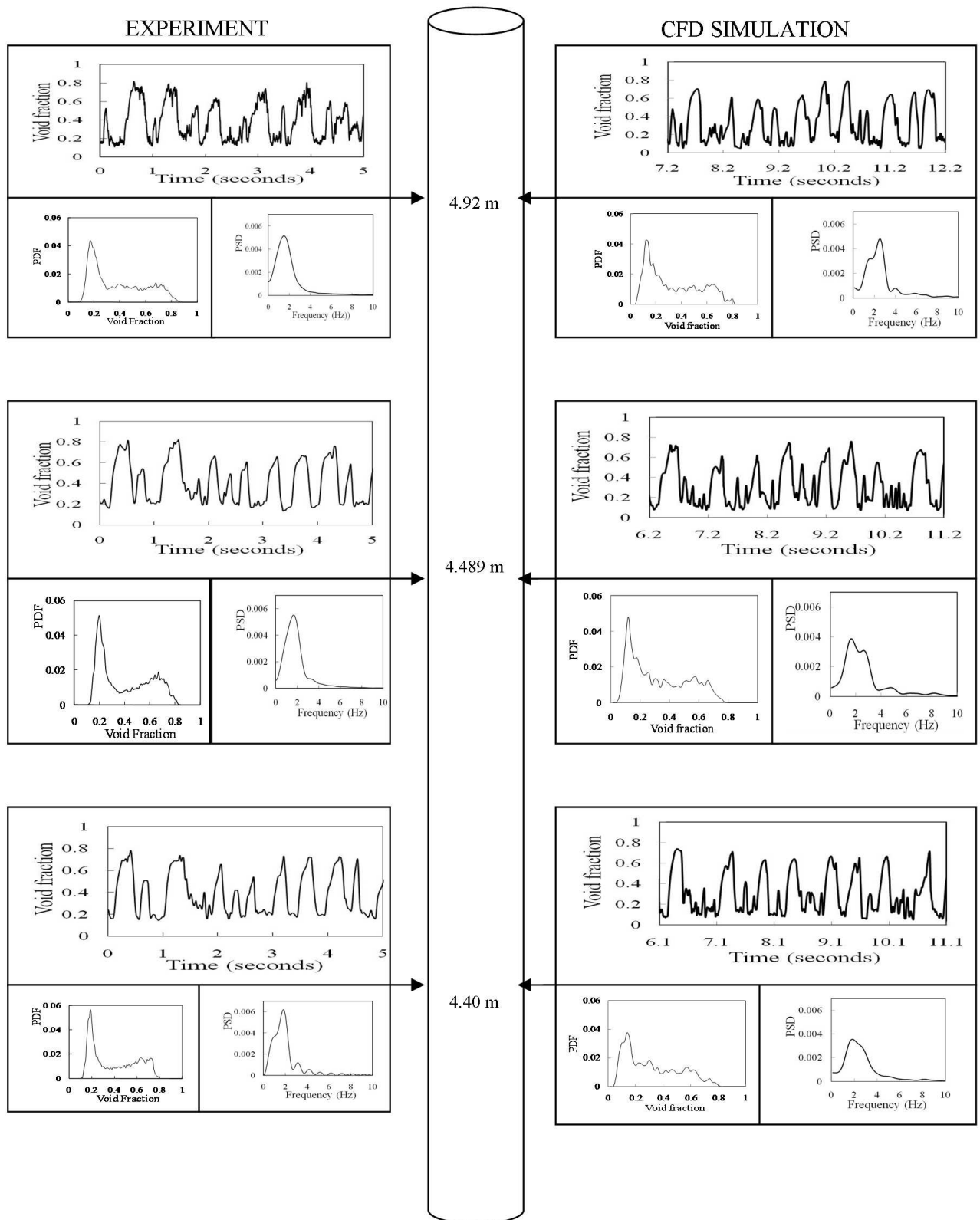


Figure 9.1: Comparison between experimental data and CFD simulation results at steady-state (different methods of introducing liquid into the flow domain). The time difference observed in the CFD is due to the different times recorded for the Taylor bubble to arrive the measurement locations. Locations 4.4 m, 4.489 m and 4.92 m corresponds to ECT-plane 1, ECT-plane 2 and WMS, respectively.

The contours of phase distribution reported in Figures 9.2 (a-d) and Figures 9.3 (a-d) for the Taylor bubble obtained from both CFD and experiment show that the CFD results are in better agreement with those obtained from the WMS. On the contrary, the comparison between the CFD and ECT is poor. It is worth mentioning that it is difficult to measure experimentally the velocity for these conditions due to the presence of the bubbles and the highly turbulent flow field. However, this has been successfully modelled and is represented in Figure 9.4, by means of velocity vectors. From the figure, three regions can be observed from the velocity vectors: the Taylor bubble, falling film and the wake region. Interestingly, the Taylor bubble can be seen moving vertically upwards whilst the liquid film on the other hand is moving downwards. A similar observation was reported by Mao and Dukler (1991), Legius et al. (1995), van Hout et al. (2002) and Hernandez-Perez (2008). The falling film with some entrained bubbles drop into the wake region and a vortex region is created. Furthermore, the liquid film and some of the entrained bubbles are subsequently carried upwards by the incoming gas phase. This behaviour is similar to that observed by Fernandes et al. (1983) and Shemer et al. (2004) who worked on slug flow in a vertical pipe using air-water as the model fluid. They claimed that the bubbles in the liquid slug rise due to entrainment in the wake of the Taylor bubble and that much of this entrained gas is swept around a vortex in the Taylor bubble wake and may coalesce with the trailing Taylor bubble.

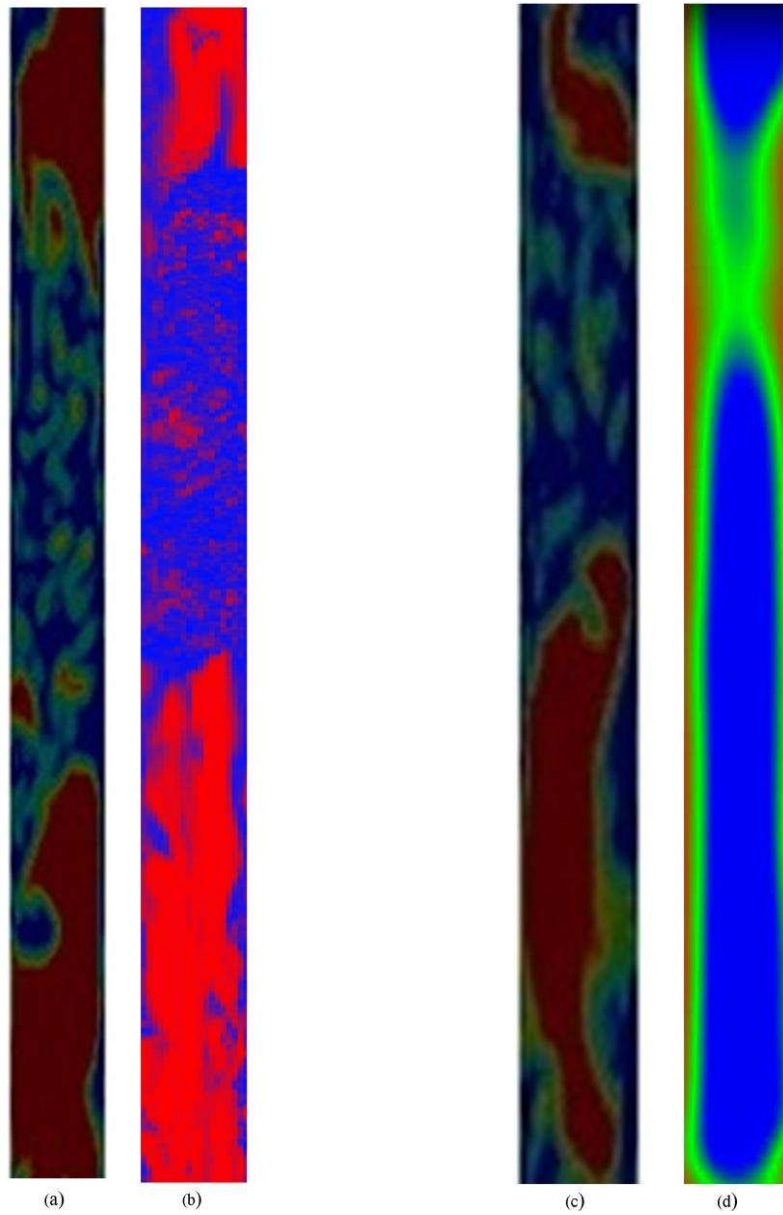


Figure 9.2: Comparison of contours of phase distribution, same inlet velocity condition for between (a) CFD and (b) WMS and for (c) CFD and (d) ECT. For the CFD and WMS comparison, the liquid and gas phases are represented by red and blue colours, respectively. On the contrary, blue represents gas phase for the ECT

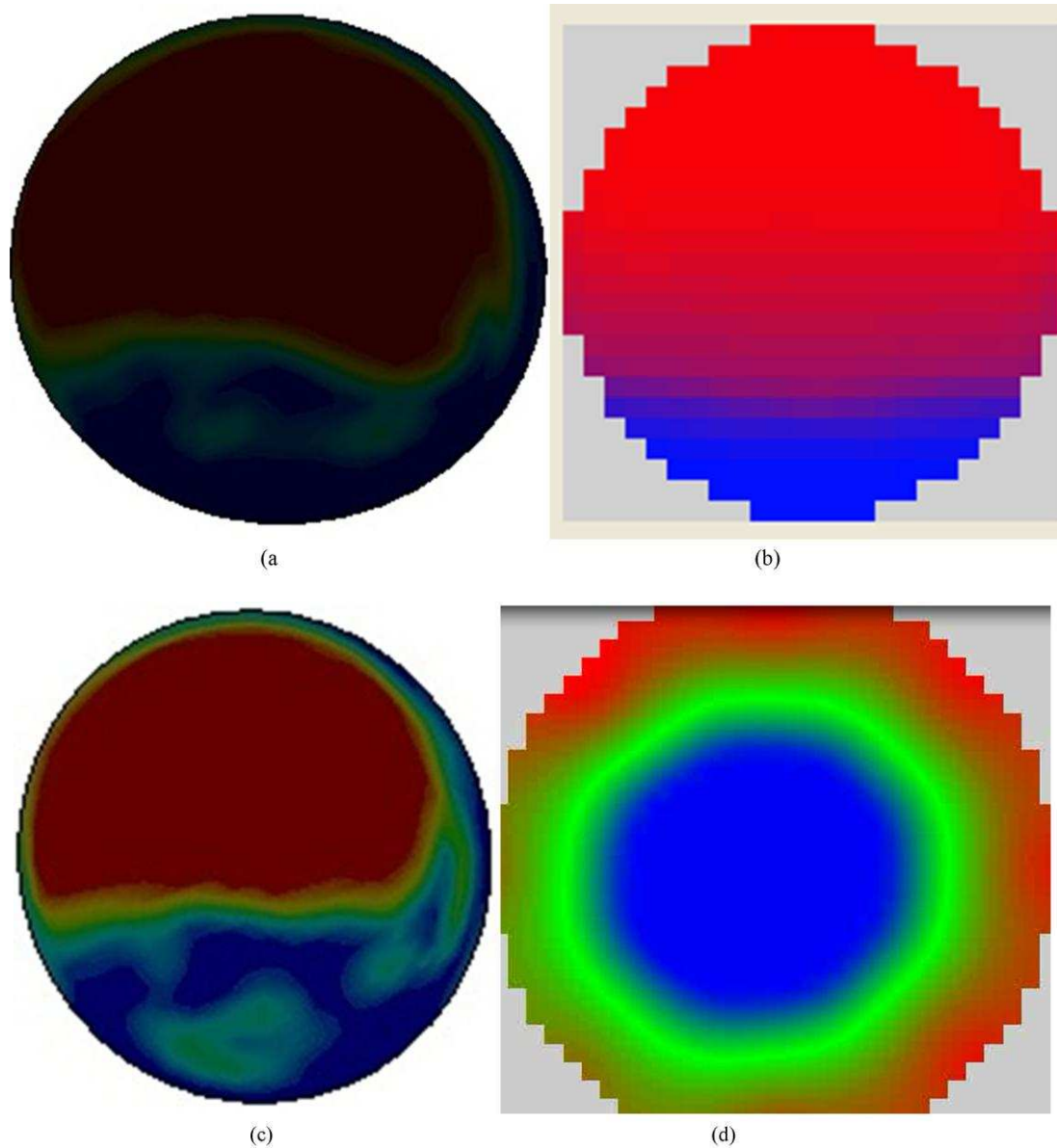


Figure 9.3: Contours of phase distribution (cross-sectional void fraction of air) for the Taylor bubble obtained from (a) CFD and (b) WMS and for (c) CFD and (d) ECT. For the CFD and WMS comparison, the liquid and gas phases are represented by red and blue colours, respectively. On the contrary, blue represents gas phase for the ECT. Screen shots taken at liquid and gas superficial velocity of 0.05 and 0.34 ms^{-1} , respectively.

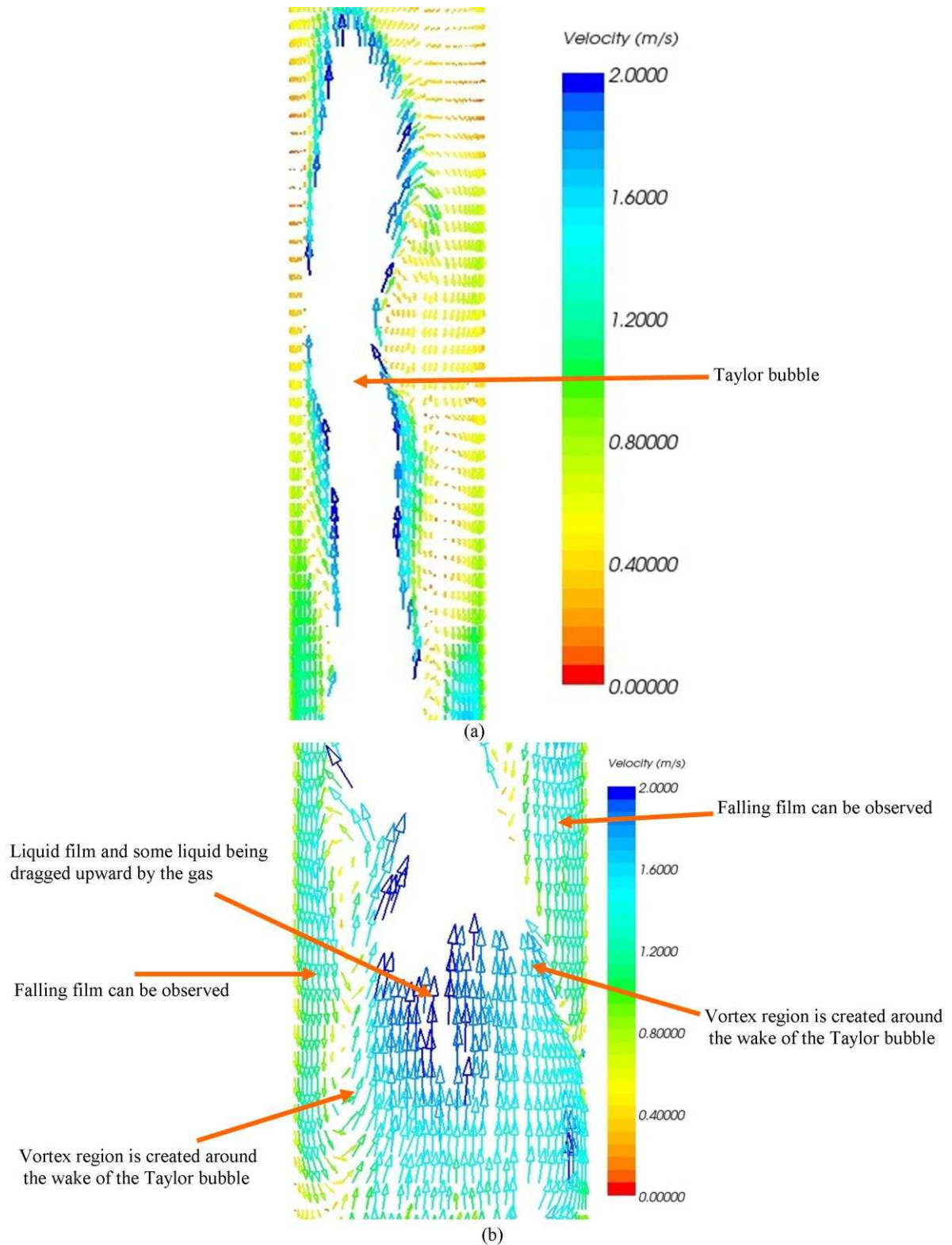


Figure 9.4: Velocity field around the (a) Taylor bubble (b) Wake region of the Taylor bubble for liquid and gas superficial velocity of 0.05 and 0.34 ms^{-1} , respectively obtained from CFD

It can be concluded that the different method of introducing the liquid into the flow domain ceases to be an issue once the flow reaches steady state. Hence, the results of the comparison at steady-state are reasonably good.

9.2.2 Quantitative comparison between CFD and experiment:

In this section, the experiment was repeated with the pipe first full of liquid, before injecting air (gas), as was done for the CFD. Here, only the ECT is used for comparison between CFD and experiment. Here again, the liquid and gas superficial velocities are 0.05 ms^{-1} and 0.34 ms^{-1} , respectively. The experimental data was obtained over an interval of 60 seconds whilst for the CFD, 16 seconds. Readings were taken when the Taylor bubble arrived at the measurement sections. An attempt will be made to compare the time series of void fraction for the large trailing Taylor bubble (start-up) and leading train of Taylor bubbles (steady-state) obtained from the CFD and experiments. It will also for the large trailing Taylor bubble (Tables 9.2a and 9.2b), compare the slug flow characteristics, velocity of the back and front of the Taylor bubble, length of the Taylor bubble, void fraction in the Taylor bubble and the liquid film thickness obtained from CFD and experiment. For the leading train of Taylor bubbles (Table 9.3b), comparisons between CFD and experiment will be based on the velocity of the Taylor bubble, slug frequency, the lengths of the liquid slug, Taylor bubble and of the slug unit, void fractions in both the liquid slug and Taylor bubble. The methodology for the determination of these parameters has been discussed in Chapter 4 and hence omitted here. A comparison will finally be made between CFD and experiment based on static pressure. The errors between

experimental measurement and predictions are listed in Tables 9.2 and 9.3. The error % is evaluated as follows:

$$\text{Error} = \left| \frac{X_{\text{experimental}} - X_{\text{simulated}}}{X_{\text{experimental}}} \right| \times 100 \quad (9.1)$$

Where X is the time average of the variable for which the error is computed. The purpose is to compare the predictions once the code has reached a steady-state.

Table 9.2a: Comparison between the CFD and experiments for the large trailing Taylor bubble (Start-up)

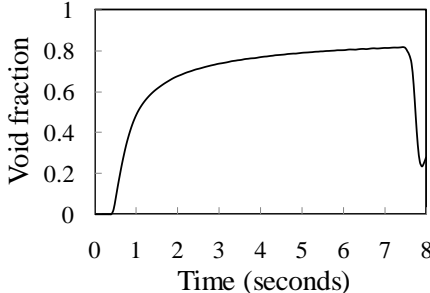
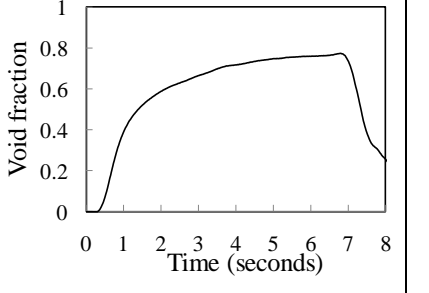
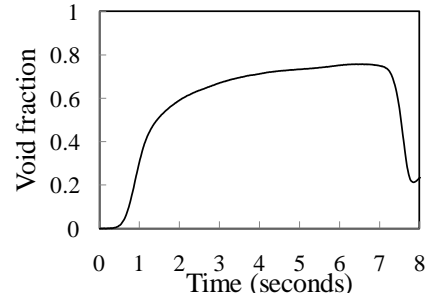
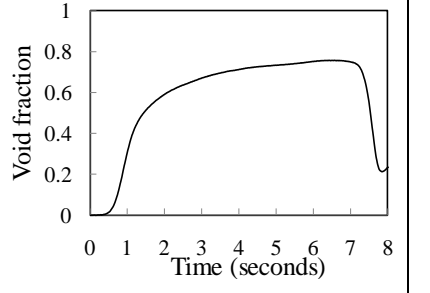
Parameters	CFD	EXPERIMENT	% ERROR
	ECT - PLANE 1(4.4 m)		
			
Velocity of the back of the Taylor bubble (ms ⁻¹)	0.89	0.84	5.95
Velocity of the front of the Taylor bubble (ms ⁻¹)	0.89	0.84	5.95
Length of Taylor bubble (m)	0.89	0.84	5.95
Void fraction in the Taylor bubble	0.8	0.77	3.90
Liquid film thickness (mm)	3.54	4.10	13.66

Table 9.2b: Comparison between the CFD and experiments for the large trailing Taylor bubble (Start-up)

	CFD	EXPERIMENT	% error
	ECT –PLANE 2 (4.489 m)		
Parameters			
Velocity of the back of the Taylor bubble (ms^{-1})	0.89	0.82	8.54
Velocity of the front of the Taylor bubble (ms^{-1})	0.89	0.82	8.54
Length of slug unit (m)	0.89	0.82	8.54
Void fraction in the Taylor bubble	0.80	0.76	5.26
Liquid film thickness (mm)	3.54	4.30	21.47

It can be concluded that the best degree of agreement in terms of slug flow characterisation for the large trailing Taylor bubble between CFD and experiment is the void fraction in the Taylor bubble while the least is the liquid film thickness.

Tables 9.2a and 9.2b presents a summary of the quantitative comparison between CFD and experiment for the large trailing Taylor bubble in terms of different characteristics of slug flow in the riser. The velocity of the back and front of the Taylor bubble for the CFD based on ECT- plane 1 is 0.89 ms^{-1} whilst for the experiment, 0.84 ms^{-1} . This represents an error of 5.95 %, which can be attributed to the different time delays obtained for both methods, 0.1 seconds for the CFD and 0.108 seconds for the experiment. The length of the Taylor bubble for the CFD compares well with the experiment. The void fraction in the Taylor bubble for the CFD and experiment are also compared, for this case the CFD prediction is quite accurate. The liquid film thickness was also determined from the CFD and experiment. For the CFD, the liquid film thickness obtained is 3.54 mm while 4.10 mm for the experiment which means that it under predicts it.

As the large Taylor bubble reached the ECT-plane 2 (Table 9.2b), a similar comparison of the slug flow characterisation was also carried out. The velocity of the large trailing Taylor remains same for the CFD whilst 0.82 ms^{-1} for the experiment. The drop in the velocity of the Taylor bubble from 0.84 to 0.82 ms^{-1} for the experiment may be due to a decrease in the volume of gas occupied by it, 0.77 to 0.76. As expected, the length of the Taylor bubble also dropped for the experiment but remains unchanged for the CFD. The values of the void fraction in the Taylor bubble and liquid film thickness for the experiment changed from (0.77 and 4.10 mm) to (0.76 and 4.30 mm) but remain unchanged for the CFD.

Table 9.3a: Comparison between the CFD and experiments for the leading Taylor bubble (Fully developed)

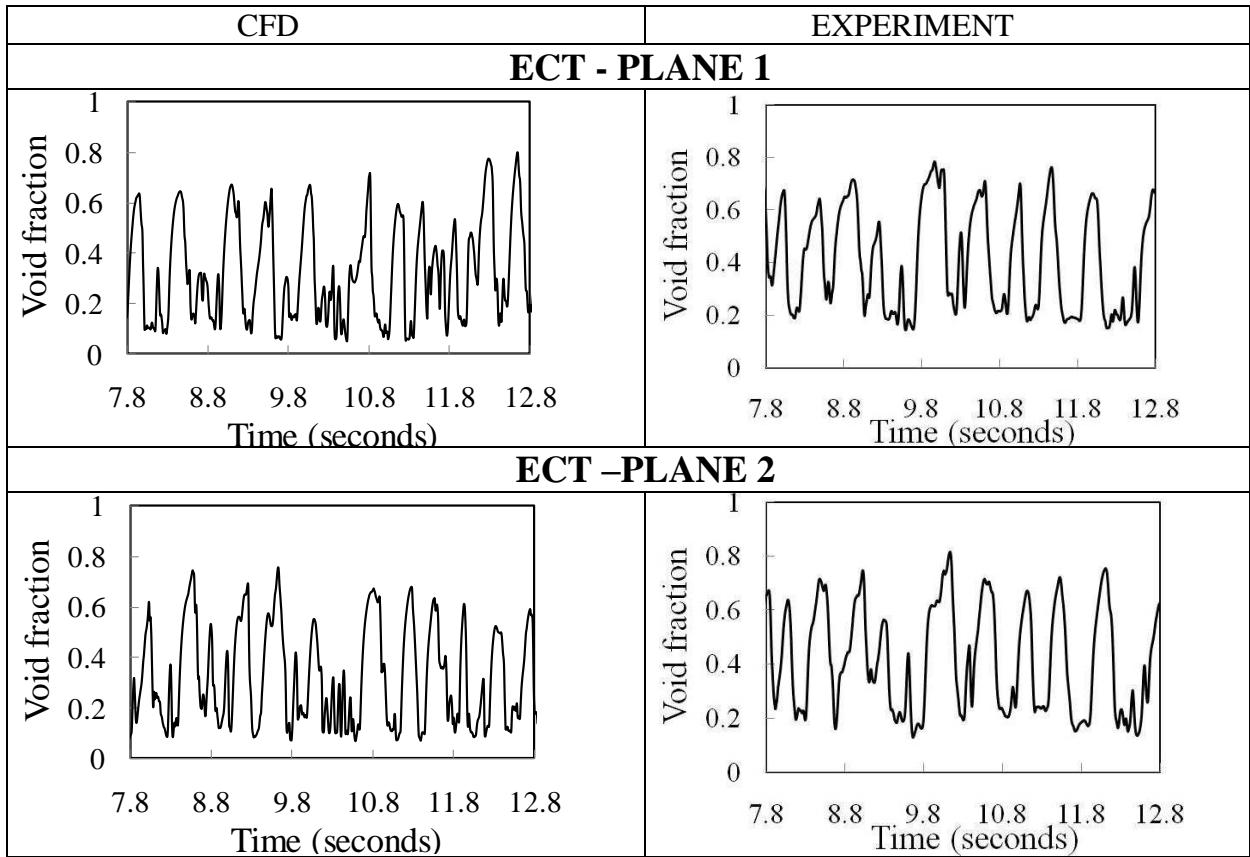


Table 9.3b: Comparison between the CFD and experiments for the leading Taylor bubble (Fully developed)

Slug characteristics	(CFD)		Experiment		% error	
	Plane 1	Plane 2	Plane 1	Plane 2	Plane 1	Plane 2
Void fraction in liquid slug	0.14	0.13	0.17	0.16	17.6	18.75
Void fraction in Taylor bubble	0.60	0.56	0.65	0.62	7.69	9.68
Frequency	1.8	2.40	2.0	2.0	9.6	20
Translational velocity of the Taylor bubble (ms^{-1})	1.48		1.59		6.9	
Length of the slug unit (m)	0.82		0.80		2.5	
Length of the Taylor bubble (m)	0.5		0.49		2.04	
Length of the liquid slug (m)	0.32		0.31		3.23	
Peak of time series of void fraction	0.77	0.74	0.76	0.78	1.3	5.13

For the leading Taylor bubble (Table 9.3b), it can be concluded that the best degree of agreement in terms of comparison between CFD and experiment is the length of the Taylor bubble while the least, void fraction in the liquid slug.

The maximum height of the peak of the void fraction from the time trace of void fraction for the CFD and experiment are 0.77 and 0.76, respectively. The % error is 1.3. The CFD predicts that the slug frequency is 1.80 Hz whilst for the experiment it is 2.0 Hz. This corresponds to an error of 9.6 %. This discrepancy may be due to the time intervals that the measurements were taken.

The time of passage of the Taylor bubble from ECT-plane 1 to 2 based on CFD and an experiment is 0.1 seconds. The peak of void fraction in CFD and experiment based on ECT-plane 2 as shown in Table 9.3b are 0.74 and 0.78, respectively. This represents a 5.13 % error. Both CFD and experiment predict the flow pattern as slug flow, same flow pattern as for plane 1. However, the appearance of slug flow according to Table 9.3a is more obvious than for plane 1. This may be due to the fact that at 4.489 m from the mixing section (plane 2), the flow is more fully developed. The slug frequency for both the CFD and experiment are now 2.4 and 2.0 Hz, respectively. This corresponds to 20 % error. This may be due to the fact that the experimental measurements were taken over 60 seconds whilst for the CFD 16 seconds.

The translational velocity of the leading Taylor bubble has been calculated for the CFD as well as for the experimental study as shown in Figure 9.5. The figure illustrates the procedure to calculate the translational velocity of the Taylor bubble for both the CFD and experiment. The results show that translational velocity of the Taylor bubble for the CFD is 1.48 ms^{-1} whilst for the experiment, 1.59 ms^{-1} . This represents an error of 6.9 %, which can be attributed to the different time delays obtained from both methods 0.06 seconds for the CFD and 0.056 seconds for the experiment.

The lengths of both the liquid slug, Taylor bubble and slug unit were also obtained from CFD and from experiments. From the experiments as shown on Table 9.3b, the lengths of the liquid slug, Taylor bubble and slug unit are 0.32, 0.5 and 0.82 m, respectively while for the CFD, 0.31, 0.49 and 0.80 m.

A comparison between the CFD simulation and the experiments was also made based on the void fractions in both the liquid slug and the Taylor bubble. The values obtained are reasonably good as shown in Table 9.3b.

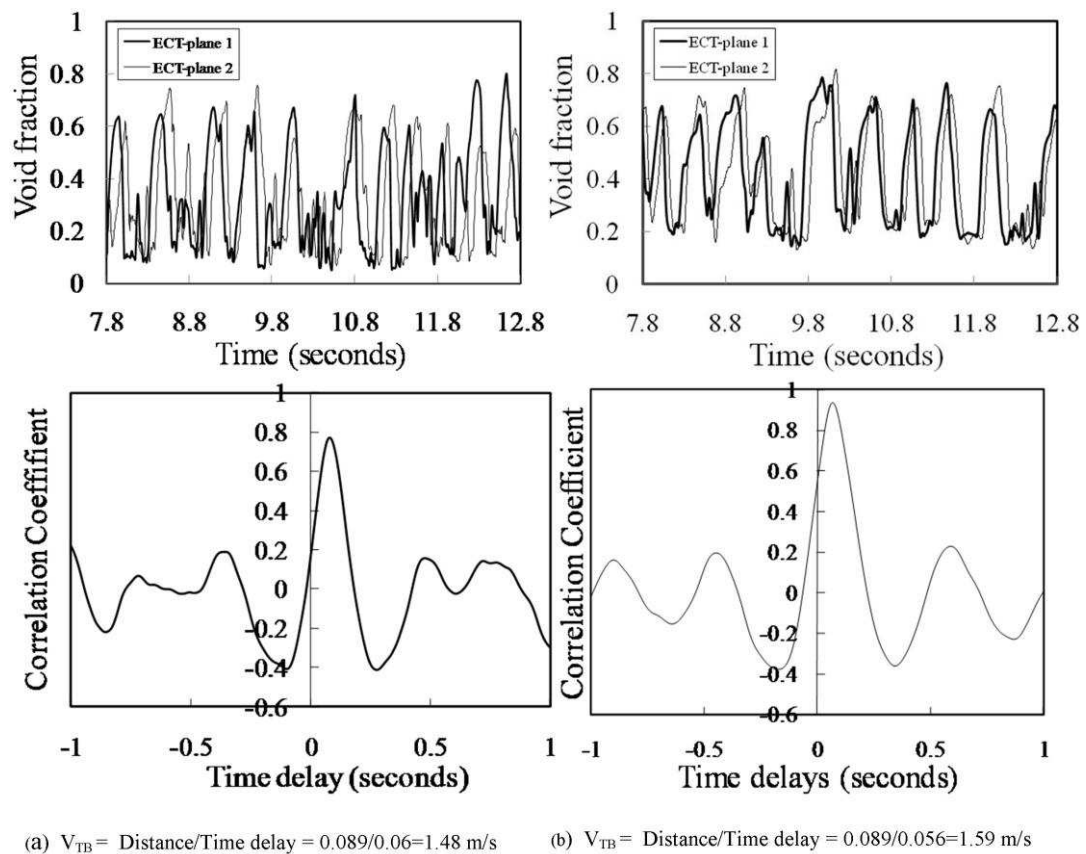


Figure 9.5: Time delay of a Taylor bubble passing through two different measuring locations along the pipe. The liquid and gas superficial velocities are 0.05 and 0.34 ms^{-1} , respectively. (a) CFD and (b) Experiment

A comparison is also made between experiment and CFD based on static pressure. The value obtained from experiment is $3.42 \times 10^4 \text{ Pa}$ whilst for the CFD

as shown on the pressure contour plot (Figure 9.6) is 3.37×10^4 Pa. The simulation under predicts the experiment by 1.5 %. The value obtained from experiment was evaluated as follows:

$$\Delta P_{\text{Static}} = \rho_m g h \quad (9.2)$$

Where ρ_m is the mixture density and is obtained based on the knowledge of the cross-sectional void fraction and h is the height of the riser.

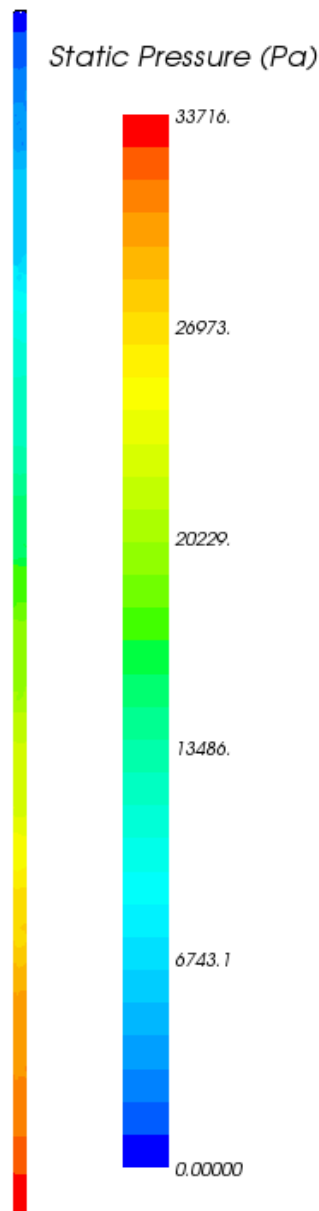


Figure 9.6: Static pressure plot for liquid and gas superficial velocities of 0.05 and 0.34 ms^{-1} , respectively obtained from CFD

9.2.3 Summary for the comparison between the results of CFD and experiments: Riser

A comparison between the results of slug flow characterization obtained from CFD simulation and experiments has been successfully carried out for a 67 mm internal diameter vertical riser with air and silicone oil as the model fluids and the following conclusions can be drawn:

- 1) The method of introducing liquid into the flow domain ceases to be an issue once the flow reaches steady-state. At steady-state, both the CFD and experiment predict similar behaviors.
- 2) The slug flow pattern can be considered fully developed at 4.0 m (60 pipe diameters).
- 3) A reasonably good agreement between CFD and experiment was obtained. CFD simulation can be used to characterize slug flow parameters with a good level of confidence. However, further parametric studies are required to close some of the gaps between CFD and experimental results.
- 4) This work confirms the results reported in the literature for the characteristics of slug flow.
- 5) The best degree of agreement in terms of the slug flow characterization for the large trailing Taylor bubble between CFD and experiment is the void fraction in the Taylor bubble whilst the least is the liquid film thickness. On the other hand, the length of the Taylor bubble and the void fraction in the liquid slug, respectively, represent the best and the least degree of agreement for the leading Taylor bubble between CFD and experiment.

- 6) The comparison between CFD and experiment based on static pressure is qualitatively good.

9.3 Results and discussion for characteristics of slug flow in a vertical 90° bend using experiments and CFD:

This section will involve the comparison between experiments and CFD for the case of slug flow in a vertical 90° bend using air-silicone oil as the model fluids. The comparison between the results obtained from the CFD simulation and experiment involving both before and after the vertical 90° bend will be based again on the time series of void fraction and PDF of void fraction. To achieve this, two experimental campaigns were conducted using the ECT and WMS. The first experimental campaign involved the use of ECT and WMS placed at: before the bend using both instruments at different sections of the pipe. On the other hand, the second experiment campaign which is concerned with the downstream of the bend involved the use of only the WMS placed some distance after the bend. This will be carried out at same liquid and gas superficial velocities of 0.05 and 0.34 ms⁻¹, respectively. The model fluid is still air-silicone oil. The number of cells used for the CFD calculation is 500,000 cells. This is based on the grid convergence studies carried out by Tkaczyk (2011).

9.3.1 Comparison between the Computational fluid dynamics (CFD) and experiment before the vertical 90° bend (first case):

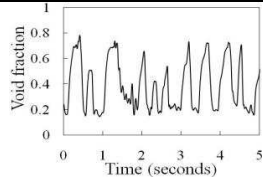
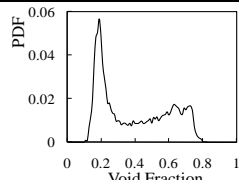
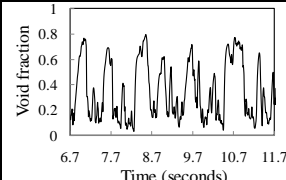
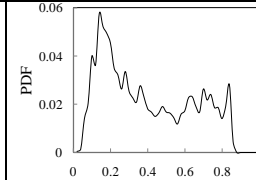
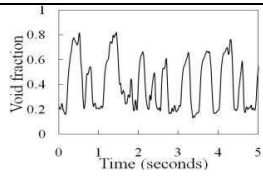
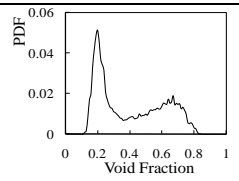
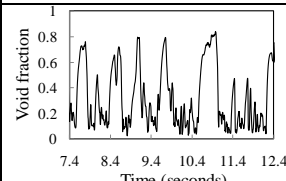
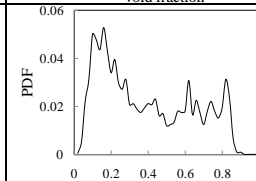
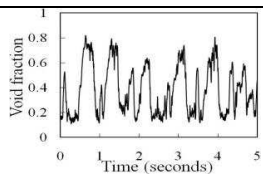
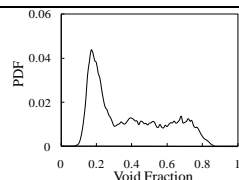
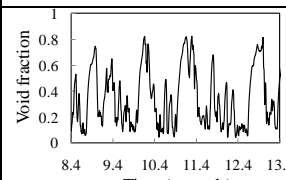
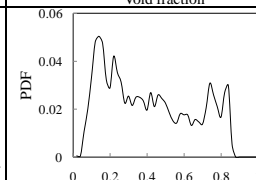
Here, we will compare the results of CFD and experiment before the vertical 90° bend based on the time series of void fraction and PDF of void fraction. The experimental part as stated earlier will involve the use of ECT and WMS placed upstream of the bend. The ECT is made up of 2 planes, planes 1 and 2 separated by a distance of 89 mm. ECT-plane 1 is located at 4.4 m downstream of the mixer. The WMS on the other hand, is located at a distance of 4.92 m away from the two-phase mixing section. The CFD simulation similar to the experimental arrangements had three measurement sections, ECT-plane 1, ECT-plane 2 and WMS corresponding to the same measurement location of the experiment. This will provide the opportunity of comparing like with like in terms of measurement locations.

Table 9.4 show a reasonably good agreement between CFD and experiments based on the time series of void fraction and PDF of void fraction. Table 9.4 shows that at liquid and gas superficial velocity of 0.05 ms^{-1} and 0.34 ms^{-1} , respectively before the bend, using both the ECT (ECT-plane 1 and ECT-plane 2) and WMS, the experiment and CFD predict same flow pattern, slug flow. This is according to the time series of void fraction and PDF of void fraction. Though, the shape of the PDF of void fraction for both the CFD and Experiment are similar. The plot for the experiment is smoother than that of the CFD. This is to be expected considering the fact that the experiment was carried within a duration of 60 seconds whilst the CFD, 23 seconds.

It is interesting to observe that at steady state, the time series of void fraction for the experiment, involving the ECT-plane 1, ECT-plane 2 and WMS are very similar to those of the CFD. For the ECT-plane 1, the height of the peak of the void fraction for the experiment and CFD are 0.79 and 0.795, respectively. The % error is 0.6. Moving to the ECT-plane 2 shows the height of the peak of the void fraction for both the experiment and CFD has increased to 0.81. At the location of the WMS, the height of the peak of the void fraction remained same as that of ECT-plane 2.

On the other hand, the PDF of fraction for the experiment involving ECT-plane 1, show a double peak: one at a lower void fraction representing liquid slug and the other at a higher void fraction, Taylor bubble. The height of the peak of the PDF of void fraction though is 0.058. The CFD scenario also shows a double peak, but with the height of the peak equal to 0.04. The % error is 31. For the ECT-plane 2, the heights of the PDF of void fraction for both the experiment and CFD have dropped to 0.058 and 0.37, respectively. Though, both the experiment and CFD both predict same flow pattern, slug flow. For the WMS, both the experiment and CFD also predict same flow pattern, slug flow. The height of the PDF of void fraction for both the experiment and CFD are 0.42 and 0.32, respectively. This corresponds to an error of 24 %.

Table 9.4: Flow pattern comparison between experiment and CFD before the vertical 90° bend
(Steady-state)

Instrument @ location	EXPERIMENT		CFD	
	Time series of void fraction	PDF of void fraction	Time series of void fraction	PDF of void fraction
ECT-Plane 1 @ 4.4 m				
ECT-Plane 2 @ 4.489 m				
WMS @ 4.92 m				

The contour plot of void fraction presented in Figure 9.7 show a detailed appearance of a train of Taylor bubbles separated by liquid slugs. It is interesting to observe from the figure, the comparison between the outputs of the experiment (ECT and WMS) and the CFD and also the confirmation by the high speed video image.

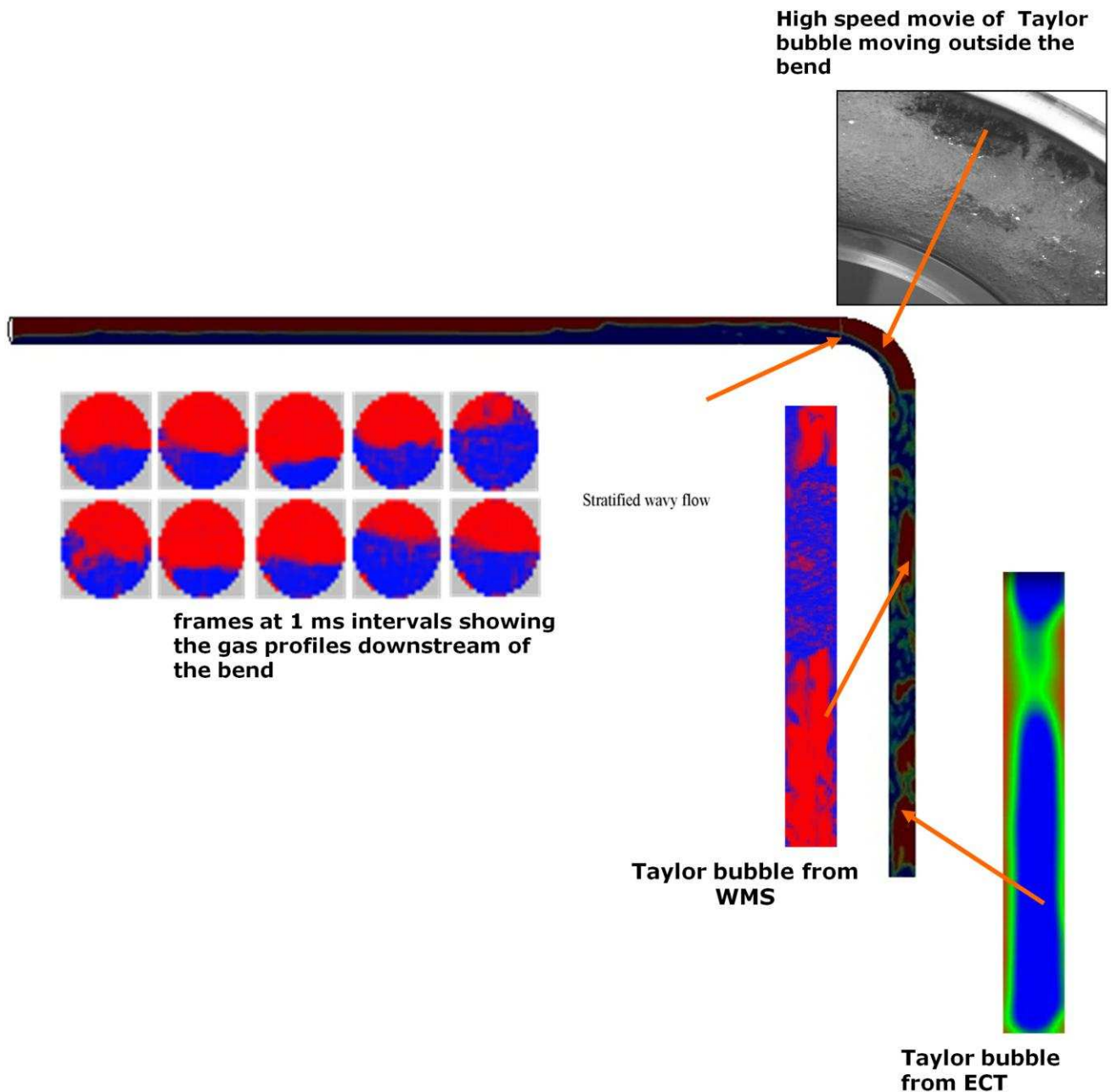


Figure 9.7: Contour plot of void fraction

9.3.2 Comparison between the Computational fluid dynamics (CFD) and experiment after the vertical 90° bend (second case):

The flow pattern approaching the vertical 90° bend as shown in Figure 9.7 is slug flow. After the bend, the two-phase flow distribution is completely different when compared to the flow upstream of it. At the bend in a vertical plane, one would

expect separation tendencies to increase with density difference and axial velocity and to decrease with bend radius. According to Carver and Salcudean (1986), separation force depends on the vectorial sum of the gravitational and centrifugal forces, which varies throughout the bend. Therefore, the variation of the orientation will greatly affect the phase distribution and can lead to separation. Again, Carver and Salcudean (1986) claimed that when the phase separation is observed, one can distinguish three phases namely, continuous liquid, continuous gas and dispersed phase.

From Figure 9.7, as the Taylor bubble and liquid slug gets to the bend, the gravity forces move the Taylor bubble and liquid slug to the outside of the bend, the liquid film in the annulus and liquid in the liquid slug starts to drain out and fall to the bottom of the bend. This interesting observation is depicted in Figures 9.7 and 9.8. This behaviour is similar to the observations reported by Abdulkadir et al. (2011) who carried out experimental work on a vertical and horizontal 90° bends using air and silicone oil as the model fluids.

The time series and PDF of void fraction obtained downstream of the bend shows that the prevailing flow pattern is stratified wavy as shown in Table 9.5. This is confirmed by the cross-sectional contour plot of void fraction shown in Figures 9.8 and 9.9. The time series of void fraction presented in Table 9.5 for both the experiment and CFD show maximum peaks of 0.82 and 0.81, respectively. The % error is 1. On the other hand, the PDF of void fraction show highest peaks of 0.08 and 0.09 for experiment and CFD, respectively. For the experiment, the void fraction corresponding to the maximum peak of void fraction is 0.8 but with a

broadening tail down to 0.2 while for the CFD, the void fraction is 0.75 with a tail down to 0.25.

Table 9.5: Flow pattern comparison between experiment and CFD after the vertical 90° bend

	EXPERIMENT		CFD	
Instrument @ location	Time series of void fraction	PDF of void fraction	Time series of void fraction	PDF of void fraction
WMS @ 0.21 m				

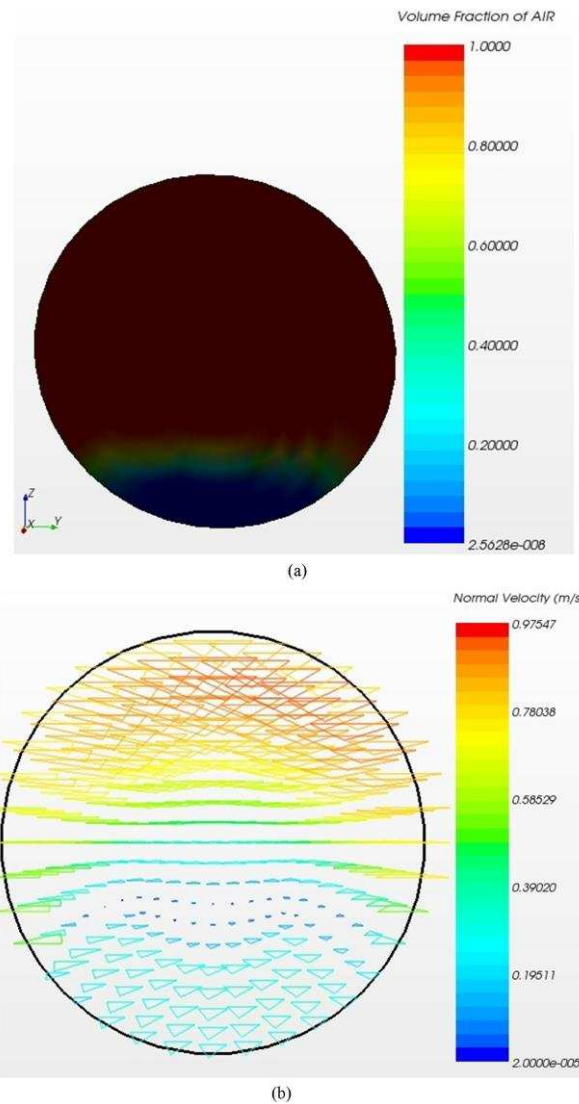


Figure 9.8: (a) Cross-sectional contour plot of void fraction at 90° into the bend and (b) velocity vector plot of void fraction at 90° into the bend

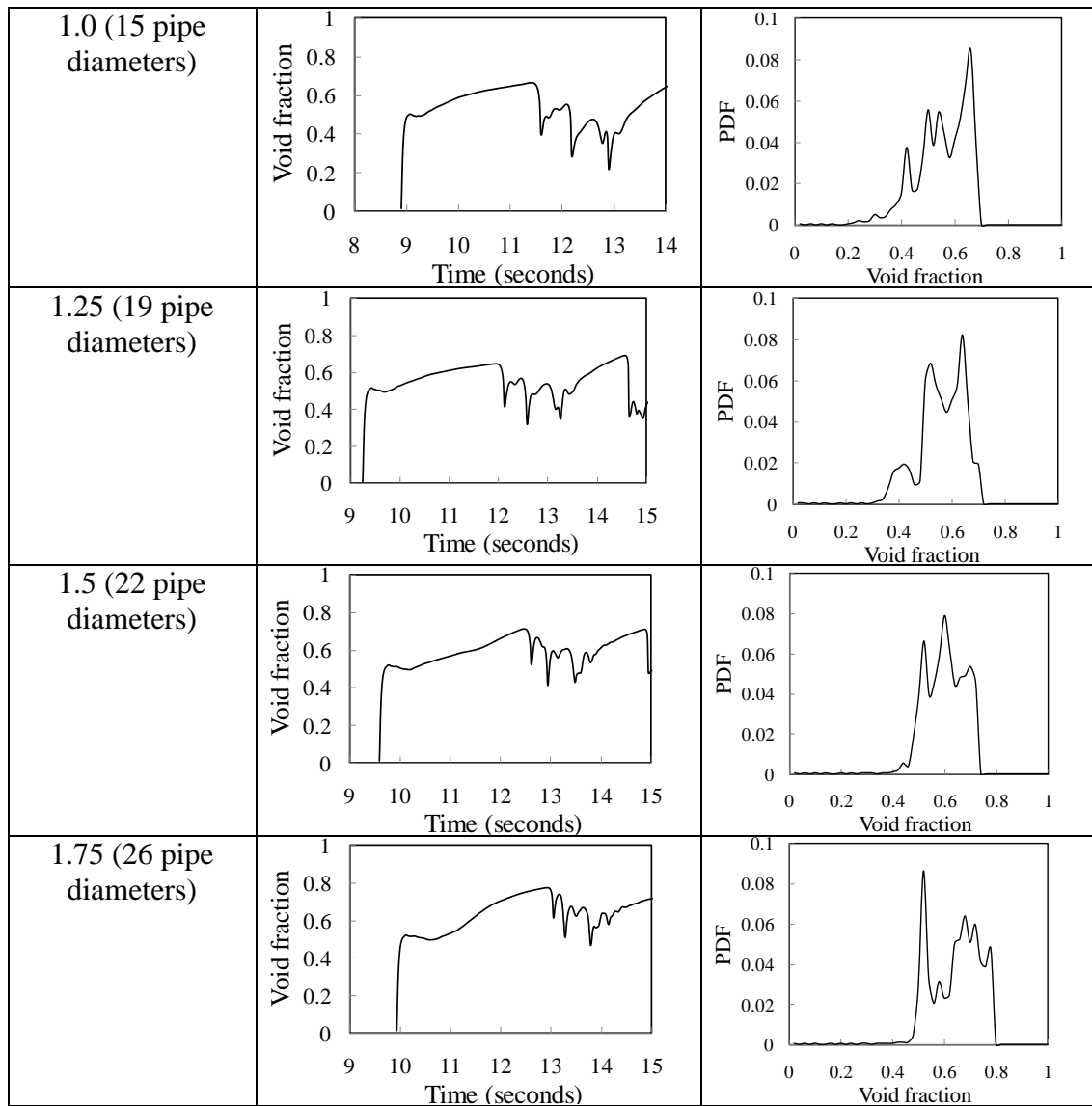
9.3.3 Flow development downstream of the bend:

The comparison between the results obtained from experiments and CFD downstream of the bend was carried out at 0.21 m using the WMS. However, the most distant section (length of the horizontal flowline) from the bend is 2 m (26 pipe diameters). In the literature some researchers, including Hernandez-Perez (2008), have recommended a development distance of about 40 pipe diameters for a horizontal pipe. In addition, the flow pattern frequently depends upon the observation position along the test section. It is very important to know at what

location downstream of the bend the flow can be considered to be fully developed. This knowledge will inform flow assurance experts where to place partial phase separators or dividing junctions in order to collect the separated phases. To circumvent this problem, a flow development study is carried out in this section using CFD. This involved selecting seven measurement locations downstream of the bend as illustrated in Table 9.6.

Table 9.6: Interrogating flow development downstream of the bend

Location after the bend (m)	Time series of void fraction	PDF of void fraction
0.21 (3 pipe diameters)		
0.5 (7 pipe diameters)		
0.75 (11 pipe diameters)		



Time series of void fraction, and PDF of void fraction obtained from the CFD simulation are used to assess the change in flow characteristics with distance downstream of the bend. The simulations were performed within a flow domain of 6 m long vertical pipe joined to a 2 m horizontal flowline via a 0.154 m radius of curvature vertical 90° bend. Table 9.6 shows simulation results of time varying void fraction and PDF of void fraction derived from the seven measurement locations at liquid and gas superficial velocities of 0.05 and 0.34 ms⁻¹, respectively.

It can be observed from the time series of void fraction shown in Table 9.6 that the length of the trailing bubbles increases with an increase in the axial distance. This can be explained by the occurrence of bubble coalescence. The PDF of the time series of void fraction at 0.21 m, just downstream of the bend, shows a characteristic signature of stratified wavy flow. It also shows that the results obtained from 0.21 m are initially affected by the bend. This is further reinforced by the PDF of void fraction. The flow patterns begin to change to stratified flow at a distance of about 1.25 m (19 pipe diameters) from the bend. At a distance of 1.25 m from the bend, both the time series and PDF of void fraction begin to take the shape of stratified flow. Though, it becomes more apparent at 1.5 m from the bend.

It is worthy of mention that at a distance of 1.75 m as depicted in Table 9.6, due to exit effect, the flow pattern has changed to stratified wavy flow. It can be concluded based on the time series and PDF of void fraction that at 1.75 m the flow has changed from a developed flow to a no developing one. This is because the flow is still changing with axial distance. It is advisable to place the partial phase separator or dividing junction at 1.5 m (22 pipe diameters) downstream of the bend.

9.3.4 Summary for the comparison between the results of CFD and experiments: Vertical 90° bend

A comparison between the results obtained from the CFD simulation and experiments has been carried out and the following conclusions can be drawn:

- 1) The CFD simulation is able to predict both the flow pattern before and after the bend.

- 2) A reasonably good agreement was obtained, and the CFD simulation can be used to locate the position of the gas in the bend with confidence. However, further parametric CFD studies might be required to close the gap between CFD simulations and the experimental results.

- 3) The flow pattern downstream of the bend is developed at 1.5 m (22 pipe diameters) and that the partial phase separator or dividing junction should be designated at this location.

Conclusion and further work

This section provides conclusions to the work carried out and the recommendations for further work.

Gas-liquid flow in a vertical 67 mm pipe

Characteristics of slug flow in a vertical riser pipe:

The flow characteristics were measured and characterised using non-intrusive instrumentation, including electrical capacitance tomography (ECT) and a differential pressure cell. The following conclusions may be drawn:

- (1) To study the characteristics of slug flow in a vertical pipe, the data of the ECT without either the WMS or bend placed downstream of it should be considered only. Otherwise, it cannot be established whether any difference in the result is due to the bend or the WMS
- (2) A linear relationship was obtained between structure velocity and mixture superficial velocity. A comparison of this data with the empirical relationships proposed by Nicklin et al. (1962) and Mao and Dukler (1985) showed good qualitative agreement. The best quantitative agreement was obtained with the relationship proposed by Nicklin et al. (1962).
- (3) The drift velocity discussed in the literature was developed by consideration a static liquid column and also using potential flow analysis which assumes no

surface tension and viscosity effects on the drift velocity. The experimental results reveal that a continuous liquid, surface tension and viscosity are significant parameters for drift velocity. Drift velocity for an air-silicone oil flow is higher than that of air-water system.

(4) For a given liquid flow rate, as the gas flow rate was increased, the experimental average void fractions in the liquid slug and the Taylor bubble were found to increase, whilst the liquid film thickness was found to decrease. The liquid superficial velocity has no significant influence on the void fractions in the liquid slug and the Taylor bubble. These findings were found to agree well with those made by previous published studies.

(5) The total pressure drop along the riser was found to decrease as the gas superficial velocity increases, whilst the measured frictional pressure drop was found to increase.

(6) The slug frequency increased with an increase in the liquid superficial velocity, whilst the dimensionless Strouhal number was found to decrease with corresponding increases in the liquid quality and the Lockhart-Martinelli parameter.

(7) The dimensionless lengths of the Taylor bubbles, and the slug units were found to increase with an increase in the gas superficial velocity. However, the length of the liquid slug was found to be changing due to a coalescence of the dispersed bubbles from the wake of a Taylor bubble with the Taylor bubble. This is in agreement with the result obtained by Akagawa and Sakaguchi (1966); Fernandes (1981) and Van Hout et al. (2002)

(8) An adequate agreement was found between the experimental liquid slug length and the Khatib and Richardson method (1984) after considering the influence of the void fraction in liquid slug.

This study has provided a more fundamental insight into the physical phenomena that govern the behaviour of slug flows and the way these parameters behave under various flow conditions.

Gas-liquid flow in bends of different orientations:

The characteristic signatures of the Probability Density Function derived from the time series of cross-sectionally averaged void fraction data were used to identify the flow patterns. Flow patterns for the vertical and horizontal 90° bends are shown on the diagram of the gas superficial velocity versus liquid superficial velocity. The results were validated by a comparative analysis with simultaneously recorded high speed video image stills taken of the flow around the bend. In this section a summary of the key findings is presented:

- The ECT and WMS measurement techniques produced same flow pattern signatures.
- An increase in the gas superficial velocity from 0.05 to 4.73 ms⁻¹ resulted in spherical cap bubble, slug, unstable slug and churn flows being observed in the vertical riser whilst in the horizontal flowline: plug, slug, stratified wavy and annular flows were formed. Buoyancy force plays an important role in the formation of the different flow patterns.
- Bends have significant effect on the gas-liquid flow regimes. In both the vertical riser and horizontal 90° bends the gravitational force tends to move the

liquid to the inside of the bend whilst the gas migrates to the outside of the bend. Some big spherical cap bubble and Taylor bubbles break up in the bends due to the any imbalance in the centrifugal and the surface tension forces. The bubbles become more uniform. Dry patches in the bend were observed in the slug and unstable slug flows. As a result, after the vertical bend the spherical cap bubble flow became bubbly flow, stable and unstable slug to stratified wavy flows and the churn flow turn to stratified wavy and semi-annular flows. The horizontal bend has less effect on the flow patterns compared with the vertical bend.

- At low liquid and high gas superficial velocities, both the vertical and horizontal 90° bends have the same effect on the two-phase air-silicone oil flow, the flow pattern downstream of the bend is annular.
- No slug flow was observed at low liquid flow rate both for the upstream and downstream sections of the horizontal 90° bend.
- In general, the mean void fraction was found to monotonically increase with gas superficial velocity both before and after the bend. Little difference in the mean void fractions for the vertical riser and horizontal flowline before the bend were detected, whilst the mean void fractions after the vertical bend were significantly higher than those after the horizontal bend. The effect of the liquid superficial velocity on the mean void fraction is more complicated. More work is required before any concrete conclusion can be drawn on the flow regimes created by thus rig configuration.
- The validity of the criterion proposed by Gardner and Neller (1969) which is

based on a modified form of Froude number ($Fr_{\theta} = U_m^2 / Rg \sin \theta = 1$) has been confirmed by the results of the current experimental studies for a liquid of a different surface tension and viscosity different to those used by Gardner and Neller.

Gas-liquid flow in a 127 mm pipe and bend:

(a) film fraction distribution around the 180° bend:

- 1) A remarkable similarity was observed between the shape of the time series of film fraction, PDF distribution and location of the frequency in the PDF and PSD plots of the three probes. This therefore, is an indication that equilibrium has been reached and therefore confirms the results reported in the literature that the flow is fully developed at 64 pipe diameters from the mixer.
- 2) The plot of the time series of dimensionless liquid film thickness at high liquid flow rate revealed the merging and collapsing of waves as they move from the riser to the downcomer through the bends. The waves are created due to the high gas shear stress acting on the gas-liquid interface. The waves are able to remain on the gas-liquid interface because the gas inertia is able to overcome the gravitational force which may want to collapse them. Because of the wavy nature of the liquid film they lead to surface tension differentials and as a consequence disrupt it.
- 3) The average film fraction is found to be higher in the straight pipes than in bends. This is because at the bend the slip is less than that of the straight pipes and as a consequence results in a lower film fraction.
- 4) The study also found that at low gas superficial velocities that the average film fraction for the riser was generally greater than for the downcomer. This is

because in downward flow (downcomer) the buoyancy force is acting on the gas phase in a direction opposite to the main flow, while in upflow (riser) it complements the main flow. The effect is such that the actual gas velocity is mostly greater in upward flow than in downward flow. This results in a higher film fraction for upward flow for the same liquid and gas superficial velocities.

- 5) For low liquid flow rates and high gas superficial velocities, film break down (burn out) occurs at the 45° position around the bend. The burn out phenomenon was clearly the result of total loss of liquid from the liquid film by evaporation and entrainment. This is confirmed by the liquid film thickness measurement.
- 6) The study found that the effect of gravity is insignificant at the highest gas superficial velocity. This is because the average film fraction for the riser is almost same as for the downcomer.
- 7) The condition for which the liquid goes to the outside or inside of the bend can be identified based on a modified form of Froude number, a proposal first made by Oshinowo and Charles (1974). A plot of the modified form of Froude number against gas superficial velocities was used to locate position of the liquid in the bend. From the plot, there was one combination of flow rate (Froude number equals to 1) where it was not clear whether it was liquid or gas which was on the outside of the bend. For flow rates which gave a low Froude number, the flow patterns in the riser approaching the 135° bend through the 45 and 90° bends was annular flow. For annular flow, since the gas superficial velocity is greater than that for the liquid and on the other hand the liquid density is much greater than that for the gas, gravity therefore dominates

and the liquid moved to the inside of the 45, 90 and 135° bends. When the Froude number is negative it tells us furthermore that the liquid is being driven to the inside of the bend independently of gravity. For churn flow, the modified form of Froude number is > 1 and we would expect the liquid to move to the outside of the 45° bend, as in fact observed. As both the mixture move from the 90 to the 135° bend through the 45° bend, gravity slows them down and throws the liquid to the bottom of the bend and the gas to the outside.

- 8) The plot of liquid superficial velocity versus gas superficial velocity using the Usui et al. (1983) did not give a reasonably good agreement. At higher gas superficial velocities, the two lines depicted in the map corresponding to the location of the liquid in the 90° and 135° bend positions are in contrast with the present study. Based on the present study, the liquid is inside the 90° and 135° bend locations for all the gas flow rates considered. In addition, Usui et al. (1983) did not present the 45° bend location in the map.
- 9) The comparison between the results of the plot of mean film fraction obtained from the present study and those of Hills (1973) showed the same tendency. Though, the values of mean film fraction obtained from the work of Hills are higher than those of present study. This might be due to the fact that the amount of entrainment of liquid drops in the gas core in large diameter pipe is greater than that of smaller pipes. Therefore there is less liquid in the film in the large diameter case.

Film thickness distribution within the 180° bend:

A comprehensive set of measurements has been taken to study the effect of bend on the liquid film thickness distribution at various gas and liquid flow rates. The liquid film thickness distribution in the bend has been measured with pin and wire probes. With the former for measuring very thin films outside the bend while the latter for very thick liquid films inside the bend. These measurements have been supplemented by visual observation.

- For the lowest liquid and gas superficial velocities, the relationship between the average liquid film thickness and the bend angle is like a scalene triangle with the position of the maximum value at the 90° bend. This is because at these flow rates and at the 90° bend, the effect of gravity is great and as a result, liquid films accumulate there. As the gas superficial velocity is gradually increased, the triangular relationship begins to diminish and tends towards linear. This is as a result of shear forces overcoming gravity and as a result the thickness of the liquid film at the 90° decreased while it increased at the other locations. At the highest gas superficial velocity, the relationship between them is linear. At higher liquid superficial velocities because of high degree of entrainment in the gas core, the tendency towards a linear relationship occurred much sooner than at the other liquid flow rates.
- Deposition of entrained droplets, which has a higher momentum than the gas which carries them, keeps the liquid film on the outside of the bend supplied with the liquid. This is consistent with the observations reported

by Flores et al. (1995). This will be of vital importance in applications where it is desirable to maintain a liquid film on the pipe wall.

- At higher liquid flow rates, although the liquid film thickness is always relatively high on the inside of the bend due both to the lower interfacial shear stress and to gravity drainage of the liquid film to the bottom of the pipe. The liquid film thins out in the three bends location. Gravity appears to be the main cause of this breakdown. The flow pattern is stratified flow.
- The comparison between CFD and experiment showed a very good agreement. The double peak found on the liquid film thickness which Adechy and Issa (2004) made an effort to replicate without success is correctly predicted by Tkaczyk (2011).

Modelling slug flow two-phase flow with CFD:

(a) Comparison between the results of CFD and experiments: Riser

A comparison between the results of slug flow characterization obtained from CFD simulation and experiments has been successfully carried out for a 67 mm internal diameter vertical riser with air and silicone oil as the model fluids and the following conclusions can be drawn:

- 1) The method of introducing liquid into the flow domain ceases to be an issue once the flow reaches steady-state. At steady-state, both the CFD and experiment predict similar behaviors.
- 2) The slug flow pattern can be considered fully developed at 4.0 m (60 pipe diameters).

- 3) A reasonably good agreement between CFD and experiment was obtained. CFD simulation can be used to characterize slug flow parameters with a good level of confidence. However, further parametric studies are required to close some of the gaps between CFD and experimental results.
- 4) This work confirms the results reported in the literature for the characteristics of slug flow.
- 5) The best degree of agreement in terms of the slug flow characterization for the large trailing Taylor bubble between CFD and experiment is the void fraction in the Taylor bubble whilst the least is the liquid film thickness. On the other hand, the length of the Taylor bubble and the void fraction in the liquid slug, respectively, represent the best and the least degree of agreement for the leading Taylor bubble between CFD and experiment.
- 6) The comparison between CFD and experiment based on static pressure is qualitatively good.

Comparison between the results of CFD and experiments: Vertical 90° bend

A comparison between the results obtained from the CFD simulation and experiments has been carried out and the following conclusions can be drawn:

- 1) The CFD simulation is able to predict both the flow pattern before and after the bend.
- 2) A reasonably good agreement was obtained, and the CFD simulation can be used to locate the position of the gas in the bend with confidence. However, further parametric CFD studies might be required to close the gap between CFD simulations and the experimental results.

- 3) The flow pattern downstream of the bend is developed at 1.5 m (22 pipe diameters) and that the partial phase separator or dividing junction should be designated at this location.

Suggestions for further work:

During the course of this observation, a number of aspects, which require further work, have been identified. These aspects are discussed in this section.

Rotameters:

The error analysis carried out in Chapter 3 showed that for the lowest flow rates, an error of 100 % and 62 % were determined for the liquid and gas rotameters, respectively. Though, the errors were observed to decrease exponentially with an increase in either liquid or gas superficial velocities. That notwithstanding, the significant errors observed at the lowest flow rates places a question mark on the integrity of the rotameters. To circumvent this problem, it is recommended that for further work, the rotameters should be replaced with more precise ones.

Gas-liquid flow in a vertical 67 mm pipe

Characteristics of slug flow in a vertical riser pipe:

Slug flow belongs to a class of intermittent flows that has very distinctive features. The flow as seen by an observer is an unsteady phenomenon, dispersed flow appearing alternately with separated flow. It was quite obvious that visual examination of the flow through the transparent walls of the experimental 'acrylic resin' tubes was useful, but the limitations of such observations are well known. It is often difficult to see far into the flow, and results can hardly be more than qualitative. In vertical flow (upstream of the bend), the large bubbles rise with a

round shaped front followed by a cylindrical main body surrounded by an annular liquid film. Under certain conditions small bubbles are entrained in the slug; they may either coalesce at the front of the following bubble or flow in the next falling film. When the pipe is other than vertical (again upstream of the bend), the symmetry of the long bubbles is lost. Even for small deviation angles, the transverse component of gravity and density difference between the two phases causes the interface structure of long bubbles to evolve from an annular to a stratified flow pattern. However, no information is available for the characterisation of slug flow downstream of the bend.

From the experiments carried out and discussed in Chapters 3 and 4, the ECT was only placed upstream of the bend and as a consequence only the characterisation of slug flow before the bend is possible. The question begging for an answer therefore is “what is the effect of the bend on the characteristics of slug flow downstream of the bend”? In order to answer this question, further work should look at studying the effects of changing the orientation of the bends on overall slug flow behaviour using the data obtained from the ECT. This will involve placing the ECT immediately upstream and immediately downstream of the vertical and horizontal 90° bends. This will provide the opportunity of comparing the characteristics of slug flow before and after the bends and to generate new data which would lead to model development for specific geometries. The ability to model such regime will result in a greater understanding of entry flows into gas-liquid separators or slug catchers.

Modelling Slug Two-Phase Flow with CFD:

The CFD calculation for the cases of slug flow in a vertical riser and vertical 90° bend were carried out using a mesh size of 500,000 cells. The simulation for the former lasted for 16 seconds whilst 23 seconds for the latter. It is worth mentioning that the 16 seconds and 23 seconds simulation time translates to 4 and 6 months, respectively. This implies that the duration for individual simulation is too long. To negate the too long a period for the CFD calculations, further work should employ the use of super computers or cluster computers.

Gas-liquid flow in a 127 mm pipe and bend:

In Chapter 7, the data obtained from the ring, pins and wire probes were used to investigate the effect of 180° bends on two-phase air-water flows. These instruments were located at 17 and 21 diameters, respectively upstream and downstream of the bend, 45°, 90° and 135° bends. However, no data was obtained from 0 and 180° bends, respectively, entry and exit of the bend. This is because the wire probes could not be placed at the stated locations: the probes may collapse due to the impact of the bend on it, i.e., the meeting point of the bend and riser and downcomer.

In addition, when the liquid films outside the bend became thicker than 2.5 mm, the pin probes became saturated. Similarly, when the liquid film inside the bend is thin, the wire probes also became saturated. To circumvent these challenges further should consider the use of conductance WMS sensor placed at different locations in the bend, 0, 45, 90, 135 and 180° bends.

It will be interesting to investigate the effect of changing the direction of flow, centrifugal and gravity forces and shear stress. To achieve this, further work should also look at changing the orientation of the inverted U-bend, to a U-shape and then to a C-shaped bend.

References

Abbas, H.A.M., 2010. Multiphase flow rate measurement using a novel conductance venture meter: Experimental and theoretical study in different flow regimes. PhD thesis, University of Huddersfield.

Abdulkadir, M., Zhao, D., Sharaf, S., Abdulkareem, L., Lowndes, I.S., Azzopardi, B. J., 2011. Interrogating the effect of 90° bends on air - silicone oil flows using advanced instrumentation. *Chemical Engineering Science* 66, 2453-2467.

Adechy, D and Issa, R. I., 2004. Modelling of annular flow through pipes and T-junctions. *Computers and Fluids* 33, 289-313.

Akagawa, K., and Sakaguchi, T., 1966. Fluctuation of void fraction in gas-liquid two-phase flow. *Bulletin JSME*, 9, 104-110.

Alves, G. E., 1954. Co-current liquid-gas flow in a pipeline contactor. *Chemical Engineering Progress* 50, No. 9.

Anderson, G.H., and Hills, P. D., 1974. Two-phase annular flow in tube bends. *Symposium on Multiphase flow Systems*, University of Strathclyde, Glasgow, Paper J1. Published as Institution of Chemical Engineers Symposium, Series No. 38.

Azzi, A., Azzopardi, B.J., Abdulkareem, L.A., Hilal, N., and Hunt, A., 2010. Study of fluidisation using electrical capacitance tomography. 7th International Conference on Multiphase Flow, Tampa, Florida, USA May 30-June 4

Azzi, A., and Friedel, L., 2005. Two-phase upward flow 90 degree bend pressure loss model, *Forschung im Ingenieurwesen* 69, 120- 130.

Azzi, A., Friedel, L., and Belaadi, S., 2000. Two-phase gas/liquid flow pressure loss in bends. *Forschung im Ingenieurwesen* 65, 309- 318.

Azzi, A., Friedel, L., Kibboua, R., and Shannak, B., 2002. Reproductive accuracy of two-phase flow pressure loss correlations for vertical 90 degree bends. *Forschung im Ingenieurwesen* 67, 109-116.

Azzopardi, B. J., 2006. Gas-liquid flows, Begell house

Azzopardi, B.J., 1997. Drops in annular two-phase flow. *International Journal of Multiphase Flow* 23, 1-53

Azzopardi, B. J., Abdulkareem, L.A., Sharaf, S., Abdulkadir, M., Hernandez-Perez, V., and Ijioma, A., 2010. Using tomography to interrogate gas-liquid flow. In: 28th UIT Heat Transfer Congress, Brescia, Italy, 21-23 June.

Azzopardi, B. J., Taylor, S., and Gibbons, D.B., 1983. Annular two phase flow in large diameter pipes. Proceedings of the International Conference on the Physical Modelling of Multiphase Flow, Coventry, pp. 256-267.

Azzopardi, B. J. and, Whalley, P. B., 1980. Artificial waves in annular two phase flow. ASME Winter Annual Meeting, Chicago, published in Basic Mechanics in Two Phase Flow and Heat Transfer.

Baker, O., 1954. Simultaneous flow of oil and gas. Oil and Gas Journal 53, 185-195

Baker, G., 2003. Separation and control of gas-liquid flows at horizontal T-junctions. PhD thesis, University of Nottingham

Balfour, J. D., and Pearce, D.L., 1978. Annular flows in horizontal 180° bends: measurements of water rate distributions in the film and vapour core. C.E.R.L. Note No. RD/L/N96/78.

Barnea, D., and Brauner, N., 1993. A model for slug length distribution in gas-liquid slug flow. International Journal of Multiphase Flow 19, 829-838

Barnea, D. and Shemer, L., 1989. Void fraction measurements in vertical slug flow: applications to slug characteristics and transition. International Journal of Multiphase Flow 15, 495-504.

Barnea, D., and Taitel, Y., 1993. A model for slug length distribution in gas-liquid slug flow. International Journal of Multiphase flow 19, 829-838.

Banerjee, S., Rhodes, E. and Scott, D. S., 1967. Film inversion of cu-current two-phase flow in helical coils. AIChE Journal 13, 189-191.

Belt, R.J., 2006. On the liquid film in inclined annular flow. PhD thesis, Delft University of Technology, Netherlands.

Bendat, J., and Piersol, A., 1980. Engineering application of correlation and spectral analysis. John Wiley and Sons, New York, USA.

Bolton, G.T., Korchinsky, W.J., and Waterfall, R.C., 1998. Calibration of capacitance tomography system for liquid-liquid dispersions. Measurement Science Technology 9, 1797-1800.

Brackbill, J.U., Kothe, D.B., and Zemach, C., 1992. A continuum method for modelling surface tension. Journal of Computational Physics 100, 335-354.

Brauner, N., and Barnea, D., 1986. Slug/churn transition in upward gas-liquid flow. Chemical Engineering Science 41, 159-163.

Brauner, N., and Ullmann, A., 2004. Modelling of gas entrainment from Taylor bubbles, Part A: Slug flow. International Journal of Multiphase flow 30, 239-272.

- Brown, R. A. S., 1965. The mechanics of large gas bubbles in tubes: I. Bubble velocities in stagnant liquids. *Canadian Journal of Chemical Engineering*, 43, 217-223
- Brown, R.C., Andreussi, P., and Zanelli, S., 1978. The use of wire probes for the measurement of liquid film thickness in annular gas-liquid flows. *The Canadian Journal of Chemical Engineering* 56, 754-757.
- Bugg, J.D., Mack, K., and Rezkallah, K.S., 1998. A numerical model of Taylor bubbles rising through stagnant liquid in vertical tubes. *International Journal of Multiphase Flow* 24, 271–281.
- Carver, M.B., 1984. Numerical computation of phase separation in two fluid flow, ASME Paper No. 82-FE-2, Vol. 106/153
- Carver, M.B, and Salcudean, M., 1986. Three-dimensional numerical modelling of phase distribution of two- fluid flow in elbows and return bends. *Numerical Heat Transfer* 10, 229-251
- Chen, I. Y., Wu, Y. S., Chang, Y. J. & Wang, C. C., 2007. Two-phase frictional pressure drop of R-134 a and R-410 refrigerant oil mixtures in straight tubes and U-type wavy tubes. *Experimental Thermal Fluid Science* 31, 291-299
- Chen, I. Y., Wu, Y. S., Liaw, J. S. & Wang, C. C., 2008. Two-phase frictional pressure drop measurements in U-type wavy tubes subject to horizontal and vertical arrangements. *Applied Thermal Engineering* 28, 847-855
- Chisholm, D., 1980. Two-phase flow in bends. *International Journal of Multiphase Flow* 6, 363-367
- Chong, L. Y., Azzopardi, B. J., and Bate, D. J., 2005. Calculation of conditions at which dryout occurs in the serpentine channels of fired reboilers. *Chemical Engineering Research and Design* 83, 412-422
- Clarke, A., and Issa, R. I., 1997. A numerical model of slug flow in vertical tubes. *Computers and Fluids* 26, 395-415.
- Collier, J.G., and Thome, J.R., 1994. *Convective boiling and condensation*. Third edition, Oxford University Press, New York (Chapter 5, 134-168).
- Cook, M., and Behnia, M., 2001. Bubble motion during inclined intermittent flow. *International Journal of Multiphase Flow* 22, 543 - 551.
- Costigan, G., and Whalley, P. B., 1997. Slug flow regime identification from dynamic void fraction measurements in vertical air-water flows. *International Journal of Multiphase Flow* 23, 263-282
- Collins, R., De Moraes, F. F., Davidson, J. F., and Harrison, D., 1978. The motion of a large gas bubble rising through liquid flowing in a tube. *Journal of Fluid Mechanics* 89, 497-514.

- Coney, M. W. E., 1973. The theory and application of conductance probes for the measurement of liquid film thickness in two phase flow. *Journal of Physics, E: Scient. Instrum* 6, 903-910
- Conte, G., 2000. An experimental study for the characterisation of gas/liquid flow splitting at t-junctions. PhD thesis, University of Nottingham.
- Conte, G., and Azzopardi, B.J., 2003. Film thickness variation about a T-junction. *International Journal of Multiphase Flow* 29, 305-325
- da Silva, M.J., Thiele, S., Abdulkareem, L., Azzopardi, B.J., and Hampel, U., 2010. High-resolution gas-oil two-phase flow visualization with a capacitance wire-mesh sensor. *Flow Measurement and Instrumentation* 21, 191-197.
- Davies, R.M., and Taylor, G.I., 1950. The mechanics of large bubbles rising through extended liquids and through liquids in tubes. *Proceedings of the Royal Society, A* 200, 375-395
- Dean, W.R., 1927. Note on the motion of a fluid in a curved pipe. *Phil. Mag.*4, 208-223.
- Dean, W.R., 1928. Stream- line motion of a fluid in a curved pipe. *Phil. Mag.*5, 673-695.
- de Chard, F. and Delhaye, J. M., 1996. A slug-churn flow model for small-diameter airlift pumps. *International Journal of Multiphase Flow* 22, 627-649
- DeJesus, J.M., 1997. An experimental and numerical investigation of two-phase slug flow in a vertical tube. PhD thesis, University of Toronto, Canada.
- DeJesus, J.M., Ahmad, W., and Kawaji, M., 1995. Experimental study of flow structure in vertical slug flow. *Advances in Multiphase Flow* 31, 105-118
- Delhaye, J.M., Giot, M., and Riethmuller, M.L., 1981(Eds). *Thermal-hydraulics of two-phase systems for industrial design and nuclear engineering*. Hemisphere McGraw-Hill Press, New York.
- Dewhurst, S. J., Martin, S.R., Jayanti, S., and Costigan, G., 1990. Flow measurements using 3-D LDA system in a square section 90 degree bend. Report AEA-In Tech-0078
- Domanski, P.A., and Hermes, C.J.L., 2006. An improved two-phase pressure drop correlation for 180° return bends. 3rd Asian Conference on Refrigeration and Air-Conditioning, Gyeongju, Korea, May 21-23.
- Dukler, A.E., and Taitel, Y., 1986. Flow pattern transitions in gas-liquid systems: measurement and modelling. *Multiphase Science and Technology* 2, 53-57.
- Dumitrescu, D. T. 1943. Stromung an einer luftblase in senkrechten rohr Z angrew *Math Mech*, 23, 139-149
- Egorov, Y., 2004. Contact condensation in stratified steam-water flow. EVOL-ECORA-D 07.

- Ellul, I.R., and Issa, R.I., 1987. Prediction of the flow of interspersed gas and liquid phases through pipe bends. *Transaction of Institution of Chemical Engineers* 65, 84-96.
- Eustice, J., 1910. Flow of water in curved pipes. *Proceedings of the Royal Society* A84, 107-118
- Fabre, J., and Line, A., 1992. Modelling of two-phase slug flow. *Annual Review of Fluid Mechanics* 24, 21-46
- Fernandes, R. C., 1981. Experimental and theoretical studies of isothermal upward gas-liquid flows in vertical tubes. PhD thesis, University of Houston, USA.
- Fernandes, R. C., Semiat, R., and Dukler, A.E., 1983. Hydrodynamics model for gas-liquid slug flow in vertical tubes. *AIChE Journal* 29, 981-989
- Ferziger, J.H. and Peric, M., 2002. *Computational Methods for Fluid Dynamics*. 3rd edition, Springer – Verlag, Berlin.
- Fitzsimmons, D. E., 1964. Two-phase pressure drop in piping components. In: HW-80970, General Electric Hanford Laboratories, Richland, OH, Rev
- Fletcher, C.A.J., 1991. *Computational techniques for fluid dynamics*. Volume 1, 2nd edition, Berlin: Springer.
- Flores, A.G., Crowe, K.E., and Griffith, P., 1995. Gas-phase secondary flow in horizontal, stratified and annular two-phase flow. *International Journal of Multiphase flow* 21, 207-221.
- Friedel, L., 1980. Pressure drop during gas/vapour-liquid flow in pipes. *International Chemical Engineering* 20, 352-367
- Fokeer, S., 2006. An investigation of geometrically induced swirl applied to lean phase pneumatic flows. PhD thesis, University of Nottingham.
- Fossa, M., 1998. Design and performance of a conductance probe for measuring the liquid fraction in two-phase gas-liquid flows. *Flow Measurement and Instrumentation* 9, 103-109
- Gardner, G. C., and Neller, P.H., 1969. Phase distributions flow of an air-water mixture round bends and past obstructions. *Proceedings of Institution of Mechanical Engineers* 184, 93-101
- Geary, D.F., 1975. Return bend pressure drop in refrigeration systems. *ASHRAE Transactions* 81, 250-265.
- Geraci, G., Azzopardi, B.J., and Van Maanen, H.R.E., 2007a. Inclination effects on circumferential film distribution in annular gas/liquid flows. *AIChE Journal* 53, 1144-1150.

- Geraci, G., Azzopardi, B.J., and Van Maanen, H.R.E, 2007b. Effects of inclination on circumferential film thickness variation in annular gas/ liquid flows. *Chemical Engineering Science* 62, 3032-3042.
- Gill, L.E., Hewitt, G.F., Hitchon, J.W., and Lacey, P.M.C, 1963. Sampling probe studies of the gas core in annular two phase flow-1: The effect of length on phase and velocity distribution. *Chemical Engineering Science* 18, 525-535
- Godbole, S. P., Honath, M. F., and Shah, Y. T., 1982. Holdup structure in highly viscous Newtonian and non-Newtonian liquids in bubbles. *Chemical Engineering Communications* 16, 119-134.
- Govier, G.W., and Aziz, K., 1972. *Flow of complex mixtures in pipes*. Princeton, New Jersey, USA.: Van-Nostrand-Reinhold.
- Govier, G.W., Radford, B.A., and Dunn, J.S.C., 1957. The upward vertical flow of air-water mixtures. *The Canadian Journal of Chemical Engineering* 35, 58-70.
- Griffith, P., and Wallis, G. B., 1961. Two-phase slug flow. *Journal of Heat Transfer* 83, 307-320.
- Gregory, G. A., and Scott, D.S., 1978. Correlation of liquid slug velocity and frequency in horizontal co-current gas-liquid slug flow. *AIChE Journal* 15, 833-835
- Hammer, E. A., 1983. Three-component flow measurement in oil/gas/water mixtures using capacitance transducers. PhD thesis, University of Manchester
- Hernandez-Perez, V., 2008. Gas-liquid two-phase flow in inclined pipes. PhD thesis, University of Nottingham.
- Hernandez Perez, V., Azzopardi, B. J., Kaji, R., da Silva, M. J., Beyer, M., and Hampel, U., 2010. Wisp-like structures in vertical gas-liquid pipe flow revealed by Wire Mesh Sensor studies. *International Journal of Multiphase Flow* 36, 908-915.
- Hernandez-Perez, V., Abdulkadir, M., & Azzopardi, B. J., 2011. Grid generation issues in the CFD modelling of two-phase flow in a pipe. *The Journal of Computational Multiphase Flow* 3, 13-26.
- Hewitt G. F., 1978. *Measurements of two-phase flow parameters*, London: Academic Press.
- Hewitt G. F., 1982. Flow regimes. *Handbook of multiphase systems*, ed. Hetsroni. Hemisphere Publication Corporation, New York.
- Hewitt G. F., 1990. Non-equilibrium two-phase flow, proceedings of the 9th International Heat Transfer Conference, Jerusalem 1, 383-394.
- Hewitt, G. F., and Jayanti, S., 1992. Prediction of film inversion in two-phase flow in coiled tubes. *Journal of Fluid Mechanics* 236, 497-511

- Hewitt G. F., and Lacey, P.M.C, 1965. The breakdown of the liquid film in annular two-phase flow. *International Journal of Heat and Mass Transfer* 8, 781-786
- Hewitt G. F., and Lovegrove, P.C, 1969. Frequency and velocity measurements of disturbance waves in annular two-phase flow. UKAEA Report AERE-R4304.
- Hewitt G. F., and Nicholls, B., 1969. Film thickness measurements in annular flow two-phase flow using a fluorescence spectrometer technique. UKAEA Report AERE-R4506.
- Hewitt, G. F., and Whalley, P. B., 1989. Vertical annular two phase flow. *Multiphase Science and Technology* 4, Chapter 2, Hemisphere Publishing, New York.
- Hills, P. D., 1973. A study of two-phase (gas-liquid) flow in a tube bend. PhD thesis, Imperial College, London.
- Hirt, C. W., and Nichols, B. D., 1981. Volume of Fluid (VOF) Method for the Dynamics of Free Boundaries. *Journal of Computational Physics* 39, 201.
- Hoang, K., and Davis, M.R., 1984. Flow structure and pressure loss for two-phase flow in round bends. *Journal of Fluids Engineering* 106, 30 -37
- Holman, J.P., 2008. *Experimental Methods for Engineers*, 8th edn, McGraw-Hill Inc, New York
- Holt, A.J., 1996. Pressure drop and void fraction in narrow channels. PhD thesis, University of Nottingham
- Huang, S. M., 1995. Impedance sensors-dielectric systems. In R. A. Williams, and M. S. Beck (Eds.). *Process Tomography*, Cornwall: Butterworth-Heinemann Ltd.
- Huang, S. M., Plaskowski, A.B., Xie, C.G., and Beck, M.S., 1989. Tomographic imaging of two-component flow using capacitance sensors. *Journal of Physics. E: Science and Instrumentation* 22, 173-177.
- Huang, Z., Wang, B., and Li, H., 2003. Application of electrical capacitance tomography to the void fraction measurement of two-phase flow. *IEEE Transactions on Instrumentation and Measurement* 52, 7-12.
- Hubbard, M. G., 1965. An analysis of horizontal gas-liquid slug. PhD Thesis, University of Houston.
- Hubbard, M. B., and Dukler, A.E., 1966. The characterisation of flow regimes for horizontal two-phase flow. *Proceedings of 1966 Heat Transfer and Fluid Mechanics Institution* 101-121.
- Hunt, A., Pendleton, J., and Byars, M., 2004. Non-intrusive measurement of volume and mass using electrical capacitance tomography. ESDA 2004-58398,

7th Biennial ASME Conference on Engineering System Design and Analysis, Manchester

Ishii, M., and Zuber, N., 1979. Drag coefficient and relative velocity in bubbly, particulate and droplet flows. *AIChE Journal* 25, 843-850

James, P. W., Azzopardi, B. W., Graham, D. I., and Sudlow, C.A., 2000. The effect of a bend on droplet distribution in two-phase flow. *International Conference on Multiphase Flow in Industrial Plants*, Bologna, 13-15 September.

Jayanti, S., 1990. Contribution to the study of non-axisymmetric flows. PhD Thesis, Imperial College London.

Jayanti, S., and Hewitt, G.F., 1992. Prediction of the slug-to-churn flow transition in vertical two-phase flow. *International Journal of Multiphase Flow* 18, 847-860.

Jepson, W. P., and Taylor, R. E., 1993. Slug flow and its transition in large diameter horizontal pipes. *International Journal of Multiphase flow* 19, 411-420

Jones, O.C., and Zuber, N., 1975. The interrelation between void fraction fluctuations and flow pattern in two-phase flow. *International Journal of Multiphase flow* 2, 273.

Kaul, A., 1996. Study of slug flow characteristics and performance of corrosion inhibitors in multiphase flow in horizontal oil and gas pipelines. PhD Thesis, Ohio University, USA.

Keska, J.K., and Williams, B.E., 1999. Experimental comparison of flow pattern detection techniques for air-water mixture flow. *Experimental Thermal Fluid Science* 19, 1-12.

Khatib, Z., and Richardson, J. F., 1984. Vertical co-current flow of air and shear thinning suspensions of kaolin. *Chemical Engineering Research and Design* 62,139-154

Kim, S.E., and Boysan, F., 1999. Application of CFD to environmental flows. *Journal of Wind Engineering and Industrial Aerodynamics* 81,145-158.

Knol, G. F., 1979. Radiation detection and measurement. John Wiley and Sons, New York

Koskie, J.E., Mudawar, I., and Tiederman, W.G., 1989. Parallel wire probes for measurement of thick liquid films. *International Journal of Multiphase flow* 15, 521-530.

Kutataledze, S.S., Nakoryakov, V.E., Burdukov, A.P., Tatevpsyan, Y.V., and Kuzmin, V.A., 1972. Spectral characteristics of vertical two-phase flow. *Sov. Phys. Dokl.* 16, 718-719.

Kvicinsky, S., Longatte, F., Kueny, J.L., and Avellan, F., 1999. Free surface flows: Experimental validation of Volume of Fluid (VOF) method in the plane wall case. *Proceedings of the 3rd ASME, JSME Joint Fluids Engineering Conference*, San Francisco, California.

- Lauder, B., and Spalding, D., 1974. The numerical computation of turbulent flows, *Computer Methods in Applied Mechanics and Engineering* 3, 269-289.
- Legius, H. J. W. M., 1997. Propagation of pulsations and waves in two-phase pipe systems. PhD thesis, Delft University of Technology, Netherlands.
- Legius, H. J. W. M., Narumo, T.J., and van den Akker, H.E.A., 1995. Measurements on wave propagation and bubble and slug velocities in concurrent upward two-phase flow. In: Celata, G.P., and Shah, R.K. (Eds.), *Two-Phase Flow Modelling and Experimentation*, Rome, 907-914.
- Legius, H. J. W. M., and van den Akker, H.E.A., 1997. Numerical and experimental analysis of translational gas-liquid pipe flow through a vertical bend. *Proceedings of the 8th International Conference*, BHR Group, Cannes, France
- Laurinat, J.E., Hanratty, T.J., and Jepson, T.W., 1985. Film thickness distribution for gas-liquid annular flow in a horizontal pipe. *PhysicoChem. Hydrodynamics* 6, 179-195.
- Lo, S., and Zhang, D., 2009. Modelling of break-up and coalescence in bubbly two-phase flows. *The Journal of Computational Multiphase Flow* 1, 23-38
- Loilier, P., 2006. Numerical simulation of two-phase gas-liquid flows in inclined and vertical pipelines. PhD thesis, Cranfield University.
- Maddock, C., Lacey, P.M.C., and Patrick, M.A., 1974. The flow structure of two-phase flow in a curved pipe. In: *Symposium on Multiphase Flow*. Institution of Chemical Engineers Symposium Series, University of Strathclyde.
- Mahalingam, R., and Valle, M., 1972. Momentum transfer in two-phase of gas-pseudoplastic liquid mixtures, *Industrial and Engineering Chemistry Fundamentals* 11, 470-477
- Mandal, A., Kundu, G., and Mukherjee, D., 2004. Studies on frictional pressure drop of gas-non-Newtonian two-phase flow in a co-current downflow bubble column. *Chemical Engineering Science* 59, 3807-3815
- Mandhane, J.M., Gregory, G.A., and Aziz, K., 1974. A flow pattern map for gas-liquid flow in horizontal pipes. *International Journal of Multiphase Flow* 1, 537-553.
- Manolis, I. G., Mendes-Tatsis, M.A., and Hewitt, G. F., 1995. The effect of pressure on slug frequency on two-phase horizontal flow. *Proceedings of the 2nd International Conference on Multiphase flow*, Kyoto, Japan, April 3-7.
- Mao, Z. S., and Dukler, A.E., 1985. Brief communication: Rise velocity of a Taylor bubble in a train of such bubbles in a flowing liquid. *Chemical Engineering Science* 40, 2158-2160.
- Mao, Z. S., and Dukler, A. E., 1990. The motion of Taylor bubbles in vertical tubes. I. A numerical investigation for the shape and rise velocity of Taylor

- bubbles in stagnant and flowing liquid. *Journal of computational physics* 91, 132-160.
- Mao, Z. S., and Dukler, A. E., 1991. The motion of Taylor bubbles in vertical tubes. II. Experimental data and simulations for laminar and turbulent flow. *Chemical Engineering Science* 46, 2055-2064.
- Mao, Z. S., and Dukler, A.E., 1993. Brief communication: The myth of churn flow. *International Journal of Multiphase flow* 19, 377-383.
- Matsui, G., 1984. Identification of flow regimes in vertical gas-liquid two-phase flow using differential pressure fluctuations. *International Journal of Multiphase flow* 10, 711-719.
- Mckeen, T., and Pugsley, T., 2003. Simulation and experimental validation of a freely bubbling bed of FCC catalyst. *Powder Technology* 129, 139-152.
- McQuillan, K.W., and Whalley, P.B., 1985. Flow patterns in vertical two-phase flow. *International Journal of Multiphase Flow* 11, 161-175.
- Mishima, K., and Ishii, M., 1984. Flow regime transition criteria for upward two-phase flow in vertical tubes. *International Journal of Heat & Mass Transfer* 27, 723-737.
- Miya, M., 1970. Properties of roll waves. PhD thesis, University of Illinois, Urbana.
- Miya, M., Woodmansee, D.E., and Hanratty, T.J., 1971. A model for roll waves in gas-liquid flow. *Chemical Engineering Science* 26, 1915-1931.
- Moffat, R.J., 1988. Describing the uncertainties in experimental results. *Experimental Thermal and Fluid Science* 1, 3-17.
- Moissis, R., 1963. The transition from slug to homogeneous two-phase flows. *ASME Journal of Heat Transfer*, 29-39
- Moissis, R., and Griffith, P., 1962. Entrance effects in two-phase slug flow. *ASME Journal of Heat Transfer*, 366-370
- Mori, K., Kaji, M., Miwa, M., and Sakaguchi, K., 1999. Interfacial structure and void fraction of liquid slug for upward gas-liquid two-phase slug flow, *Two phase flow modelling and experimentation*, Edizioni ETS, Pisa
- Muzaferija, S., and Peric, M., 1999. Computation of free surface flows using interface-tracking and interface-capturing methods, Chap.2 in O. Mahrenholtz and M. Markiewicz (eds.), *Nonlinear Water Wave Interaction*. Computational Mechanics Publication, WIT Press, Southampton
- Nicklin, D. J., Wilkes, J. O., and Davidson, J. F., 1962. Two-phase flow in vertical tubes. *Transaction of Institution of Chemical Engineers* 40, 61-68
- Nishikawa, K., Sekoguchi, K., and Fukano, T., 1969. On the pulsation phenomena in gas-liquid two-phase flow. *Bulletin JSME* 12, 1410-1416.

- Nydal, O. J., 1991. An experimental investigation of slug flow. PhD thesis, University of Oslo
- Oliemans, R.V.A, and Ooms, G., 1986. Core-annular flow of oil and water through a pipeline. *Multiphase Science and Technology*, 2.
- Omebere-Iyari, N. K., 2006. The effect of pipe diameter and pressure in vertical two-phase flow. PhD Thesis, University of Nottingham,
- Omebere-Iyari, N. K., Azzopardi, B. J., Lucas, D., Beyer, M., Prasser, H.M., 2008. Gas/liquid flow in large risers. *International Journal of Multiphase Flow* 34, 461-476
- Omebere-Iyari, N.K., and Azzopardi, B.J., 2007. A study of flow patterns for gas/liquid flow in small diameter tubes. *Chemical Engineering Research and Design* 85, 180-192.
- Owhadi, A., and Bell, K.J., 1967. Forced convection boiling inside helically-coiled tubes. *International Journal of Heat and Mass Transfer* 10, 397-401.
- Oshinowo, T., and Charles, M. E., 1974. Vertical two-phase flow- Part 1: Flow pattern correlations. *Canadian Journal of Chemical Engineering* 52, 25-35.
- Patankar, S.V., and Spalding, D.B., 1972. A calculation procedure for heat, mass and momentum transfer in three dimensional parabolic flows. *International Journal of Heat and Mass Transfer* 15, 1787.
- Pearlman, M.D., 1963. Dynamic calibration of wave probes. Department of Naval Architecture and Marine Engineering, MIT, USA
- Pinto, A. M. F. R., and Campos, J. B. L. M., 1996. Coalescence of two gas slugs rising in a vertical column of liquid, *Chemical Engineering Science* 51, 45-54
- Pope, S.B., 2000. *Turbulent flow*. Cambridge: Cambridge University Press.
- Poulson, B., 1991. Measuring and modelling mass transfer at bends in annular flow two-phase flow. *Chemical Engineering Science* 46, 1069-1082.
- Prasser, H. M., Bottger, A., and Zschau, J., 1998. A new electrode-mesh tomograph for gas-liquid flows. *Flow Measurement and Instrumentation* 9, 111-119.
- Prasser, H. M., Krepper, E., and Lucas, D., 2002. Evolution of the two-phase flow in a vertical tube-decomposition of gas fraction profiles according to bubble size classes using wire mesh sensors. *International Journal of Thermal Science* 41, 17-28
- Prasser, H. M., Scholz, D., and Zippe, C., 2001. Bubble size measurement using wire mesh sensors. *Flow Measurement and Instrumentation* 12, 299-312.
- Ramos-Banderas, A., Morales, R. D., Sanchez-Perez, R., Garcia-Demedices, L., and Solorio-Diaz, G, 2005. Dynamics of two-phase downwards flow in

submerged entry nozzles and its influence on the two-phase flow in the mold. *International Journal of Multiphase Flow* 31, 643-665.

Rea, S. And Azzopardi, B. J., 2001. The split of horizontal stratified flow at a large diameter T-junction. *Transaction of the Institution of Chemical Engineers* 79 A, 470-476

Reinecke, N., Petrisch, G., Boddem, M., and Ivanov, I., 1998. Tomographic imaging of the phase distribution in a two-phase slug flow. *International Journal of Multiphase Flow* 24, 617-634.

Rhee, S.H., Makarov, B.P., Krishnan, H., and Ivanov, I., 2004. Assessment of numerical techniques in Volume of Fluid method for free-surface wave flows. 9th Symposium on Practical Design of Ships and other Floating Structures, Luebeck-Travemuende, Germany

Ribeiro, A.M., Bott, T.R., and Jepson, D.M., 2001. The influence of a bend on drop sizes in horizontal annular two-phase flow. *International Journal of Multiphase Flow* 27, 721-728.

Ros, N. C. J., 1961. Simultaneous flow of gas and liquid as encountered in well tubing. *Journal of Petroleum Technology* 13, 1037-1049

Sakaguchi, T., Hosokawa, S., Fujii, Y., Minagawa, H., Nakamori, N., Ueno, T., Kodama, J., 1995. Flow characteristics of gas-liquid two-phase flow in a horizontal U bend pipe. 804-814.

Sakamoto, G., Doi, T., Murakami, Y., and Usui, K., 2004. Profiles of liquid film thickness and droplet flow rate in U-bend annular mist flow. 5th International Conference on Multiphase Flow, ICMF 2004, Japan, May 30-June 4.

Savalaxs, S. A., Steward, F. R., and Lister, D. H., 2005. Modelling of two-phase flow in pipe bends. *Transactions of the ASME* 127, 204-209

Sekoguchi, K., Tanaka, O., Esaki, S., Sugi, H., and Ueno, O., 1980. Flow characteristics of gas-liquid two-phase flow in wedge-shaped duct. *Proceedings of the 17th National Heat Transfer Symposium of Japan*, 352-354

Shannak, B., Al-Shannag, M., and Al-Anber, Z. A., 2009. Gas-liquid pressure drop in vertically wavy 90° bend. *Experimental Thermal and Fluid Science* 33, 340-347.

Shemer, L., Gulitski, A., and Barnea, D., 2004. Velocity field in the Taylor bubble wake measurements in pipes of various diameters. 24nd European Two-phase Flow Group Meeting, Geneva

Shoham, O., 2005. Mechanistic modelling of gas-liquid two-phase flow in pipes. *Society of Petroleum Engineers*, USA

Simmons, M.J.H., and Hanratty, T.J., 2000. Transition from stratified to intermittent flows in small angle upflows. *International Journal of Multiphase Flow* 27, 599-616.

- Spedding, P.L., and Benard, E., 2006. Gas-liquid two-phase flow through a vertical 90 degree elbow bend. *Experimental Thermal and Fluid Science* 31,761-769.
- Spedding, P.L., Benard, E., and McNally, G.M., 2004. Fluid Flow through 90 Degree Bends. *Development of Chemical Engineering Mineral Process* 12, 107-128.
- STAR-CD Version 4.10 and STAR-CCM+ Documentation, 2009. CD-adapco
- Sylvester, N.D., 1987. A mechanistic model for two-phase vertical slug flow in pipes. *Journal of Energy Resources Technology* 109, 206-213
- Taha, T., & Cui, Z.F., 2006. CFD modelling of slug flow in vertical tubes. *Chemical Engineering Science* 61, 676-687
- Taitel, Y., 1986. Stability of severe slugging. *International Journal of Multiphase flow* 12, 203-217.
- Taitel, Y., and Dukler, A.E., 1976. A model for predicting flow regime transition in horizontal and near horizontal gas-liquid flow. *AIChE Journal* 22 47-55.
- Taitel, Y., and Dukler, A.E., 1977. A model for slug frequency during gas-liquid flow in horizontal and near horizontal pipes. *International Journal of Multiphase flow* 3, 585-596.
- Taitel, Y., Barnea, D., and Dukler, A.E., 1980. Modelling flow pattern transitions for steady upward gas-liquid flow in vertical tubes. *AIChE Journal* 26, 345-354.
- Takemura, T., Roko, K., and Shiraha, M., 1986. Dryout characteristics and flow behaviour of gas-water flow through U-shaped and inverted U-shaped bends. *Nuclear Engineering Design* 95, 365-373.
- Tatterson, D.F., 1975. Rates of atomization and drop size in annular two-phase flow. PhD thesis, University of Illinois, Urbana.
- Taylor, G. I., 1961. Disposition of a viscous fluid on the wall of a tube, Part ii, *Journal of Fluid Mechanics* 10, 161.
- Thiele, S., Da Silva, M.J., Hampel, U., Abdulkareem, L., and Azzopardi, B.J., 2008. High-resolution oil-gas two-phase flow measurement with a new capacitance wire-mesh tomography. In: 5th International Symposium on Process Tomography, Poland, Zakopane, 25-26 August.
- Tingkuan, C., Zhihua, Y., and Qian, W., 1986. Two-phase flow and heat transfer in vertical U-shaped tubes (I) Flow pattern transitions in the bend. *Journal of Chemical Industry and Engineering (China)* 1, 1-12.
- Tkaczyk., P., 2011. CFD simulation of annular flows through bends. PhD thesis, University of Nottingham.
- Tutu, N.K., 1982. Pressure fluctuations and flow pattern recognition in vertical two-phase gas-liquid flows. *International Journal of Multiphase flow* 8, 443.

- Ubbink, O., 1997. Numerical prediction of two fluid systems with sharp interfaces. PhD thesis, University of London
- Ueda, T., 1958. Studies on the flow of air-water mixtures-the upward flow in a vertical tube. Bulletin of JSME 1, No. 139.
- Ueyama, K., and Miyauchi, T., 1979. Properties and recirculating turbulent two-phase flow in gas bubble columns. AIChE Journal 25, No. 258.
- Usui, K., 1992. Annular two-phase flow in a C-shaped bend (liquid film flow). Transactions of the Japan Society of Mechanical Engineers 58, 200-205.
- Usui, K., 1993. Annular two-phase flow in a C-shaped bend (flow of liquid drop entrained in the gas core). Transactions of the Japan Society of Mechanical Engineers 59, 214-219.
- Usui, K., Aoki, S., and Inoue, A., 1980. Flow behaviour and pressure drop of two-phase flow through C-shaped bend in a vertical plane-I: Upward Flow. Journal of Nuclear Science and Technology 17, 875-887.
- Usui, K., Aoki, S., and Inoue, A., 1983. Flow behaviour and phase distributions in two-phase flow around inverted U-bend. Journal of Nuclear Science and Technology 20, 915-928.
- Van der Meulen, G.P., Zangana, M., Zhao, D., and Azzopardi, B.J., 2009. Phase distribution measurements by conductance probes and pressure drop in gas-liquid flows. ExHFT-7, 28 June-30 July.
- van Houst, R., Shemer, L., and Barnea, D., 1992. Spatial distribution of void fraction within a liquid slug and some other related slug parameters. International Journal of Multiphase flow 18, 831-845.
- van Houst, R., Barnea, D., and Shemer, L., 2002. Translational velocities of elongated bubbles in continuous slug flow. International Journal of Multiphase flow 28, 1333-1350.
- van Houst, R., Shemer, L., and Barnea, D., 2003. Evolution of hydrodynamic and statistical parameters of gas-liquid slug flow along inclined pipes. Chemical Engineering Science 58, 115-133.
- Versteeg, H.K., and Malalasekera, W., 2007. An Introduction to Computational Fluid Dynamics: the Finite Volume Method. 2nd ed. Pearson Educational Limited.
- Vince, M. A., and Lahey, R. T., 1982. On the development of an objective flow regime indicator. International Journal of Multiphase flow, 8, 93-124.
- Wallis, G. R., 1969. One-dimensional two-phase flow. McGraw-Hill, New York
- Wang, C. C., Chen, I. Y., Yang, Y. W. and Chang, Y. J., 2003. Two-phase flow pattern in small diameter tubes with the presence of horizontal return bend. International Journal of Heat and Mass Transfer 46, 2976-2981

- Wang, C. C., Chen, I. Y., Yang, Y. W. and Hu, R., 2004. Influence of horizontal return bend on the two-phase flow pattern in small diameter tubes. *Experimental Thermal and Fluid Science* 28, 145-152
- Wang, C. C., Chen, I. Y., Lin, Y. T. and Chang, Y. J., 2008. A visual observation of the air-water two-phase flow in small diameter tubes subject to the influence of vertical return bends. *Chemical Engineering Research and Design* 86, 1223-1235
- Wang, S.J., Dyakowski, T., Xie, C.G., Williams, R. A., and Beck, M.S., 1995. Real time capacitance imaging of bubble formation at the distributor of a fluidized bed. *Chemical Engineering Journal* 56, 95-100
- Weisman, J. And King, S.Y., 1981. Flow pattern transitions in vertical and upwardly inclined lines. *International Journal of Multiphase flow* 7, 271-291.
- White, E. T. & Beardmore, R. H., 1962. The velocity of rise of single cylindrical air bubbles through liquids contained in vertical tubes. *Chemical Engineering Science* 17, 351-361.
- Xie, C.G., Huang, S.M., Hoyle, B.S., Thorn, R., Lenn, C., Snowden, D., and Beck, M.S., 1992. Electrical capacitance tomography for flow imaging: system model for development of image reconstruction algorithms and design of primary sensors. *IEE Proceedings G* 139, 89-97.
- Yang, W. Q., 1996. Calibration of capacitance tomography system: a new method for setting measurement range. *Measurement Science Technology* 7, 863-867.
- Zhan, W. R. J, 1964. *Journal of Heat Transfer, Trans. ASME* 86, Issue 417
- Zangana, M., 2011. Film behaviour of vertical gas-liquid flow in a large diameter pipe. PhD thesis, University of Nottingham.
- Zhu, K., Madhusudana Rao, S., Wang, C., and Sundaresan, S., 2003. Electrical capacitance tomography measurements on vertical and inclined pneumatic conveying of granular solids. *Chemical Engineering Science* 58, 4225-4245.
- Zoetewij, M.L., 2007. Long liquid slugs in horizontal tubes: development study and characterisation with electrical conductance techniques. PhD thesis, Delft University of Technology, Netherlands.
- Zun, I., 1987. Transition from wall void peaking to core void peaking in turbulent bubbly flow. *Proceedings of ICHMT Seminar on Transient Phenomena in Multiphase Flow, Dubrovnik, Yugoslavia*

NOMENCLATURE

Symbol	Description, Units
C_0	Distribution coefficient, dimensionless
D	Pipe diameter, m
f	Frequency, Hz
g	Gravity constant, 9.81 ms^{-2}
U_M	Mixture superficial velocity, ms^{-1}
U_N	Structure velocity or nose velocity of a Taylor bubble, ms^{-1}
U_{SG}	Gas superficial velocity, ms^{-1}
U_{SL}	Liquid superficial velocity, ms^{-1}
U_{GLS}	Gas superficial velocity in liquid slug, ms^{-1}
U_{LLS}	Liquid superficial velocity in liquid slug, ms^{-1}
U_0	Terminal velocity of a bubble rising through fluid, ms^{-1}
x	Liquid quality, $x = \frac{U_{SL}}{U_{SL} + U_{SG}}$
ρ	Density, kgm^{-3}
ρ_{ab}	Population correlation coefficient
η	Viscosity, $\text{kgm}^{-1}\text{s}^{-1}$
μ_a, μ_b	Mean of the corresponding series
σ	Surface tension, Nm^{-1}
ΔU_N	Increment of U_{ST} as defined in equation (1), ms^{-1}
$\frac{\Delta P}{\Delta L}$	Pressure drop, Nm^{-1}
ε_{gs}	Void fraction in liquid slug, dimensionless
ε_{TB}	Void fraction in Taylor bubble, dimensionless
δ	Liquid film thickness, mm
β	Ratio of void fraction in liquid slug and Taylor bubble, dimensionless
ε_g	Mean void fraction, dimensionless
E	Expected value operator
$R_{ab}(\tau)$	Cross-correlation function between a (t) and b (t)
A	Area, m^2
F	Frequency, Hz

ε_g	Void fraction
ε_{gs}	Void fraction in the liquid slug
ε_{TB}	Void fraction in the Taylor bubble
V_{TB}	Structure velocity, ms^{-1}
L_{SU}	Length of the slug unit, m
L_S	Length of the liquid slug, m
L_{TB}	Taylor bubble length, m
k	Turbulence kinetic energy, m^2s^{-2}
n	number of phases
t	Time, s
u	Velocity, ms^{-1}
μ	Dynamic viscosity, $\text{kgm}^{-1}\text{s}^{-1}$
i, j	Space directions
q	Phase index

Dimensionless numbers

Eotvos number,
$$Eo = \frac{D^2 g \rho}{\sigma}$$

Froude Number,
$$Fr_m = U_m^2 / GD$$

Morton number,
$$Mo = \frac{g \eta^4}{\rho \sigma^3}$$

Dimensionless inverse viscosity number,
$$N_f = \left[\frac{Eo^3}{Mo} \right]^{1/4}$$

Lockhart-Martinelli parameter,
$$X = \sqrt{\frac{\left[\frac{\Delta P}{\Delta L} \right]_L}{\left[\frac{\Delta P}{\Delta L} \right]_G}}$$

Strouhal Number,
$$St = \frac{FD}{U_{SL}}$$

Subscripts

G	Gas phase
L	Liquid phase
LLS	Liquid in liquid slug
GLS	Gas in liquid slug
s	Slug
M	Mixture

APPENDIX A

SUMMARY OF EXPERIMENTAL DATA

Table A.1: Air/silicone oil flow before the 67 mm diameter riser pipe attached to the vertical 90° bend at ambient temperature

S/No	U _{SL} (m/s)	U _{SG} (m/s)	Pressure (Psig)	U _{SG} (m/s) after correcting for pressure
1	0.05	0.05	8.7	0.0752
2	0.05	0.061	8.4	0.0966
3	0.05	0.288	6.6	0.418
4	0.05	0.344	6.2	0.489
5	0.05	0.404	5.9	0.567
6	0.05	0.544	4.9	0.725
7	0.05	0.709	4.6	0.931
8	0.05	0.945	3.8	1.190
9	0.05	1.418	3.3	1.736
10	0.05	1.891	3.0	2.277
11	0.05	2.363	2.8	2.813
12	0.05	2.836	2.7	3.357
13	0.05	4.73	3.4	5.820
14	0.071	0.05	8.9	0.0759
15	0.071	0.061	8.6	0.0974
16	0.071	0.288	6.8	0.422
17	0.071	0.344	6.4	0.494
18	0.071	0.404	6.0	0.570
19	0.071	0.544	5.3	0.740
20	0.071	0.709	4.8	0.941
21	0.071	0.945	4.3	1.222
22	0.071	1.418	3.8	1.785
23	0.071	1.891	3.3	2.315
24	0.071	2.363	3.2	2.878
25	0.071	2.836	3.0	3.415
26	0.071	4.73	3.6	5.884
27	0.095	0.05	9.0	0.0762
28	0.095	0.061	8.7	0.0978
29	0.095	0.288	6.9	0.424
30	0.095	0.344	6.5	0.496
31	0.095	0.404	6.2	0.575
32	0.095	0.544	4.9	0.725
33	0.095	0.709	4.5	0.926
34	0.095	0.945	4.2	1.215
35	0.095	1.418	3.9	1.794
36	0.095	1.891	3.7	2.367
37	0.095	2.363	3.8	2.974
38	0.095	2.836	3.6	3.531
39	0.095	4.73	4.4	6.161
40	0.14	0.05	9.0	0.0760
41	0.14	0.061	8.9	0.0986
42	0.14	0.288	7.1	0.428

43	0.14	0.344	6.8	0.503
44	0.14	0.404	6.5	0.584
45	0.14	0.544	6.0	0.765
46	0.14	0.709	5.5	0.974
47	0.14	0.945	5.2	1.280
48	0.14	1.418	4.5	1.852
49	0.14	1.891	4.2	2.431
50	0.14	2.363	4.2	3.039
51	0.14	2.836	5.0	3.801
52	0.14	4.73	6.0	6.656
53	0.28	0.05	9.0	0.0762
54	0.28	0.061	8.9	0.0986
55	0.28	0.288	7.7	0.440
56	0.28	0.344	7.3	0.515
57	0.28	0.404	7.1	0.600
58	0.28	0.544	6.6	0.788
59	0.28	0.709	6.2	1.008
60	0.28	0.945	5.9	1.325
61	0.28	1.418	5.2	1.920
62	0.28	1.891	5.2	2.559
63	0.28	2.363	5.2	3.199
64	0.28	2.836	5.8	3.955
65	0.28	4.73	7.9	7.267
66	0.38	0.05	8.9	0.0759
67	0.38	0.061	8.9	0.0986
68	0.38	0.288	7.9	0.443
69	0.38	0.344	7.7	0.524
70	0.38	0.404	7.4	0.608
71	0.38	0.544	6.8	0.795
72	0.38	0.709	6.6	1.027
73	0.38	0.945	6.3	1.350
74	0.38	1.418	6.1	2.006
75	0.38	1.891	6.0	2.662
76	0.38	2.363	6.2	3.360
77	0.38	2.836	6.6	4.109
78	0.38	4.73	8.7	7.524

Table A.2: Air/silicone oil flow after the 67 mm diameter riser pipe attached to the vertical 90° bend at ambient temperature

S/No	U _{SL} (m/s)	U _{SG} (m/s)	Pressure (Psig)	U _{SG} (m/s) after correcting for pressure
1	0.05	0.05	8.7	0.0752
2	0.05	0.061	8.4	0.0966
3	0.05	0.288	6.6	0.418
4	0.05	0.344	6.2	0.489
5	0.05	0.404	5.9	0.567
6	0.05	0.544	4.9	0.725
7	0.05	0.709	4.6	0.931
8	0.05	0.945	3.8	1.190
9	0.05	1.418	3.3	1.736
10	0.05	1.891	3.0	2.277

11	0.05	2.363	2.8	2.813
12	0.05	2.836	2.7	3.357
13	0.05	4.73	3.4	5.820
14	0.071	0.05	8.9	0.0759
15	0.071	0.061	8.6	0.0974
16	0.071	0.288	6.8	0.422
17	0.071	0.344	6.4	0.494
18	0.071	0.404	6.0	0.570
19	0.071	0.544	5.3	0.740
20	0.071	0.709	4.8	0.941
21	0.071	0.945	4.3	1.222
22	0.071	1.418	3.8	1.785
23	0.071	1.891	3.3	2.315
24	0.071	2.363	3.2	2.878
25	0.071	2.836	3.0	3.415
26	0.071	4.73	3.6	5.884
27	0.095	0.05	9.0	0.0762
28	0.095	0.061	8.7	0.0978
29	0.095	0.288	6.9	0.424
30	0.095	0.344	6.5	0.496
31	0.095	0.404	6.2	0.575
32	0.095	0.544	4.9	0.725
33	0.095	0.709	4.5	0.926
34	0.095	0.945	4.2	1.215
35	0.095	1.418	3.9	1.794
36	0.095	1.891	3.7	2.367
37	0.095	2.363	3.8	2.974
38	0.095	2.836	3.6	3.531
39	0.095	4.73	4.4	6.161
40	0.14	0.05	9.0	0.0760
41	0.14	0.061	8.9	0.0986
42	0.14	0.288	7.1	0.428
43	0.14	0.344	6.8	0.503
44	0.14	0.404	6.5	0.584
45	0.14	0.544	6.0	0.765
46	0.14	0.709	5.5	0.974
47	0.14	0.945	5.2	1.280
48	0.14	1.418	4.5	1.852
49	0.14	1.891	4.2	2.431
50	0.14	2.363	4.2	3.039
51	0.14	2.836	5.0	3.801
52	0.14	4.73	6.0	6.656
53	0.28	0.05	9.0	0.0762
54	0.28	0.061	8.9	0.0986
55	0.28	0.288	7.7	0.440
56	0.28	0.344	7.3	0.515
57	0.28	0.404	7.1	0.600
58	0.28	0.544	6.6	0.788
59	0.28	0.709	6.2	1.008
60	0.28	0.945	5.9	1.325
61	0.28	1.418	5.2	1.920
62	0.28	1.891	5.2	2.559
63	0.28	2.363	5.2	3.199
64	0.28	2.836	5.8	3.955
65	0.28	4.73	7.9	7.267
66	0.38	0.05	8.9	0.0759

67	0.38	0.061	8.9	0.0986
68	0.38	0.288	7.9	0.443
69	0.38	0.344	7.7	0.524
70	0.38	0.404	7.4	0.608
71	0.38	0.544	6.8	0.795
72	0.38	0.709	6.6	1.027
73	0.38	0.945	6.3	1.350
74	0.38	1.418	6.1	2.006
75	0.38	1.891	6.0	2.662
76	0.38	2.363	6.2	3.360
77	0.38	2.836	6.6	4.109
78	0.38	4.73	8.7	7.524

Table A.3: Air/silicone oil flow before the 67 mm diameter horizontal pipe attached to the horizontal 90° bend at ambient temperature

S/No	U _{SL} (m/s)	U _{SG} (m/s)	Pressure (Psig)	U _{SG} (m/s) after correcting for pressure
1	0.05	0.05	0.5	0.0489
2	0.05	0.061	0.6	0.0640
3	0.05	0.288	0.4	0.296
4	0.05	0.344	0.4	0.353
5	0.05	0.404	0.5	0.418
6	0.05	0.544	0.3	0.555
7	0.05	0.709	0.3	0.723
8	0.05	0.945	0.5	0.977
9	0.05	1.418	0.7	1.486
10	0.05	1.891	0.9	2.006
11	0.05	2.363	1.2	2.556
12	0.05	2.836	1.2	3.067
13	0.05	4.73	2.1	5.402
14	0.095	0.05	0.6	0.0492
15	0.095	0.061	0.7	0.0644
16	0.095	0.288	0.7	0.302
17	0.095	0.344	0.6	0.358
18	0.095	0.404	0.7	0.424
19	0.095	0.544	0.5	0.562
20	0.095	0.709	0.6	0.738
21	0.095	0.945	0.6	0.984
22	0.095	1.418	0.8	1.495
23	0.095	1.891	1.1	2.032
24	0.095	2.363	1.3	2.572
25	0.095	2.836	1.6	3.145
26	0.095	4.73	3.2	5.756
27	0.14	0.05	0.6	0.0492
28	0.14	0.061	0.5	0.0635
29	0.14	0.288	0.5	0.298
30	0.14	0.344	0.6	0.358
31	0.14	0.404	0.6	0.421
32	0.14	0.544	0.6	0.566
33	0.14	0.709	0.7	0.743

34	0.14	0.945	0.7	0.990
35	0.14	1.418	1.2	1.534
36	0.14	1.891	1.3	2.058
37	0.14	2.363	1.5	2.604
38	0.14	2.836	1.9	3.203
39	0.14	4.73	3.6	5.884
40	0.19	0.05	0.5	0.0489
41	0.19	0.061	0.5	0.0635
42	0.19	0.288	0.5	0.298
43	0.19	0.344	0.5	0.356
44	0.19	0.404	0.5	0.418
45	0.19	0.544	0.6	0.566
46	0.19	0.709	0.7	0.743
47	0.19	0.945	1.0	1.010
48	0.19	1.418	1.2	1.534
49	0.19	1.891	1.3	2.058
50	0.19	2.363	1.7	2.637
51	0.19	2.836	2.1	3.241
52	0.19	4.73	4.5	6.174
53	0.24	0.05	0.5	0.0489
54	0.24	0.061	0.5	0.0635
55	0.24	0.288	0.6	0.300
56	0.24	0.344	0.6	0.358
57	0.24	0.404	0.7	0.424
58	0.24	0.544	0.8	0.573
59	0.24	0.709	0.9	0.752
60	0.24	0.945	1.1	1.016
61	0.24	1.418	1.5	1.563
62	0.24	1.891	1.7	2.109
63	0.24	2.363	2.1	2.701
64	0.24	2.836	2.4	3.299
65	0.24	4.73	5.0	6.334
66	0.28	0.05	0.6	0.0492
67	0.28	0.061	0.5	0.0635
68	0.28	0.288	0.7	0.302
69	0.28	0.344	0.7	0.360
70	0.28	0.404	0.7	0.424
71	0.28	0.544	0.7	0.569
72	0.28	0.709	1.0	0.757
73	0.28	0.945	1.2	1.022
74	0.28	1.418	1.4	1.553
75	0.28	1.891	1.8	2.122
76	0.28	2.363	2.1	2.701
77	0.28	2.836	2.6	3.338
78	0.28	4.73	6.0	6.656
79	0.38	0.05	0.6	0.0492
80	0.38	0.061	0.6	0.0640
81	0.38	0.288	0.7	0.302
82	0.38	0.344	0.8	0.363
83	0.38	0.404	0.9	0.429
84	0.38	0.544	1.0	0.582
85	0.38	0.709	1.2	0.767
86	0.38	0.945	1.3	1.029
87	0.38	1.418	1.8	1.592
88	0.38	1.891	2.3	2.186
89	0.38	2.363	2.9	2.830

90	0.38	2.836	3.2	3.453
91	0.38	4.73	6.0	6.656
92	0.47	0.05	0.9	0.0502
93	0.47	0.061	1.0	0.0656
94	0.47	0.288	1.2	0.312
95	0.47	0.344	1.2	0.372
96	0.47	0.404	1.2	0.438
97	0.47	0.544	1.3	0.592
98	0.47	0.709	1.6	0.786
99	0.47	0.945	1.7	1.055
100	0.47	1.418	2.2	1.630
101	0.47	1.891	2.8	2.251
102	0.47	2.363	3.5	2.926
103	0.47	2.836	4.2	3.646
104	0.47	4.73	7.2	7.042

Table A.4: Air/silicone oil flow after the 67 mm diameter horizontal pipe attached to the horizontal 90° bend at ambient temperature

S/No	U _{SL} (m/s)	U _{SG} (m/s)	Pressure (Psig)	U _{SG} (m/s) after correcting for pressure
1	0.05	0.05	0.5	0.0489
2	0.05	0.061	0.6	0.0640
3	0.05	0.288	0.4	0.296
4	0.05	0.344	0.4	0.353
5	0.05	0.404	0.5	0.418
6	0.05	0.544	0.3	0.555
7	0.05	0.709	0.3	0.723
8	0.05	0.945	0.5	0.977
9	0.05	1.418	0.7	1.486
10	0.05	1.891	0.9	2.006
11	0.05	2.363	1.2	2.556
12	0.05	2.836	1.2	3.067
13	0.05	4.73	2.1	5.402
14	0.095	0.05	0.6	0.0492
15	0.095	0.061	0.7	0.0644
16	0.095	0.288	0.7	0.302
17	0.095	0.344	0.6	0.358
18	0.095	0.404	0.7	0.424
19	0.095	0.544	0.5	0.562
20	0.095	0.709	0.6	0.738
21	0.095	0.945	0.6	0.984
22	0.095	1.418	0.8	1.495
23	0.095	1.891	1.1	2.032
24	0.095	2.363	1.3	2.572
25	0.095	2.836	1.6	3.145
26	0.095	4.73	3.2	5.756
27	0.14	0.05	0.6	0.0492
28	0.14	0.061	0.5	0.0635
29	0.14	0.288	0.5	0.298
30	0.14	0.344	0.6	0.358
31	0.14	0.404	0.6	0.421

32	0.14	0.544	0.6	0.566
33	0.14	0.709	0.7	0.743
34	0.14	0.945	0.7	0.990
35	0.14	1.418	1.2	1.534
36	0.14	1.891	1.3	2.058
37	0.14	2.363	1.5	2.604
38	0.14	2.836	1.9	3.203
39	0.14	4.73	3.6	5.884
40	0.19	0.05	0.5	0.0489
41	0.19	0.061	0.5	0.0635
42	0.19	0.288	0.5	0.298
43	0.19	0.344	0.5	0.356
44	0.19	0.404	0.5	0.418
45	0.19	0.544	0.6	0.566
46	0.19	0.709	0.7	0.743
47	0.19	0.945	1.0	1.010
48	0.19	1.418	1.2	1.534
49	0.19	1.891	1.3	2.058
50	0.19	2.363	1.7	2.637
51	0.19	2.836	2.1	3.241
52	0.19	4.73	4.5	6.174
53	0.24	0.05	0.5	0.0489
54	0.24	0.061	0.5	0.0635
55	0.24	0.288	0.6	0.300
56	0.24	0.344	0.6	0.358
57	0.24	0.404	0.7	0.424
58	0.24	0.544	0.8	0.573
59	0.24	0.709	0.9	0.752
60	0.24	0.945	1.1	1.016
61	0.24	1.418	1.5	1.563
62	0.24	1.891	1.7	2.109
63	0.24	2.363	2.1	2.701
64	0.24	2.836	2.4	3.299
65	0.24	4.73	5.0	6.334
66	0.28	0.05	0.6	0.0492
67	0.28	0.061	0.5	0.0635
68	0.28	0.288	0.7	0.302
69	0.28	0.344	0.7	0.360
70	0.28	0.404	0.7	0.424
71	0.28	0.544	0.7	0.569
72	0.28	0.709	1.0	0.757
73	0.28	0.945	1.2	1.022
74	0.28	1.418	1.4	1.553
75	0.28	1.891	1.8	2.122
76	0.28	2.363	2.1	2.701
77	0.28	2.836	2.6	3.338
78	0.28	4.73	6.0	6.656
79	0.38	0.05	0.6	0.0492
80	0.38	0.061	0.6	0.0640
81	0.38	0.288	0.7	0.302
82	0.38	0.344	0.8	0.363
83	0.38	0.404	0.9	0.429
84	0.38	0.544	1.0	0.582
85	0.38	0.709	1.2	0.767
86	0.38	0.945	1.3	1.029
87	0.38	1.418	1.8	1.592

88	0.38	1.891	2.3	2.186
89	0.38	2.363	2.9	2.830
90	0.38	2.836	3.2	3.453
91	0.38	4.73	6.0	6.656
92	0.47	0.05	0.9	0.0502
93	0.47	0.061	1.0	0.0656
94	0.47	0.288	1.2	0.312
95	0.47	0.344	1.2	0.372
96	0.47	0.404	1.2	0.438
97	0.47	0.544	1.3	0.592
98	0.47	0.709	1.6	0.786
99	0.47	0.945	1.7	1.055
100	0.47	1.418	2.2	1.630
101	0.47	1.891	2.8	2.251
102	0.47	2.363	3.5	2.926
103	0.47	2.836	4.2	3.646
104	0.47	4.73	7.2	7.042

Table A.5: Air/water flow experimental conditions for film fraction using the conductance ring probes around the vertical 180° return bend at liquid superficial velocity = 0.02 ms⁻¹ at ambient temperature

17 pipe diameters upstream of the bend (Gas superficial velocity (m/s))	45° Gas superficial velocity (m/s)	90° Gas superficial velocity (m/s)	135° Gas superficial velocity (m/s)	21 pipe diameters downstream of the bend (Gas superficial velocity (m/s))
6.17	6.17	6.17	6.17	6.17
8.56	8.56	8.56	8.56	8.56
9.42	9.42	9.42	9.42	9.42
10.31	10.31	10.31	10.31	10.31
11.05	11.05	11.05	11.05	11.05
11.83	11.83	11.83	11.83	11.83
12.52	12.52	12.52	12.52	12.52
12.98	12.98	12.98	12.98	12.98
13.25	13.25	13.25	13.25	13.25
13.68	13.68	13.68	13.68	13.68
13.97	13.97	13.97	13.97	13.97
14.22	14.22	14.22	14.22	14.22

14.63	14.63	14.63	14.63	14.63
14.96	14.96	14.96	14.96	14.96
15.31	15.31	15.31	15.31	15.31
15.50	15.50	15.50	15.50	15.50
16.05	16.05	16.05	16.05	16.05

Table A.6: Air/water flow experimental conditions for film fraction using the conductance ring probes around the vertical 180° return bend at liquid superficial velocity = 0.04 ms⁻¹ at ambient temperature

17 pipe diameters upstream of the bend (Gas superficial velocity (m/s))	45° Gas superficial velocity (m/s)	90° Gas superficial velocity (m/s)	135° Gas superficial velocity (m/s)	21 pipe diameters downstream of the bend (Gas superficial velocity (m/s))
6.38	6.38	6.38	6.38	6.38
7.8	7.8	7.8	7.8	7.8
8.87	8.87	8.87	8.87	8.87
10.01	10.01	10.01	10.01	10.01
10.78	10.78	10.78	10.78	10.78
11.52	11.52	11.52	11.52	11.52
12.28	12.28	12.28	12.28	12.28
12.61	12.61	12.61	12.61	12.61
12.92	12.92	12.92	12.92	12.92
13.25	13.25	13.25	13.25	13.25
13.70	13.70	13.70	13.70	13.70
14.03	14.03	14.03	14.03	14.03
14.34	14.34	14.34	14.34	14.34
14.78	14.78	14.78	14.78	14.78
15.12	15.12	15.12	15.12	15.12

15.33	15.33	15.33	15.33	15.33
15.60	15.60	15.60	15.60	15.60

Table A.7: Air/water flow experimental conditions for film fraction using the conductance ring probes around the vertical 180° return bend at liquid superficial velocity = 0.08 ms⁻¹ at ambient temperature

17 pipe diameters upstream of the bend (Gas superficial velocity (m/s))	45° Gas superficial velocity (m/s)	90° Gas superficial velocity (m/s)	135° Gas superficial velocity (m/s)	21 pipe diameters downstream of the bend (Gas superficial velocity (m/s))
5.72	5.72	5.72	5.72	5.72
7.03	7.03	7.03	7.03	7.03
8.09	8.09	8.09	8.09	8.09
9.04	9.04	9.04	9.04	9.04
9.92	9.92	9.92	9.92	9.92
10.79	10.79	10.79	10.79	10.79
11.49	11.49	11.49	11.49	11.49
11.89	11.89	11.89	11.89	11.89
12.29	12.29	12.29	12.29	12.29
12.49	12.49	12.49	12.49	12.49
13.08	13.08	13.08	13.08	13.08
13.25	13.25	13.25	13.25	13.25
13.72	13.72	13.72	13.72	13.72
14.18	14.18	14.18	14.18	14.18
14.56	14.56	14.56	14.56	14.56
14.90	14.90	14.90	14.90	14.90
15.22	15.22	15.22	15.22	15.22

Table A.8: Air/water flow experimental conditions for film fraction using the conductance ring probes around the vertical 180° return bend at liquid superficial velocity = 0.1 ms⁻¹ at ambient temperature

17 pipe diameters upstream of the bend (Gas superficial velocity (m/s))	45° Gas superficial velocity (m/s)	90° Gas superficial velocity (m/s)	135° Gas superficial velocity (m/s)	21 pipe diameters downstream of the bend (Gas superficial velocity (m/s))
4.64	4.64	4.64	4.64	4.64
6.68	6.68	6.68	6.68	6.68
7.74	7.74	7.74	7.74	7.74
8.81	8.81	8.81	8.81	8.81
9.59	9.59	9.59	9.59	9.59
10.46	10.46	10.46	10.46	10.46
11.24	11.24	11.24	11.24	11.24
11.55	11.55	11.55	11.55	11.55
11.88	11.88	11.88	11.88	11.88
12.33	12.33	12.33	12.33	12.33
12.74	12.74	12.74	12.74	12.74
13.12	13.12	13.12	13.12	13.12
13.44	13.44	13.44	13.44	13.44
13.83	13.83	13.83	13.83	13.83
14.14	14.14	14.14	14.14	14.14
14.52	14.52	14.52	14.52	14.52
14.8	14.8	14.8	14.8	14.8

Table A.10: Air/water flow experimental conditions for film fraction using the conductance ring probes around the vertical 180° return bend at liquid superficial velocity = 0.2 ms⁻¹ at ambient temperature

17 pipe diameters upstream of the bend (Gas superficial velocity (m/s))	45° Gas superficial velocity (m/s)	90° Gas superficial velocity (m/s)	135° Gas superficial velocity (m/s)	21 pipe diameters downstream of the bend (Gas superficial velocity (m/s))
3.45	3.45	3.45	3.45	3.45
6.06	6.06	6.06	6.06	6.06
7.18	7.18	7.18	7.18	7.18
8.18	8.18	8.18	8.18	8.18
9.07	9.07	9.07	9.07	9.07
9.92	9.92	9.92	9.92	9.92
10.78	10.78	10.78	10.78	10.78
11.1	11.1	11.1	11.1	11.1
11.47	11.47	11.47	11.47	11.47
11.74	11.74	11.74	11.74	11.74
12.15	12.15	12.15	12.15	12.15
12.52	12.52	12.52	12.52	12.52
12.88	12.88	12.88	12.88	12.88
13.28	13.28	13.28	13.28	13.28
13.58	13.58	13.58	13.58	13.58
13.93	13.93	13.93	13.93	13.93
14.22	14.22	14.22	14.22	14.22

Table A.11: Air/water flow experimental conditions for liquid film thickness distribution using pin and wire probes within the vertical 180° return bend at ambient temperature

Liquid superficial velocity = 0.02 ms⁻¹

45° Gas superficial velocity (m/s)	90° Gas superficial velocity (m/s)	135° Gas superficial velocity (m/s)
6.17	6.17	6.17
8.56	8.56	8.56
9.42	9.42	9.42
10.31	10.31	10.31
11.05	11.05	11.05
11.83	11.83	11.83
12.52	12.52	12.52
12.98	12.98	12.98
13.25	13.25	13.25
13.68	13.68	13.68
13.97	13.97	13.97
14.22	14.22	14.22
14.63	14.63	14.63
14.96	14.96	14.96
15.31	15.31	15.31
15.50	15.50	15.50
16.05	16.05	16.05

Liquid superficial velocity = 0.04 ms⁻¹

45° Gas superficial velocity (m/s)	90° Gas superficial velocity (m/s)	135° Gas superficial velocity (m/s)
6.38	6.38	6.38
7.8	7.8	7.8
8.87	8.87	8.87
10.01	10.01	10.01
10.78	10.78	10.78
11.52	11.52	11.52
12.28	12.28	12.28
12.61	12.61	12.61
12.92	12.92	12.92
13.25	13.25	13.25
13.70	13.70	13.70
14.03	14.03	14.03
14.34	14.34	14.34
14.78	14.78	14.78
15.12	15.12	15.12
15.33	15.33	15.33
15.60	15.60	15.60

Liquid superficial velocity = 0.08 ms⁻¹

45° Gas superficial velocity (m/s)	90° Gas superficial velocity (m/s)	135° Gas superficial velocity (m/s)
5.72	5.72	5.72
7.03	7.03	7.03
8.09	8.09	8.09
9.04	9.04	9.04
9.92	9.92	9.92
10.79	10.79	10.79
11.49	11.49	11.49
11.89	11.89	11.89
12.29	12.29	12.29
12.49	12.49	12.49
13.08	13.08	13.08
13.25	13.25	13.25
13.72	13.72	13.72
14.18	14.18	14.18
14.56	14.56	14.56
14.90	14.90	14.90
15.22	15.22	15.22

Liquid superficial velocity = 0.1 ms⁻¹

45° Gas superficial velocity (m/s)	90° Gas superficial velocity (m/s)	135° Gas superficial velocity (m/s)
4.64	4.64	4.64
6.68	6.68	6.68
7.74	7.74	7.74
8.81	8.81	8.81
9.59	9.59	9.59
10.46	10.46	10.46
11.24	11.24	11.24
11.55	11.55	11.55
11.88	11.88	11.88
12.33	12.33	12.33
12.74	12.74	12.74
13.12	13.12	13.12
13.44	13.44	13.44
13.83	13.83	13.83
14.14	14.14	14.14
14.52	14.52	14.52
14.8	14.8	14.8

Liquid superficial velocity = 0.2 ms^{-1}

45° Gas superficial velocity (m/s)	90° Gas superficial velocity (m/s)	135° Gas superficial velocity (m/s)
3.45	3.45	3.45
6.06	6.06	6.06
7.18	7.18	7.18
8.18	8.18	8.18
9.07	9.07	9.07
9.92	9.92	9.92
10.78	10.78	10.78
11.1	11.1	11.1
11.47	11.47	11.47
11.74	11.74	11.74
12.15	12.15	12.15
12.52	12.52	12.52
12.88	12.88	12.88
13.28	13.28	13.28
13.58	13.58	13.58
13.93	13.93	13.93
14.22	14.22	14.22

APPENDIX B

UNCERTAINTY AND ERROR ANALYSIS

Uncertainty propagation analysis was performed for liquid, gas and mixture superficial velocities in this study.

If R is a given function of the independent variables $x_1, x_2, x_3, \dots, x_n$. Thus

$$R = R(x_1, x_2, x_3, \dots, x_n) \quad (B.1)$$

Let w_R be the uncertainty in the result and w_1, w_2, \dots, w_n be the uncertainties in the independent variables. If the uncertainties are all given with same odds, then the uncertainty in the result having these odds is given in Holman (1994) as:

$$w_R = \left[\left(\frac{\partial R}{\partial x_1} w_1 \right)^2 + \left(\frac{\partial R}{\partial x_2} w_2 \right)^2 + \dots + \left(\frac{\partial R}{\partial x_n} w_n \right)^2 \right]^{\frac{1}{2}} \quad (B.2)$$

where $\frac{\partial R}{\partial x_i}$ is the partial derivative of R with respect to x_i . If all uncertainties w_i in equation (B.1) are estimated at 95% confidence level, w_R is also estimated at a 95% confidence level. The relative probable error is calculated as $\frac{w_R}{R}$.

The uncertainties in the calculated values of the liquid and gas superficial velocities were estimated as outlined in the following sections.

- a) Liquid (silicone oil) superficial velocity

The liquid superficial velocity (U_{SL}) is calculated from the measured flow rate of silicone oil and the cross-sectional area of the test section (A).

$$U_{SL} = \frac{Q}{A} \quad (B.3)$$

The area A is calculated as $A = \frac{\pi D^2}{4}$. Therefore, U_{SL} can be expressed as a function of Q and D as follows:

$$U_{SL} = \frac{4Q}{\pi D^2} \quad (B.4)$$

The partial derivatives of U_{SL} with respect to Q and D are

$$\frac{\partial U_{SL}}{\partial Q} = \frac{4}{\pi D^2} \frac{\partial}{\partial Q}(Q) = \frac{4}{\pi D^2} \quad (B.5)$$

$$\frac{\partial U_{SL}}{\partial D} = \frac{4Q}{\pi} \frac{\partial}{\partial D} \left(\frac{1}{D^2} \right) = -\frac{8Q}{\pi D^3} \quad (B.6)$$

$$\partial U_{SL} = \pm \sqrt{\left[\left(\frac{\partial Q}{\partial Q} \frac{4}{\pi D^2} \right)^2 + \left(\frac{\partial D}{\partial D} \frac{-8Q}{\pi D^3} \right)^2 \right]} \quad (B.7)$$

where

∂D is the uncertainty in the diameter of the test tube

∂Q is the uncertainty in the measured liquid flow rate.

$$D = 0.067 \text{ m}$$

The uncertainties in the calculated values of U_{SL} are then calculated from equation (B.7)

$$\text{For } Q = \frac{10 \text{ L}}{\text{min}} = 1.667 \times 10^{-4} \text{ m}^3 / \text{s}$$

Based on information provided by the manufacturer of the test tube, ∂D is estimated at $\pm 0.5 \text{ mm}$, and ∂Q is obtained by reading the number in the scale of the liquid

rotameter that has a least count of 20L/min. The uncertainty in reading the liquid rotameter is $\partial Q = 0.5 \times$ the least count

Using these estimates of ∂D and ∂Q , the uncertainties in the calculated values of U_{SL} are calculated using equation (B.7)

$$\partial U_{SL} = \pm \sqrt{\left[\left(1.667 \times 10^{-4} \frac{4}{\pi \times 0.067^2} \right)^2 + \left(5 \times 10^{-4} \frac{-8 \times 1.667 \times 10^{-4}}{\pi \times 0.067^3} \right)^2 \right]}$$

$$\partial U_{SL} = \pm \sqrt{\left[(4.728 \times 10^{-2})^2 + (7.057 \times 10^{-4})^2 \right]}$$

$$\partial U_{SL} = \pm 0.0473 \text{ m/s}$$

b) Superficial gas velocity

The superficial velocity of gas U_{SG} is calculated from the measured mass velocity of air (G) and the density of air (ρ_G).

$$U_{SG} = \frac{G}{\rho_G} \quad (\text{B.8})$$

Also

$$PV = nRT \quad (\text{B.9})$$

$$n = \frac{m}{M} \quad (\text{B.10})$$

$$PV = \frac{mRT}{M}$$

$$PM = \frac{mRT}{V}$$

$$PM = \rho RT$$

$$\rho_g = \frac{PM}{RT} = \frac{P}{RT} \quad (\text{B.11})$$

$$U_{SG} = \frac{GRT}{P} \quad (\text{B.12})$$

The partial derivatives of U_{SG} with respect to T , G and P are

$$\frac{\partial U_{SG}}{\partial T} = \frac{\partial}{\partial T} \left(\frac{GRT}{P} \right) = \frac{GR}{P} \quad (\text{B.13})$$

$$\frac{\partial U_{SG}}{\partial G} = \frac{\partial}{\partial G} \left(\frac{GRT}{P} \right) = \frac{RT}{P} \quad (\text{B.14})$$

$$\frac{\partial U_{SG}}{\partial P} = \frac{\partial}{\partial P} \left(\frac{GRT}{P} \right) = -\frac{GRT}{P^2} \quad (\text{B.15})$$

$$\partial U_{SG} = \pm \sqrt{\left[\left(\partial T \frac{GR}{P} \right)^2 + \left(\partial P \frac{-GRT}{P^2} \right)^2 + \left(\partial G \frac{RT}{P} \right)^2 \right]} \quad (\text{B.16})$$

where ∂P , ∂G and ∂T are the uncertainties in the pressure, mass flux and temperature of the test pipe respectively. Using these estimates of ∂P , ∂G and ∂T , the uncertainties in the calculated values of U_{SG} is calculated using equation B.16.

Sample calculation:

For $q = 1000\text{L}/\text{min}$

$$\partial T = \pm 0.5^\circ \text{C}$$

$$\partial G = \pm 1.234 \text{ kg/m}^2 \text{ s}$$

$$P = 1.013 \times 10^5 \text{ N/m}^2 + 62052.816 \text{ N/m}^2 = 1.6335 \times 10^5 \text{ N/m}^2$$

$$\partial P = \pm 0.5 \text{ psia} = \pm 3445.6 \text{ N/m}^2 \text{ (0.5} \times \text{least count)}$$

$$G = U_{SG} \times \rho_G = 4.727 \text{ m/s} \times 1.2 \text{ kg/m}^3 = 5.6724 \text{ kg/m}^2 \text{ s}$$

$$T = 25^\circ \text{C} = 298^\circ \text{C}$$

$$\partial U_{SG} = \pm \sqrt{\left[\left(0.5 \times \frac{5.6724 \times 8.314}{1.0 \times 10^5} \right)^2 + \left(0.5 \times 3445.6 \times \frac{-8.314 \times 295 \times 5.6724}{(1.0 \times 10^5)^2} \right)^2 + \left(\frac{1.234 \times 8.314 \times 295}{1.0 \times 10^5} \right)^2 \right]}$$

$$\partial U_{SG} = \pm \sqrt{\left[(0.000236)^2 + (0.002397)^2 + (0.0303)^2 \right]}$$

$$\partial U_{SG} = \pm 0.0304 \text{ m/s}$$

c) Mixture superficial velocity

The mixture superficial velocity is obtained from the summation of liquid and gas superficial velocities.

$$U_M = U_{SL} + U_{SG} \quad (\text{B.17})$$

But, the summation of the uncertainties the liquid and gas superficial is given as

$$\partial U_M = \partial U_{SL} + \partial U_{SG} \quad (\text{B.18})$$

$$\partial U_M = \pm \sqrt{(\partial U_{SL})^2 + (\partial U_{SG})^2} \quad (\text{B.19})$$

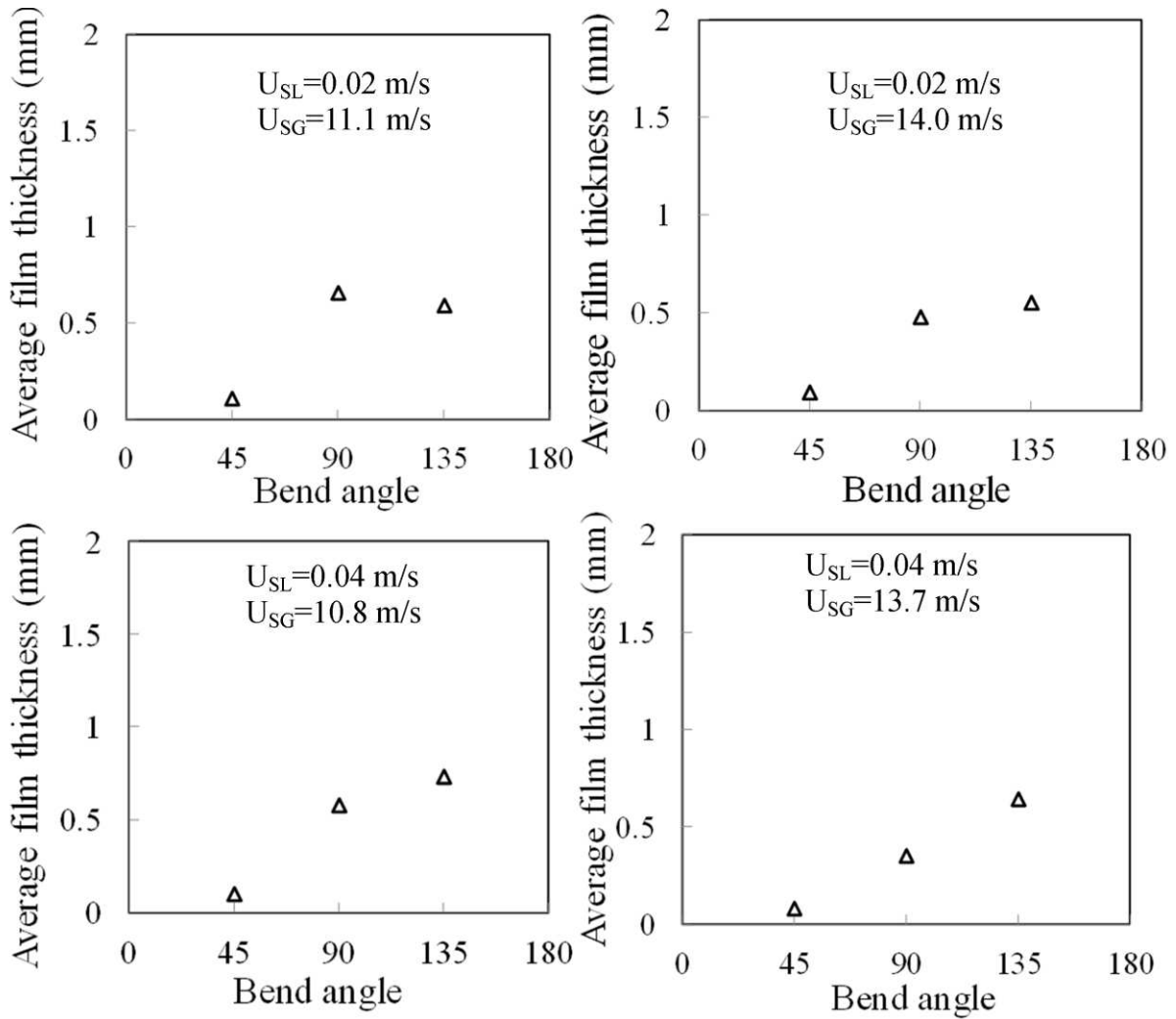
The values of ∂U_{SL} and ∂U_{SG} are then substituted into equation (B.19) to obtain the value of ∂U_M .

$$\delta U_m = \pm \sqrt{[(0.0473)^2 + (0.0304)^2]}$$

$$\delta U_m = \pm 0.0563 \text{ m/s}$$

APPENDIX C

TIME AVERAGED CROSS-SECTIONAL LIQUID FILM IN THE 180° BEND



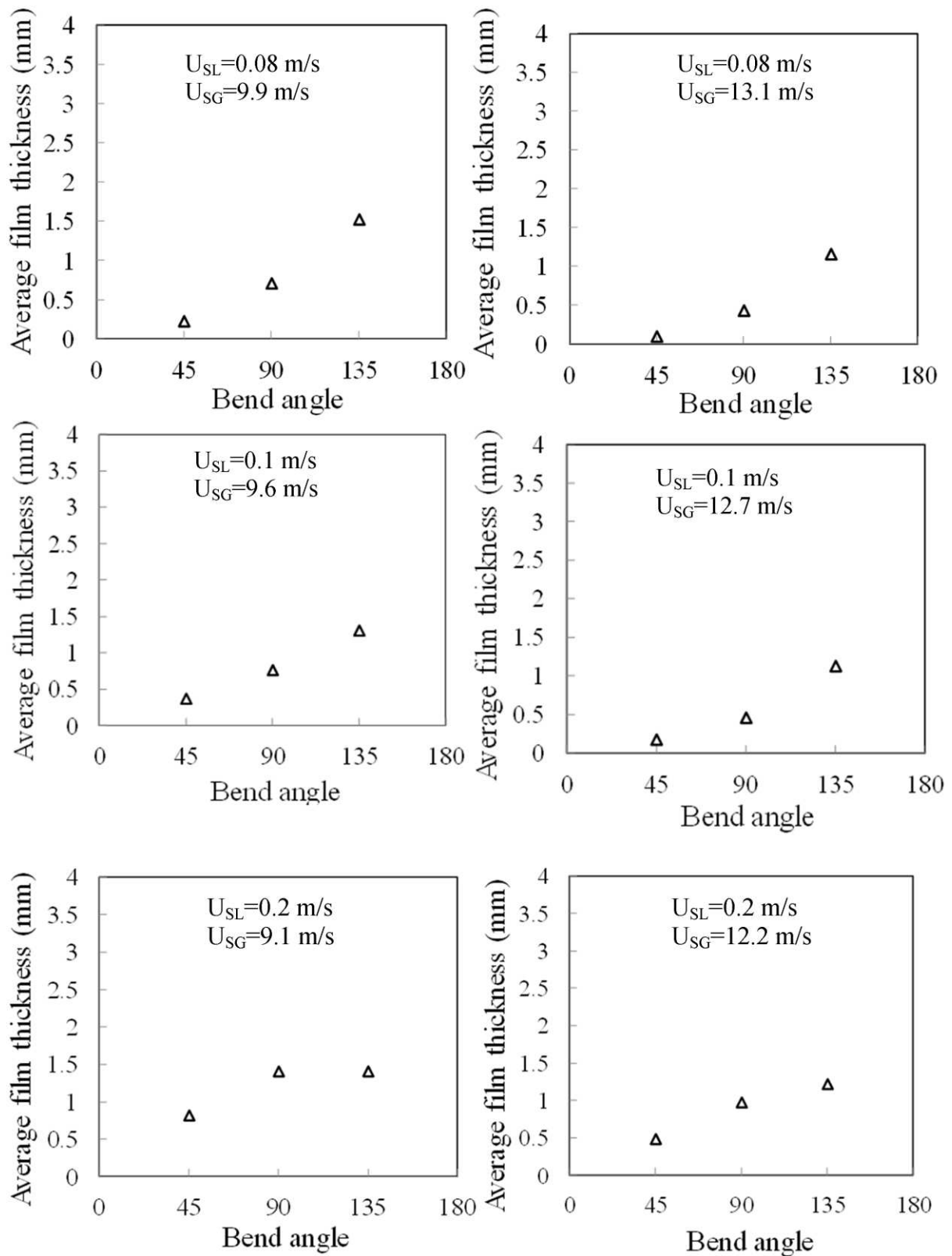
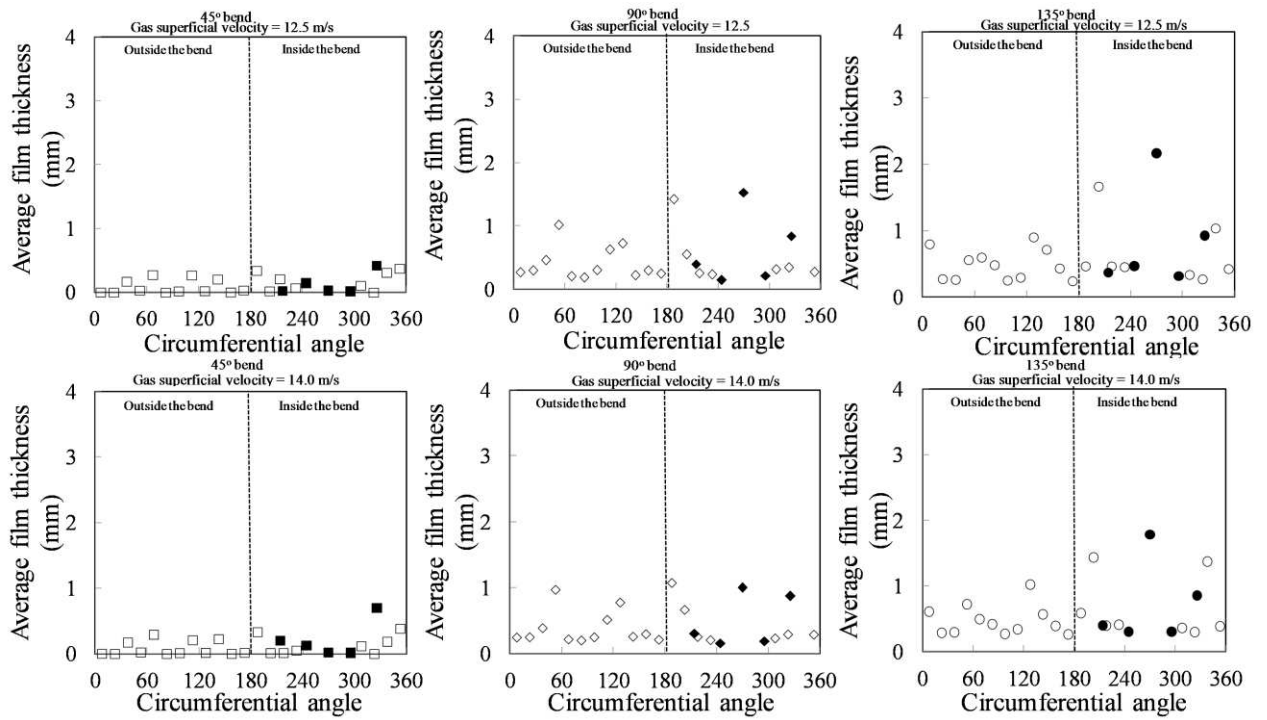
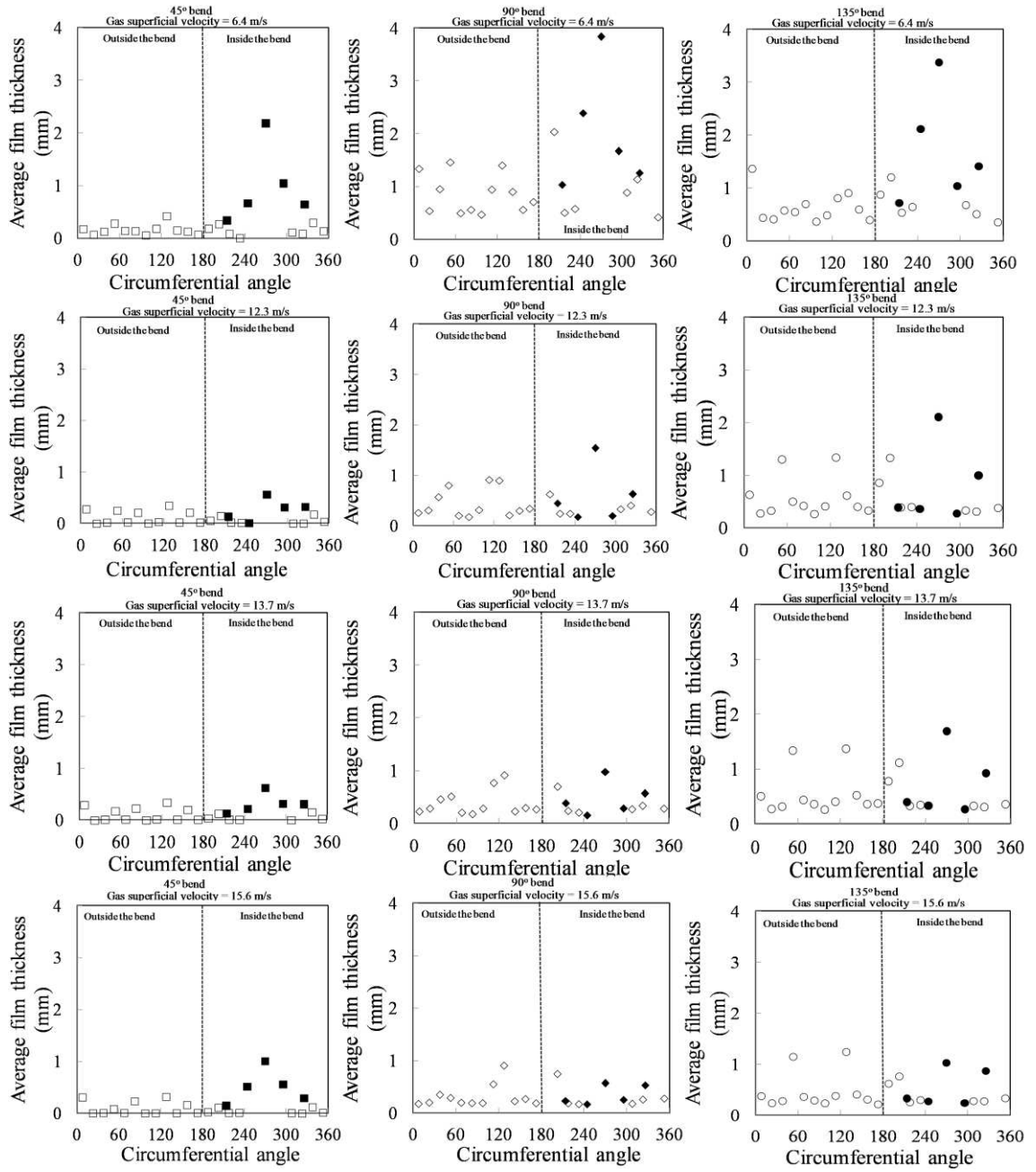


Figure D.1: Variartion of liquid film thickness with the bend angle at liquid superficial velocity of (a) 0.02 ms^{-1} (b) 0.04 ms^{-1} and (c) 0.08 ms^{-1} (d) 0.1 ms^{-1} (e) 0.2 ms^{-1}

APPENDIX D

SPACIAL LIQUID FILM DISTRIBUTION WITHIN THE 180° BEND





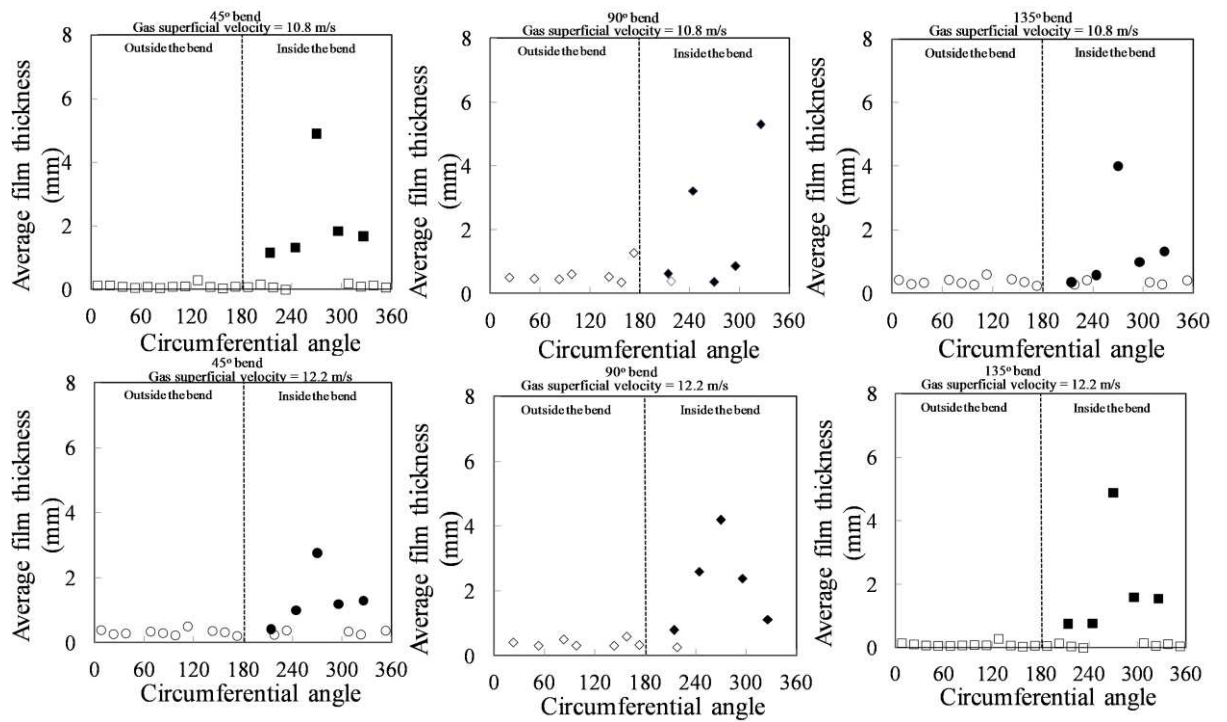


Figure D.1: Spatial liquid film thickness distribution at liquid superficial velocity of (a) 0.02 ms^{-1} (b) 0.04 ms^{-1} and (c) 0.2 ms^{-1} . Closed symbols-wire probes; open symbols-pin probes.